Phase transitions : dynamics and disorder

Francesco Chippari

SORBONNE UNIVERSITÉ

LPTHE
LABORATOIRE DE PHYSIQUE THEORIQUE ET HAUTES ENERGIES

Phase transitions: dynamics and disorder

Thèse de doctorat de Sorbonne Université

Specialité: Physique

École doctorale: Physique en Île-de-France

Realisée au LPTHE

présentée par: Francesco Chippari (fchippari@lpthe.jussieu.fr)

pour obtenir le grade de:
Docteur de Sorbonne Université

Jury composé de:

Prof. **Maria Barbi** (LPTMC, Sorbonne Université) - Examinatrice interne

Prof. **Raffaella Burioni** (Université de Parme) - Examinatrice externe

Dr. **Christophe Chatelain** (LPCT, Université de Lorraine) - Rapporteur

Dr. **Marco Picco** (LPTHE, Sorbonne Université) - Directeur de thèse

Prof. **Pierre Pujol** (LPT, Université de Toulouse) - Rapporteur

Dr. **Marco Tarzia** (LPTMC, Sorbonne Université) - Examinateur interne

Preface

Resumé

Cette thèse présente une étude détaillée sur les transitions de phase, se concentrant principalement sur le modèle q-Potts. Elle utilise une combinaison de méthodologies numériques et analytiques pour explorer un large spectre de sujets en mécanique statistique, incluant la dynamique associée aux transitions de phase du premier ordre, les impacts de la topologie du réseau sur les processus d'équilibrage, et l'évolution des systèmes désordonnés corrélés à longue portée critique sous le flot du groupe de renormalisation.

La première partie de l'étude aborde la dynamique vers l'équilibre au travers d'une transition de phase de premier ordre, en exploitant la limite de grand q du modèle Potts en dimension $d = \{2, 3\}$ après un refroidissement instantané. En utilisant l'algorithme de Monte Carlo de "heat bath", l'existence d'états quasi stable, le phénomène de "freezing" du système et le mécanisme de "coarsening" ultérieur sont minutieusement explorés. De plus, le rôle de la topologie du réseau dans la dynamique du système, et notamment son effet sur les tendances à la congélation, est analysé.

La deuxième partie de la thèse examine le modèle ($q \leq 4$)-Potts critique en deux dimensions avec du désordre corrélé à longue distance via des calculs de Monte Carlo et en tenant compte de différentes distributions de désordre. Un des principaux résultats est l'obtention et l'exploration d'un diagramme de phase avec la description d'un point fixe du flux du groupe de renormalisation du modèle pour $q \in [1, 4]$. Ce diagramme de phase est obtenu en mesurant la dimension fractale des amas FK du modèle de q-Potts au point auto-dual pour différentes valeurs de l'exposant de la loi de puissance a et intensités de désordre r.

Les dernières sections de l'étude étendent l'analyse pour englober des calculs perturbatifs dans le cadre du groupe de renormalisation, générant de nouvelles valeurs pour

les exposants critiques à longue portée. L'application de la méthode du groupe de renormalisation valide les études numériques, confirmant notamment l'existence d'un nouveau point fixe attractif "à longue portée". Un des résultats principaux est le calcul de l'exposant thermique ν^{LR} pour les modèles Potts et Ising, et les déterminations des conditions sous lesquelles la conjecture de Weinrib-Halperin peut être violée pour les distributions de désordre non-Gaussiennes au point fixe.

En résumé, cette recherche contribue à une compréhension plus profonde des comportements du modèle q-Potts avec ou sans désordre. Ces conclusions ouvrent de nouvelles voies pour explorer les transitions de phase et les phénomènes critiques en mécanique statistique.

Abstract

This thesis provides a comprehensive investigation into phase transitions, concentrating predominantly on the q-Potts model. It uses a combination of numerical and analytical methodologies to delve into a broad spectrum of topics within statistical mechanics, including dynamics associated with first-order phase transitions, impacts of lattice topology on equilibration processes, and the evolution of critical long-range correlated disordered systems under the renormalization group flow.

The first part of the study address the equilibration dynamics through a first-order phase transition, exploiting the large q limit of the Potts model in dimension $d = \{2, 3\}$ following instantaneous quenches. Utilizing the heat bath Monte Carlo algorithm, the complexities of metastability, the system's freezing phenomena, and the subsequent escape-coarsening mechanism are thoroughly explored. Additionally, the role of lattice topology in system dynamics, especially its effect on freezing tendencies, is analyzed.

The second part of the thesis scrutinizes the critical disordered two-dimensional ($q \leq 4$)-Potts model, leveraging Monte Carlo methodologies and accounting for varying disorder distributions. A key accomplishment here is the formulation and exploration of a phase diagram that illustrates the fixed point of the renormalization group flow of the model for $q \in [1, 4]$. This phase diagram is created by measuring the fractal dimension of the q-Potts FK clusters at the self-dual point under different power-law exponent a values and disorder intensities r.

The latter sections of the study extend the analysis to encompass perturbative calculations via renormalization group computations, generating new values for long-range

critical exponents. The application of the renormalization group method validates the numerical studies, particularly confirming the existence of a novel "long-range" fixed point attracting the model. One of the key outcomes is the ascertainment of the thermal exponent ν^{LR} for the Potts and Ising models, and the circumstances under which the Weinrib-Halperin conjecture can be violated for a non-Gaussian disorder distribution at this very fixed point.

In summary, this research contributes a more profound understanding of the q-Potts model's behaviors with and without disorder. These findings open new avenues for exploring phase transitions and critical phenomena in statistical mechanics.

Aims and layout of the thesis

The general aim of this thesis is to deepen the knowledge around phase transitions in statistical physics models. The thesis is basically divided into two parts. The first part is about the out-of-equilibrium dynamics through a first-order thermal ferromagnetic-paramagnetic phase transition. The second part is about the study of the influence of a long-range correlated weak quenched disorder on a second-order phase transition. The Potts model [1–4] is used to achieve this goal since it allows the analysis of both phenomena.

The thesis is organized as follows: before splitting it into the two main parts, a general introduction to phase transitions is given. Here, the mathematical tools and physical concepts employed are mostly introduced. The introduction is an "operative" one, indeed concepts do not follows the classic flow of a statistical physics book. Instead, notion are introduced as and when required to describe the particular facets of the phenomenon in analysis.

On one hand, the first part is based on the findings presented in [5, 6] about the kinetics of the Potts ferromagnetic-paramagnetic transition. The results obtained in this part are mostly numerical.

On the other hand, the second part is rooted in the findings of [7, 8] about the influence of disorder on phase transitions. In this part, new analytical results will be compared with new numerical results.

Finally, the conclusion section will synthesize and merge all the findings of this PhD work.

1 List of publications

1. F. Chippari, L. F. Cugliandolo, and M. Picco, **"Low-temperature universal dynamics of the bidimensional Potts model in the large q limit"**, Journal of Statistical Mechanics: Theory and Experiment, vol. 2021, no. 9, p. 093201, 2021.

2. F. Chippari and M. Picco, **"Freezing *vs.* equilibration dynamics in the Potts model"**, Journal of Statistical Mechanics: Theory and Experiment, vol. 2023, no. 2, p. 023201, 2023.

3. F. Chippari, M. Picco, and R. Santachiara, **"Long-range quenched bond disorder in the bidimensional Potts model"**, Journal of Statistical Mechanics: Theory and Experiment, vol. 2023, no. 4, p. 043301, 2023.

4. F. Chippari, M. Picco, and R. Santachiara, **"Two-dimensional Ising and Potts model with long-range bond disorder"**, arXiv:2306.01887, preprint, 2023.

2 Major results

1. Universal $d = 2$ low temperature dynamics in the $(q \gg 1)$-Potts model and location of the (pseudo)-spinodal temperature.

2. Characterization of the $d = 3$ dynamics of the cubic $(q \gg 1)$-Potts model with location of the (pseudo)-spinodal and definition of a topological criterium to distinguish whether the dynamics will freeze or not.

3. Numerical phase diagram of the long-range random bond Potts, Ising and $q \to 1$ percolation limit. Description of the geometrical features of random clusters.

4. Renormalisation group reconstruction of the aforementioned long-range random bond Potts and Ising model's phase diagram. Proof that the Halperin-Weinrb argument is broken for a non-Gaussian disorder at 2-loops. New analytical long-range fixed points and critical exponents.

Contents

Chapter 1

General and common introduction

1.1 Phenomenology and historical introduction

It is a common knowledge that substances like water appear in different states of aggregation or phases. They can indeed exist in the liquid, solid (ice), or gas (vapor) phases.

In these three states of matter, atoms and molecules are arranged and aggregated in an extremely different way. For example, in ice, there is a crystalline structure, while water does not have one. Also, in water, molecules are kept together by means of weak hydrogen bonds, while this does not happen in gases, leading to a lower density in the latter. This induces intrinsic and fundamental physical differences among the distinct states. Indeed, these phases do not share the same mechanical properties, heat capacity, or optical features, *etc.*

Another piece of shared and common knowledge is that lowering liquid water's temperature to about $T_s = 0°$ C brings it to ice, while heating water around $T_g = 100°$ C makes it boil. T_s and T_g are the so called critical temperatures of the solidification and vaporization phase transitions, respectively. As could be simply understood by its name, a phase transition is a physical transformation between two different phases. These transition phenomena are ubiquitous in the most diverse domains of science, ranging from the simple liquid-gas transition described before, to the ferromagnetic-paramagnetic transition in the Ising model, to which all the statistical physicists refer, to the more disparate industrial processes in nuclear plants.

The mathematical and physical description of these phenomena is far from being as easy as its definition, so it is better to start with a simple phenomenological analysis. One can start by considering a generic experiment in which a piece of solid is in contact with an external bath. After some time, the solid and the bath reach thermal equilibrium and share the same temperature. Temperature is thus a tunable parameter describing the experimental setting. As has been said for water, tuning its temperature leads to a phase transition, the same can be done in this generic experiment. Temperature is therefore the simplest example of what, in statistical physics, is a control parameter. Other examples of this kind of parameter are magnetic field (h), pressure, *etc.*

The experimentalist also needs something to properly describe the different phases of the transition in analysis. What is usually done in these cases is to define a so called order parameter. This is a parameter that assumes two strongly different values being on one side or the other of the transition threshold. For this experiment, an order parameter, which usually is an intensive quantity (*i.e.* independent of the size of the system), can be the density (ρ) of the material, being extremely different in the liquid phase and in the solid phase. It is not always simple to define an order parameter, and there are also transitions which happen without such a quantity. In the following part of this manuscript, this is going to be analyzed in a deeper way.

So, the experimentalist can tune the control parameter (T) and measure the order parameter ($\rho(T)$) as a function of the control one, building what is called a phase diagram, see for example Fig. (1.1). By building such diagrams, the experimentalist can locate the point in the order parameter curve where a net and sharp change emerges. At this point, the order parameter assumes what is called a critical value, which manifests to the experimentalist that a phase transition has occurred. Thus, building such diagrams provides an helpful point of view in the description of the global behavior of the piece of material in analysis.

The study of phase transitions has brought significant contributions to the field of statistical physics. It has allowed for a better understanding of the behavior of matter and systems at different temperatures, pressures, and other control parameters, and has provided insights into the fundamental nature of the universe.

Specifically, these studies have led to the development of powerful theoretical tools, such as the renormalisation group, scaling theory and numerical algorithms, that can be used to describe a wide variety of phenomena. These tools have been used to make predictions about the behavior of complex systems, such as magnets, fluids, and even the early universe, and have been verified through numerous experimental studies.

Moreover, by studying phase transitions, scientists were led to the discovery of new states of matter, such as the Bose-Einstein condensate, which has opened up new avenues of research in condensed matter physics and beyond. The investigation of phase transitions has also yielded practical applications, including the development of novel materials with tailored properties, as well as the design of industrial processes.

In the following there is just an extremely short list of books and articles coming from studies related to phase transitions and statistical physics that have been crucial in a direct or indirect way, for building the mathematical and physical set up who lead to the writing this thesis:

- 1738 - Daniel Bernoulli publishes "Hydrodynamica," in which he presents his kinetic theory of gases, laying the foundation for statistical physics, [9].
- 1872 - Ludwig Boltzmann formulates the concept of entropy in statistical mechanics, explaining the connection between the microscopic behavior of atoms and the macroscopic behavior of matter, [10].
- 1905 - Albert Einstein introduces the concept of Brownian motion, [11].
- 1938 - László Tisza and Lev Landau independently develop the concept of phase transitions, describing the sudden changes in the behavior of matter that occur at critical points, [12, 13].
- 1944 - Lars Onsager solves the bidimensional Ising model, providing a mathematical framework for understanding phase transitions and establishing the field of critical phenomena, [14].
- 1957 - Hugh Everett Broadbent and John Michael Hammersley, contributed to the mathematical field of percolation theory, which studies the behavior of connected clusters in a random graph. [15].
- 1970s - Kenneth Wilson develops the renormalisation group, a powerful mathematical tool for understanding critical phenomena and phase transitions, which allows physicists to study the behavior of systems at all scales, [16].
- 1973 - Rodney Baxter solves the $d = 2$ Ising model by developing the method of corner transfer matrices, which becomes a powerful technique for solving a wide range of $d = 2$ statistical models, like the Potts'one. [17]
- 1975 - Philip W. Anderson proposes Anderson localization, describing the phenomenon of disorder-induced localization of electronic states in disordered systems, [18].
- 1984 - Giorgio Parisi proposes the replica symmetry breaking solution to the glass transition problem, which explains the complex behavior of glasses and disordered systems and led it to the nobel prize in 2021, [19, 20].
- 1985 - Amnon Aharony and Dietrich Stauffer propose the concept of percolation transitions, which describe the abrupt change in connectivity of a system as a function of a control parameter, [21, 22].

1.2 Thermodynamics of phase transition

Phase transitions are collective phenomena that arise due to interactions among an extensive number of entities, such as particles, spins, *etc.* To describe these phenomena properly in an actual thermodynamic setup, the thermodynamic limit is crucial. This limit is defined as the number of entities being sent to infinity, as long as the volume of the system. This is because the critical point is usually located by spotting non-analyticities of the thermodynamic potential, such as the Helmholtz free energy [23]. These non-analyticities manifest themselves only in this particular limit. Thus, since it is needed to deal with an infinite number of interacting particles, the branch of theoretical physics

tailored for these kinds of analyses is statistical physics, as appointed before. The basic principles of Statistical Physics are stated in many works; here is just a short list: [23–28].

Again, using the mathematical and physical tools provided by this theoretical setting, various phenomena can be studied, ranging from simple gas-liquid transitions to Bose-Einstein condensation in ultra-cold atoms [29], as well as percolation [30] and paramagnetic-ferromagnetic phase transitions [28], which are crucial for the understanding of this work.

To initiate a phase transition, the control parameter, such as temperature, magnetic field, or occupation probability, needs to be triggered below (or above) the critical point. During a transition, a phase becomes unstable under the given thermodynamic conditions, resulting in a sharp change of physical observables, including the most important order parameter. Thanks to the order parameter it is possible to give information and characterize the features of the phase in analysis. The most common order parameters are magnetization density [28], probability of being in a percolating cluster [30], mass density *etc.* The order parameter has to be selected depending on the analysed transition, and as said previously, this is not always an easy task. For thermal phase transitions, the order parameter has a vanishing thermal value above the critical point and a non-vanishing value below it, and this makes less complicated its choice. The deeper the system is in that phase, the greater the value of the average of the order parameter. This statistical average is calculated with respect to the probability distribution function that defines the statistical ensemble describing the system [23].

Once selected the proper order parameter, one aims to locate the critical curves of the control parameters in the phase diagram and investigate the so called critical phenomenon that occur near the phase transition, when a critical phenomenon is present. The presence or not of the so called critical phenomenon, leads to distinction and classification between different classes of phase transitions. Indeed, these can be categorized based on different criteria such as the presence or absence of an order parameter and the nature of the transition (continuous or discontinuous). A common way of classification is based on the behavior of the order parameter close to the critical point.

In continuous phase transitions or second order ones, the order parameter changes smoothly as the control parameter is varied and critical exponents describe the scaling behavior of thermodynamic quantities close to the critical point. Examples of continuous phase transitions include the Ising model, liquid-gas transitions and superconducting transitions [24, 25]. In all the second order phase transitions one can study the formerly mentioned critical phenomenon. Indeed, at the critical points, systems have a peculiar scale invariance behaviour due to the divergence of the correlation length, see Sec. (1.3). Observables, thus, follows particular power laws and unusual properites arise, *i.e.* emergent behaviour. In essence, critical phenomena, happering in second order phase transitions, encompass the distinctive behavior observed in physical systems when they approach their critical points. These phenomena are marked by scale invariance and power-law scaling. Another peculiar distinction, regarding second order phase transitions, is the one due to the fact that these can belong to a certain class of universality.

Indeed, two completely different systems made by different microscropic constituents, can have the same macroscopic behavior close to the phase transition, *i.e.* the same critical expontents. Phenomena sharing the same critical exponents, thus, belong to the same universality class. Universality classes and critical exponents are concept that will be better analysed in the followings section, see Sec. (1.3).

Conversely, discontinuous or first order phase transitions represent a type of phase transformation where a system's characteristics undergo non-continuous changes. The first order label is derived from mathematical continuity concepts and relates to the shift seen in the system's thermodynamic properties. These transitions exhibit a sudden shift in these variables that can't be mapped with a continuous function, leading to a discontinuous order parameter. A latent factor, such as latent heat, typically characterizes these transitions. This refers to the energy either absorbed or released by a system during a phase transition under stable temperature and pressure conditions. This principle is particularly applicable to transitions such as melting (from solid to liquid) and evaporation (from liquid to gas), where heat is absorbed, and solidification (from liquid to solid) and condensation (from gas to liquid), where heat is released. In first order phase transitions, hysteresis can occur. This is a phenomenon where the transition temperature of a system is not only reliant on the current conditions but also on the system's past states. Hysteresis is exemplified by the temperature difference at which a substance melts and freezes. During a first order transition, both initial and final phases can exist simultaneously. For example, during the melting process (from solid to liquid), both the solid and liquid states can be present at the melting point.

Topological phase transitions [31,32], instead, are another class of phase transitions that do not involve an order parameter but are characterized by changes in the topology of the system's ground state or excited states. These transitions can even occur at zero temperature, dragged by quantum fluctuaions and examples include the quantum Hall effect and Superfluid-Mott Insulator in the Bose-Hubbard model [33, 34]. Those two latter kinds of transition, will not be considered in this thesis, while first and second order ones will be extensively deepened respectively in the first and second part of this thesis.

The phase diagrams in Fig. (1.1), in which the control parameters versus the order parameters are shown, giving two examples of the two kinds of phase transitions mentioned before.

In the analysis of critical phenomena, mean-field theories [23, 24, 28] have proven to be very useful in capturing the overall behavior of macroscopic systems, although they cannot reproduce details such as the functional form of order parameters and peculiarities of critical phenomena. However, these provide insight into what is happening and help the understanding of the quantitative behavior of real systems. In contrast, another theory called scaling theory [25,35] has been successful in describing the phenomenology of phase transitions and has been justified by the development of renormalisation group ideas [16, 25], which allow for the calculation of critical exponents. These two latter

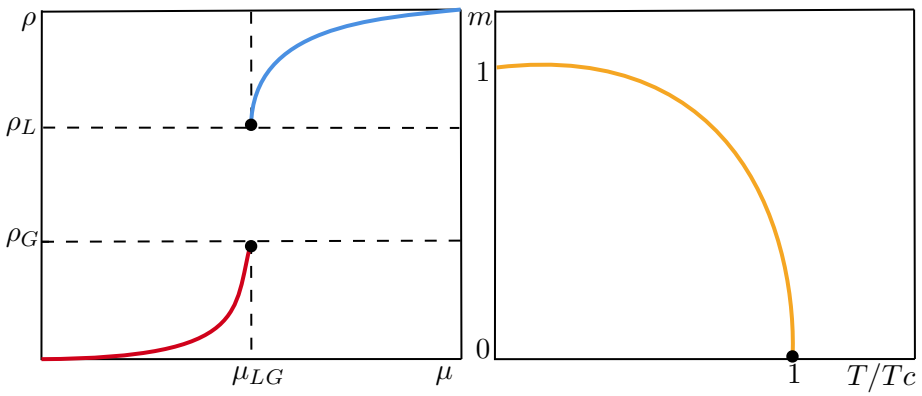

Figure 1.1. Phase diagram for the liquid-gas first order phase transition on the left and for the ferromagnetic-paramagnetic second order phase transition in the Ising model on the right. On the y axis the order parameter is shown while on the x axis there is the control parameter. T_C and μ_{LG} are the critical points.

tools, contrary to mean field theories, will be largely used to obtain the results given by this work.

As said previously, phase transitions involve an huge number of interacting entities. This, is mathematically modelled by the, already quoted, thermodynamic limit. This is then defined by, $V \to \infty$, $N \to \infty$, with $V/N = O(1)$, where V is the volume of the system and N, is its number of particles or spins. This limit applies to all intensive quantities, such as density of energy and density of magnetization, and it is responsible of the non-analyticites at the transition point. To locate the sought non-analyticites it is needed to define the statistical ensemble and the thermodynamic potential [23] employed. If not explicitely stated, in this work, the ensemble is the canonical one and its related thermodynamic potential is the Helmotz free energy, $\mathcal{F}$.

1.2.1 Ferromagnetic-paramagnetic transition and the Ising model

It is, thus, possible to give a brief describtion of a well known phase transition, the ferromagnetic-paramagnetic one in the bidimensional Ising model, to warmp up with the tools and methods. This model gives a simplified version of an actual ferromagnet whose Hamiltonian has been coarsened up until only the degrees of freedom describing a magnetic properties are left, *i.e.* the so called Ising classical spins, s_i. The Ising model [2, 4, 14, 23–25, 28, 36], is the milestone of the statistical toy-models, but is far from being poor of interesting features. Indeed, its study has contributued strongly in the developent of an enormous number of tools and concepts, extremely important in statistical physics, and beyond. In dimensions d, on a discrete regular lattice, it is

defined by the Hamiltonian:

$$\mathcal{H}_I(\{s_i\}) = -J \sum_{\langle i,j \rangle} s_i s_j, \tag{1.1}$$

where there are $N = L^d$ of such s_i spins on the vertices of this generic lattice, whose side is L. The sum is restricted to nearest neighbors on the lattice, $\langle i, j \rangle$. J is the coupling constant describing the interaction among spins. In particular, the value of such spins is discrete, *i.e.*

$$s_i = \begin{cases} +1 \text{ spin up}, \\ -1 \text{ spin down}. \end{cases} \tag{1.2}$$

This Hamiltonian has a $\mathbb{Z}_2$ symmetry, indeed $\mathcal{H}_I(\{s_i\}) = \mathcal{H}_I(\{-s_i\})$, *i.e.* flipping all the spins conserves the energy of the model. The sign of J, defines if the energy is the lowest when spins are all aligned *i.e.* all up (down), or antialigned. In the first case, J is strictly positive, $J \geq 0$ and the model handled is a ferromagnetic one. This is the one who passes trough a ferromagnetic-paramagnetic transition, and it is the model analysed in this chapter. By contrary, if J is strictly negative the model is an anti-ferromagnetic model, and will not be considered in this thesis. As already savored, for the transition in analysis, this energy function, is minimised by having all the spins in the up (down) state. This configuration is the ground state of the ferromagnetic Ising model. It is evident its double degenerancy. This model, does not contain an intrinsic dynamics. Thus, to describe an eventual phase transition, it needs to be coupled to a thermal reservoir, usually called thermal bath, as prescribed by the canonical formulation. The system thus, exchange energy with the bath, and, at thermal equilibrium the concept of temperature comes into play and this can be used as control parameter. In this model the magnetization density $m = \dfrac{1}{N} \displaystyle\sum_{i=1}^{N} \langle s_i \rangle$ serves as the order parameter. The symbol $\langle \cdots \rangle$ means mean value with respect to the chosen statistical ensemble. So, in the ground states the magnetisation is equal to, $m_0 = 1$. This is just a naive explication, indeed to prove that the state with magnetisation $m_0 = 1$ is a stable ground state one can use the Peirl's argument, [37]. Also, being $d = 2 < d_{uc}$, where d_{uc} is the upper critical dimension, implies that mean field techniques, which usually simplify the computations, are not exact. Thus one is left to solve the model in fully glory *à la* Onsager, [14], or by means of numerical simulation and scaling arguments. Solving the model means computing the partition function and the free energy, to whom all physical observable are linked. The partition function is simply defined by:

$$\mathcal{Z} = \sum_{\{s_i\}} e^{-\beta \mathcal{H}_I(\{s_i\})}, \tag{1.3}$$

where β is the inverse temperature, *i.e.* $\beta = 1/k_B T$, with k_B the renowed Boltzmann factor and $\sum_{s_i}(\cdots)$ the sum over all the possible spin configuration of the model. The free energy $\mathcal{F}$, it is instead defined by:

$$\mathcal{F} = -\frac{1}{\beta}\log \mathcal{Z}, \tag{1.4}$$

and finally, in the canonical ensemble at equilibrium:

$$\langle s_i \rangle = \frac{1}{\mathcal{Z}} \sum_{\{s_i\}} s_i e^{-\beta \mathcal{H}_I(\{s_i\})}. \tag{1.5}$$

Onsager solution is way beyond the aim of this introduction, for this reason details will not be given on this. Still, by using thermodynamics principles is it possible, with a simple argument, to give some informations about the phases of the model. In particular,

$$\mathcal{F} = \langle \mathcal{H} \rangle - T\mathcal{S}, \tag{1.6}$$

where $\langle \mathcal{H} \rangle$ is the internal energy and $\mathcal{S}$ is the entropy of the system.

The minima of the free energy correspond to thermodynamical stable states. Of course, the ground state is located at the absoulute minimum. Thus, in $\mathcal{F}$ there is an energy-entropy competition. The interplay between the contributions of energy and entropy in a system can result in a phase transition at a specific temperature.

Setting the control parameter, $T \to 0$, it is obtained that the free energy is equivalent to the internal energy, and in a system with ferromagnetic couplings between adjacent spins, the energy is minimized when these are aligned, as stated before. However, at finite temperatures, thermal agitation comes into play and the entropic factor is woken up. Indeed, entropy can cause the spins to reorient and misalign. At infinite temperature, for example, the entropic contribution dominates, and spins point in completely random directions to maximize entropy. This means that the internal energy goes to zero. The order parameter assumes very different values at low and high temperatures, indeed:

$$m = \begin{cases} \pm 1, \ T \to 0 \\ 0, \ T \to \infty. \end{cases} \tag{1.7}$$

What does this mean? This is an evidence of the appearence of a phase transition at a certain temperature T_c, since the order parameter assumes extremely different as a function of the control parameter.

Yet, this transition is far from being fully mathematically characterised. Indeed, emphasis should still be placed on the fact that a divergence in the thermodynamic potential is possible only if $N \to \infty$, since the $\mathcal{Z}$ function is a sum of positive and analytic terms. Also, due to the $\mathbb{Z}_2$ symmetry the magnetization should be zero for each T. How it is possible to have the ordered state, so?

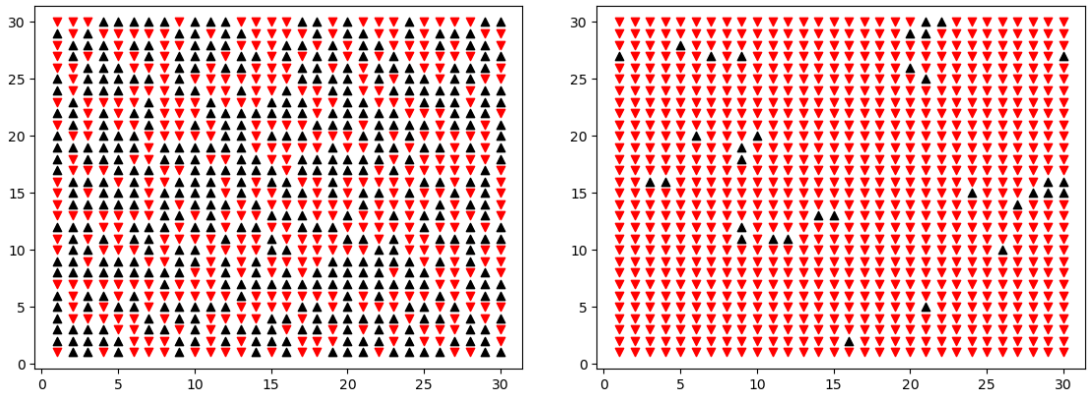

(a) Above T_c. **(b)** Below T_c.

Figure 1.2. Disordered and ordered configuration in the bidimensional ferromagnetic Ising model with nearest neighbour interaction on an $L = 30$ square lattice. Black spins are pointing down ($s_i = -1$), while red ones are pointing up ($s_i = +1$). The Wolff algorithm, [38], has been employed to obtain the equilibrium configuration.

The transition, moreover, breaks also the ergodicity [23, 24, 28] of the system. This, is a feature of certain systems whereby they explore all feasible configuration over time, and each of these has an equal probability of occurring. In simpler terms, a system is regarded as ergodic if its average behavior over time is equivalent to its behavior observed over multiple identical systems, *i.e.* ensemble average. As a result, the statistical features of a system can be deduced by averaging across numerous identical systems rather than monitoring its behavior over time, this is known as Gibbs hypothesis and it is very important in statistical physics, [23]. To see this ergodicity breaking, one needs to introduce the concept of time and a certain generic spin dynamics into play. Once this has been done, one can notice that statistical average of the magnetisation $\langle s_i \rangle$ and the temporal one $\overline{s_i} = \dfrac{1}{t_{mes}} \displaystyle\int_0^{t_{mes}} dt' s_i(t')$, with t_{mes} finite, are conceptually different. In fact, in the low temperature phase the statistical average is always supposed to be zero, but this is not the case for the time average. This means that ergodicity is broken. Indeed, one needs to sent t_{mes} to infinity and wait for an extremely rare thermal fluctuation who made all the spins flip in order to restore ergodicity.

Also, to properly describe the phenomenon and solve these problems, one needs to introduce a pinning field, h, and the concept of spontaneous symmetry breaking. The Hamiltonian becomes, thus:

$$\mathcal{H}_I(\{s_i\}, h) = -J \sum_{\langle i,j \rangle} s_i s_j - h \sum_{i=1}^{N} s_i. \tag{1.8}$$

The h field models the small residual magnetic field that is not detectable by instruments and is normally present during experiments. This, indeed, breaks the $\mathbb{Z}_2$ symmetry and describe the spontaneous breaking of this symmetry at the critical point. The right way to obtain a non zero magnetisation is thus,

$$m = \lim_{h\to 0^+} \lim_{N\to\infty} \langle s_i \rangle = - \lim_{h\to 0^-} \lim_{N\to\infty} \langle s_i \rangle. \tag{1.9}$$

Once the h field has been added to the model, one can also consider it as a control parameter and study the magnetisation in function of this. One obtains that the $m = 0$ whenever $h = 0$, while it is $m \neq 0$ for $h \neq 0$. A discontinuoity in m comes out. What does this mean? To answer one can notice that,

$$m = -\frac{1}{N}\frac{\partial \mathcal{F}}{\partial h}. \tag{1.10}$$

Thus, a discontinuity in m is trivially related to a non analiticity in $\mathcal{F}$. This means that the transition with respect to the magnetic field is a first order one or discontinous one.

In short, during the transition, the $\mathbb{Z}_2$ symmetry is spontaneously broken and this is modelled by the addiction of the pinning field. This kind of transitions are called transition with spontaneous symmetry breaking (SSB). For a transition with spontaneous symmetry breaking, self-evidently, the system has phases with different symmetry elements.

1.3 Statistical field theory: coarse graining a first approach

If one is not interested in the individual micro-state but aims to study the model's phenomenology in a broader sense, a shift in approach may lead to valuable insights from a lattice point of view. Particularly, in the vicinity of the critical point, it is possible to develop a continuous formulation and employ field theory tools such as Feynman diagrams to examine the critical point's neighborhood *i.e.* to study the critical phenomenon in second order phase transitions. This region is crucial for understanding the model's phenomenology [25, 39].

The motivation behind limiting the validity of field theories to the vicinity of the critical point lies in the coarse graining process involved in constructing such theories. To build these theories, one must introduce some fundamental observables in statistical physics, namely, the correlation function and the correlation length [39].

The correlation function, which is a covariance, is defined as:

$$G(r) = \langle s_i s_j \rangle - \langle s_i \rangle \langle s_j \rangle, \tag{1.11}$$

where, r represents the distance between the positions of spin i and spin j. It is worth noting that, due to the spatial translational invariance, this quantity depends solely on

the distance between the two spins. One can write:

$$G(r) = e^{-r/\xi}. \tag{1.12}$$

Here, ξ denotes the correlation length, which represents the typical length scale at which the correlation function deviates from zero. In other words, it characterizes the system by indicating the length scale below which spin fluctuations are correlated. Notably, the correlation length is divergent (in the thermodynamic limit) at the transition point. This can be explained by the fact that a collective phenomenon, involving all the system's entities, happen at the transition point [23, 24]. Consequently, thermal fluctuations of these variables are correlated at all length scales.

Therefore, in the vicinity of the critical point, one can follow the below-mentioned procedure. Given that $\xi \gg l$, where l is the lattice spacing, one can divide the lattice into boxes of a certain linear size l_{box}, such that $a \ll l_{box} \ll L$. These boxes can be represented by a spatial variable x, which corresponds to their center. Then, observables can be averaged within these boxes, and for each position x, a continuous value $\phi(x)$ can be assigned as follows: $\phi(x) = \dfrac{1}{(l_{box})^d} \displaystyle\sum_{i \in \, box} s_i$. This operation is known as coarse graining, and thanks to its construction, $\phi(x)$ is a smooth field. This, is ensured by the fact that boxes are correlated being, $\xi \gg l_{box}$. This approach provides information about the system from a coarser viewpoint, and the order parameter is represented as a field $\phi(x)$. This is a field description of a lattice model or a statistical field theory.

By utilizing the model's symmetries, one can construct the ϕ^4 action, denoted by $\mathcal{S}[\phi(x)]$, see Eq. (1.13). This action allows the characterisation of the phenomenology of phase transitions by using coefficients such as $r(T)$ and $c(T)$, as well as quantum field theory techniques like Feynman diagrams [39]. In practice, these coefficients are challenging to compute from axioms, so intuitive arguments are used to fix them phenomenologically, ensuring that they accurately reproduce the continuous transition when crossing T_c.

$$\mathcal{S}[\phi(x)] = \int d^d x \, \frac{1}{2} r(T) \, \phi^2(x) + \frac{1}{2} \, c(T) (\nabla \phi(x))^2 + \phi^4(x) + \cdots \tag{1.13}$$

With the ϕ^4 action, one can study the second order phase transition in the Ising model, particularly the critical phenomenon *i.e.* compute the critical exponents [39]. The actual computation of these goes beyond the sake of this introduction. But, it is well known that for this type of model, physical observables follow power laws in proximity of the critical point.

For the Ising model, in dimension d, one has:

$$m \sim |T - T_c|^{\beta} \tag{1.14}$$
$$\chi \sim |T - T_c|^{-\gamma} \tag{1.15}$$
$$\xi \sim |T - T_c|^{-\nu} \tag{1.16}$$
$$\mathcal{C}_v \sim |T - T_c|^{-\alpha} \tag{1.17}$$
$$G(r) \sim r^{-(d-2+\eta)} \tag{1.18}$$

where $\chi = \frac{\partial m}{\partial h}|_{h=0}$ is the magnetic susceptibility, and $\mathcal{C}_v = \frac{\partial \langle H \rangle}{\partial T}$ is specific heat per spin.

The set, $\{\alpha, \beta, \gamma, \eta\}$ are the critical exponents of the Ising transition [28, 39].

It happens that models with the more disparate microscopic details have the same critical exponents, *i.e.* they are in the same class of universality. This is one of the most beautiful results of statistical physics [16] and it is due to the fact that, at the transition point, or in its neighborhood, the entities of the system are correlated at every scale, so one loses the importance of microscopic details. More precisely, these exponents do not depend on the Hamiltonian, as long as it brings to a transition of the second order, nor on the lattice details. They only depend on the dimensionality d, which is far from being a microscopic detail, and on the tensorial dimension of the order parameter[1], $\mathcal{D}$, which is a scalar for what concerns this thesis. $(d, \mathcal{D})$ form a class of universality.

This overall structure close to the critical point is actually common to all equilibrium critical phenomena, and these ideas are strongly related to one of the most important tools of statistical field theory, the renormalisation group (RG). With this tool one can study critical phenomena in second order phase transitions and compute the critical exponents of Eq. (1.14). The second part of this thesis is rooted in this method, thus a more precise introduction to this will be given in the following.

1.4 Phase transition and the Potts model

The Potts model is a comprehensive and versatile model used to investigate phase transitions [1,2,4]. It is an extension of the Ising model where the spin variables have q integer values (often interpreted as colors) and are coupled ferromagnetically to their nearest neighbors, favoring equal spin values (colors). The analysis of its critical properties has been instrumental in the development of the conformal field theory apparatus [40] and, more recently, the bootstrap approach has been applied to this problem [41–43]. The impact of quenched randomness on the order and universality of phase transitions has been mainly studied using weakly disordered Potts ferromagnets as a paradigm [8,44–47]. The second part of this thesis focuses on the study of this particular phenomenon for

[1] Indeed, the order parameter can be a scalar, a vector, a matrix.

long-range correlated disorders. In addition to statistical physics, this model is widely used in many research fields, such as biophysics and bioinformatics to investigate protein evolution and folding [48, 49], quantitative social sciences and network theory [50], or high-energy physics [51] to study the quark gluon plasma-hadron first order phase transition in the scattering of heavy ions. The model is defined by:

$$\mathcal{Z} = \sum_{\{s_i\}} e^{-\beta \mathcal{H}_P(\{s_i\})}, \tag{1.19}$$

with the Hamiltonian given by:

$$\mathcal{H}_P[\{s_i\}] = -J \sum_{\langle i,j \rangle} \delta_{s_i,s_j}, \tag{1.20}$$

where $J > 0$, $s_i = \{1, \ldots, q\}$ and the sum runs over nearest-neighbors on the lattice (each bond contributing once to the sum). In this work periodic boundary conditions are always considered. At the critical temperature, the model experiences an equilibrium phase transition that can be either of the first or second order, depending on the value of q and the dimension of the space, d. In two dimensions ($d = 2$), the transition is of second order for $2 \leq q \leq 4$, while for $q > 4$, it is of first order. In $d = 3$, instead the transition become of the first order already for $q > 2$. In the first part of this thesis, the analysis of the discontinuous phase transitions will be crucial. In particular, the large q limit ($q \gg 1$ and $q \to \infty$) will be employed to study the kinetics of the ferromagnetic paramagnetic transition in the Potts model. For this reason, it is worth to determine the critical temperature in this very limit, in $d = 2$ and $d = 3$. The critical temperature is determined by various factors such as the coupling strength (J), the dimension (d), and the coordination of the lattice (z). On the square lattice, $z = 4$ and [1, 2, 4], lead to:

$$T_c^{\text{square}} = \frac{J}{\log\left(1 + \sqrt{q}\right)} \quad \to \quad T_c^{\text{square}} \simeq \frac{2J}{\log q}, \quad \text{for } q \gg 1. \tag{1.21}$$

($k_B = 1$ henceforth). On the triangular and honeycomb lattices the critical temperatures are given by implicit expressions [2]:

$$\begin{aligned} (i)\ 0 &= x^3 - 3x + 2 - q && \text{triangular } z = 6\,, \\ (ii)\ 0 &= x^3 - 3x^2 - 3(q-1)x + 3q - 1 - q^2 && \text{honeycomb } z = 3\,, \end{aligned} \tag{1.22}$$

with $x = e^{\beta_c J}$ and $\beta = 1/T$. In the large q limit $\beta_c J \gg 1$, implying $x^3 \gg x^2 \gg x$, and

$$T_c^{\text{triang}} \simeq \frac{3J}{\log q}, \qquad T_c^{\text{honey}} \simeq \frac{3J}{2\log q}. \tag{1.23}$$

Therefore, in the three cases

$$T_c \simeq \frac{zJ}{2\log q}, \text{ for } q \gg 1. \tag{1.24}$$

and T_c decreases logarithmically with q.

The critical temperature, T_c, in $d = 3$ dimensions has not been rigorously determined analytically, in contrast to the situation in $d = 2$. Instead, numerical simulations can be used to obtain T_c as a function of q. However, it is possible to obtain an approximate value of T_c by comparing the probability of a paramagnetic state to that of a ferromagnetic state. This approach has been used in several recent studies [5, 6], and provides a reasonably accurate estimate of T_c for large values of q. The argument proceeds as follows (hereafter assuming $J = 1$). Just like the Ising case, at high temperatures, the system is disordered and paramagnetic. Thus, the probability of each disordered state can be approximated by $\mathcal{P}_{dis} \simeq q^N/\mathcal{Z}$. On the other hand, at low temperatures, the system is ordered and ferromagnetic. For each completely ordered state, the probability can be approximated by $\mathcal{P}_{ord} \simeq e^{\beta N z/2}\mathcal{Z}$, where z is the coordination number of the lattice and $\beta = 1/T$. A visual representation of this argument is provided in Fig. (1.3). At the critical temperature T_c, these two probabilities should be equal.

$$e^{\beta_c N z/2} = q^N, \tag{1.25}$$

and thus $\beta^*(q) \simeq (2/z)\log(q)$, where the index β^* is used to differentiate it from the exact value β_c. Note that this argument is valid in any dimension.

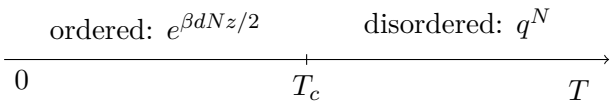

Figure 1.3. Different phases and their total Boltzmann weight as a function of the temperature for the d dimensional q states Potts model, taken from [6].

In $d = 2$, $z = 4$ for the square lattice, this simple argument predicts $\beta^*(q) = \frac{1}{2}\log(q)$. The exact result, given in Eq. (1.21), [4] is $\beta_c(q) = \log(1+\sqrt{q}) = \frac{1}{2}\log(q) + q^{-\frac{1}{2}} + \cdots$. Thus in the large q limit, $\beta^*(q)$ goes to the exact result with a correction $O(1/\sqrt{q})$. One can also consider the case of the triangular lattice with $z = 6$. The argument's prediction is $\beta^*(q) = \frac{1}{3}\log(q)$. The critical value is obtained by solving the equation: $x^3 - 3x + 2 - q = 0$, Eq. (i) (1.22) with $x = e^{\beta_c}$. For $q > 4$, the solution is given by:

$$x = 2\cosh\left\{\frac{2}{3}\log\left(\frac{\sqrt{q}}{2} + \left(\frac{q}{4} - 1\right)^{\frac{1}{2}}\right)\right\}. \tag{1.26}$$

In the large q limit, the leading orders are $\beta_c(q) = \frac{1}{3}\log(q) + q^{-2/3} + O(q^{-1})$ which again converges toward $\beta^*(q)$. For the honeycomb lattice with $z = 3$, one needs to solve the equation: $x^3 - 3x^2 - 3(q-1)x + 3q - 1 - q^2 = 0$, Eq. (ii) (1.22), for which it is obtained $\beta_c(q) = \frac{2}{3}\log(q) + \frac{\sqrt{5}-1}{2}q^{-1/3} + \cdots$, compared with $\beta^*(q) = \frac{2}{3}\log(q)$. Thus this naive argument gives a good approximation in $d = 2$ in the large q limit.

After verifying the argument in a bidimensional setting, the analysis is extended to the three-dimensional case. However, unlike the bidimensional scenario, no theoretical predictions for the critical temperature are available for comparison. Therefore, the determination of the critical temperature relies on numerical measurements.

To illustrate this, one can consider the cubic lattice where, in the large q limit, $\beta^* = \frac{1}{3}\log(q)$. To numerically determine the critical temperature for finite q, two simulations are conducted for each q value.

In the first simulation, the system starts from a completely ordered state at zero temperature and the temperature is gradually increased to a high value T_1. The simulation is continued until a disordered state is reached, which indicates that the critical temperature has been crossed. This process is repeated with decreasing T_1 values, and the smallest temperature value that yields a disordered state before a fixed large time (chosen as $t_{max} = 20000 \times L^3$ updates) is defined as T_c^+. A non-local cluster algorithm, the Swendsen–Wang algorithm [52], is used for all simulations due to its smaller autocorrelation time near the critical point compared to local algorithms.

In the second simulation, the system starts from a completely disordered state and is gradually cooled to a low temperature T_2. The simulation is continued until an ordered state is reached. This process is repeated with increasing T_2 values, and the highest temperature value at which an ordering is observed within a time less than t_{max} is defined as T_c^-. The critical temperature is defined as $T_c = (T_c^+ + T_c^-)/2$, with $\Delta T_c = |T_c^- - T_c^+|/2$. The simulations are performed on cubic lattices with periodic boundary conditions of size $L = 32$ for $q \leq 10$ and $L = 10$ for larger values of q. The results are presented in Figure (1.4), which confirms the results obtained in [53,54] for $q = 3$ and $q = 4$.

For large values of q and quenches from high to low temperatures, metastability must be considered [55], this phenomenon will be introduced in Sec. (2.4). In essence, metastable states of a certain dynamical evolution are essentially points of temporary equilibrium or relative minima in the free energy landscape, see Fig. (2.6). A dynamic system can get trapped in these states for prolonged periods before eventually finding its way to the absolute lowest energy state, or the global minimum. This issue can impact the estimation of the critical temperature. In fact, one might mistakenly assume that the system has reached equilibrium after a certain lengthy duration, leading to incorrect assumptions about the system's relative positioning with respect to T_c^-. In reality, the system may still be stuck in a metastable state. As the parameter q increases, the measured T_c^- value is often underestimated because the span of the metastable state expands with q, necessitating more time to reach the true equilibrium state, [55].

Therefore, to mitigate the impact of metastability, only small system sizes ($L = 10$) are simulated when dealing with large q values. The plot in Figure (1.4) shows $\beta_c = 1/T_c$ as a function of q, which is compared with the value $\beta^* = \log(q)/3$. For large q values, the measurements are close to the expected value, although a small deviation exists due to the effect of metastability. A fit to the form $\log(q)/3 + aq^{-b}$ is also presented, with excellent agreement and $a = 0.27(1)$ and $b = 0.35(3)$. The value $b = 1/3$ is imposed in Figure (1.4) and in the subsequent analysis, with $a \simeq 0.267$. Thus, one can concludes saying that for large values of q, $T_c(q) \simeq 3/\log(q)$.

From the fit in Fig. (1.4), it can be obtained $T_c(q = 100) \simeq 3/\log(100) \times (1 - 0.0339)$, $T_c(q = 1000) \simeq 3/\log(1000) \times (1 - 0.0103)$ and $T_c(q = 10000) \simeq 3/\log(q) \times (1 - 0.0035)$, *i.e.* small deviations that are taken into account in the following.

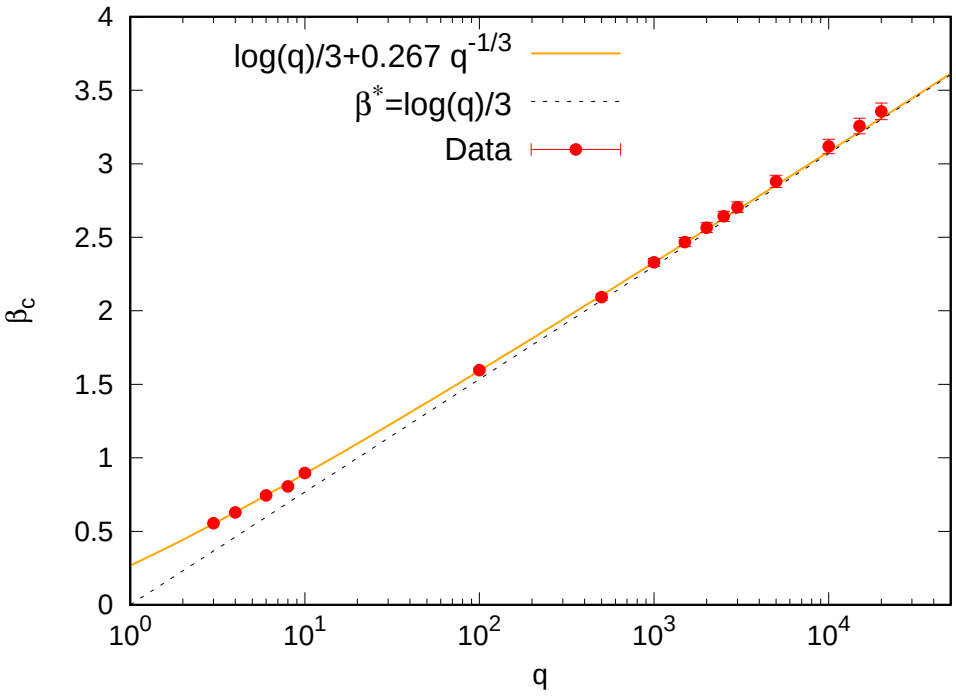

Figure 1.4. β_c as a function of q for the cubic lattice. This is compared to β^* and a best fit to the form $\log(q)/3 + aq^{-1/3}$, taken from [6].

Thus, after this analysis, it can be said that in the large q limit, also for the cubic lattice,

$$T_c \simeq \frac{zJ}{2\log q}, \text{ for } q \gg 1. \tag{1.27}$$

with $z = \{3, 4, 6, 6\}$ respectively for the honeycomb, square, triangular and cubic lattices.

1.5 Kinetic point of view of phase transitions

While the thermodynamical (equilibrium) theory of phase transitions is centered around the characterization of the equilibrium phases of a certain phase transition, the kinetic theory investigates how, dynamically, those phases are formed. In this section, principles and tools of this theory are given for non disordered (pure) systems. This section aims in introducing to the first part of the thesis.

As said previously, the Potts or the Ising models are not featured with an intrinsic dynamics. One, so, couples the spin degrees of freedom to a certain thermal bath at a temperature T and introduces thermal fluctuations into play. Because of this, spins can change their state following a given dynamics. For the sake of this introduction, the so called Glauber dynamics [27, 56–58] suits perfectly.

The Glauber dynamics for the Ising model, on a regular lattice with coordination $z = 4$, for example, follows these rules:

1. At a certain instant of time, a spin of the system is chosen randomly, $s_i(t)$.
2. The $\mathcal{S}_{um} = \sum_{j \in \mathcal{N}(i)} s_j(t)$ is computed. In this realm, $j \in \mathcal{N}(i)$ means the set of neighbors of the i-spin.
3. The energy difference of the eventual flip of the i spin, $\Delta\mathcal{E} = 2 \times s_i(t) \times \mathcal{S}_{um}$, is computed.
4. The spin is actually flipped, *i.e.* , $s_i(t + \delta t) = -s_i(t)$ with probability, $\mathcal{P}^{flip} = \dfrac{e^{-\beta\Delta\mathcal{E}}}{1 + e^{-\beta\Delta\mathcal{E}}}$.
5. Iterate.

In studies of equilibrium, the properties of the transition are completely determined once the partition function is computed. However, in non-equilibrium studies, the properties and features of the phenomenon depend on the chosen dynamics. Nonetheless, if equilibrium is ultimately achieved, different types of dynamics should lead to the same equilibrium properties.

This is guaranteed if the dynamics satisfies a certain condition known as the detailed balance condition [27]. The chosen dynamical settings in this work adhere to all the conditions imposed by the detailed balance condition. As a result, all the simulated dynamical processes using different microscopic dynamical rules ultimately converge to the same equilibrium properties. The subsequent sections will provide more information on algorithms and the detailed balance condition.

Therefore, with this knowledge, the analysis of the equilibration processes towards a first order phase transition can begin, which is one of the objectives of this thesis.

Readers interested in a comparable dynamic analysis can refer to Burioni's work [59], which uses the Ising model and explores continuous phase transitions. Specifically, this study investigates quench dynamics across various lattice structures, including fractal ones.

1.5.1 Quench dynamics and the Potts model

As mentioned several times, the ferromagnetic Potts model in $d = 2$ undergoes a ferromagnetic-paramagnetic phase transition when brought to a sub-critical temperature. The most common approach to simulate this phenomenon is to quench it from a super-critical temperature to a sub-critical one. This involves starting with a disordered configuration, $T_i \to \infty$, and then rapidly quenching to $T \leq T_c$. As a result, the microscopic spin dynamics begin to align the spins. For the Potts model, this means that larger and larger clusters of spins with the same color gradually start to appear. This phenomenon continues until the equilibrium configuration is reached. Typically, the equilibrium configuration comprises large islands with flat and stable interfaces, or, if the temperature is very close to zero, a completely ordered state of spins with the same color. This is a simplified view of the equilibration phenomenon. In reality, by tuning parameters such as the final temperature T, the number of states q, the dimensionality d, and the lattice topology, one can experience extremely different dynamical regimes. This makes the Potts model a perfect laboratory for analysing this transition.

Indeed, the primary focus of the first part of this thesis is to investigate how the different dynamical behaviors of the process, by which equilibrium is reached in this particular ferromagnetic-paramagnetic first order phase transition, are influenced by these parameters.

An example of a disordered initial lattice configuration and a partially ordered final configuarion, is shown in Fig. (1.5) through snapshots of the lattice at the initial and final time.

1.5.2 Out-of-equilibrium statistical physics tools

To address these phenomena, some out-of-equilibrium techniques are necessary. In fact, when the system experiences the shock of passing instantaneously from $T_i \to \infty$ to $T < T_c$, it needs to stabilize. To do so, it reorganizes itself to minimize the free energy in the new phase. Because the quench is very rapid, the system does not have the means to equilibrate without exploring some out-of-equilibrium steady states. In fact, by performing a quasi-static transformation (*i.e.* changing the control parameter very slowly), the system finds its final configuration by going through only equilibrium states, which are usually analyzed by equilibrium statistical mechanics and thermodynamics.

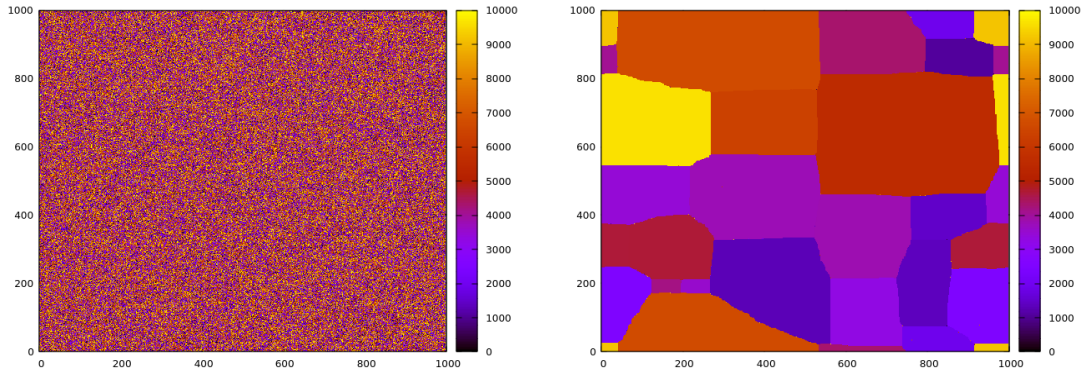

(a) Initial disordered configuration after 10 Monte Carlo steps.

(b) Evolved configuration with cluster of aligned spin and some flat interfaces after $3{\cdot}10^6$ Monte Carlo steps.

Figure 1.5. Example of initial and final configuration for a Potts model simulation with $q = 10^4$, $T = 0.90T_c$ and $L = 1000$.

This is not the case for instantaneous quenches. The references [27, 58, 60–62] provide a comprehensive and detailed explanation of equilibrium and non-equilibrium states. However, delving into such topics is beyond the scope of this thesis. It is sufficient to understand that the thermodynamic ordered and disordered states, occurring in the low and high temperature phases, represent the equilibrium states. States other than these two are classified as non-equilibrium states. There are various approaches to this kind of out-of-equilibrium physics, but, for the purposes of this thesis, the numerical one is the most useful. Indeed, the equilibration phenomena have been extensively simulated by means of massive Monte Carlo simulations.

Monte Carlo-Markov chains

A Markov process can be either continuous or discrete in time and is a stochastic process. For simplicity, a discrete formulation of the process is introduced. The process is represented by a state variable x_t, where $t \in \{1, \ldots, T_{fin}\}$ and $x_t \in \Omega$, which is the space of all possible configurations that can be explored by the stochastic process. The dimension of this space is $\| \Omega \| = 2^N$ for the Ising model and $\| \Omega \| = q^N$ for the Potts model.

The distinguishing characteristic of a Markov process, setting it apart from other stochastic processes, is its memorylessness or Markovian property. This means that the probability of transitioning from a current state x_t to the next state in time x_{t+1} depends

solely on x_t, *i.e.* the current state.

$$\begin{aligned}\mathcal{P}_{i,j} = \mathcal{P}_{i\to j} &= \mathcal{P}(x_{t+1} = j | x_t = i, x_{t-1} = i_{t-1}, ..., x_0 = i_0) \\ &= \mathcal{P}(x_{t+1} = j | x_t = i), \forall t, i, j, i_{t-1}, ..., i_0 \text{ allowed.}\end{aligned} \tag{1.28}$$

It is worth noting that the probability distribution function $\mathcal{P}_{i,j}$ depends on the target state j. The transition probabilities $\mathcal{P}_{i,j}$ can be organized into a non-negative matrix $\widehat{\mathbf{P}}$, where the rows add up to one, *i.e.* a stochastic matrix:

$$\widehat{\mathbf{P}} = \begin{pmatrix} \mathcal{P}_{1,1} & \mathcal{P}_{1,2} & \mathcal{P}_{1,3} & \dots & \mathcal{P}_{1,N} \\ \mathcal{P}_{2,1} & \mathcal{P}_{2,2} & \mathcal{P}_{2,3} & \dots & \mathcal{P}_{2,N} \\ \mathcal{P}_{3,1} & \mathcal{P}_{3,2} & \mathcal{P}_{3,3} & \dots & \mathcal{P}_{3,N} \\ \vdots & \vdots & \vdots & \ddots & \vdots \\ \mathcal{P}_{N,1} & \mathcal{P}_{N,2} & \mathcal{P}_{N,3} & \dots & \mathcal{P}_{N,N} \end{pmatrix}. \tag{1.29}$$

One has:

$$\bullet \mathcal{P}_{i,j} > 0, \ \forall i, j, \tag{1.30}$$

$$\bullet \sum_j \mathcal{P}_{i,j} = 1, \ \forall i. \tag{1.31}$$

Markov chains play a critical role in the development of Monte Carlo numerical methods [63], enabling the sampling of ensemble probability distribution functions such as the canonical distribution. To accomplish this, the chain explores all reachable configurations through an ergodic random walk, following mathematical rules that characterize the chain's dynamics. To ensure convergence of the chain to the correct sampled distribution, in this case the Boltzmann distribution, one must establish the microscopic spin dynamics rules that satisfy the detailed balance condition [27, 58, 64].

This is defined by:

$$\pi^{eq}(\{s_i\})\mathcal{P}_{\{s_i\}\to\{s_i'\}} = \pi^{eq}(\{s_i'\})\mathcal{P}_{\{s_i'\}\to\{s_i\}}. \tag{1.32}$$

Where,

- $\{s_i\}$ and $\{s_i'\}$ are two spin configurations differing by just one spin.
- $\mathcal{P}_{\{s_i\}\to\{s_i'\}}$ is the transition probability to go from the configuration $\{s_i\}$ to $\{s_i'\}$.

For a spin model, one defines $\pi^{(t)}(\{s_i\})$ as the time dependent configuration probability, which is straightforwardly, the probability of having such spin configutation $\{s_i\}$ at time t.

At equilibrium, this is described by the ensemble physics, *i.e.*

$$\pi^{eq}(\{s_i\}) = \frac{1}{\mathcal{Z}} e^{-\beta \mathcal{H}_P(\{s_i\})}. \tag{1.33}$$

Heat bath algorithm

An example of Markovian Monte Carlo dynamics for spin systems is the Glauber dynamics [27, 56–58], which is described in Section (1.5).

However, for the type of transition studied in this work, a more appropriate spin dynamics needs to be defined. This is known as the heat bath dynamics [65], named for simulating the dynamics of a system coupled with a heat source much larger than the system itself, a heat reservoir. At each time step, a spin is randomly selected and (eventually) modified. For a system with N spins, one Monte Carlo step consists of N updates. The heat bath rules are formally defined by:

1. By using an uniform probability distribution, a random spin k, between the N available, is chosen.
2. A new state $n \in \{1, \cdots, q\}$, is chosen for the spin s_k, no matter its old value. This, with a probability proportional to the Boltzmann weight, $e^{\beta \mathcal{E}_n}$. This value is drawn from a so called heat bath, thus:

$$\mathcal{P}_{\{s_i\}\to\{s_i'\}} = \mathcal{P}_n(s_k = n) = \frac{e^{-\beta \mathcal{E}_n}}{\sum_{m=1}^{q} e^{-\beta \mathcal{E}_m}}, \tag{1.34}$$

   where:

   - $\{s_i'\} = \{s_1, .., s_k = n, .., s_N\}$, the transition probability depends only on the state in which $s_k = n$.
   - $\mathcal{E}_n = \mathcal{H}_P(\{s_1, .., s_k = n, .., s_N\})$ is the energy of the system if the k_{th} spin assumes the value $n \in \{1, .., q\} \in \mathbb{N}$.

Few things must be noticed:

- The transition probabilities depend only on the final state.
- The algorithm is a single spin flip, where only one spin is changed at each update.
- The probabilities add up to one, and so a spin is modified for each step, even if it is possible to choose the old color again. This corresponds to a ”rejection” in Monte

Carlo terms. However, this is highly unlikely in the large q case, except for certain situations with ordered and stable states.

- This dynamics is non-conservative, meaning that modifying the color of the spins at each update necessarily modifies the magnetization and energy.

It can be proven that the heat bath dynamics fulfils the detailed balance condition, Eq. (1.32) and this ensures the convergence of the numerical method to the right canonical equilibrium state. Indeed:

- To move from a state in which $s_k = n$ to a state with $s_k = n'$ there is a probability $\mathcal{P}_{n'}(s_k = n')$.
- To move back to the state with $s_k = n$ there is a probability $\mathcal{P}_n(s_k = n)$.

thus:

$$\pi^{eq}(\{s_1, .., s_k = n', .., s_N\})\mathcal{P}_n(s_k = n) = \pi^{eq}(\{s_1, .., s_k = n, .., s_N\})\mathcal{P}_{n'}(s_k = n')$$
$$\frac{e^{-\beta\mathcal{E}'_n}}{\mathcal{Z}} \frac{e^{-\beta\mathcal{E}_n}}{\sum_{m=1}^{q} e^{-\beta\mathcal{E}_m}} = \frac{e^{-\beta\mathcal{E}_n}}{\mathcal{Z}} \frac{e^{-\beta\mathcal{E}'_n}}{\sum_{m=1}^{q} e^{-\beta\mathcal{E}_m}} \tag{1.35}$$

The heat bath dynamics algorithm is well-suited for the type of transition being analyzed. At low temperatures and for large q, an algorithm like the Glauber one would require many Monte Carlo steps to find the correct transition, *i.e.* the color which lowers the energy. This is not the case with the heat bath dynamics. In fact, a spin is flipped regardless of its initial state, and rejection in the large q case are extremely rare. This, makes this algorithm much more efficient, in particular it is q times faster than the usual Glauber algorithm. This allows to use rather large lattice sizes.

Continuous time Monte Carlo method

Another important feature can be added to the algorithm to avoid getting too slow in certain situations. The Continuous time Monte Carlo method [66–68] can be used for this purpose. This method is extremely helpful in simulating systems at low temperatures close to a stable configuration. When the system reaches such configurations and T is very close to 0, the algorithm evolves very slowly because it rejects almost every proposed spin-change. This is because for $T \to 0$ or $\beta \to \infty$, the Boltzmann factor $e^{-\beta\mathcal{E}} \to 0$, and the algorithm wastes time while trying to randomly update the configuration. After a large number of Monte Carlo steps, the system may evolve, but it quickly returns to the starting stable state, where it falls again. These states cause the algorithm to visit all possible configurations of the system in an extremely slow way. Although this dynamic behavior is reasonable for a system cooled down to low temperatures, it can

waste a significant amount of computer time. To simplify things and speed up the algorithm, one can say that the system will spend a certain amount of time, sampled from a suitable probability distribution, in the current stable state before moving to an excited one. One, thus, can skip all the useless time-steps and move straight to the time when the excitation is reached. In this method, the time step changes depending on how long one need to wait before the system moves to the next state. In the simulations of Chapter (2), a continuous-time heat bath algorithm has been employed to obtain some of the most important results of this thesis.

1.6 Disordered systems

Disordered systems, which exhibit randomness or disorder in their underlying structure, have been extensively studied across various scientific disciplines and engineering fields. The exploration of disorder systems, spanning condensed matter physics, statistical mechanics, materials science, and complex networks, has yielded valuable insights into the behavior of complex systems.

Disorder can manifest in physical systems through diverse sources, including material impurities, random particle interactions, or heterogeneous environments. While disorder was initially viewed as an undesirable aspect to be minimized or eliminated, it has become increasingly evident that disorder can profoundly influence the properties and behavior of systems. In fact, disorder can give rise to intriguing phenomena, such as phase transitions, localization and the emergence of novel collective effects [19, 20, 44, 69, 70].

However, comprehending and characterizing disorder systems present significant challenges due to their inherent complexity and randomness. Unlike pure systems characterized by well-defined and predictable interactions, disordered systems exhibit intricate and nontrivial behavior. Consequently, studying disordered systems often necessitates sophisticated theoretical frameworks, advanced computational methodologies, and experimental techniques.

Disordered systems and spin models are intimately connected in the realm of condensed matter physics and statistical mechanics. Spin models provide a powerful framework for studying the complex behavior of such systems. These models have been extensively investigated both theoretically and numerically. Theoretical approaches involve techniques like mean-field theory, renormalisation group methods, and replica theory to capture the complex interplay between disorder and spin interactions. While those techniques are rather powerful, the complexity of the problem makes impossible to not use Monte Carlo simulation to study such phenomena.

In this section, and in general when dealing with disordered system in this work, the equilibrium of the spin systems under analysis is restored. This implies that thermal equilibrium has been attained, and the spins no longer undergo flipping according to a particular stochastic dynamics. In other words, the interaction between the spins and the thermal bath can be disregarded. However, the analysis becomes significantly more intriguing and diverse when randomness or disorder is introduced into the system. This has led to incredible breakthroughs in the fields of physics and statistical physics. Two Nobel laureates, Anderson [18] and Parisi [19, 20], are particularly emblematic examples. Their works have paved the way for numerous enthusiastic studies across diverse domains of theoretical and applied physics, spanning over more than a generation [44, 46, 69–76].

In this work, the term ”disorder” has two distinct meanings. The first one, which has already been mentioned, refers to the disordered paramagnetic configuration of the spin system. This occurs when the system is above its critical temperature or in a metastable disordered state where the magnetization (order parameter) is zero. The second meaning,

which is crucial for this section, pertains to the random selection of physical parameters such as the spin couplings $J_{i,j}$ from a probability distribution function. A simple example of such a distribution could be a Gaussian centered at zero with unit variance. This distribution results in random alternations of positive and negative couplings on the lattice, favoring the alignment or antialignment of the spins, respectively. It is evident that this disorder has an impact on the physical properties of the system's phase.

The objective of this section is to familiarize the reader with the realm of disordered systems, enabling a better understanding of the influence of such randomness on phase transitions and facilitating comprehension of the second conceptual part of this thesis. The setup of the addition of disorder to the study is the following:

1. One starts by studying the pure system at thermal equilibrium.
2. Addiction of disorder to the pure system.
3. Examination of the effects of randomness.

The primary focus of this work lies in bidimensional classical spin systems that undergo a second order phase transition. The objective is to examine the impact of randomness when the system is at criticality, specifically to study the effects of disorder on the critical phenomenon.

1.6.1 Different disorders

Disorder can be of the quenched or of the annealed type. Quenched disorder refers to a type of disorder that remains unchanged or "frozen" throughout the system's evolution or analysis. In essence, the disorder remains constant and unaffected by the system's behavior or the passage of time. This form of disorder typically arises from random or disordered parameters, such as impurities scattered within a material or randomly distributed interactions within a spin system. Quenched disorder is considered an inherent property of the system and is often modeled as static or spatially correlated. It can significantly impact the system's behavior, leading to phenomena such as localization, modification of the phase transitions, or the emergence of glassy behavior.

In contrast, annealed disorder refers to a type of disorder that is treated as dynamic and subject to change over time. Here, the disorder is not fixed but rather fluctuates or averages out during the system's evolution. Annealed disorder is commonly associated with a statistical average or ensemble approach, wherein the disorder is treated as a random variable sampled or averaged over. It is often assumed to be uncorrelated or independent of the system's variables. Annealed disorder is frequently employed in theoretical calculations or simulations to simplify the analysis of complex systems.

In the light of this, one can define two kind of averages: the quenchend and annealed averages and, by consequence, the quenched ($\mathcal{F}_q$) and annealed ($\mathcal{F}_a$) free enrgies. The quenched average involves fixing the disorder (*i.e.* the set of couplings $J_{i,j}$) for each thermal integration over the spins. This means that the couplings $\{J_{i,j}\}$ are considered

constant or frozen within a particular realization of the disorder. The average is then taken over different realizations of the disorder. On the other hand, the annealed average treats the disorder and degrees of freedom (spins) on the same footing. The disorder and spins fluctuate together, implying that the time scale of variation for the disorder and spins is the same.

If one calls $\langle \cdots \rangle = \int \mathcal{D}s \, (\cdots) \, e^{-\mathcal{H}(\{s_i\},\{J_{i,j}\})}$ the canonical thermal average and $\mathbb{E}[\cdots] = \int \mathcal{D}J \, (\cdots) \, \mathcal{P}(J_{i,j})$ the average over the disorder distribution $\mathcal{P}(J_{i,j})$, one has:

$$\mathcal{F}_q = -\frac{1}{\beta} \int \mathcal{D}J \, \mathcal{P}(J_{i,j}) \, \log \int \mathcal{D}s \, e^{-\mathcal{H}(\{s_i\},\{J_{i,j}\})} = -\frac{1}{\beta} \mathbb{E} \left[\log \left(\mathcal{Z} \right) \right], \tag{1.36}$$

$$\mathcal{F}_a = -\frac{1}{\beta} \log \int \mathcal{D}J \, \mathcal{P}(J_{i,j}) \int \mathcal{D}s \, e^{-\mathcal{H}(\{s_i\},\{J_{i,j}\})} = -\frac{1}{\beta} \log \left(\mathbb{E} \left[\mathcal{Z} \right] \right), \tag{1.37}$$

with $H(\{s_i\}, \{J_{i,j}\})$ a generic spin Hamiltonian at a fixed disorder $\{J_{i,j}\}$ while $\mathcal{D}J$ and $\mathcal{D}s$ are generic differentials that run over all the values of the bond disorder and of the spins, being them on lattice edges and vertices or in the continuous space. At high temperatures, where the effect of disorder-induced frustration is negligible, the annealed average may be valid. However, at low temperatures, the spins freeze into a state determined by the specific values of the quenched disorder, and the annealed average is generally incorrect. In this work, the only average computed is the quenched one, which will be referred to as simply $\mathcal{F}$, to keep the notation light. However, Eq. (1.36) is made unworkable by the average of the logarithm of a partition function. Thus, one need to introduce a common trick in disordered system, the replica trick, to deal with it, see Sec. (1.6.4).

Another distinction that can be made is between weak and strong disorder: Weak disorder refers to a situation where the disorder has a relatively minor influence on the behavior of the system. The system's behavior and properties are primarily determined by the underlying order or regularity, with disorder introducing only minor deviations or fluctuations *i.e.* the disorder does not modify the phases on one side or the other of the transition. Weak disorder is often associated with scenarios where disorder can be treated as a small perturbation to an otherwise pure system. Analytical techniques, such as perturbation theory, can be employed to study weak disorder effects. An instance of this type of disorder is demonstrated by employing random couplings, all of which are ferromagnetic in nature.

On the contrary, strong disorder refers to a scenario where disorder assumes a prominent role and exerts a profound influence on the characteristics of the system's phases. In particular, the presence of disorder leads to significant modifications in these phases. In such cases, the properties of the system are predominantly governed by the disorder, resulting in behavior that is qualitatively distinct from that of a pure system. Strong dis-

order can give rise to various phenomena such as glassy behaviors, phase transitions, and localization effects. An illustrative example of this type of disorder is the incorporation of random couplings involving both antiferromagnetic and ferromagnetic interactions.

In this work, the emphasis is on weak quenched disorder, which remains fixed and does not alter the phases undergoing transition. For this reason, in this section, only features and properties of this kind of disorder will be introducted. Thus, rather important concepts in disordered systems studies like frustration, glassiness or self averageness will not be touched.

1.6.2 Random bond Potts model

The choice of utilizing the disordered Potts model [77] to study phase transitions is motivated by its versatility and its ability to capture the effects of disorder. In particular, by tuning the parameter q, various scenarios can be explored, ranging from percolation ($q \to 1$), Ising model ($q = 2$) and Potts ($q > 2$). Moreover, the disordered Potts model allows for the investigation of both continuous and discontinuous phase transitions for different values of q, see Sec. (1.4). In particular, this model provides a framework to study how the introduction of different types of disorder can smooth a first order phase transition into a second order one. This last phenomenon will not be touched in this thesis, since the focus is on the modification of the critical behaviour (continuous phase transition) due to the perturbation given by the disorder. To say it better, and to give an insight on what will be in the second part of the thesis, the $d = 2$ pure Potts model is represented at criticality by its continuous formulation in the conformal field theory (CFT) approach. Disorder will be added as a small perturbation to this theory at the non-disordered pure fixed point (P) to study whether the model flows to another fixed point or not. If a flow occurs, the objective is to characterize this fixed point(s) that emerges as a result of the flow.

It is important to note that the P fixed point, is characterized by an interacting theory. This aspect adds significant interest to the study, particularly in comparison to studies that focus on perturbing non-interacting free field theories.

This thesis solely concentrates on bond-type disorders in spin models, while acknowledging that disorders can also be present on the sites of the model, which give rise to distinct phenomena, see all the literature on the random field Ising model [78]. Incorporating disorder into the model involves employing a probability distribution function to randomly draw the couplings or bonds. This implies that:

$$J \to J_{i,j} = J_c + \delta J_{i,j}. \tag{1.38}$$

where J_c is deterministic and $\delta J_{i,j}$ is stochastic. Is it simple to understand that now the couplings are position dependent. Thus,

$$\mathcal{H}_P^{dis}(\{s_i\},\{J_{i,j}\}) = -\sum_{\langle i,j\rangle} J_{i,j}\delta_{s_i,s_j}. \tag{1.39}$$

This approach enables the examination of the influence of disorder on the system's behavior and the resulting phase transitions. When dealing with critical random Potts, $\beta = 1/k_BT$ is usually put to 1, the same will be done in this thesis. One is thus left with $J_{i,j}$ to be tuned in order to be at criticality. How to be at the critical point will be explained in the following. $\beta = 1$, so, implies that the partition function reads:

$$\begin{aligned}\mathcal{Z}_P^{dis}\left(\{J_{ij}\}\right) &= \sum_{\{s_i\}} e^{-\mathcal{H}_P^{dis}(\{s_i\},\{J_{i,j}\})} \\ &= \sum_{\{s_i\}}\prod_{\langle i,j\rangle}\left[1+\underbrace{\left(e^{J_{i,j}}-1\right)}_{v(\{J_{i,j}\})}\delta_{s_i,s_j}\right] \\ &= \sum_{\{s_i\}}\prod_{\langle i,j\rangle}\left[1+v(\{J_{i,j}\})\delta_{s_i,s_j}\right].\end{aligned} \tag{1.40}$$

Considering Eq. (1.40), it is common and useful to extend the number of states, q, of the Potts spins to real numbers and map the Potts model to a random cluster model using the following approach.

In the Potts model, if two neighboring spins s_i and s_j are in the same state, the δ-function equals 1, contributing to a reduction in the configuration's energy by a factor of $-J_{i,j}$. These spins are said to share a bond, suggesting that they belong to the same cluster. When summing over all possible spin configurations in the partition function, it is equivalent to summing over all possible bond configurations, see Fig. (1.6). In other words, if a configuration contains a bond between two neighboring spins, it signifies that they are in the same state.

Let $\mathcal{G}(V,E)$ be a generic graph belonging to the space G of all graphs. $\mathcal{G}(V,E)$ consists of activated bonds (neighboring spins in the same state) with $|E|$ edges and $|V|$ vertices, where E represents the set of possible edges and $|E|$ is the number of edges, and V represents the set of possible vertices and $|V|$ is the number of vertices. Let $\mathcal{C}_c(\mathcal{G})$ denote the number of connected components of this graph. Notably, in the partition function, there is a product of $|E|$ terms composed of two subterms, namely $(1 + v(J_{i,j}\delta_{i,j}))$, representing the presence $(v(J_{i,j}\delta_{i,j}))$ or absence (1) of a bond. This can be expressed as:

$$
\begin{aligned}
\mathcal{Z}_P^{dis}\left(\{J_{ij}\}\right) = \cdots &= \sum_{\{s_i\}} \prod_{\langle i,j\rangle} \left[1 + v(\{J_{i,j}\})\delta_{s_i,s_j}\right] \\
&= \sum_{\mathcal{G}\subset G} q^{\mathcal{C}_c(\mathcal{G})} \left(\prod_{\langle i,j\rangle \in E} v(J_{i,j}) \right) \\
&= \sum_{\mathcal{G}\subset G} q^{\mathcal{C}_c(\mathcal{G})} \left(\prod_{\langle i,j\rangle \in E} \underbrace{e^{J_{i,j}}}_{1/(1-p(J_{i,j}))} \underbrace{(1 - e^{-J_{i,j}})}_{p(J_{i,j})} \right) \\
&= \sum_{\mathcal{G}\subset G} q^{\mathcal{C}_c(\mathcal{G})} \left(\prod_{\langle i,j\rangle \in E} \frac{p(J_{i,j})}{(1-p(J_{i,j}))} \underbrace{\prod_{\langle i,j\rangle \notin E} \frac{1-p(J_{i,j})}{1-p(J_{i,j})}}_{1} \right) \\
&= \sum_{\mathcal{G}\subset G} q^{\mathcal{C}_c(\mathcal{G})} \left(\prod_{\langle i,j\rangle \in E} p(J_{i,j}) \prod_{\langle i,j\rangle \notin E} 1-p(J_{i,j}) \prod_{\langle i,j\rangle} \frac{1}{1-p(J_{i,j})} \right) \\
&= \cancel{\prod_{\langle i,j\rangle} e^{J_{i,j}}} \sum_{\mathcal{G}\subset G} q^{\mathcal{C}_c(\mathcal{G})} \left(\prod_{\langle i,j\rangle \in E} p(J_{i,j}) \prod_{\langle i,j\rangle \notin E} 1-p(J_{i,j}) \right) \\
&= \sum_{\mathcal{G}\subset G} q^{\mathcal{C}_c(\mathcal{G})} \underbrace{\left(\prod_{\langle i,j\rangle \in E} p(J_{i,j}) \prod_{\langle i,j\rangle \notin E} 1-p(J_{i,j}) \right)}_{\pi(\mathcal{G}) \textit{ i.e. } \text{probability of a certain graph.}} \\
&= \sum_{\mathcal{G}\subset G} q^{\mathcal{C}_c(\mathcal{G})} \pi(\mathcal{G}).
\end{aligned}
\tag{1.41}
$$

In the third-to-last line, a global and insignificant factor has been removed. This method of constructing the partition function is known as the Fortuin-Kasteleyn (FK) construction [2, 4, 79], where $p(J_{i,j}) = 1 - e^{-J_{i,j}}$ represents the probability of adding a bond to a so called FK-cluster. In this formulation, the Potts model is equivalent to the random cluster model [79]. By promoting q to real numbers and employing this formulation, this model becomes a powerful tool with a wide range of applications.

The exactly same random cluster construction can be done in the pure Potts case where $J_{i,j} = J$, $\forall(i,j)$. In this case, things become simpler since $v(\{J_{i,j}\}) \to v = e^J - 1$ and thus the partion functions reads:

$$
\mathcal{Z}_P\left(\{J_{ij}\}\right) = \cdots = \sum_{\mathcal{G}\in G} q^{\mathcal{C}_c(\mathcal{G})} v^{|E(\mathcal{G})|}. \tag{1.42}
$$

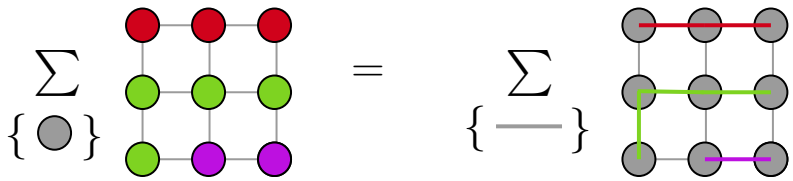

Figure 1.6. Sketch of the mapping between the sum over the spins configurations and the sum over the bond configurations. The q-degenerancy is represented by bonds of different colours.

One is left with the location of the critical point (line). It is well known [2–4, 80] that for the Potts model and for its random version, duality between the low temperature and high temperature expansions of the partition function fixes the critical line to be:

$$(e^{J_1} - 1)(e^{J_2} - 1) = q. \tag{1.43}$$

Where J_1, J_2 and q need to be fixed. One can thus, simply use bimodal couplings fulfilling Eq. (1.43) to be on the, so called, self-dual critical line.

Thus:

$$J_{i,j} = \begin{cases} J_1, \text{ with probability } 1/2. \\ \\ J_2, \text{ with probability } 1/2. \end{cases} \tag{1.44}$$

1.6.3 Percolation

Percolation is a fascinating phenomenon that has captivated the interest of researchers in various scientific disciplines. It is a concept that merge the field of statistical physics with diverse areas such as materials science, network theory, epidemiology, and transportation systems.

At its core, percolation is concerned with the study of connectivity in random or disordered systems. It investigates how the arrangement of components or elements in a system affects the emergence of a continuous path or cluster spanning across the system. This path, known as the percolating cluster, plays a crucial role in determining the system's behavior and properties.

In a percolation process, the system is typically represented as a lattice or a network of interconnected nodes. Each node or site can be in one of two states: occupied or vacant. The occupation of sites is determined probabilistically, following a certain probability distribution. As the occupation probability is varied, the system undergoes a phase transition from a disconnected state to a connected state, thus the occupation probability $\mathcal{P}^{occ}$ is the control parameter.

The critical point of percolation, known as the percolation threshold, $\mathcal{P}_c^{occ}$, represents the transition point where the percolating cluster emerges and spans the entire system. Below this threshold, the system consists of isolated clusters, while above the threshold, a giant connected cluster emerges, connecting the sites from one extremity of the system to the others. This means, that the probability of having a giant cluster, which is zero on the left of the treshold and non-zero on its right, is the order parameter, $\mathcal{P}^{giant}$.

Percolation theory provides a framework to analyze the properties of percolating clusters and their behavior near the critical point. It enables the study of various quantities, such as cluster size distribution, cluster connectivity, fractal dimension of clusters and the scaling behavior of the percolation process.

Understanding percolation phenomena has significant implications in many practical applications. For example, it helps to analyze the flow of fluids through porous media, the conductivity of materials, the spread of diseases in a population, and the resilience of networks to failures. It also serves as a fundamental model for exploring the behavior of complex systems and the emergence of collective phenomena.

For the sake of this thesis, it is important to distinguish between two kinds of percolation processes. The first one is the one shown in Fig. (1.7) in which the percolating cluster is made up of random bonds connecting vertices of the square lattice; this is called bond percolation. Alternatively, one can study the percolation of sites/vertices shown in Fig. (1.8), in which the giant cluster is composed of sites/vertices of the square lattice.

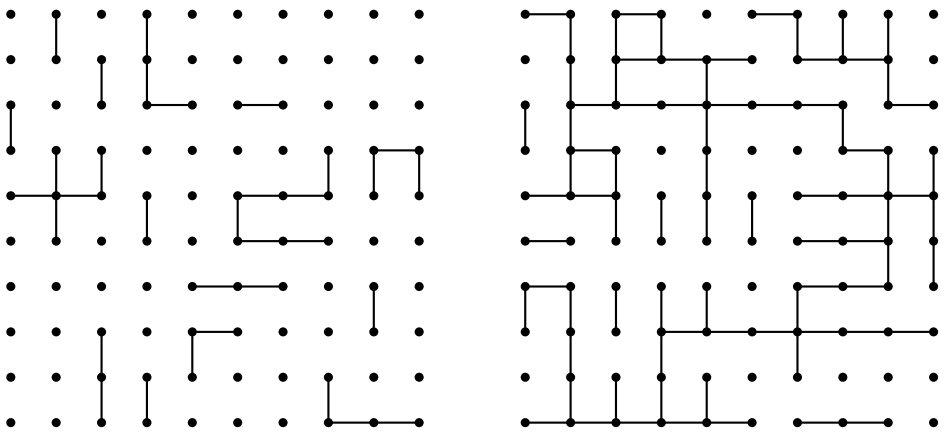

(a) $\mathcal{P}^{occ} < \mathcal{P}_c^{occ}$, implying $\mathcal{P}^{giant} = 0$. **(b)** $\mathcal{P}^{occ} > \mathcal{P}_c^{occ}$, implying $\mathcal{P}^{giant} \neq 0$.

Figure 1.7. Example of not-percolating (a) and percolating (b) clusters of random bond (black lines) on a square lattice.

The location of the critical point depends on geometric properties, such as the underlying lattice topology and the type of percolation being analyzed. For a more detailed analysis, the interested reader is referred to the review by Saberi [30].

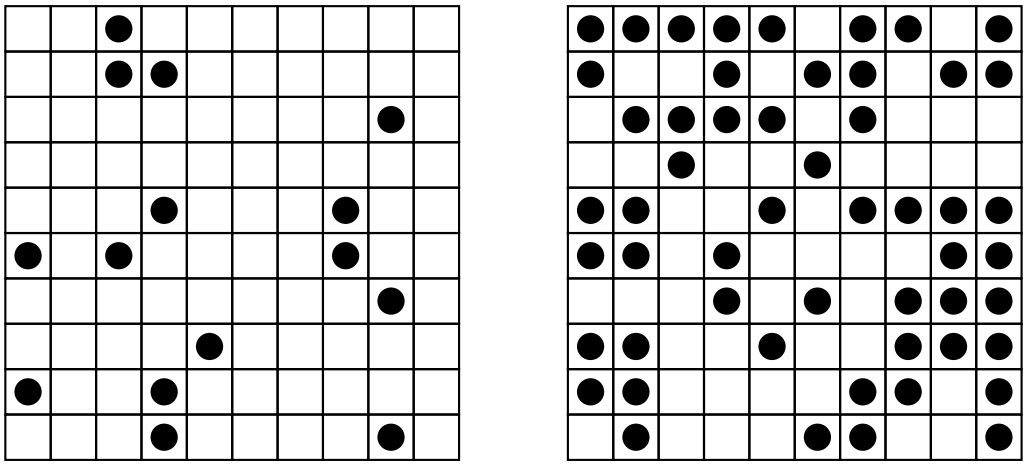

(a) $\mathcal{P}^{occ} < \mathcal{P}_c^{occ}$, implying $\mathcal{P}^{giant} = 0$. **(b)** $\mathcal{P}^{occ} > \mathcal{P}_c^{occ}$, implying $\mathcal{P}^{giant} \neq 0$.

Figure 1.8. Example of not-percolating (a) and percolating (b) clusters of random sites (black dots) on a square lattice.

The percolation transition is of a continuous nature (second order), allowing for the study of critical phenomena and the computation of critical exponents in the thermodynamic limit. This limit corresponds to the scenario where the number of vertices of the square lattice graph tends to infinity, along with the number of components of the percolating/giant cluster.

- The order parameter goes as $\mathcal{P}^{giant} \sim (\mathcal{P}^{occ} - \mathcal{P}_c^{occ})^{\beta}$ for $\mathcal{P}^{occ} > \mathcal{P}_c^{occ}$.
- The characteristic size of the largest (finite) clusters diverges as $l_{finite} \sim |\mathcal{P}^{occ} - \mathcal{P}_c^{occ}|^{-\nu}$.
- The characteristic mass (number of sites in the cluster) of the largest (finite) clusters diverges as $m_{finite} \sim |\mathcal{P}^{occ} - \mathcal{P}_c^{occ}|^{-1/\sigma}$.
- The large clusters are fractals and their fractal dimension $d_f \sim 1/\nu\sigma$.

Percolation problems sharing the same critical exponents are in the same universality class.

The upper critical dimension *i.e.* the space dimension above which mean field results are exact is $d_{uc}^{perc} = 6$.

Potts and bond percolation

If one considers a bond percolation problem, each bond-configuration on the underlying lattice, is related to a sub-graph of the lattice itself, $\mathcal{G}$ with $|E|$ bonds. It is easy, thus, to write the probability of such configurations, considering edge independent occupancy probabilty and N_b as the total number of possible bonds:

$$\pi(\mathcal{G}) = \mathcal{P}^{occ|E(\mathcal{G})|}(1-\mathcal{P}^{occ})^{(N_b - |E(\mathcal{G})|)}. \tag{1.45}$$

Thus, one can sum over all the possible graphs to obtain the partition function of the percolation problem, or:

$$\mathcal{Z}_{Perc} = \sum_{\mathcal{G}\in G} \mathcal{P}^{occ|E(\mathcal{G})|}(1-\mathcal{P}^{occ})^{(N_b - |E(\mathcal{G})|)}. \tag{1.46}$$

Now if one comes to the Potts model and takes the partion function defined in Eq. (1.42) by imposing $v = 1 - e^{-J} = \dfrac{\mathcal{P}^{occ}}{1-\mathcal{P}^{occ}}$ one obtains:

$$\mathcal{Z}_P(\{J_{ij}\}) = \sum_{\mathcal{G}\in G} q^{\mathcal{C}_c(\mathcal{G})} v^{|E(\mathcal{G})|} = \sum_{\mathcal{G}\in G} q^{\mathcal{C}_c(\mathcal{G})} \mathcal{P}^{occ|E(\mathcal{G})|}(1-\mathcal{P}^{occ})^{-|E(\mathcal{G})|}. \tag{1.47}$$

It is evident that, apart from a trivial and graph-independent factor $(1-\mathcal{P}^{occ})^{N_b}$, in the limit of $q \to 1$, the Potts model is formally equivalent to a percolation model. To ensure this equivalence, it is important to take the limit of $q \to 1$ rather than abruptly setting $q = 1$, in order to avoid obtaining a trivial and constant partition function.

The same reasoning can be applied when considering edge-dependent occupancy probability and the disordered Potts model.

This mapping between the Potts model and bond percolation has been made possible due to the analytical continuation of the Potts partition function to real values of q.

For the purpose of this thesis, only the mapping between the Potts model and bond percolation is necessary. However, it is also possible to map the Potts model to a site percolation problem.

1.6.4 Field theory and the disorder-perturbation

To characterize the impact of disorder on phase transitions and critical phenomena, a common approach involves introducing a small disorder perturbation of a weak nature to a pure model at its critical point. This allows for observing whether the perturbation

causes the model to flow to another critical point. The influence of disorder on phase transitions will be discussed in Section (1.6.5), while the purpose of this section is to introduce a perturbed continuous formulation of the Potts model.

Specifically, at the critical point, the two-dimensional (pure) Potts model can be represented by a conformal field theory using an action ($\mathcal{S}^{\text{Potts}}$) composed of primary fields with well known scaling dimension [25, 39, 44–46, 81, 82]. The detailed form of this action is not necessary for the purpose of this thesis. In the presented perturbation scenario, quantities such as correlation functions are computed using a conformal bootstrap approach, requiring only the scaling dimensions of the fields and the Coulomb-gas representation [8, 82].

However, to describe the disordered Potts model within the continuous framework, it is necessary to include the disorder perturbation. In the case of random bond models, this perturbation locally couples with the energy fields, as evident from the lattice formulation mentioned in Eq. (1.39). Therefore, at the critical point, one can express this as:

$$\mathcal{S} = \mathcal{S}^{\text{Potts}} + g \int d^2 x \, \phi(x) \, \varepsilon(x), \tag{1.48}$$

where x is a generic position in a continuous space, $\phi(x)$ is a generic disorder-perturbation operator[2] with scaling dimension h_ϕ, $\varepsilon(x)$ is the continuous representation of the energy density of the Potts model, *i.e.* a scaling operator with scaling dimension h_ε [25, 39], and g is a scaling variable, see Sec.(1.7) for the definitions of these quantities. It is, still, important to put emphasis on the fact that $\mathcal{S}^{\text{Potts}}$, being the perturbed action, is an interacting one. This will make the analysis more difficult but interesting at the same time. The reader will find a chapter on how to deal with this kind of problems in Section (1.7.3).

Being at criticality means that $J(x) = J_c + \delta J(x)$ (see Eq. (1.38) for a lattice version) satisfies Eq. (1.43). To proceed with the computations, one requires certain tools to handle the perturbation term and the disorder field $\phi(x) \propto \delta J(x)$.

[2] In this work operators are always commuting entities.

The replica trick

The replica trick, initially introduced by Edwards and Anderson in [83], is a powerful mathematical technique that has led to breakthroughs in statistical physics and the theory of disordered systems, including the development of the replica symmetry breaking scenario and the recognition of Parisi's Nobel Prize in 2021 [19]. This approach involves creating multiple replicas or copies of the system, performing calculations based on the number of replicas, and subsequently analytically extending the results back to the original case. By employing this method, it becomes possible to compute quantities that are challenging to obtain directly.

$$\begin{aligned}\log(\mathcal{Z}) &= \lim_{n\to 0}\frac{\mathcal{Z}^n-1}{n} = \lim_{n\to 0}\frac{e^{n\log(\mathcal{Z})}-1}{n} = \lim_{n\to 0}\frac{n\log(\mathcal{Z})+\frac{1}{2}\left(n\log(\mathcal{Z})\right)^2+\cdots}{n}\\ &= \cdots = \log(\mathcal{Z}).\end{aligned} \tag{1.49}$$

One can use this formula during the calculation of quenched free energies, being:

$$\mathcal{F} = -\mathbb{E}\left[\log(\mathcal{Z})\right] = -\lim_{n\to 0}\mathbb{E}\left[\frac{\mathcal{Z}^n-1}{n}\right]. \tag{1.50}$$

If n is taken to be an integer positive number[3] one can write:

$$\begin{aligned}\mathbb{E}\left[\mathcal{Z}^n\right] &= \int \mathcal{D}s^{(1)}\cdots\mathcal{D}s^{(n)}\,\mathbb{E}\left[e^{-\mathcal{H}(\{s_1\},\{J_{i,j}\})}\cdots\mathcal{H}(\{s_n\},\{J_{i,j}\})\right]\\ &= \int\prod_{\alpha=1}^{n}\mathcal{D}s^{(\alpha)}\,\mathbb{E}\left[e^{-\mathcal{H}(\{s^{(\alpha)}\},\{J_{i,j}\})}\right],\end{aligned} \tag{1.51}$$

with the same set of couplings $\{J_{i,j}\}$ for each replica. To be clear, one identifies the differential $\mathcal{D}s^{(\alpha)} = \prod_{i=1}^{N} ds_i$, where α labels the replicas from 1 to n and i labels one of the N spins in each replica. Eq. (1.51) is much simpler to compute compared to Eq. (1.36).

However, considering n as an integer and taking the limit $n \to 0$ after the thermodynamic computation is far from being a straightforward operation. These replicated quantities need to be handled with special care [20].

[3] Not evident at all, since one has to take the limit $n \to 0$.

Another useful formulation of this technique is presented in [84]. It involves computing the quenched average of a generic observable, denoted as $\mathbb{E}[\langle\mathcal{O}\rangle]$.

$$\begin{aligned}\mathbb{E}[\langle\mathcal{O}\rangle] &= \mathbb{E}\left[\frac{1}{\mathcal{Z}}\int \mathcal{D}s\,\mathcal{O}(\{s_i\})e^{-\mathcal{H}(\{s_i\},\{J_{i,j}\})}\right] \\ &= \mathbb{E}\left[\lim_{n\to 0}\mathcal{Z}^{n-1}\int \mathcal{D}s\,\mathcal{O}(\{s_i\})e^{-\mathcal{H}(\{s_i\},\{J_{i,j}\})}\right] \\ &= \lim_{n\to 0}\int \mathcal{D}s^{(1)}\cdots\mathcal{D}s^{(n)}\,\frac{1}{n}\sum_{\alpha=1}^{N}\left(\mathcal{O}(\{s^{(\alpha)}\})\right)\,\mathbb{E}\left[\exp\left\{-\sum_{\alpha=1}^{n}\mathcal{H}(\{s^{(\alpha)}\},\{J_{i,j}\})\right\}\right].\end{aligned} \tag{1.52}$$

In both formulations, it is evident that the spin configuration has been replicated n times at a fixed disorder.

Although a lattice Hamiltonian has been used in this section, the trick applies in the same way to actions of the form of Eq. (1.48).

Usually, the distribution of the disorder is included in the action as an auxiliary term ($\mathcal{S}^{\text{aux}}[\phi(x)]$). Therefore, after replicating the Potts action and the perturbation term, one obtains:

$$\mathcal{S}^{(n)} = \mathcal{S}^{\text{aux}} + \sum_{\alpha=1}^{n}\mathcal{S}^{(\alpha)-\text{Potts}} + g\sum_{\alpha=1}^{n}\int d^2\,x\,\phi(x)\,\varepsilon^{(\alpha)}(x). \tag{1.53}$$

In the RG computation performed in [44], the average over the (uncorrelated Gaussian) disorder distribution is explicitly computed. This averaging process produces a term that couples two different replicas at the same position, which is commonly observed in studies of disordered systems: $g_1\sum_{\alpha=1}^{n}\int d^2x\,\varepsilon^{(\alpha)}(x)\varepsilon^{(\beta)}(x)$. Similarly, this term is generated from the action of Eq. (1.53), without averaging over the disorder, through the operator product expansion (OPE) in the RG procedure, see Sections (1.7.3, 4.2.3). Therefore, it is worth incorporating this replica-replica term into the action, resulting in:

$$\begin{aligned}\mathcal{S}^{(n)} &= \mathcal{S}^{\text{aux}} + \sum_{\alpha=1}^{n}\mathcal{S}^{(\alpha)-\text{Potts}} + \underbrace{g\sum_{\alpha=1}^{n}\int d^2\,x\,\phi(x)\,\varepsilon^{(\alpha)}(x) + g_1\sum_{\alpha\neq\beta=1}^{n}\int d^2\,x\,\varepsilon^{(\alpha)}(x)\varepsilon^{(\beta)}(x)}_{\mathcal{S}^{(\alpha)-\text{pert}}} \\ &= \mathcal{S}^{\text{aux}} + \sum_{\alpha=1}^{n}\left[\mathcal{S}^{(\alpha)-\text{Potts}} + \mathcal{S}^{(\alpha)-\text{pert}}\right].\end{aligned} \tag{1.54}$$

At this stage of the computation, the reason why the average over disorder is not explicitly performed is twofold. Firstly, there is no need to specify the form of the disorder in

terms of its cumulants. Secondly, when utilizing a disorder with long-range correlations, challenging non-local terms do not arise during the computation [7, 8].

With this in mind, one can express the replicated partition function in the perturbation scheme ($g, g_1 \ll 1$) as:

$$\begin{aligned}
\mathcal{Z}^n &= \int \mathcal{D}\phi \mathcal{D}s^{(1)} \cdots \mathcal{D}s^{(n)} e^{\mathcal{S}^{(n)}} \\
&= \int \mathcal{D}\phi \mathcal{D}s^{(1)} \cdots \mathcal{D}s^{(n)} \exp\left[\underbrace{\mathcal{S}^{\text{aux}} + \sum_{\alpha=1}^{n} \mathcal{S}^{(\alpha)-\text{Potts}}}_{\mathcal{S}^*} + \sum_{\alpha=1}^{n} \mathcal{S}^{(\alpha)-\text{pert}} \right] \\
&= \int \mathcal{D}\phi \mathcal{D}s^{(1)} \cdots \mathcal{D}s^{(n)} \exp\left[\mathcal{S}^*\right] \times \exp\Big[g \sum_{\alpha=1}^{n} \int d^2\, x\, \phi(x)\, \varepsilon^{(\alpha)}(x) + \\
&\quad + g_1 \sum_{\alpha \neq \beta = 1}^{n} \int d^2\, x\, \varepsilon^{(\alpha)}(x) \varepsilon^{(\beta)}(x) \Big].
\end{aligned} \tag{1.55}$$

Now, calling $\mathcal{Z}^* = \int \mathcal{D}\phi \mathcal{D}s^{(1)} \cdots \mathcal{D}s^{(n)} \exp\left[\mathcal{S}^{\text{aux}} + \sum_{\alpha=1}^{n} \mathcal{S}^{(a)-\text{Potts}}\right]$ and $\langle \cdots \rangle_{\mathcal{S}^*}$ the average computed with $e^{\mathcal{S}^*}$ as weighting factor, one has:

$$\begin{aligned}
\mathcal{Z}^n = \mathcal{Z}^* \Big\langle 1 &+ g \sum_{\alpha=1}^{n} \int d^2\, x\, \phi(x) \varepsilon^{(\alpha)}(x) + g_1 \sum_{\alpha \neq \beta = 1}^{n} \int d^2\, x\, \varepsilon^{(\alpha)}(x) \varepsilon^{(\beta)}(x) + \\
&+ \frac{1}{2!} g^2 \sum_{\alpha=1}^{n} \sum_{\beta=1}^{n} \iint d^2\, x\, d^2\, y\, \phi(x) \varepsilon^{(\alpha)}(x)\, \phi(y) \varepsilon^{(\beta)}(y) + \\
&+ \frac{1}{2!} g_1^2 \sum_{\alpha=1}^{n} \sum_{\beta=1}^{n} \iint d^2\, x\, d^2\, y\, \phi(x) \varepsilon^{(\alpha)}(x) \phi(y) \varepsilon^{(\beta)}(y) + \\
&+ g \times g_1 \sum_{\alpha=1}^{n} \sum_{\beta \neq \gamma = 1}^{n} \iint d^2\, x\, d^2\, y\, \phi(x) \varepsilon^{(\alpha)}(x)\, \varepsilon^{(\beta)}(y) \varepsilon^{(\gamma)}(y) + \cdots \Big\rangle_{\mathcal{S}^*}.
\end{aligned} \tag{1.56}$$

Thus, one will effectively compute the average over the disorder at the level of correlation functions and will need to specify the disorder distribution. Eq. (1.56) will serve as the core of the perturbative RG computation in the second part of the thesis.

1.6.5 The influence of the disorder on phase transitions: the Harris and extended Harris criteria

To address the question of the influence of disorder on phase transitions, an important criterion needs to be introduced: the Harris criterion. The Harris criterion, originally proposed by Harris in 1974 [85], provides a framework for understanding the impact of disorder on phase transitions, particularly in the case of uncorrelated disorder (*e.g.* $\mathbb{E}\left[J(x)\,J(y)\right] \propto \delta(x-y)$). This criterion was later extended by Weinrib and Halperin in 1983 to also include correlated disorders (*e.g.* $\mathbb{E}\left[J(x)\,J(y)\right] \propto |x-y|^{-a}$ for large distances).

In pure systems without disorder, the critical behavior of phase transitions is characterized by power-law scaling and universal properties determined by the symmetry and dimensionality of the system, as discussed previously. However, the introduction of disorder can have a significant impact on the critical behavior, potentially leading to a change in the universality class of the phase transition, meaning that the system flows towards a new critical point.

The relevance of disorder refers to its effect on modifying the critical exponents, causing them to deviate from their values in the absence of disorder. If disorder is relevant, it alters the critical behavior, while if it is irrelevant, the critical behavior remains unchanged, falling into the same universality class as the pure system. The usual Harris criterion [85] states that uncorrelated disorder is relevant when the specific heat exponent of the pure system is positive, *i.e.* $\alpha^{\text{pure}} > 0$. Conversely, when the disorder is irrelevant, $\alpha^{\text{pure}} < 0$, the critical behavior remains unaffected, and the system belongs to the same universality class as the pure system. In the case where $\alpha^{\text{pure}} = 0$, the criterion is inconclusive.

The concept of relevance and irrelevance of disorder will be revisited when the Renormalisation Group (RG) is introduced, see Sec. (1.7). In the RG framework, the relevance or irrelevance of disorder is determined by examining the flow of disorder-related operators during the RG transformation. Through the RG flow, operators have their RG eigenvalue (spatial dimension - scaling dimension of such operator). If the eigenvalue of a disorder-related operator becomes negative under the RG transformation, it is considered irrelevant, indicating that disorder effects become less and less pronounced at larger length scales. In this scenario, the critical behavior of the system remains dominated by the pure, disorder-free fixed point. Conversely, if the eigenvalue of a disorder-related operator becomes positive, it is considered relevant, meaning that disorder effects are more and more important at larger length scales and the model is described by a new random-fixed point.

The extended Harris criterion, proposed by Weinrib and Halperin [86], takes into account the power-law decay exponent of the disorder correlations. It states that when $a < d$, where d is the spatial dimension of the system, the disorder is irrelevant if $a\nu^{\text{pure}} > 0$, and relevant otherwise. When $a > d$, the extended Harris criterion reduces to the usual Harris criterion.

These criteria are based on the observation that disorder introduces fluctuations and inhomogeneities in the system. If these fluctuations are strong enough, they can alter the behavior of critical modes and influence the scaling properties of the system.

The proof of the extended[4] criterion follows the arguments presented in works such as [85–87]:

Consider a disordered spin system in d dimensions at a temperature $T \gtrsim T_c$, where T_c is the critical temperature after the introduction of disorder. The disorder in the system exhibits long-range correlations, characterized by $\mathbb{E}\left[J(x)\,J(y)\right] \propto |x-y|^{-a}$ for large distances. The system can be divided into blocks labeled by their positions x, each with a size of $\xi(T) \gg 1$. Here, $\xi(T)$ represents the correlation length of the disordered model at the operating temperature. $\xi(T \gtrsim T_c) \gg 1$ and $\xi(T_c)$ diverges. Due to the presence of impurities, each block possesses its own local critical temperature, denoted as $T_c(x)$.
Spins within the same block are correlated, while spins belonging to different blocks are not. Consequently, it is possible to view each block as a collective entity, analogous to a super-spin. To analyze the behavior of the system, an isotropic correlation function can be defined as $g(|x-y|) = \mathbb{E}\left[T_c(x)T_c(y)\right] - \mathbb{E}\left[T_c(x)^2\right]$. It is observed that for long distances, the disorder follows an algebraic decay law, leading to $g(|x|) \sim |x|^{-a}$.
Introducing the reduced temperature $t = \dfrac{T-T_c}{T_c}$ and its local version $t(x) = \dfrac{T-T_c(x)}{T_c}$, where $\mathbb{E}[t(x)] = t$, one can note that $t \sim \xi^{-\nu^{pure}}$ close to the critical point.
The goal of this analysis is to determine whether the system can undergo a uniform transition, meaning that all blocks behave ferromagnetically below the global T_c and paramagnetically above it. In simpler terms, it examines whether the local critical temperatures $T_c(x)$ are such that all blocks are on the same side of the transition.
If this is not the case, it implies that the disorder shifts the local critical temperatures in a way that some blocks are on one side of the transition while others are on the other side. As a result, an uniform transition becomes impossible, leading to a modified critical behavior with different critical exponents compared to the pure model.

[4] It is easy to obtain the usual Harris criterion by putting $a = 0$, for example.

To proceed, one can calculate the fluctuations of the local critical temperatures:

$$\begin{aligned}\Delta^2 =& \frac{1}{\xi^{2d}} \int_{\xi^d} d^d x \int_{\xi^d} d^d y \, \mathbb{E}\left[t(x)t(y)\right] - \mathbb{E}\left[t(x)^2\right] \\ &= \frac{1}{T_c^2 \xi^{2d}} \int_{\xi^d} d^d x \int_{\xi^d} d^d y \, g(|x-y|) \\ &\propto \xi^{-d} \int_0^{\xi} dx \, x^{d-1} g(x) \\ &\propto \xi^{-d} \int_0^{\xi} dx \, x^{d-1-a} \\ &\sim \begin{cases} \xi^{-d} \times \text{constant, if } a > d. \\ \xi^{-d} \times \log(\xi), \text{ if } a = d. \\ \xi^{-a}, \text{ if } a < d. \end{cases}\end{aligned} \tag{1.57}$$

The transition is considered uniform if the fluctuations of the local critical temperatures, denoted as Δ^2, and the quadratic deviation of the working temperature from the global critical temperature, denoted as t, are of the same order. In other words, the ratio Δ^2/t^2 tends to zero as t approaches zero. This condition implies the following relationship:

$$\frac{\Delta^2}{t^2} \sim \begin{cases} t^{-d\nu^{\text{pure}}-2}, \text{ if } a > d. \\ t^{-d\nu^{\text{pure}}-2} \times \log\left(t^{-\nu^{\text{pure}}}\right), \text{ if } a = d. \\ t^{a\nu^{\text{pure}}-2}, \text{ if } a < d. \end{cases} \tag{1.58}$$

To determine the stability of the pure system, the following conditions need to be satisfied:

$$\begin{cases} d\nu^{\text{pure}} - 2 = -\alpha^{\text{pure}} > 0, \text{ if } a \geq d, \text{ Usual Harris.} \\ a\nu^{\text{pure}} - 2 > 0, \text{ if } a < d, \text{ Extended Harris.} \end{cases} \tag{1.59}$$

Where $\alpha^{\text{pure}} = 2 - d\nu^{\text{pure}}$ is obtained through hyperscaling relations [86].
It should be noted that for $a < d$, one has $a\nu^{\text{pure}} - 2 < d\nu^{\text{pure}} - 2$, indicating that the extended criterion is more restrictive than the usual one.
In the case of uncorrelated disorder, $g(|x-y|) \to \delta(|x-y|)$, one recovers the usual Harris criterion [85]:

$$\text{Critical behaviour} = \begin{cases} \text{Untouched, if } \alpha^{\text{pure}} < 0. \\ \text{Modified, if } \alpha^{\text{pure}} > 0. \\ \text{Criterion is inconclusive, if } \alpha^{\text{pure}} = 0. \end{cases} \tag{1.60}$$

It is important to note that these criteria only determine whether the critical behavior is modified or not, but they do not provide information about how it is modified or where the new random-fixed point is located. To address these deeper questions, a renormalisation group analysis is required.

1.7 Perturbative real space renormalisation group

The renormalisation group (RG) is a powerful theoretical framework in physics that has had a transformative impact on the understanding of critical phenomena and system behavior across varying length scales. It finds its origins in the early development of quantum field theory and statistical mechanics.

The concept of the RG can be traced back to the pioneering work of Kadanoff in the 1960s [88] and Wilson in the early 1970s [16]. Wilson introduced a systematic approach to analyze the effects of fluctuations in physical systems, proposing the RG as a method to examine how a system's behavior changes when observed at different energy scales.

Wilson's key insight involved dividing a system into two distinct parts: high-energy and low-energy modes. By integrating out the high-energy modes, responsible for short-range fluctuations, he demonstrated that the low-energy effective theory remains unchanged while its parameters are modified. This process, known as "renormalisation", enables consistent treatment of divergences and yields physically meaningful predictions.

The RG gained significant momentum in the field of particle physics with the emergence of quantum chromodynamics (QCD), the theory of strong interactions. Through RG analysis, the understanding of asymptotic freedom, the phenomenon where the coupling constant decreases at high energies, represented a major breakthrough [89].

In condensed matter physics, the RG has played a pivotal role in comprehending phase transitions and critical phenomena. For instance, Kadanoff's work on the Ising model showcased the efficacy of RG techniques in describing the universal properties of critical systems [88], laying the groundwork for the modern understanding of universality classes and scaling laws.

Since its inception, the RG has evolved into a versatile and widely applicable tool across various domains of physics. Its applications span from quantum field theory and condensed matter physics to cosmology and complex systems. The development of different RG schemes, such as the Wilsonian RG, the functional RG, the RG in the real space and the RG in the momentum space has further expanded its scope and applicability, [25].

The term "renormalisation group" can be considered somewhat misleading because the transformations employed do not constitute a group in the conventional group theory sense. Additionally, the concept of renormalisation in quantum field theory is not a fundamental requirement, despite some technical similarities. Instead, the crucial aspect lies in the process of coarse graining and scale invariance.

In this work, the real space renormalisation group technique is employed to investigate the perturbed q-Potts interacting and conformal field theory in two dimensions, $d = 2$. The application of the RG method allows for the study of the system's behavior under renormalisation transformations, which help to understand its critical properties.

While a comprehensive review of all RG techniques is beyond the scope of this thesis, this section will provide with the necessary information to facilitate a general understanding of the results presented in the second part of the thesis. The reader is referred to [25, 39, 44], from which this introductory section is inspired, for a deeper introduction to this technique.

It must be stressed that the RG is a framework which needs to be adapted and reshaped depending on the problem in analysis.

1.7.1 The RG idea

The fundamental concept of the renormalisation group approach is that there exists a continuous family of transformations for the coupling constants involved in the statistical description of a physical theory, corresponding to changes in the length scale of the system under analysis.

In any physical system, interactions take place at various length scales. The RG procedure is based on the assumption that these scales are locally interconnected. Consequently, it becomes possible to describe physical phenomena by disregarding interactions that are irrelevant at a specific scale. This concept can be visualized using a shell structure, where each scale corresponds to an effective action containing relevant parameters and degrees of freedom.

It is worth noting that a small change in a particular parameter, which might be insignificant at one scale, can be amplified through the other scales, resulting in significant macroscopic changes. This behavior arises from the hierarchical structure of interactions within the system.

To apply the RG procedure, one begins by selecting a desired length scale through an appropriate choice of action. The subsequent step involves finding a procedure that facilitates the transition to the next length scale. In the context of statistical physics, this entails averaging fluctuations within a specific range of length, denoted as r, which serves as the RG scale. It is essential for r to be larger than the lattice spacing l (for discrete systems) and smaller than the correlation length of the physical entities, denoted as ξ. By integrating out these fluctuations, one obtains a system with a new lattice spacing, denoted as $l' = r \times l$, or equivalently, a new length scale $x' = x/r$, where x is the length scale before rescaling. This effectively allows for the examination of the system at a different length scale.

Following the averaging process, the unaffected degrees of freedom can be described using a new effective action. This procedure, corresponds to the coarse graining discussed in

Section (1.3). By iteratively applying the coarse graining operation, it becomes possible to compute amplifying or de-amplifying factors, denoted as λ^i, which are the eigenvalues of the linearized version of the RG transformation. If a coupling constant is amplified, it is referred to as a relevant coupling, whereas if it is reduced, it is termed an irrelevant coupling.

1.7.2 RG procedure on a discrete lattice

The name "real space RG" derives from the fact that the RG transformation, described in this section, occurs in position space on a lattice or a continuous space.

To be more clear, one can consider a statistical spin system defined on a regular lattice with spacing l, where $d > 1$ denotes the dimensionality of the space. The system is described by a Hamiltonian $\mathcal{H}(s_i, c_k)$, where c_k represents the set of all possible coupling constants allowed by the symmetry and nature of the spin degrees of freedom. It's worth noting that there is a change in notation here. Previously, the couplings were denoted as $J_{i,j}$. However, these specific couplings are just an example within the more general set c_k, which encompasses other interactions such as next-to-nearest neighbor interactions and so on.

Typically, the couplings in the statistical theory are defined with the inclusion of the inverse Boltzmann weight, which is also the case in this study. Consequently, for a given value of c_k, a correlation length $\xi(c_k)$ is associated. As usual, this effectively measures the extent of correlation between spins. A smaller value of $\xi(c_k)$ corresponds to a more accurate perturbative description of the statistical theory.

Based on this understanding, comes the idea of scale-transforming $l \to r \times l$. Through this transformation, a correspondence is established between a correlation length on a lattice with spacing l and one with a lattice spacing $l' = r \times l$, specifically $\xi' = \xi/r < \xi$. If such a transformation exists, it can lead to a simpler or solvable reformulation of the problem.

It is important to note that in the case of a critical theory, where $\xi \to \infty$, the scale invariance preserves the correlation length.

The degrees of freedom within a sphere of radius $r \times l$, where $l \ll r \times l \ll \xi$, can be treated as a single entity. Therefore, one can imagine magnifying the lattice and considering these spins as a collective unit. This division of the system into blocks B_k with r^d spins allows for the assignment of a value to each block according to a reasonable statistical rule f:

$$s_i^{(1)} = f(\{s_i^{(0)}\} \in B_k). \tag{1.61}$$

After applying the rule of Eq. (1.61) to all the spins, only the lattice spacing is rescaled back to its original value, without altering the spin values, in order to obtain the same

lattice as the initial one. This procedure is referred to as an RG step and is schematically represented in the following Figure (1.9).

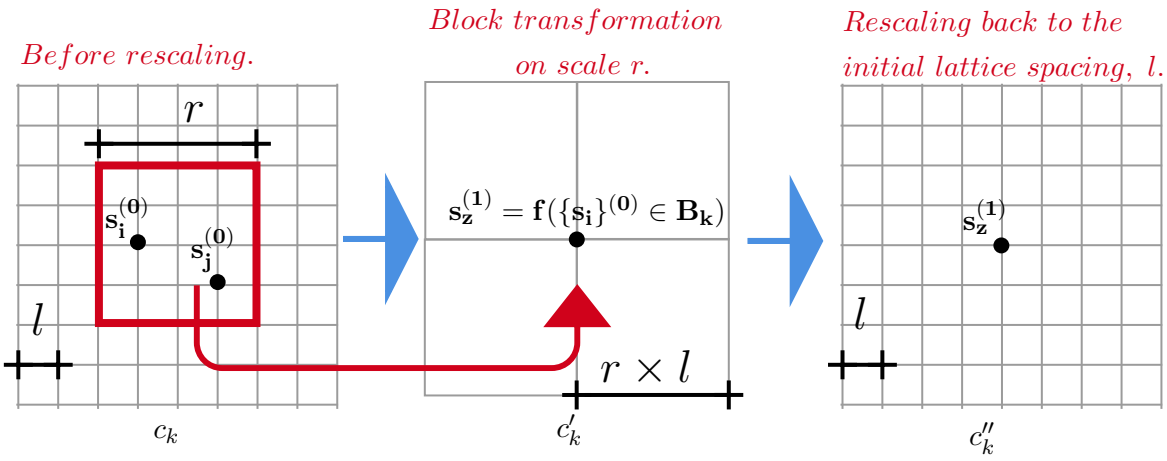

Figure 1.9. Graphical sketch of the RG procedure on a lattice with initial lattice spacing l. r is the RG scale, the red square represent the block B_k and $f(\cdots)$ is the statistical rule that assigns a value to the new spin, $s_z^{(1)}$. The sets, c_k, c'_k, and c''_k are respectively the original couplings, the couplings after the block transformation, and the couplings once the system has been scaled back to the original lattice spacing.

There is a wide range of choices for the law f, with decimation and majority rule being the most common ones [39]. However, what truly matters is the asymptotic behavior in the limit of a large number of RG steps, $n_{\mathrm{RG}} \gg 1$. Therefore, different laws may lead to the same physical picture.

An important requirement for these transformations is that they must preserve the partition function after each RG step, *i.e.*

$$\mathcal{Z}^{(n_{\mathrm{RG}}+1)}(c_k^{(n_{\mathrm{RG}}+1)}) = \mathcal{Z}^{(n_{\mathrm{RG}})}(c_k^{(n_{\mathrm{RG}})}). \tag{1.62}$$

The invariance of the partition function implies the invariance of the entire probability measure.

Hence, the partition function at the $(n_{\mathrm{RG}}+1)$-step is connected to the effective Hamiltonian, denoted as $\mathcal{H}^{(n_{\mathrm{RG}}+1)}$. For the procedure to be successful, it is crucial that the functional form of the Hamiltonian at the $(n_{\mathrm{RG}}+1)$-step remains the same as that at the n_{RG}-step. The difference lies in the couplings used in the Hamiltonians. To guarantee this consistency, it is essential to start with all the possible and permissible couplings from the beginning of the computation.

Couplings, flow and fixed points

At this stage, one can associate the set of all couplings $\{c^{(n_{\mathrm{RG}})}\} = \{c_1^{(n_{\mathrm{RG}})}, c_2^{(n_{\mathrm{RG}})}, \cdots, c_k^{(n_{\mathrm{RG}})}\}$ with the effective Hamiltonian $\mathcal{H}^{(n_{\mathrm{RG}})}$. This set of couplings forms a manifold in the coupling space. Each RG step corresponds to the movement of a point within this manifold, following a certain law:

$$\{c^{(n_{\mathrm{RG}})}\} = \mathcal{T}(\{c^{(n_{\mathrm{RG}})}\}). \tag{1.63}$$

By iterating the RG steps, one can traverse the coupling manifold by following the trajectories determined by a generic and typically nonlinear map $\mathcal{T}$.

After applying Eq. (1.63), the correlation length should be measured with respect to the rescaled lattice spacing:

$$\xi(c^{(n_{\mathrm{RG}}+1)}) = r^{-1}\xi(c^{(n_{\mathrm{RG}})}). \tag{1.64}$$

Therefore, at each iteration, the correlation length decreases, indicating a progressive coarsening of the system.

Upon studying the RG trajectories, it is commonly observed that they exhibit a smooth convergence towards specific fixed points. These fixed points are characterized by the property that the couplings remain unchanged under the RG transformation, representing stationary points of the flow:

$$c^* = \mathcal{T}(c^*). \tag{1.65}$$

At these fixed points, the correlation length can be either zero or infinite, indeed:

$$\xi(c^*) = r^{-1}\xi(c^*). \tag{1.66}$$

It is well known that when the correlation length diverges, the system is at a critical point. Therefore, fixed points with a diverging correlation length correspond to critical points, while fixed points with a vanishing correlation length are referred to as trivial fixed points.

Additionally, fixed points can be classified as follows:

- Attractive: The flow converges towards this point.
- Repulsive: The flow diverges close to this point.
- Mixed: The flow can either converge or diverge depending on the direction of the flow close to this point.

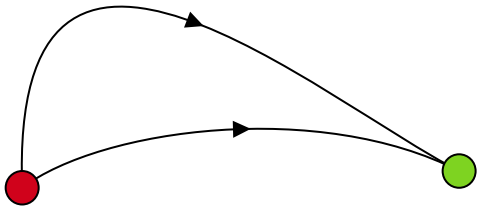

Figure 1.10. The figure illustrates the trajectories of the RG flow (black) along with an attractive fixed point (green) and a repulsive fixed point (red).

One can gain insights into the nature of a fixed point by examining a linearized version of the flow in its vicinity, where the coupling constant is perturbed as $c = c^* + \delta c$, with δc being infinitesimal. This can be expressed as:

$$c^* + \delta c' = \mathcal{T}(c^* + \delta c) \simeq \mathcal{T}(c^*) + \mathcal{M}\,\delta c, \tag{1.67}$$

By introducing the notation $\delta c'_a = \mathcal{M}_{a,b}\,\delta c_b$, where $\mathcal{M}_{a,b}$ is the matrix defined as the partial derivative of $\mathcal{T}_a$ with respect to c_b, $\mathcal{M}_{a,b} = \dfrac{\partial \mathcal{T}_a}{\partial c_b}$, one can identify the eigenvalues λ^i and eigenvectors Δ^i of $\mathcal{M}$. Consequently, it becomes possible to define a linear combination of the shifts δc_a as follows:

$$g_i = \sum_a \Delta^i_a \delta c_a. \tag{1.68}$$

The scaling variable g_i is so named because it possesses the property of undergoing multiplicative transformations under RG transformations, meaning that it transforms as:

$$g'_i = \sum_a \Delta^i_a \delta c'_a = \sum_{a,b} \Delta^i_a\, \mathcal{M}_{a,b} \delta c_b = \sum_b \lambda^i\, \Delta^i_b\, \delta c_b = \lambda^i\, g_i = r^{y_i}\, g_i. \tag{1.69}$$

The eigenvalues λ^i are commonly expressed as functions of the RG scale r, $\lambda^i = r^{y_i}$, where y_i are (improperly) called the eigenvalues of the RG transformation.

- If $y_i > 0$, the scaling variable g_i is considered relevant, indicating that this variable drives the flow away from the fixed point.
- If $y_i < 0$, the scaling variable g_i is considered irrelevant, indicating that this variable is suppressed and tends towards zero under the RG flow.
- If $y_i = 0$, the scaling variable g_i is considered marginal, meaning that its value remains unchanged under the RG transformation.

An important clarification regarding notation needs to be made. The scaling variables consist of shifts in the Hamiltonian's couplings c, and they are coupled to the scaling operator. Therefore, for these reasons, they are referred to as couplings. If the usage of the term could potentially cause confusion, it will be explicitly stated.

To conclude, one can list the properties of the RG flow:

- RG trajectories intersect only at fixed points.
- Activation of a relevant scaling variable in the Hamiltonian at a fixed point causes the system to move away from that fixed point.
- During the flow, trajectories can come close to other fixed points, leading to crossover phenomena between the fixed points.

1.7.3 Field theoretical formulation

In the vicinity of a critical point, which is the focus of this work, a statistical system can be described by a statistical field theory associated with a generic action, denoted as $\mathcal{S}$ (see Sec.(1.3) and Eq.(1.48)). The partition function can be related to this action through a functional integral, given by:

$$\mathcal{Z}(\{c\}, l) = \int \mathcal{D}\psi \, e^{-\mathcal{S}(\psi, \{c\})}. \tag{1.70}$$

Here, $\{c\}$, represents the manifold of couplings, and l corresponds to the previous lattice spacing. In a continuous theory, l serves as a cutoff, preventing ultraviolet (UV) divergences from arising. Usually the UV cutoff is implied.

If one imagine to be at a new fixed point, described by $\mathcal{S}^*$, with n_{rel} relevant scaling variables, $\{u_1, \cdots, u_{n_{\text{rel}}}\}$ associated to the fields $\{\psi_1, \cdots, \psi_{n_{\text{rel}}}\}$, one has:

$$\mathcal{S} = \mathcal{S}^* + \sum_{i=1}^{n_{\text{rel}}} g_i \int d^d x \, \psi_i(x), \tag{1.71}$$

which has exactly the same form as Eq. (1.48), thus, $\mathcal{S}^*$ can and will be an interacting theory in this study.

When a scaling transformation is applied in the RG step, one has:

$$\begin{aligned} &x \to x' = x/r, \\ &g_i \to g_i' = r^{y_i}\, g_i, \\ &d^d\, x \to d^d\, x' = r^{-d}\, d^d\, x, \\ &\psi_i \to \psi_i' = r^{(d-y_i)}\psi_i, \text{ with } d - y_i = h_i, \text{ the scaling dimension.} \end{aligned} \tag{1.72}$$

When one scales back the system to the original cutoff in the RG procedure, the couplings, g, get rescaled by r^{d-h_i}, based on simple dimensional analysis.

The action is designed to be independent of the parameter r, and to achieve this, one derives the scaling behavior of the ψ operator as shown in Eq. (1.72). Through this scaling analysis, one can define the scaling dimension, denoted as h_i.

Having established the concept of scaling dimension, an important result can be derived concerning the two-point correlation function:

$$G(|x_1 - x_2|) = \langle \psi_i(x_1)\psi_i(x_2)\rangle_{\mathcal{S}^*} = \frac{1}{|x_1 - x_2|^{2h_i}}. \tag{1.73}$$

The proof is beyond the scope of this thesis but can be found in [25, 39].

Thus, to summarize, a change in the coupling constants c and, consequently g, resulting from a rescaling by r, leaves the physical features of the theory unaltered. One can choose r to be infinitesimally close to 1, $r = 1 + \delta r$ and obtain an infinitesimal modification of the couplings, *i.e.*

$$g_a \to g_a' = g_a + \frac{dg_a}{dr}\delta r + \mathcal{O}((\delta r)^2). \tag{1.74}$$

Thus, one can express the RG transformation through a differential equation, called β-function:

$$\beta_a(\{g\}) = r\frac{dg_a}{dr}, \tag{1.75}$$

whose zeros correspond to fixed points of the theory, where the couplings are not modified. The β-functions are often known in the form of a perturbative expansion of the coupling constants. In the literature, the concept of β-functions and RG-loops is frequently encountered. Here is a breakdown:

In this formalism, β-functions at the 0-loop level have only linear terms in the couplings g. They can be computed easily using simple dimensional analysis [25], by using the results of Section (4.3.1). β-functions at the 1-loop level have quadratic terms in the couplings. They are related to the three-point function of the scaling operators [25]. β-functions at the 2-loops level have cubic terms in the couplings and are generally more challenging to calculate. They are related to the four-point function of the scaling operators. Some 2-loops β-functions will be computed in [8] and in the second part of this work.

To provide a clearer understanding of the RG procedure in the continuous limit and the concept of "loops", one can imagine that 1-loop corresponds to "putting in the same block" two operators. After the rescaling, a law describing the collapse, usually referred to as the contraction, of these two operators, in the same RG-block, is required. This defines the field in the rescaled version of the lattice. In $d = 2$ dimensions, which is the relevant dimensionality for this study, conformal field theory (CFT) provides a precise way to do this operation, by using contraction rules. These are known as the operator product expansions (OPE), [8,25,39]. At the 2-loops level, three operators are collapsed together, making the calculations more challenging.

A complete introduction to CFT and OPE goes beyond the scope of this thesis. Nevertheless, simple and useful OPE contraction rules, for the scaling operators relevant to the description of the physics of the Ising and Potts model are given in Sec (4.2.3). One can consider these rules as the general law, $f(\cdots)$, used in the discrete part of the RG introduction. Essentially, these rules provide a way to represent the merging or collapsing operators by projecting them onto another operator with appropriate weights. In Fig. (1.11) there is a graphical representation of these concepts.

Concretely, in this situation, the objective is to examine the behavior of the correlation between specific operators in the limit where these operators are very close to each other while being infinitely far away from other operators in the theory (not represented in Fig. (1.11)) *i.e.*

$$\lim_{|x_1-x_2|\gg|x_1-x_l|} \langle \psi_i(x_1)\, \psi_i(x_2) \prod_{l=2}^{n_{ope}} \psi_l(x_l) \rangle_{\mathcal{S}^*}, \tag{1.76}$$

with $\prod_{l=2}^{n_{ope}} \psi_l(x_l) = \Psi$ and n_{ope} the number of operators in the game.
The idea of the OPE is that, in this limit, Eq. (1.76) can be written in the following form:

$$\sum_k \mathcal{C}_{ijk}(|x_1 - x_2|) \langle \psi_k(x_k)\Psi \rangle_{\mathcal{S}^*}, \tag{1.77}$$

where the index k runs over scaling operators and the position x_k is the new position of the operator ψ_k, projected on Ψ. It can be proven, see [25, 39], that the function $\mathcal{C}_{ijk}$ has the form:

$$\mathcal{C}_{ijk}(|x_1 - x_2|) = \frac{c_{ijk}}{|x_1 - x_2|^{h_i+h_j-h_k}}, \tag{1.78}$$

where c_{ijk} are universal structure constants to be computed.

ϵ-expansion

The apporach that will be used in the computations is the ϵ-expansion scheme, [25, 39]. This technique is particularly useful when studying systems that exhibit two or more nearby renormalisationmalization group (RG) fixed points and involve a small parameter, typically denoted as ϵ. This parameter is often related to the system's dimensionality, d, or the number of states, q, in the case of Potts models. By adjusting ϵ, one can bring the two fixed points into close proximity.

The ϵ-expansion serves as a useful tool in situations where one aims to characterize a fixed point, referred to as the new fixed point, even when information is available just about a, so called, trivial fixed point. By employing the ϵ-expansion, universal properties associated with the new fixed point can be inferred by utilizing information obtained from the trivial fixed point. By expressing physical quantities as series expansions in terms of the parameter ϵ, a systematic framework is established for describing the behavior of the new fixed point and determining its critical exponents, scaling dimensions, and other relevant properties. This perfectly aligns with the objective of Section (4.3), where RG computations are performed. As an illustrative example, one can consider the uncorrelated disordered Potts model analyzed in [44]. Starting from the well known and "trivial" pure Potts fixed point, the goal is to compute the new critical exponents at the (eventual) newly emerged critical points as a function of $\epsilon = q - 2$. Notably, when $q = 2$, the new (eventual) random fixed point and the pure fixed point coincide, since that short-range disorder is a marginal perturbation in this case. Contrastingly, the standard example of ϵ-expansion in textbooks involves studying a ϕ^4 theory, see Eq. (1.13), near (below) the upper-critical dimension, employing $\epsilon = 4 - d$ as a small parameter. At $d = 4$, the mean field results hold true, and the system is described by the Gaussian fixed point. However, as d deviates from 4, the mean field approach becomes inadequate, and the system is governed by the Wilson-Fisher fixed point (WF), [25]. This WF point, at exactly $d = 4$, collapses with the Gaussian one. In this scenario, the perturbed theory corresponds to a free field theory.

In this approach, the β-functions are expanded perturbatively with respect to the parameter ϵ. While a comprehensive exploration of the entire ϵ-expansion theory is beyond

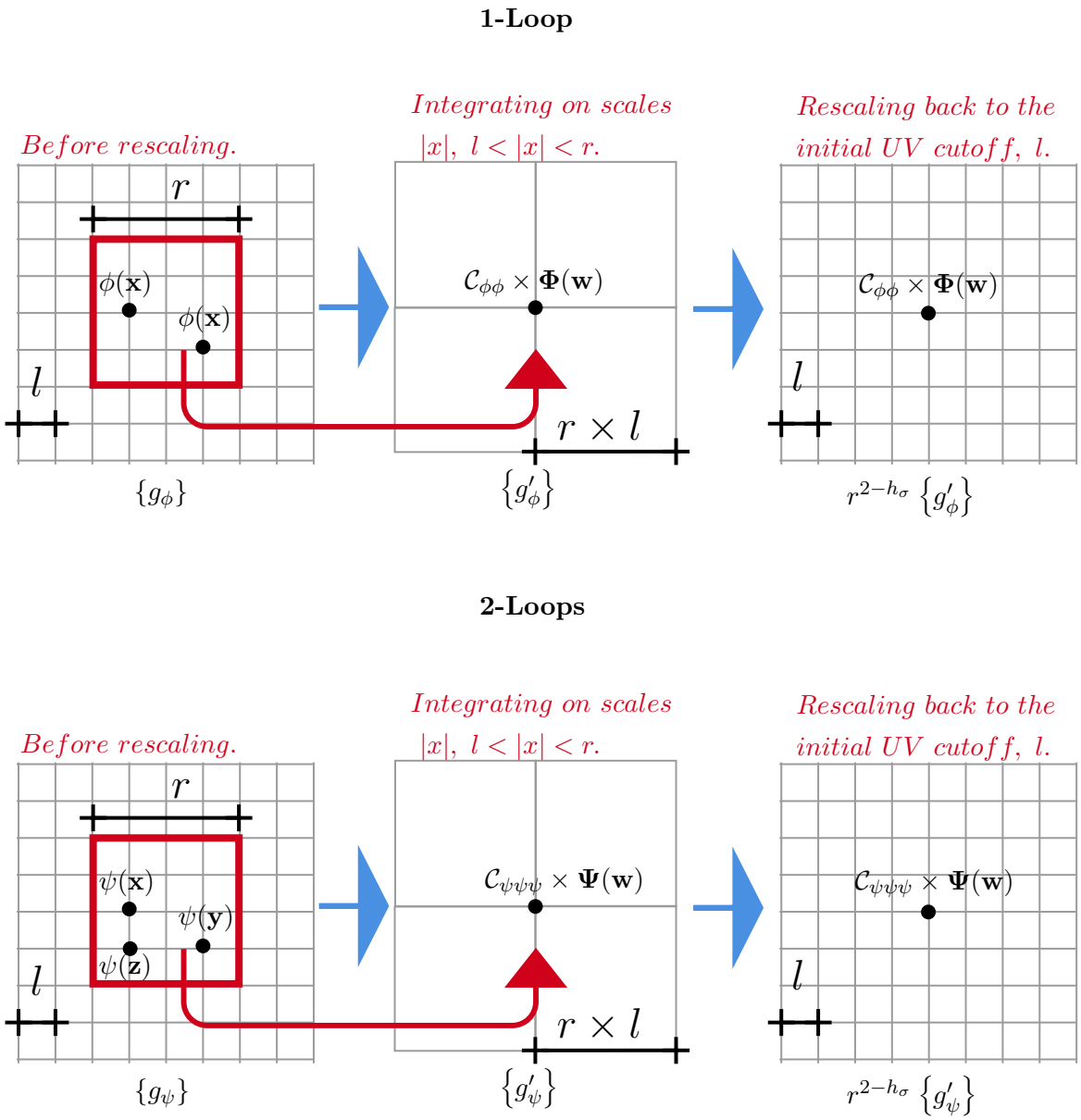

Figure 1.11. Graphical illustration of the RG procedure. The Operator Product Expansion (OPE) is utilized to express operators after the length rescaling. Therefore, the $\mathcal{C}$-coefficients are associated with this transformation. In this example, two fields ϕ are projected onto a Φ field, while the three ψ fields are projected onto a Ψ field. The new fields, Φ and Ψ are fixed by the OPE of the model.

the scope of this thesis, an illustrative example can be provided to demonstrate its application.

In this simple example, one considers a single coupling parameter g and an infinitesimal RG transformation. Without loss of generality, one can put the trivial fixed point located at $g_{\text{trivial}} = 0$ and the new fixed point at $g = g_{\text{new}} = O(\epsilon)$. It is assumed that the β-function is analytic in g and, for sufficiently small values of g, its form is fully determined by its zeros.

$$\beta(g) = r\frac{dg}{dr} = -\mathcal{V}\,(g - g_{\text{trivial}})\,(g - g_{\text{new}}) = -\mathcal{V}\,g\,(g - g_{\text{new}}), \tag{1.79}$$

with $\mathcal{V}$ a generic constant of $O(1)$. Being present just a single coupling, the RG stability matrix is given by:

$$\frac{d\beta(g)}{dg} = -\mathcal{V}\,(g - g_{\text{new}}) - \mathcal{V}\,g, \tag{1.80}$$

and thus one has:

$$\begin{cases} \text{At } g = g_{\text{trivial}} = 0 \text{ The RG eigenvalue is: } \mathcal{V}g_{\text{new}} = O(\epsilon). \\ \text{At } g = g_{\text{new}} \rightarrow \text{ The RG eigenvalue is: } -\mathcal{V}g_{\text{new}} = O(\epsilon). \end{cases} \tag{1.81}$$

If $\mathcal{V}g_{\text{new}} > 0$, the trivial fixed point is unstable and, for $g > 0$, the flow goes towards the new fixed point at g_{new}.
If now one consider another coupling, called, g_1 which is a scaling variable at the trivial fixed point, one has that its β-function for small g and g_1, with $g_1 \ll g$, is :

$$\beta(g_1) = r\frac{dg_1}{dr} = y_1 g_1 + \mathcal{X}g\,g_1 + O(g^2, g_1^2) \tag{1.82}$$

Here, $\mathcal{X}$ represents a constant and y_1 is the RG eigenvalue associated with the scaling variable g_1.
Consequently, at this order, the RG eigenvalue of g_1 at the new fixed point can be expressed as $y_1 + \mathcal{X}\,g_{\text{new}}$, indicating that it is modified by an amount of $O(\epsilon)$. This concept lies at the core of the ϵ-expansion technique.

1.7.4 RG-procedure: conformal perturbation theory with ϵ-expansion

To summarize and emphasize the key points for better comprehension of the second part of the thesis, the employed RG procedure for a disordered system in a conformal $d = 2$ scenario, unfolds as follows:

- In the case of a two-dimensional system ($d = 2$), one can leverage results from Conformal Field Theory (CFT). This includes utilizing knowledge about the interacting action of the statistical system at the trivial fixed point, denoted as $\mathcal{S}^*$, as well as the Operator Product Expansion (OPE) involving scaling operators such as ε and ϕ, for example. Additionally, the scaling dimensions of these operators, denoted as h_ε and h_σ, are also taken from these results.

- The analysis of the system begins by perturbing the action at the known fixed point using relevant scaling variables and scaling operators. This is done within a replicated formalism:

$$\mathcal{S}^{(n)} = \mathcal{S}^* + \underbrace{g \sum_{\alpha=1}^{n} \int d^2\, x\, \phi(x)\, \varepsilon^{(\alpha)}(x) + g_1 \sum_{\alpha\neq\beta=1}^{n} \int d^2\, x\, \varepsilon^{(\alpha)}(x)\, \varepsilon^{(\beta)}(x)}_{\text{perturbation with respect to the trivial fixed point.}}$$

- A series of RG steps, as described in Section (1.7.3), are performed.

- By using:

$$\begin{aligned}
\mathcal{Z}^n = \mathcal{Z}^* \big\langle 1 &+ g \sum_{\alpha=1}^{n} \int d^2\, x\, \phi(x) \varepsilon^{(\alpha)}(x) + g_1 \sum_{\alpha\neq\beta=1}^{n} \int d^2\, x\, \varepsilon^{(\alpha)}(x) \varepsilon^{(\beta)}(x) + \\
&+ \frac{1}{2!} g^2 \sum_{\alpha=1}^{n} \sum_{\beta=1}^{n} \iint d^2\, x\, d^2\, y\, \phi(x) \varepsilon^{(\alpha)}(x)\, \phi(y) \varepsilon^{(\beta)}(y) + \\
&+ \frac{1}{2!} g_1^2 \sum_{\alpha=1}^{n} \sum_{\beta=1}^{n} \iint d^2\, x\, d^2\, y\, \phi(x) \varepsilon^{(\alpha)}(x) \phi(y) \varepsilon^{(\beta)}(y) + \\
&+ g \times g_1 \sum_{\alpha=1}^{n} \sum_{\beta\neq\gamma=1}^{n} \iint d^2\, x\, d^2\, y\, \phi(x) \varepsilon^{(\alpha)}(x)\, \varepsilon^{(\beta)}(y) \varepsilon^{(\gamma)}(y) + \cdots \big\rangle_{\mathcal{S}^*}
\end{aligned}$$

  and by exploiting the partition function's invariance under RG transformations, the renormalisation of the couplings g and g_1 can be calculated.

- The β-functions of the analyzed new fixed points are determined through an ϵ-expansion.

- By examining the stability of these β-functions, one can understand the flow of the RG trajectories.

- The characteristics of the new fixed points are studied by linearizing the flow near these fixed points.

- Critical exponents of the new fixed points are computed.

Part I

Dynamics out-of-equilibrium

Chapter 2

Low-temperature dynamics of the Potts model in the $q \gg 1$ limit

Preface

Using as a starting point the work on the large q-Potts model done in [55], this chapter, derived from the papers [5, 6], focuses on out-of-equilibrium statistical physics and represents the first conceptual block of this thesis.

Synthesis of the results

The study conducted a combination of analytic arguments and numerical simulations using the Potts model on square, triangular, honeycomb, and cubic lattices with $N = L^d$, a final temperature T and $q \in \{4, \cdots, \infty\}$. All the lattice have periodic boundary conditions and the parameters L, q and T will be explicitely stated for every case. In this chapter, it is identified a temperature range around the critical one in which the $q \to \infty$ model remains metastable after both lower and upper critical quenches. Even for not-so-large values of q, the lifetime of the metastable states can exceed any numerical reachable time-span for sub-critical quenches. Also, it is determined the spinodal crossover between a region in which metastable states appears and a region where this phenomen is not present at the temperature $T_s = 2T_c(q)/z$. In the sub-spinodal region, for large q a freezing of the dynamics blocks the equilibration process in the square and honeycomb lattices. The proper physical time scale of the freezing regime has been found and tested numerically. Once rescaling by this very time the dynamics is found to be universal for any q and T in the phase space region: $q \gg 1$ and $T \leq T_s$. In the triangular lattice no freezing is observed. Additionally, the study found that freezing exists also for the cubic lattice with the same coordination number as the trinagular one. It is proposed, that the unitary structure of the lattices, composed of a central spin linked to its z neighbors, is responsible for the different behaviors at low temperatures. For lattices with cyclic unitary structure, there is no freezing, but if it is acyclic, the dynamics will freeze in blocked states.

2.1 Introduction

One of the peculiarities of studying the ferromagnetic Potts model is that, for $q > q_c = 4$, the phase transition is of first order. As a result, the quench dynamics across this transition not only involves the well-known coarsening phenomena but also the features of metastability and nucleation. The interplay between these phenomena is not yet fully understood [27, 90–97].

This chapter presents a study of the equilibration dynamics in the large q bidimensional ferromagnetic Potts model based on the results of [55]. The focus is on the coarsening process, the low-temperature freezing, and the metastability close to criticality. The influence of the final reduced temperature $T/T_c(q)$ and the number of states q on the dynamical properties is also analyzed. A significant finding of this study is the location of the crossover temperature below which high-temperature metastability in sub-critical quenches is no longer important, *i.e.* the (pseudo)-spinodal[1] [98], for various lattice geometries, in $d = \{2, 3\}$. A very important result of this work is that a freezing behavior is observed for the square and honeycomb lattice topologies but not for the triangular lattice topology. The relevant time-scale is of Arrhenius form, $e^{J/T}$, and independent of q for $q \gg 1$. Once taken into account this proper time, dynamic scaling is universal.

Thus, some questions may arise: what causes the dynamics to block for the square and honeycomb lattices but not for the triangular lattice, and what are the lattice properties that induce these two types of behavior? Following previous research findings, it was proposed that the presence or absence of freezing in the dynamics is determined by topological conditions related to the lattice's coordination number [99–101]. This hypothesis is tested in the current work by studying the cubic lattice case, which has the same coordination number as the two-dimensional triangular lattice. It is shown that freezing also occurs in the cubic lattice. The existence of a (pseudo)-spinodal temperature with freezing for quenches below this temperature up to a universal time-scale $e^{J/T}$ is observed for the cubic lattice too. It is argued that the unitary structure of the lattices, consisting of a central spin connected to its z neighbors (external spins) is responsible for the different behaviors at low temperatures. A lattice is called cyclic if any pair of external spins can be connected by a path in the unitary structure without going through the central spin, and acyclic otherwise. It is found that lattices with cyclic unitary structures exhibit no freezing, while those that are acyclic have blocked states that freeze the dynamics.

2.2 The growing lenght, $R(t)$

The phenomenon under consideration in this chapter is the dynamics of equilibration following a sudden quench from infinite temperature at a time $t = 0^-$ to a subcritical temperature T of the large q-Potts model in dimensions $d = \{2, 3\}$. It is worth noting

[1] Actual spinodals are a well defined object just in mean field theories.

that $q \gg 1$, so, it is highly likely that the configuration is composed of a, so called, "sand" of completely different spins. This means that there are no spins with neighbors in the same state, or, as will be frequently stated in this thesis, the spins have not formed any bonds with their neighbors.

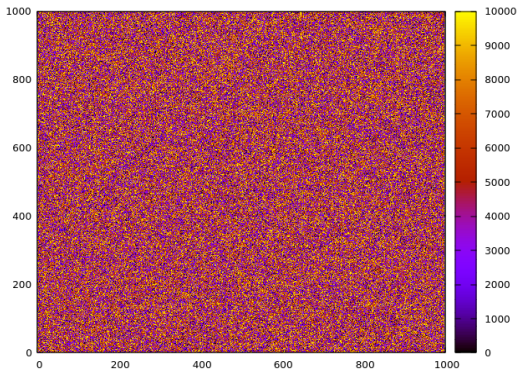

Figure 2.1. Example of initial configuration, $t = 0^-$, on a $d = 2$ square lattice $L = 100$, with $q = 10^4$. Each colour represents a spin state.

After the quench, the system passes through the first order paramagnetic-ferromagnetic phase transition line, and an ordering process will eventually take place after a certain time. However, for certain values of the parameters q and T, metastability can act against ordering, and it may happen that the latter blocks ordering for rather long times[2]. In these cases, the spins are not able to create stable bonds, and a paramagnetic metastable state persists in the ferromagnetic phase. This will be analyzed in Sec. (2.4).

If ordering starts, spins create bonds with their neighbors, and ferromagnetic clusters of same-color spins will substitute the sand configuration.

To describe this dynamical process, one needs to define an essential observable: the growing length $R(t; q, T/T_c)$. This is the typical linear size of a spin domain and is computed by measuring the density of energy at a given time t for a certain value of the number of spins' states q and at a certain temperature T. Specifically, it is given by the density of energy, $N^{-1}\mathcal{H}_P(s_i) = e(t; q, T/T_c)$. It should be noted that the Hamiltonian is not time-dependent. However, the spin configuration of the system during the dynamical process evolves every Monte Carlo step (t), and thus the density of energy depends on time and on parameters such as q and T. For this reason, every measurement is done for a certain value of q and T, and quantities like the growing length or the energy have a parametric dependence on those parameters. However, when it is not useful, this will be implied to keep the notation light. By construction, the energy is associated with the total interface between different clusters, so one can measure $R(t)$ by using the density

[2] $\simeq 10^4 - 10^6$ Monte Carlo steps, depding on T/T_c and q, [55].

of energy, *i.e.*

$$R(t; q, T/T_c) = l \times \frac{e(t \to \infty; q, T/T_c)}{e(t \to \infty; q, T/T_c) - e(t; q, T/T_c)}. \tag{2.1}$$

With l the lattice spacing, put to 1 for the sake of simplicity. For a random initial condition, $e(t = 0) \simeq 0$ for all q and T/T_c. At very low temperature $e(t \to \infty) \neq 0$, (*e.g.* , for the square lattice, $e(t \to \infty) \simeq -2J$) for all $q \geq 2$ and $R(t = 0) \simeq 1$. In Fig. (2.2) it is shown an example of spin configuration with an $R(t) = 5$.

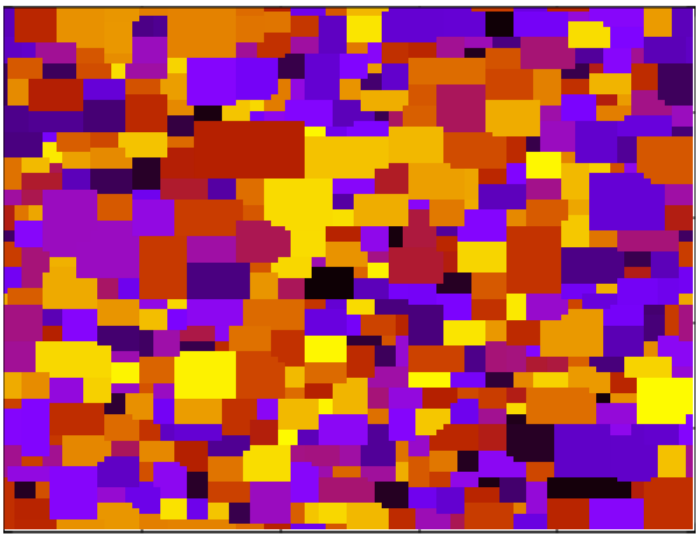

Figure 2.2. Square lattice during the equilibration, $L = 100$, $q = 10^3$, $T = T_c/4$, $R(t) = 5$.

By measuring $R(t)$, the dynamical regimes explored by the system can be understood and characterized as discussed in the following Sections (2.4), (2.5) and (2.6). For instance, in the disordered metastable state studied in Section (2.4), $e(t_{dis}; q, T/T_c) \simeq 0$, leading to $R(t) \simeq 1$. Therefore, the duration of the system's disordered state can be determined by observing the time during which $R(t) \simeq 1$.

The frozen/blocked regime, instead, is one of the most important for this thesis. It is identified by measuring $R(t)$, which remains constant but different from 1 for relatively long times [102] and Sec. (2.5).

Another crucial dynamical regime is the coarsening regime, studied in Section (2.6), characterized by $R(t) \sim t^{1/2}$ [27, 27, 58, 90, 90–93].

The nucleation phenomenon, depicted by an extremely rapid increase of $R(t)$, is not essential for the analysis in this thesis. The interested reader is referred to [103] and the references therein for a deeper analysis.

Finally, the ordered phase is reached when the linear size of the lattice is reached by $R(t)$.

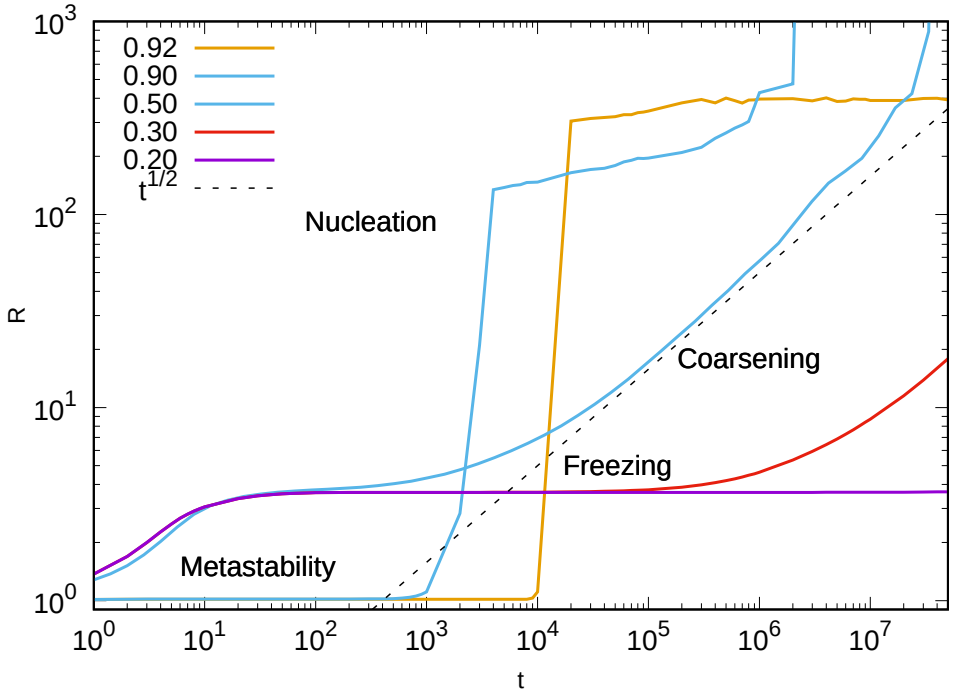

Figure 2.3. Different regimes shown by means of a log-log plot of $R(t)$ for a Potts model with $q = 10^4$ on a square lattice with $L = 10^3$. In the key the reduced temperatures are shown, together as the curve $t^{1/2}$, useful to locate the coarsening. For $T/T_c = \{0.92, 0.90\}$ metastability is observed as first dynamical regime. Then, this is escaped by nucleation. For the $T/T_c = \{0.92, 0.90\}$ curves, the dynamics freezes after a short transient. This regime is escaped, lately, and the dynamics becomes of a coarsening kind. Last, for the $T/T_c = 0.20$ curve, freezing is observed for all the simulation time span.

2.3 Stochastic microscopic dynamics

This study focuses on sub-critical quenches, where a completely disordered configuration serves as the initial condition. The system is then quenched to a subcritical temperature, $T < T_c$, at $t = 0$, and subsequent temperature updates are performed using Monte Carlo simulations. To update the system, a spin value is randomly selected and flipped according to a microscopic stochastic rule. In a system with N spins, N update attempts

correspond to a single time-step. Heat bath dynamics [65] is preferred over Glauber as it allows each move to be a Monte Carlo update, with a rejection occurring only when the new random color is the same as the starting one, which is highly unlikely due to the large q value, see Sec.(1.5.2). A continuous time version of the algorithm can be easily implemented. Details on the transition probabilities and their large q and low T limits are provided in Sec. (2.3.1).

2.3.1 Large q or $T \to 0$ limits of the heat bath rules on the square lattice

To provide a concrete example, the square lattice heat bath rules will be explicitly analyzed in this study. These rules are valid for any $q > 4$. By considering all possible local configurations and their central spin flip evolution, the ordering phenomenon can be analyzed step by step. Fig. (2.4) provides a representation of these local configurations for the square lattice and $q > 4$.

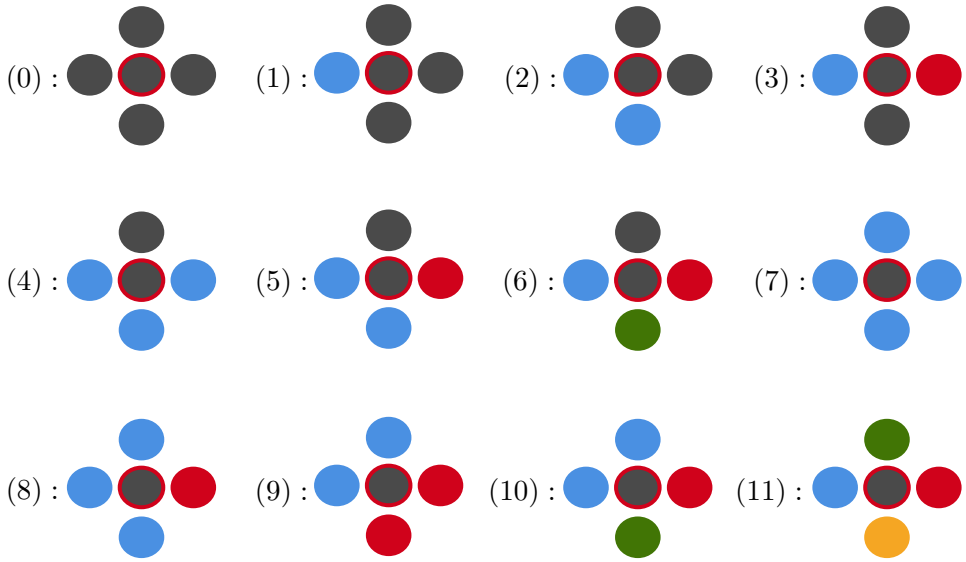

Figure 2.4. All the possible local configurations for $q > 4$, inspired from [55].

In accordance with the scheme introduced in [55] and depicted in Fig. (2.4), the number of neighboring spins, s_j, that take the same value as a spin s_i is counted and denoted as n_1. An hierarchy is then constructed in decreasing order of frequency of appearance for the number of neighbors taking other spin values, denoted as n_2, n_3, *etc.* Each possible configuration can be represented by $[n_1, n_2, \dots]$ where only non-zero values of n_i are included. In the case of the square lattice, there are 12 possible local configurations that are labeled with an integer $k = \{0, \dots, 11\}$, as shown in Fig. (2.4).

Thus, all possible single spin flip transitions can be expressed as:

$$\begin{aligned}
&(0) : [4] \to (0), (7). && (1) : [3,1] \to (1), (4), (8).\\
&(2) : [2,2] \to (2), (2), (9). && (3) : [2,1,1] \to (3), (5), (10).\\
&(4) : [1,3] \to (4), (1), (8). && (5) : [1,2,1] \to (5), (3), (10).\\
&(6) : [1,1,1,1] \to (6), (11). && (7) : [0,4] \to (7), (0).\\
&(8) : [0,3,1] \to (8), (1), (4). && (9) : [0,2,2] \to (9), (2).\\
&(10) : [0,2,1,1] \to (10), (3), (5). && (11) : [0,1,1,1,1] \to (11), (6).
\end{aligned} \tag{2.2}$$

The formulæ presented below are derived from the following reasoning. The first configuration, denoted as (0), represents a single spin surrounded by four neighbors with the same color. The central spin can either retain its current value, resulting in the (0) configuration on the right-hand side of the arrow, or flip to a different value, resulting in the new configuration $(7) : [0, 4]$. So, by applying the heat bath rules from Eq. (1.34), the local configuration (0) will remain the same with probability $\propto e^{4\beta J}$ and change with probability $\propto (q-1)\, e^{0}$ for each of the possible $(q-1)$ values of the flipped central spin. Normalizing the transition probabilities and setting $J = 1$, one obtains:

$$P_{0\to 0} = \frac{e^{4\beta}}{e^{4\beta} + q - 1}, \qquad P_{0\to 7} = \frac{q-1}{e^{4\beta} + q - 1}. \tag{2.3}$$

Following the same kind of analysis, one can write all the other transition probabilities:

$$
\begin{aligned}
P_{1\to1} &= \frac{e^{3\beta}}{e^{3\beta}+e^{\beta}+q-2}. & P_{1\to4} &= \frac{e^{\beta}}{e^{3\beta}+e^{\beta}+q-2}. & P_{1\to8} &= \frac{q-2}{e^{3\beta}+e^{\beta}+q-2}.\\
P_{2\to2} &= \frac{2e^{2\beta}}{2e^{2\beta}+q-2}. & P_{2\to9} &= \frac{q-2}{2e^{2\beta}+q-2}. & &\\
P_{3\to3} &= \frac{e^{2\beta}}{e^{2\beta}+2e^{\beta}+q-3}. & P_{3\to5} &= \frac{2e^{\beta}}{e^{2\beta}+2e^{\beta}+q-3}. & P_{3\to10} &= \frac{q-3}{e^{2\beta}+2e^{\beta}+q-3}.\\
P_{4\to4} &= \frac{e^{\beta}}{e^{\beta}+e^{3\beta}+q-2}. & P_{4\to1} &= \frac{e^{3\beta}}{e^{\beta}+e^{3\beta}+q-2}. & P_{4\to8} &= \frac{q-2}{e^{\beta}+e^{3\beta}+q-2}.\\
P_{5\to5} &= \frac{2e^{\beta}}{2e^{\beta}+e^{2\beta}+q-3}. & P_{5\to3} &= \frac{e^{2\beta}}{2e^{\beta}+e^{2\beta}+q-3}. & P_{5\to10} &= \frac{q-3}{2e^{\beta}+e^{2\beta}+q-3}.\\
P_{6\to6} &= \frac{4e^{\beta}}{4e^{\beta}+q-4}. & P_{6\to11} &= \frac{q-4}{4e^{\beta}+q-4}. & &\\
P_{7\to7} &= \frac{q-1}{e^{4\beta}+q-1}. & P_{7\to0} &= \frac{e^{4\beta}}{e^{4\beta}+q-1}. & &\\
P_{8\to8} &= \frac{q-2}{e^{3\beta}+e^{\beta}+q-2}. & P_{8\to1} &= \frac{e^{3\beta}}{e^{3\beta}+e^{\beta}+q-2}. & P_{8\to4} &= \frac{e^{\beta}}{e^{3\beta}+e^{\beta}+q-2}.\\
P_{9\to9} &= \frac{q-2}{2e^{2\beta}+q-2}. & P_{9\to2} &= \frac{2e^{2\beta}}{2e^{2\beta}+q-2}. & &\\
P_{10\to10} &= \frac{q-3}{e^{2\beta}+2e^{\beta}+q-3}. & P_{10\to3} &= \frac{e^{2\beta}}{e^{2\beta}+2e^{\beta}+q-3}. & P_{10\to5} &= \frac{2e^{\beta}}{e^{2\beta}+2e^{\beta}+q-3}.\\
P_{11\to11} &= \frac{q-4}{4e^{\beta}+q-4}. & P_{11\to6} &= \frac{4e^{\beta}}{4e^{\beta}+q-4}. & &
\end{aligned}
\tag{2.4}
$$

In the limit of large q, the transition probabilities can be simplified significantly. Using the relation $e^{\beta} = e^{\beta_c T_c/T} = (1+\sqrt{q})^{T_c/T} \simeq q^{T_c/2T}$, one can derive that $P_{11\to11}$ approaches:

- *i*) 0 for $T < T_c/2$.
- *ii*) 1 for $T_c/2 < T < T_c$.

in this limit. Similar simplifications hold for the probabilities involving states (6) and (11), whereas other probabilities take on values of either 0 or 1 for $T < T_c$. In summary, the limits of the transition probabilities are:

$$
\begin{array}{lll}
P_{0\to0} = 1. & P_{0\to7} = 0. & \\
P_{1\to1} = 1. & P_{1\to4} = 0. & P_{1\to8} = 0. \\
P_{2\to2} = 1. & P_{2\to9} = 0. & \\
P_{3\to3} = 1. & P_{3\to5} = 0. & P_{3\to10} = 0. \\
P_{4\to4} = 0. & P_{4\to1} = 1. & P_{4\to8} = 0. \\
P_{5\to5} = 0. & P_{5\to3} = 1. & P_{5\to10} = 0. \\
P_{6\to6} = 1 \ / \ 0. & P_{6\to11} = 0 \ / \ 1. & \\
P_{7\to7} = 0. & P_{7\to0} = 1. & \\
P_{8\to8} = 0. & P_{8\to1} = 1. & P_{8\to4} = 0. \\
P_{9\to9} = 0. & P_{9\to2} = 1. & \\
P_{10\to10} = 0. & P_{10\to3} = 1. & P_{10\to5} = 0. \\
P_{11\to11} = 0 \ / \ 1. & P_{11\to6} = 1 \ / \ 0. &
\end{array}
\tag{2.5}
$$

The transition probabilities involving (6) and (11) states are presented for $T < T_c/2$ and $T_c/2 < T < T_c$, respectively.

Furthermore, it can be observed that the rules for $T < T_c/2$ in the large q limit are identical to those for finite q in the limit $T \to 0$. By utilizing these rules, more information on the evolution of the system can be provided for both the cases of $q \to \infty$ and $T \to 0$.

For the large q limit, the initial configuration exclusively consists of a "sand" of (11) states. If $T > T_c/2$, the state (11) is stable, and the system remains disordered indefinitely. Conversely, if $T < T_c/2$, the (11) states transition into (6) states. In certain instances, a spin connecting to another spin may already be in a (6) state, resulting in the formation of a (3) state. Further details regarding the particular value of $T_c/2$ will be discussed in Sec. (2.4.2), for each lattice topology.

After a certain number of iterations, all the states in the system will become (0), (1), (2), or (3) states. These states are stable, meaning they will not evolve unless a neighboring spin is flipped, see Eq. (2.5).

In the case of finite q and zero temperature, the dynamics is similar to the large q limit. The main difference is that the initial configuration can contain states other than (11). Although this difference does not significantly impact influentely the dynamics, it will still be discussed in Sec. (2.5).

A similar analysis can be conducted for the microscopic updating heat bath rules on the honeycomb, triangular and cubic lattices. The honeycomb lattice has 6 states in the heat bath formulation, making the analysis even simpler than for the square lattice with the 12 states discussed earlier [55]. On the other hand, the triangular lattice has 30 states[3],

[3] Just in the case of the triangular lattice, conventional Metropolis updates have been utilized [63].

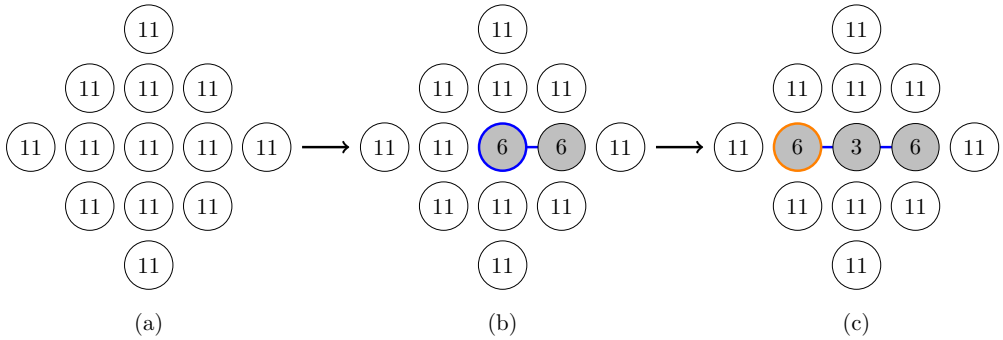

Figure 2.5. An example of transitions is presented which, starting from a fully disordered configuration (a), result in partial ordering of the system. In (b), a blue circled spin changes its value to form a bond with its right neighbor. In (c), an orange circled spin evolves to have the same color as its right neighbor. As a result, two (6) states appear in (b) and a (3) state appears in (c). The spins that have the same color are shown in grey, while the blue bonds indicate non-trivial interactions between spins, as employed in [55]. Plot taken from [5].

which makes it more tedious to write a heat bath algorithm. However, in the zero-temperature limit, the transition probabilities become simpler and more manageable. Results at finite temperature using the three four lattice geometries are presented in Sections (2.6, 2.7.2, 2.7.3, 2.7.4).

2.4 Metastable regime

At the critical temperature T_c, a phase transition separates the system into an ordered and a disordered phase. It might be naively expected that starting from an initial disordered configuration at super-critical temperature and suddenly lowering the temperature below the critical value would cause the system to order after a short transient period. However, simple considerations demonstrate that this does not always occur, particularly in the infinite q limit. The dynamics of the system can remain stuck in a metastable paramagnetic state, even at $T < T_c$, for rather long time intervals. This is because the ordered and disordered phases, separated by a first order transition, create a mixed phase region in the vicinity of T_c [58], resulting in metastability. The numerical analysis in Section (2.7) will show that, for finite but still large q, $R(t)$ remains close to one in the metastable state, *i.e.* $R(t_{\text{met}}) \simeq 1$, for rather long time intervals, see [55] for a more precise description.

Although this thesis will not include it, the investigation of metastable states and spin dynamics presents a significant and complex subject in the field of spin glasses, as demonstrated in [104], for instance.

2.4.1 Gibbs-Dhuem criterion

To properly describe the phenomenon discussed, the use of the Gibbs-Dhuem criterion is helpful [105]. In order to achieve equilibrium, it is necessary to be in an absolute minimum of a suitable thermodynamic potential, such as the Helmholtz free energy:

$$\mathcal{F} = \langle \mathcal{H} \rangle - T\mathcal{S}. \tag{2.6}$$

This potential is minimized at finite temperature by maximizing the entropy and minimizing the internal energy. The minimum of the free energy must be so for all infinitesimal variations of each phase space variable. One can expand $\Delta\mathcal{F}$ in a series of infinitesimal variations near an equilibrium point:

$$\Delta\mathcal{F} = \delta\mathcal{F} + \frac{1}{2}\delta^2\mathcal{F} + \frac{1}{3!}\delta^3\mathcal{F} + \frac{1}{4!}\delta^4\mathcal{F} + \dots \tag{2.7}$$

To be in the equilibrium configuration, the condition $\delta\mathcal{F} = 0$ is necessary. If, in addition, one has $\delta^2\mathcal{F}, \delta^3\mathcal{F}, \delta^4\mathcal{F}, \cdots > 0$, the equilibrium is stable, meaning that the system is in the absolute minimum. If instead $\delta^2\mathcal{F} > 0$ but $\delta^3\mathcal{F}, \delta^4\mathcal{F}, \cdots < 0$, the equilibrium is metastable. This indicates that the system is in a relative minimum and that the absolute minimum could be reached with some thermal perturbation. A certain barrier must be crossed to reach the stable equilibrium configuration, which can take extremely long times, even infinitely long. If $\delta^2\mathcal{F} < 0$, the equilibrium is unstable, indicating that the system is at a maximum of the free energy and that a very small perturbation can cause the system to collapse into a more stable state.

The spinodal curve is defined by the condition $\delta^2\mathcal{F} = 0$. It provides important information regarding the metastability limit of the equilibrium [105].

In the study of phase transitions, spinodals are well-defined objects only in mean field theory. Therefore, this work deals exclusively with (pseudo)-spinodals, see [106] for more insights on this phenomenon. These serve as the threshold below which metastability is not observed.

2.4.2 Spinodals in the Potts Model

In the following, the location of the (pseudo)-spinodal temperature, in the $q \to \infty$ limit, will be determined. In this limit, the critical temperatures of the square, triangular, honeycomb and cubic lattice Potts models are given by Eq. (1.27) which can also be expressed as:

$$e^{\beta_c J} \simeq q^{2/z}. \tag{2.8}$$

One can start by locating the upper (pseudo)-spinodal by considering, as a starting point, a fully ordered state at $T < T_c$ and looking for the smallest super-critical temperature above which the system starts to disorder. The Boltzmann equilibrium weight of one (out

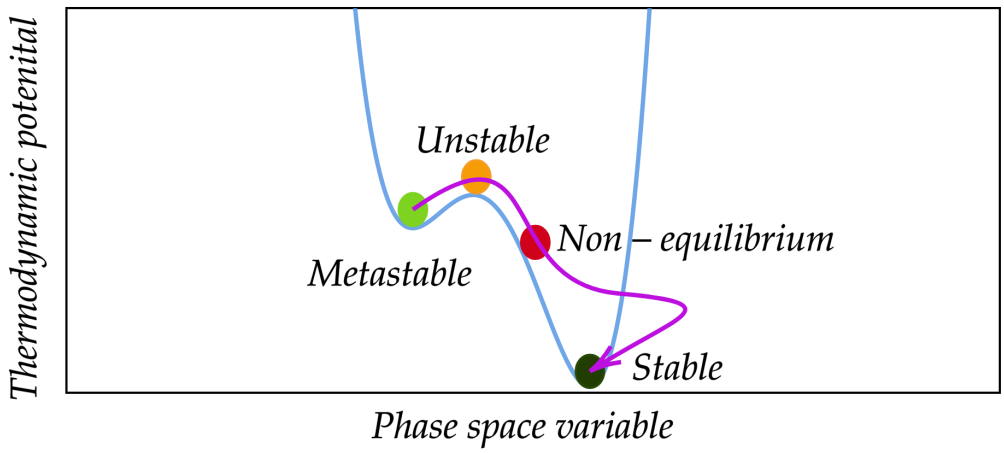

Figure 2.6. Metastable, unstable, and stable equilibria are represented by a relative minimum, a maximum, and an absolute minimum of a thermodynamic potential with respect to a phase space variable. The direction of the eventual dynamical evolution triggered by a thermal fluctuation is indicated by the violet arrow.

of q) fully ordered configurations, one of the ground states, is $\mathcal{P}_{1\text{ground}} = e^{\beta(zJ/2)N}/\mathcal{Z}$, with $\mathcal{Z}$ the partition function and N the number of spins. A first excited state is obtained from this ground state by changing a single spin to any of the other $q-1$ orientations. The energy gap is $\mathcal{E}_{\text{exc}} - \mathcal{E}_{1\text{ground}} = zJ$ and the ratio of the two probabilities tends to $\mathcal{P}_{\text{exc}}/\mathcal{P}_{1\text{ground}} \simeq qe^{-\beta zJ}$ in the large q limit. Accordingly, the change of a spin can occur, in the large q limit, if and only if $e^{\beta zJ} < q$. On the square, triangular and honeycomb lattices one can use Eq. (2.8) to prove that the disordering dynamics can be active only for:

$$\beta < \beta_c/2 \qquad \text{or} \qquad T > 2T_c. \tag{2.9}$$

Thus, starting from a completely ordered state, the system either i) remains blocked in this ground state at any temperature $T < 2T_c$ or ii) disorders completely at $T > 2T_c$.

Next, one can consider the case in which the initial state is disordered at $T > T_c$ and determine the highest sub-critical temperature below which the ordering process can start to occur. This is the lower (pseudo)-spinodal. This temperature is also of particular interest for this thesis and will be used in the following Sections. Because of the $q \to \infty$ limit, typically, each spin takes a different value. The energy of such a fully disordered configuration vanishes, $\mathcal{E}_{\text{dis}} = 0$, and its probability weight is $\mathcal{P}_{\text{dis}} = q^N/\mathcal{Z}$. After a quench to a sub-critical temperature, one of the N available spins will try to align with one of its neighbors. The energy of a state with a bond is then $\mathcal{E}_{\text{bond}} = -J$

and its probability $\mathcal{P}_{\rm bond} = (e^{\beta J}/q)\mathcal{P}_{\rm dis}$. The condition to start ordering is then:

$$\frac{\mathcal{P}_{\rm bond}}{\mathcal{P}_{\rm dis}} \geq 1 \quad \Rightarrow \quad e^{\beta J} \geq q \simeq e^{\beta_c J z/2} \quad \Rightarrow \quad \beta \geq \frac{z\beta_c}{2} \qquad \text{or} \qquad T \leq \frac{2T_c}{z} = T_s. \quad (2.10)$$

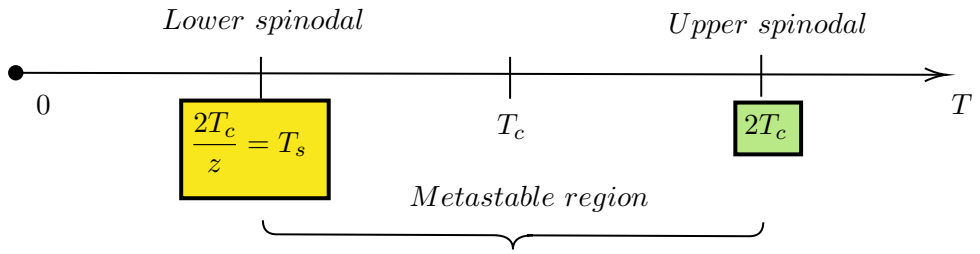

Figure 2.7. Sketch of the (pseudo)-spinodals postions.

Resuming:

Lattice	Dimensions	Coordination Number	$T_c(q \gg 1)$	$T_s(q \gg 1)$
Honeycomb	$d = 2$	$z = 3$	$3J/2\log(q)$	$2T_c/3$
Square	$d = 2$	$z = 4$	$2J/\log(q)$	$2T_c/4$
Triangular	$d = 2$	$z = 6$	$3J/\log(q)$	$2T_c/6$
Cubic	$d = 3$	$z = 6$	$3J/\log(q)$	$2T_c/6$

Table 2.1. Critical temperature and (pseudo)-spinodal for different lattice geometries in $d = 2$ and $d = 3$.

Taking into account the outcomes of the metastability analysis [55] and summarizing these observations, one can conclude that the non-trivial ordering process, in the infinite q limit, is restricted to a quench from a disordered state to $T \leq 2T_c/z = T_s$. Depending on the nature of the lattice, the phase ordering kinetics at $T \leq 2T_c/z$ may traverse temporarily blocked states (see Sec.(2.5)) characterized by intriguing patterns, like the ones depicted in Fig.(2.9) for the square geometry. These are typical zero temperature blocked states, similar to the ones analyzed in [102,107–109]. Conversely, for $T_s < T < T_c$ the dynamics become stuck in relatively prolonged metastable states [55], which can persist indefinitely as $q \to \infty$.

2.5 Blocked state regime

However, in practice, this does not mean that after a quench to $T \leq 2T_c/z$ the state will order completely, this is a very important regime for this study and thus will be analysed deeply. This particular states have been found in the square, honeycomb and cubic lattice topology. In this section the main focus is on the square lattice, for the sake of simplicity, and every time a different lattice is used is explicitely stated. However, different subsections for each lattice toplogies are present in the following section (2.7).

2.5.1 Blocked states at $q \to \infty$

For the moment, the focus is put on the square lattice problem. Indeed, by using heat bath rules in the $q \gg 1$ limit [1, 2], each spin will try to align with one of its neighbors. Thus, after a full update of the lattice, all the spins will have created a "satisfied" bond with a random neighbor. At the next update, any of these bonds can break if one of the spins in the pair changes to take the value of another neighbor.

It is easy to observe that if a spin has the same value as two of its neighbors, $\mathcal{E}_{\text{2bonds}} = -2J$, it will then be much more stable than if it aligns with only one of its neighbors, $\mathcal{E}_{\text{bond}} = -J$. If the two bonds form a corner, as shown in Fig. (2.8), then another spin which close a square will have a large probability to take the same value, adding two more bonds. It is then easy to see that squares and rectangles form the most stable structures. Consequently, after a few iterations, the configurations are filled with small squares and rectangles. In particular, one observes the existence of so called T-junctions which were identified as the main reason for which blocked states occur in finite q-Potts models at zero temperature [102, 110, 111].

Typical snapshots displaying this geometrical phenomen, are shown in Fig. (2.9), after a quench of the square lattice Potts model towards $T < T_c/2$. In the infinite q limit, the dynamics at $T < T_c/2$ is at effectively vanishing temperature, and these configurations are stable. Thus, this run has only partially ordered on the square lattice. This, can be easily seen by considering the spin labelled by (1) and (3) in Fig. (2.8), and the $q \to \infty$ limit of the heat bath transition rules. Indeed, the orange spin (1), being in configuration (1) of Fig. (2.4), can only go stay in (1) or go to configurations (4), (8), but in the infinite q limit, the stochastic rules imposes that it is stable in (1) with probability 1 since:

$$\begin{aligned} P_{1\to 1} &= \frac{e^{3\beta}}{e^{3\beta} + e^{\beta} + q - 2} \to 1, \text{ for } q \gg 1, \\ P_{1\to 4} &= \frac{e^{\beta}}{e^{3\beta} + e^{\beta} + q - 2} \to 0, \text{ for } q \gg 1, \\ P_{1\to 8} &= \frac{q-2}{e^{3\beta} + e^{\beta} + q - 2} \to 0, \text{ for } q \gg 1. \end{aligned} \tag{2.11}$$

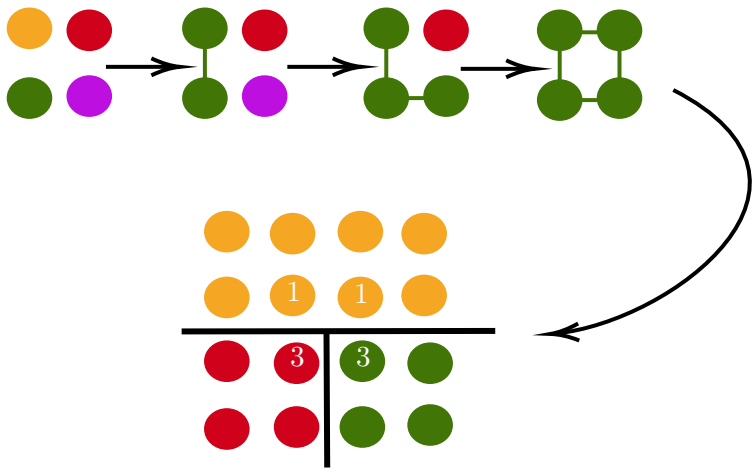

Figure 2.8. Example of the formation of a T-junction on the square lattice. In the top part of the figure a bond between spins is explicitely drawn. It is, in anyways, implied whenever two neighbouring spins are in the same state.

Same analysis can be done for the two (3) spins, the red and the green ones. They could flip to build states (5) or (10), but in the $q \to \infty$ limit, they are obliged to keep their colours and remain in (3):

$$\begin{aligned} P_{3\to 3} &= \frac{e^{2\beta}}{e^{2\beta}+2e^{\beta}+q-3} \to 1, \text{ for } q \gg 1, \\ P_{3\to 5} &= \frac{2e^{\beta}}{e^{2\beta}+2e^{\beta}+q-3} \to 0, \text{ for } q \gg 1, \\ P_{3\to 10} &= \frac{q-3}{e^{2\beta}+2e^{\beta}+q-3} \to 1, \text{ for } q \gg 1. \end{aligned} \tag{2.12}$$

For this reason, flat interfaces are stables and these highly symmetrical geometrical structures appears in snapshots of the lattice, see Fig. (2.9).

The typical linear size of the blocked states in $d = 2$

In this Section, by using the similarity of the $q \to \infty$ model quenched to $T/T_c \leq 2/z$ and the finite q model quenched to zero temperature exploited in Sec. (2.3.1) more insights on these frozen state will be given. The similarity between the two limits discussed, is proven in Fig. (2.10) where it is shown the growing length R as a function of time in various cases of interest. In the square lattice model with $q \to \infty$ quenched to $T < T_c/2$ the dynamics eventually block, in the way illustrated in Fig. (2.8), with R approaching, very quickly at $t \simeq 10$, a plateau at $R_p \simeq 3.63$ in lattice spacing units,

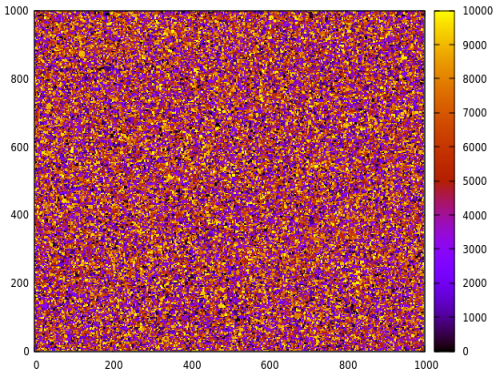

(a) Blocked state.

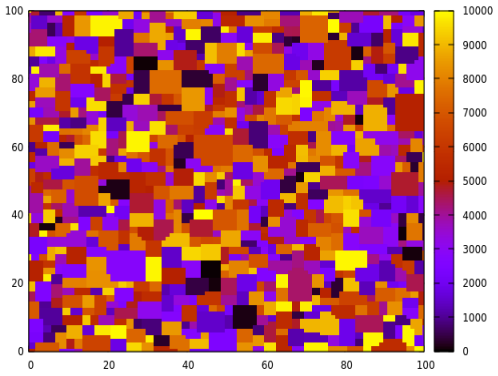

(b) Figure (a) magnified, 100×100 section of the lattice.

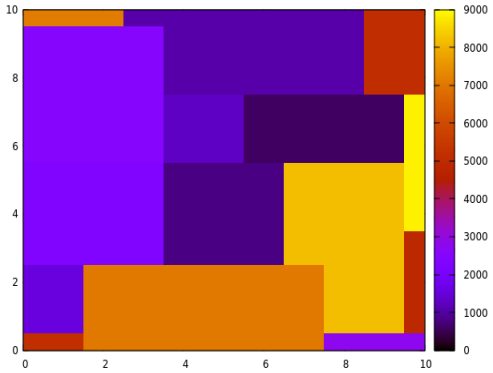

(c) Figure (a) magnified again, 10×10 section of the lattice.

Figure 2.9. Snapshots of the lattice to see blocked states for the Potts model at $T = 0.40T_c < T_s$ with $q = 10^4$, $L = 10^3$. The last two figures have been magnified to see better the interfaces. In (c), the presence of T-junctions, flat interfaces and corners is evident.

$l = 1$. Besides, the zero temperature quench of a $q = 10^3$ model shows a very similar behavior, with asymptotically blocked states of the same kind, and roughly the same value of R_p. It has been checked that the similarity persists for all $q \geq 10^2$ quenched to $T = 0$. Exceptions to the equivalence are found for sufficiently small q. For example, for $q = 10$, R_p fluctuates from sample to sample. Indeed, one can show that the value of the plateau has a weak dependence on q. Using a lattice with $L = 10^3$, one measures $R_p \simeq 3.898(1)$ for $q = 10^2$, $R_p = 3.635(1)$ for $q = 10^3$, and $R_p = 3.632(1)$ for $q = 10^5$, this last value being compatible with the infinite q one. A detailed check of all cases between $q = 10$ and $q = 10^2$ has not been done, and the analysis is thus focused on large enough q. Moreover, for large lattices such as $L = 10^3$ and $q = 10$, even at zero

temperature, some samples can escape the temporarily blocked configurations and reach a nearly equilibrated state.

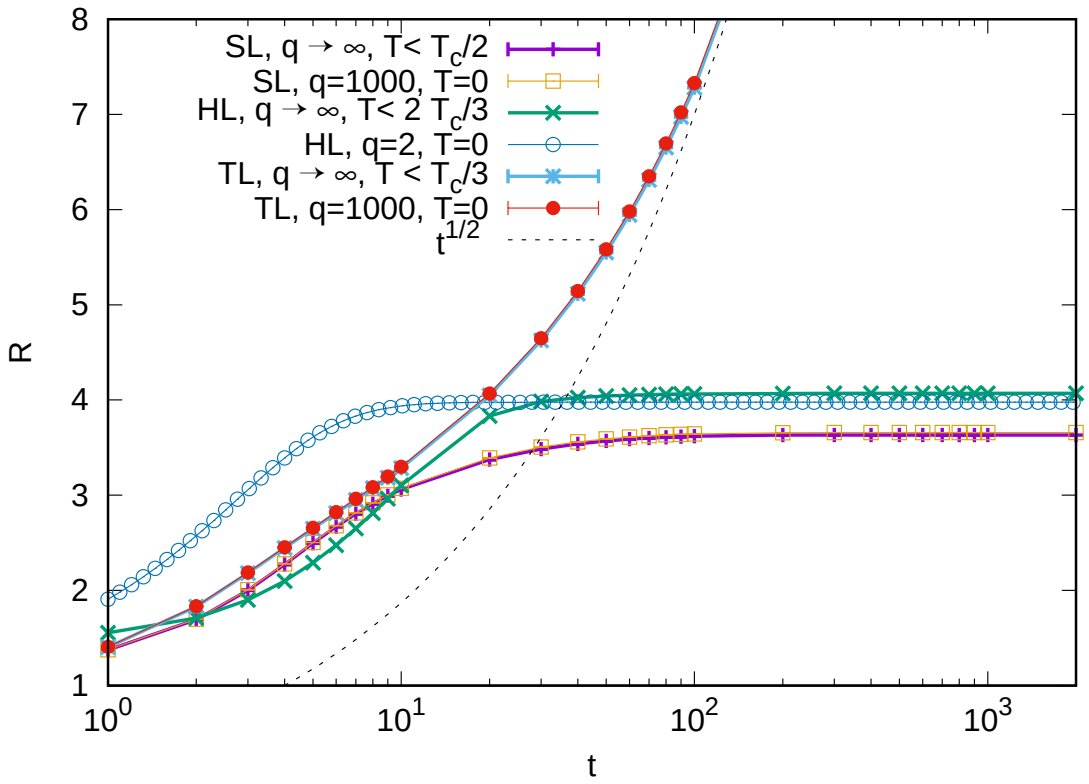

Figure 2.10. The growing length R vs. t of the Potts model on the square (SL), honeycomb (HL) and triangular (TL) lattices with $L = 10^3$. Different curves correspond to values of q and T given in the key. Note the absence of freezing in the triangular lattice case. Taken from [5].

The same equivalence is observed on the honeycomb lattice, with coordination number $z = 3$, see the other pair of curves in Fig. (2.10), which approach $R_p \simeq 4$. The curves show data for the infinite q limit with the condition $T < 2T_c/3$, and the zero temperature quench of the Ising model, $q = 2$. The latter case was already considered in [112] where it was observed that R saturates to a value $R_p \simeq 4$ after a rather short time, $t \simeq 10$. This is due to the existence of frozen configurations on the odd-coordinated honeycomb lattice, see Sec. (6.1) in [112]. Then, for this lattice, the behavior at $T < 2T_c/3$ and infinite q is similar to the one at $T = 0$ for any $q \geq 2$.

Last, one can also analyse data for the triangular lattice for the the infinite q limit with the condition $T < T_c/3$ and at $T = 0$ and $q = 10^3$. For this lattice, the dynamics does not block. For the largest times, the growing length $R(t) \sim t^{1/2}$ as expected for standard

curvature driven coarsening. The absence of blocking states at zero temperature for the triangular lattice is known since a very long time [57, 99] and was discussed in a recent work for small values of q [108]. An argument explainig this particular behavior will be given in Sec. (2.8.2).

2.5.2 Blocked states on the square lattice at finite q: the proper time t_S

One may consider, again, the blocked configuration obtained after a quench from a disordered initial state to $T < T_c/2$ in the q infinite limit of the Potts model on a $L = 10$ square lattice. Such a configuration is shown in the (a) panel of Fig. (2.11), where the state in which each boundary spin is has been highlighted, using the notation introduced in Sec. (2.3.1). For this particular configuration, a direct inspection shows that only four types of states exist, (0), (1), (2) and (3). The (3) states, shown as green squares ■, lie on the corners of the interfaces. They are spins with two neighbors taking the same value and two neighbors taking different values from the central one and being also different from each other. The (2) states, shown as a blue crosses (X), are blinking states: the central spin has two neighbors with the same value and two neighbors with an identical value which is, however, different from the central one. For the configuration shown in the (a) panel of Fig. (2.11), there is only one blinking state (close to the upper right corner). The (1) states, shown as red crosses (+), are spins at a flat interface with three neighbors being identical to the central one and one neighbor taking a different value. The (0) states, corresponding to spins in the bulk of the domains, are not shown.

Following the transition rules in Eq. (2.5), the states (0), (1) and (3) are stable and the corresponding spins cannot flip. Only the (2) state can change, producing the configuration shown in the (b) panel of Fig. (2.11). Note that under this update, the central spin in the (2) state changes but the state (2) is not modified. As a consequence of the flip of the central spin, the four neighboring spins will also change state but again for stable states: two (1) states are changed in (3) states, one (3) state in a (1) state and a (1) state in a (0) state. Thus, in this new configuration, only the same spin in the (2) state can change, which will produce again the configuration of the (a) panel in Fig. (2.11). In the infinite q limit, the only evolution corresponds to blinking between the configurations shown in the (a) and (b) panels of Fig. (2.11).

Next, it is considered the case of a large but finite q with the condition $e^{\beta} > q$ corresponding to a low temperature $T < T_c/2$. The starting point is the configuration in panel (a) of Fig. (2.11). According to the general rules for heat bath dynamics, a (0) state changes to a (7) state with probability $\simeq qe^{-4\beta}$, a (1) state changes to a (4) state with probability $\simeq e^{-2\beta}$ and to a (8) state with probability $\simeq qe^{-3\beta}$, a (2) state changes to another (2) state with probability $\simeq 1/2$ and to a (9) state with probability $\simeq qe^{-2\beta}$, and a (3) state changes to a (5) state with probability $\simeq e^{-\beta}$ and to a (10) state with probability $\simeq qe^{-2\beta}$.

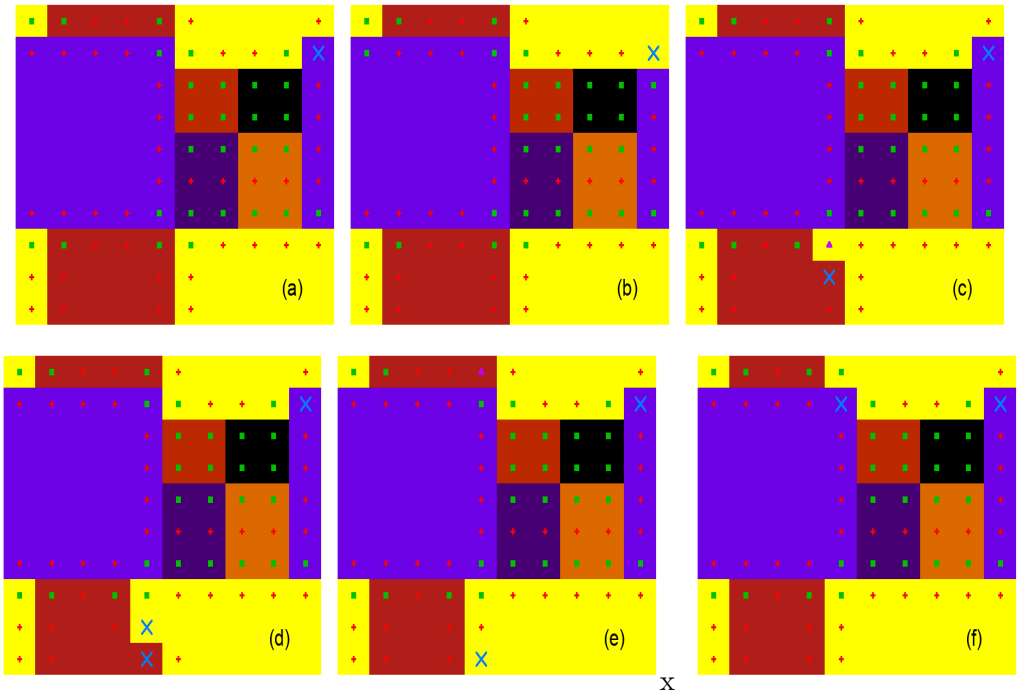

Figure 2.11. Snapshots of the Potts model in the large q limit at low temperature. The lattice is a squared one with periodic boundary conditions and $L = 10$. The domains within which the spins take the same value are painted with the same color. See the text for details on the convention used to identify the states of the spins on the domain walls, shown with small data-points with different form and color. The neighboring configurations differ by a single spin flip. Taken from [5].

In the large q limit with the condition $T < T_c/2$, $e^{-\beta}$ is very small and $qe^{-\beta} < 1$. Then the dominant changes are the flips of spins in the (2) state toward another (2) state (thus a blinking) and the next leading changes are the spins in the (3) state changed in a (5) state. The flip of a spin in the (2) state will again produce the configuration shown in the (b) panel of Fig. (2.11), which will almost surely flip back to the configuration in panel (a), etc. Thus this leads to the same blinking behavior as in the infinite q limit. But for a large and finite q, after a time $\simeq e^{\beta}$, a spin in a (3) state can also flip. Such an example is shown in the (c) panel of Fig. (2.11). The spin which changed value (from red to yellow) is now in a (5) state, shown as a purple triangle (▲). One can also observe the appearance of another (2) state just below. Of course, the spin in the (5) state is short lived (the probability that it flips back to its previous value is $\simeq 1 - 2e^{-\beta}$). But there exists a finite probability $\simeq 1/2$ that the blinking state below is updated first, producing the configuration shown in the (d) panel of Fig. (2.11). It can be seen that the (5) state is changed in a (more stable) (3) state, while the blinking state moves down. Next, there is a finite probability that the new (2) state changes color to produce the configuration seen in the (e) panel of Fig. (2.11). This configuration contains again a short lived (5)

state. Thus, from this state, there is a large probability to end in the configuration shown in the (f) panel of Fig. (2.11).

The conclusion is that starting from configuration (a), one will observe blinking between (a) and (b) configurations until, after a time $\simeq e^{\beta}$, a transition to a (c) configuration occurs. Next, with a finite probability, the state evolves to the (d) configuration and, again with a finite probability, it goes to the (e) configuration from which it evolves to the (f) configuration. This shows that the time scale for quitting the low temperature and large q blocked state is given by:

$$t_S \simeq e^{\beta J} \times t_{MCs}/l^2 = e^{J/T} \times t_{MCs}/l^2. \tag{2.13}$$

where the coupling constant J has been restored, and t_{MCs}/l^2 is just the Monte Carlo time step scale per surface unit, put to 1 for simplicity. This proper time is a major result of this work. The same time-scale was found with different arguments by Spirin et al [113] and Ferrero & Cannas [114].

Finally, one can note that this simple scenario is valid for all values of T and q as far as the conditions $e^{-2\beta} \ll e^{-\beta}$ and $qe^{-4\beta} \ll e^{-\beta}$ are satisfied. This can be rephrased by saying that one expects an universal behavior at low temperature and for large q. In the next Sections, these predictions will be tested with numerical simulations. It is worth stressing that a very similar phenomenology is found on the honeycomb lattice and cubic lattice, while a different one, with no blocked states and no plateau in R, on the triangular one.

2.6 Escaping freezing: the coarsening regime

Another fundamental dynamical regime, for the spins kinetics theory, is the coarsening one [27, 27, 90, 90–93]. In general, the class of phenomena in which there is a driven growth process of a new phase inside the old one are called coarsening phenomena. In the Potts case, coarsening is determined by a surface tension mechanism. When a subcritical quench has been done, the system is forced to start ordering, if it is not stuck in metastable states. When one has coarsening, the interior part of the new domains is thermodynamically at equilibrium. The dynamical game is all played by the interfaces between new and old phase, *i.e.* ordered phase and the "sand" made by many (11) local states. Interfaces are not always stable, indeed for the Potts model one has:

- An interface is stable if is flat.
- An interface is unstable if a curvature is present.

The following plot (2.12), by means of a sketch of a square lattice, shows an example of flat and curved interfaces.

There is curvature driven process who leads to the "ordering" of some paramagnetic phase and stabilization of the system. During this process, $R(t)$ grows until it becomes

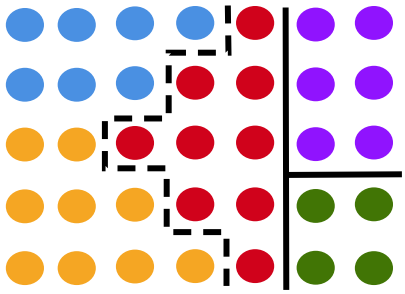

Figure 2.12. Example of flat (continuous line) and curved (dashed line) interfaces. Also a T-junction is present on the right.

as big as the lattice side L. $R(t) \simeq L$ is the witness of the fact that the system has reached the equilibrium. A graphical example on how domains coarsen is given in Fig. (2.13).

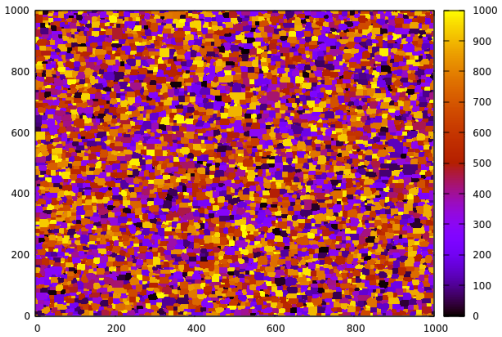

(a) $t \simeq 500$ Monte Carlo steps

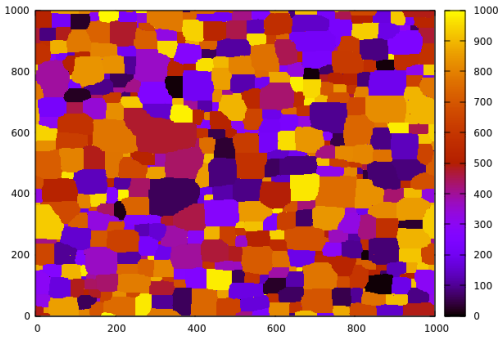

(b) $t \simeq 1500$ Monte Carlo steps

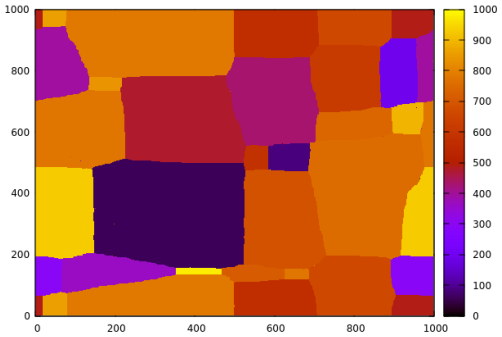

(c) $t \simeq 250 \times 10^3$ Monte Carlo steps

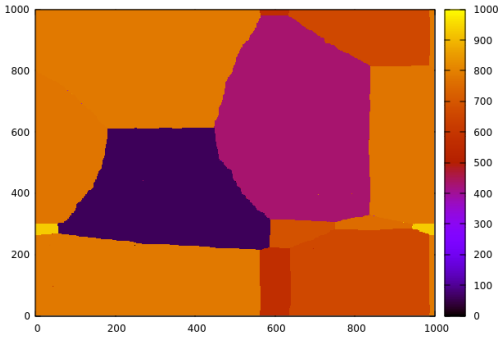

(d) $t \simeq 1 \times 10^6$ Monte Carlo steps

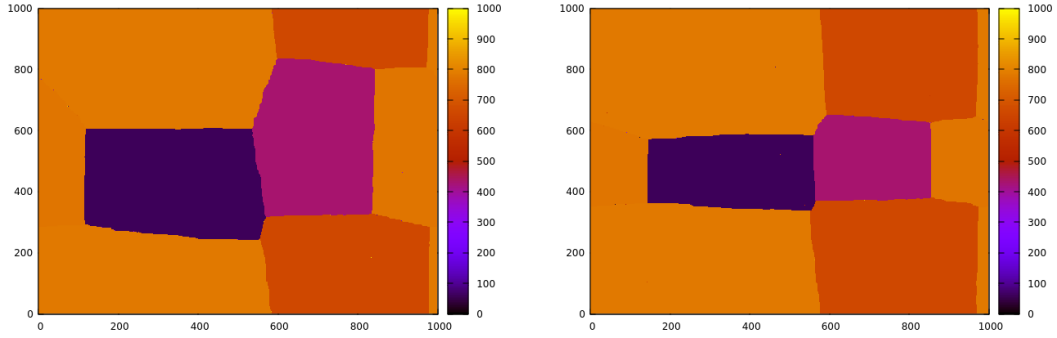

(a) $t \simeq 1.5 \times 10^6$ Monte Carlo steps **(b)** $t \simeq 2 \times 10^6$ Monte Carlo steps

Figure 2.13. Coarsening of domains for a Potts model with $q = 10^3$, $T = 0.80T_c$, $L = 1000$.

2.6.1 Dynamical scaling hypothesis

In the studying of coarsening dynamics, an important hypothesis has to be done. This is called dynamical scaling hypothesis and it states that:

A long time after the quench, if one studies the system properties in the scaling limit $r \gg \xi$, with r a generic distance and ξ is the correlation length, these can be described by an unique proper length scale which is indeed $R(t)$.
$R(t)$ is universal in this regime and follows an algebraic law in t: $R(t) \sim t^{1/z_d}$, where z_d is called dynamical exponent and characterize the kind of dynamics. Also, measuring distances in $R(t)$ units, one notice that the structures of spin clusters are statistically equivalent at different times. This holds if $R(t)$ is smaller than the linear size L and for $R(t)$ much greater than the lattice spacing l, *i.e.* $l \ll R(t) \ll L$. For spins systems with non-conservative dynamics, *i.e.* the order parameter is not kept fixed during the dynamics *e.g.* the heat bath, $z_d = 1/2$, [27, 115]. The exponent is universal and thus, independent of the parameters defining the model, which enter all in a prefactor, $\lambda_q(T/T_c)$:

$$R(t; q, T/T_c) \simeq [\lambda_q(T/T_c)t]^{1/2}. \tag{2.14}$$

2.7 Characterisation of the dynamics: parameter dependence

In this Section the analysis of the parameters (q and T/T_c) dependence of the growing length R is analysed. The aim is proving the hypothesis (2.14) and finding the explicit form of the pre-factor $\lambda_q(T/T_c)$. In the first part of this Section the work is done with

the square lattice. By the end of it, data for honeycomb lattice, which confirms the same kind of universality found on the square one, are given. The triangular lattice has been considered too, but, in this case, one observe a different behavior.

2.7.1 Freezing on the square lattice

In the left panels of Fig. (2.14), it is shown R vs. t for $q = 10^2$ and 10^6 (from top to bottom) and the reduced temperatures T/T_c given in the keys. In the right panels the time is rescaled by $t_S = e^{J/T}$, the time-scale that has been identified in Eq. (2.13).

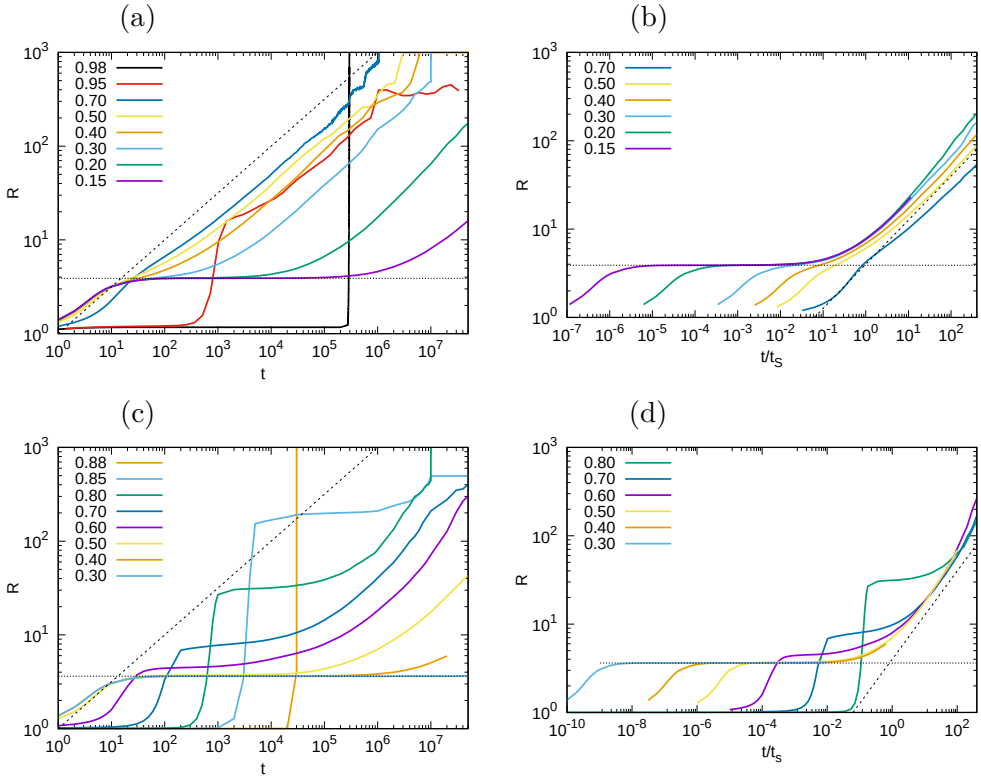

Figure 2.14. The growing length R vs. t for $q = 10^2$ (a) and (b), and 10^6 (c) and (d) in a square lattice system with $L = 10^3$ and various values of T/T_c written in the keys. In the right panels (b) and (d) is shown a rescaled version in which time is divided by $t_S = e^{J/T}$. The horizontal dotted line is at the plateau $R_p \simeq 3.63$ and the inclined dashed line is the expected asymptotic $t^{1/2}$ law. Taken from [5].

First of all, for both q, the curves show the crossover at $T/T_c = 1/2$, with $T_s = T_c/2$. At very short times, the data for $T/T_c > 1/2$ demonstrate the early establishment of the (high-temperature) metastable state with $R \simeq R_m \simeq 1$ and later evolution via the multi-nucleation process [116], while the early evolution of the curves at $T/T_c < 1/2$ is temperature independent and rapidly approaches $R_p \simeq 3.63$, to only later enter the

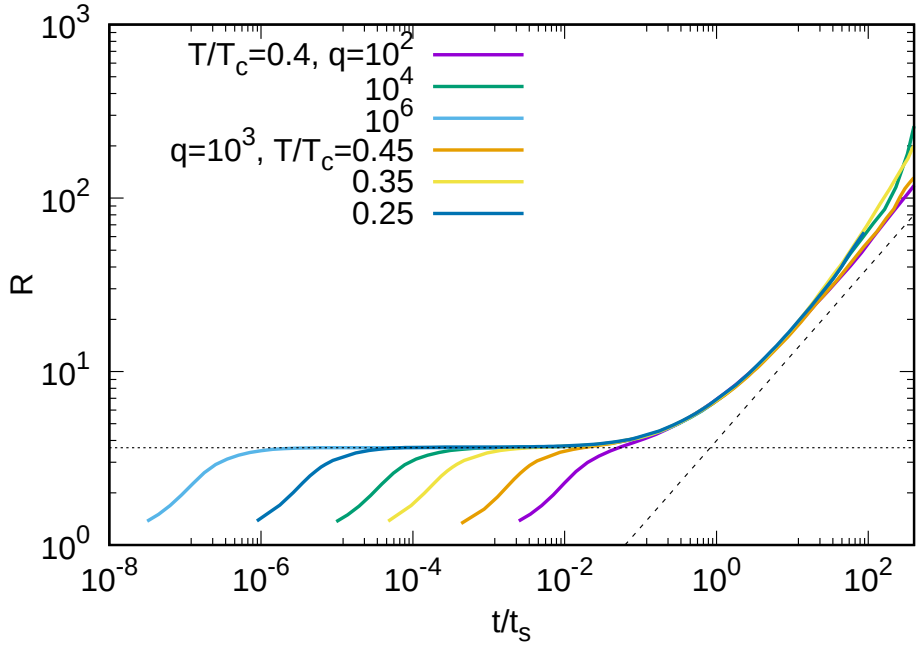

Figure 2.15. The growing length R vs. t/t_S in the square lattice model with $q = 10^2, 10^4$ and 10^6 at $T/T_c = 0.40$, and with $q = 10^3$ at $T/T_c = 0.45, 0.35$ and 0.25. The horizontal dotted lines are at the plateau $R_p \simeq 3.63$ and the inclined dashed line is the expected asymptotic $t^{1/2}$ law.

coarsening regime. Curves where $T > T_c/2$ have a different scaling with respect to the sub-spinodal ones. This is a non trivial check of the spinodal location.

The case $q = 10^2$ is analysed in more detail. At low relative temperature, up to $T/T_c \simeq 0.30$, R makes a small initial jump from $R(0) \simeq 1$ to a finite value $R_p \simeq 3.63$ and keeps this value during a time, which one can call t_p, that increases as one decreases the temperature. Next, at later times, there is a crossover towards a regime with the $R(t) \simeq t^{1/2}$ characteristic of the standard curvature driven coarsening [27, 90–93]. At higher relative temperatures, there is a similar initial rapid increase to $R_p \simeq 3.63$, next an inflection point, and then the coarsening regime. This can be seen up to $T/T_c \simeq 0.5$. For even higher relative temperature, R keeps a small value close to one, corresponding to the disordered metastable state, and this for longer and longer times t_m as one increases the temperature. For example, for $T/T_c = 0.95$, the metastable state survives up to $t_m \simeq 10^2$. Next, R increases very rapidly up to a large value R_l. After this very rapid variation, R increases very slowly first and next faster towards the conventional coarsening regime with $R(t) \simeq t^{1/2}$. Note that R_l increases as one increases T/T_c, and t_m practically diverges at $T/T_c \simeq 0.99$. More details on the multi-nucleation processes taking place above $T_c/2$ are given in [116].

In summary, for $q = 10^2$ one observes:

- At $T/T_c \leq 0.5$, there is an initial jump of R to $R_p \simeq 3.63$, a value that remains constant up to a time t_p which increases as T/T_c decreases. Afterwards, the dynamics reach the coarsening regime with R growing as $t^{1/2}$.
- At $T/T_c > 0.5$, the system remains in the metastable high-temperature state with a very small value R_m up to a time t_m which increases with T/T_c. At later times, $t > t_m$, it is observed a jump towards a finite value R_l which increases in a way similar to the increase of t_m. Next, the typical length grows very slowly, and finally reaches the curvature driven $t^{1/2}$ law.

The situation is similar for other values of q, see the other left panel in Fig. (2.14), a system with $q = 10^6$. The main difference is that for $T/T_c > 0.5$, after the jump towards R_l, one observes that the slow growth is replaced by a long-lasting plateau as q is increased. This is particularly clear for large q, see the third left panel in Fig. (2.14).

This change of behavior at $T/T_c \simeq 0.5 = 2/z$ is even better seen if time is rescaled by the time-scale $t_S(q, T/T_c) = e^{J/T}$, determined in the previous section. In the right panels of Fig. (2.14), it is shown R as a function of $t/t_S(q, T/T_c)$. It is found that, for each q, R first goes to a plateau at temperatures $T/T_c \leq 0.5$ up to a rescaled time $t/t_S \simeq 10^{-2}$ which does not depend on q (confirmed by other values of q not shown). For longer times, the plateau will be escaped in a universal way and for longer (rescaled) times, the coarsening regime will be reached with $R(t) \simeq t^{1/2}$. Note that for $q = 10^4$ and $q = 10^6$, the curves are identical for $T/T_c \leq 0.5$. For $q = 10^2$, the scaling is not as good for T/T_c close to 0.5. This is in agreement with the previous observation that the zero temperature behavior becomes universal for large q and with deviations up to $q \simeq 10^2$.

Then, for $T/T_c < 0.5$, it is claimed that the behavior of R is universal if one introduces a rescaling of time by $e^{J/T}$ such that[4]:

$$R(t, T/T_c, q) \simeq f(e^{-J/T}t) \quad \text{with} \quad f(x) \simeq \begin{cases} 3.63 & \text{for} \quad x \ll 1, \\ x^{1/2} & \text{for} \quad x \gg 1. \end{cases} \tag{2.15}$$

As usual with with these kinds of scaling laws, the coarsening behavior is restricted to $R \gg l$, with l the lattice spacing, and $R \ll L$ with L the system side where equilibration of at least some samples comes into play. The main finding is that for large q ($q \geq 10^3$, thus $q = 10^3$ is the lower bound value which defines the large q limit) and small T ($T/T_c \leq 0.5$), after a short transient the system reaches a state equivalent to the blocked state at zero temperature, with R_p determined by the lattice geometry and microscopic

[4] In [117, 118] a rather weak dependence of $\lambda_q(T = T_c/2)$ on q was claimed. Differently from here, in those papers only small values of q, $q = 2, 3, 8$, and the special temperature $T = T_c/2$ were considered.

dynamics, and that this blocked state survives up to $t_p \simeq R_p^2\, e^{J/T} = R_p^2\, t_S$, when the dynamics crosses over to the conventional coarsening one. In the above equation, the physical scales have been restored to have a dimensionful quantity. The dynamical behavior, for the square lattice, can thus be resumed by the dynamical phase diagram of Fig. (2.16), which represents one of the main results of this thesis [5].

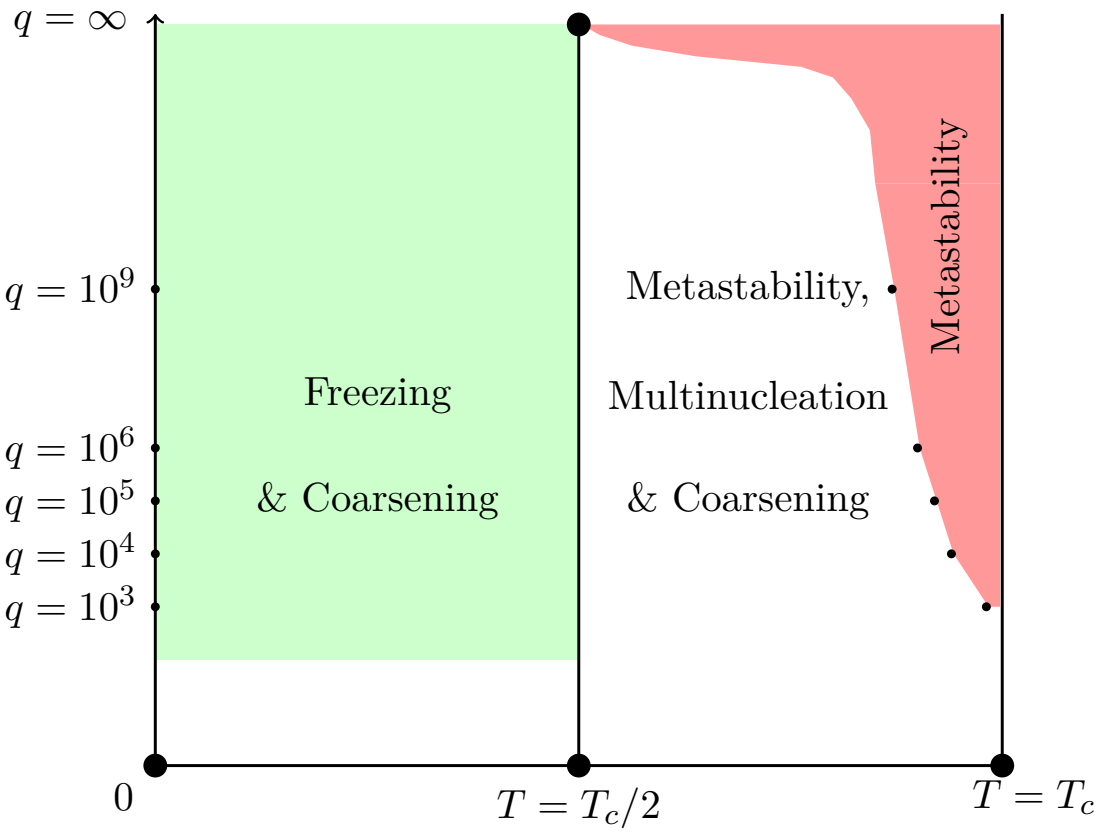

Figure 2.16. A sketch of the phase diagram of the $2d$ Potts square-lattice model. The $(T/T_c(q) \leq 1,\ q \gg 4)$ plane with the crossover lines between different types of dynamic behavior are displayed. The black dots sitting on the limit between the (pink) metastability and (white) multi-nucleation regions were obtained in [55]. This work focuses on the dynamics in the (light green) regime $T < T_c(q)/2$ while [116] concentrates on the multi-nucleation and further coarsening arising in the white region.

Snapshots

In the previous subsection, it is argued that there is universal behavior as a function of temperature after a proper rescaling. This was shown by considering the behavior of the growing length $R(t, q, T/T_c)$. In this section this result is confirmed by showing some snapshots of a system with $L = 10^2$ and $q = 10^2$, see Fig. (2.17). The instantaneous configurations at the times at which $R = \{5, 10, 20, 40 \text{ and } 80\}$ are shown, from left to right, as reached at the relative temperatures $T/T_c = \{0.2, 0.3, 0.4, 0.5\}$ from top to bottom. The main observation is that the snapshots look very much the same for fixed value of $R(t)$. The same check has been done also for other values of the number of states, $q = 10^3$ up to 10^6, and they also look the same for the same R and relative temperatures T/T_c.

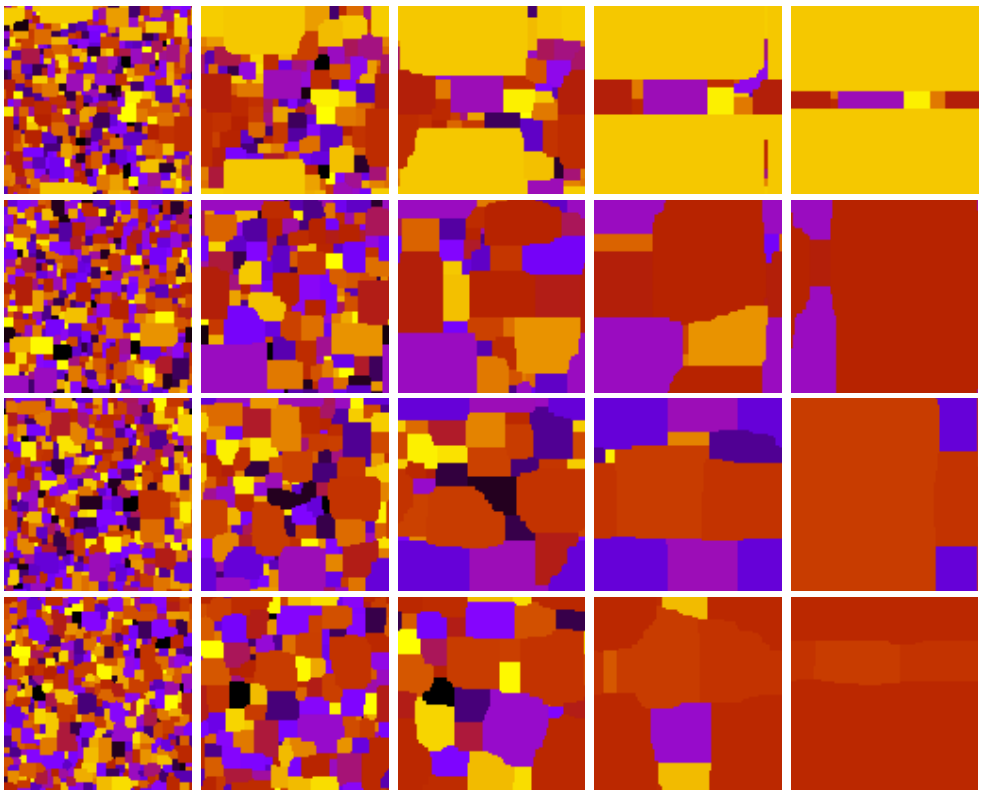

Figure 2.17. Snapshots at $R(t) = \{5, 10, 20, 40 \text{ and } 80\}$ (left to right), $L = 10^2$ and $q = 10^2$. From top to bottom $T/T_c = \{0.2, 0.3, 0.4 \text{ and } 0.5\}$.

2.7.2 Still freezing on the honeycomb lattice

To check the universality of the results over the lattice kind one can do some measurements using a honeycomb lattice. This is from a square lattice of linear size $L \times L$. At each site, the spin is connected to the left and right, and alternating, to the upper or lower raw. For a more detailed description, see [112]. One can recall that the critical temperature is given by $e^{\beta_c J} \simeq q^{2/3}$ in the large q limit. In Fig. (2.18), the time and reduced temperature dependence of the growing length R in a system with $L = 10^3$ and $q = 10^4$ is studied. In this case $T_c \simeq 0.162$. The time-dependence of R is similar to the one found on the square lattice with the same q, see Fig. (2.14). Again, at low temperatures, *i.e.* $T < 2T_c/3$, R first goes to a plateau at $R_p \simeq 4$, the same value obtained in the infinite q limit after a quench towards $T < 2T_c/3$, see Fig. (2.10). In the right part of Fig. (2.18), one can see that this plateau exists during a time $\simeq e^{J/T}$ (as was the case on the square lattice for $T < T_c/2$). At temperatures above $2T_c/z$ the system remains in the high temperature metastable state with $R \simeq 1$ until a sudden jump in R towards R_l takes it out of it. R_l increases with T.

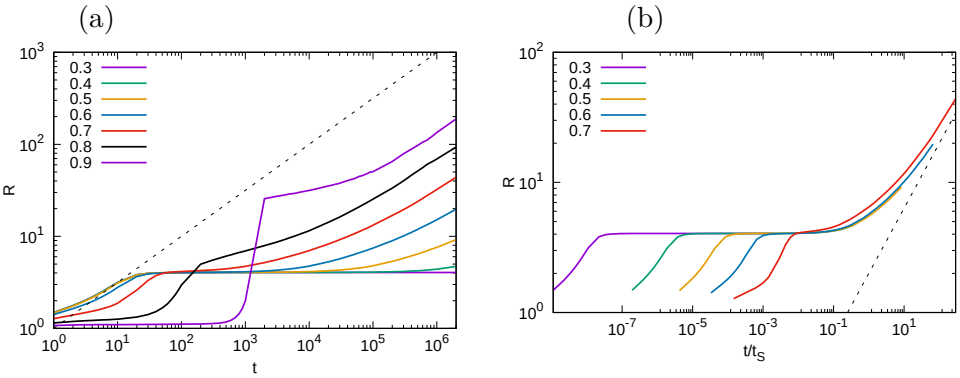

Figure 2.18. The time and temperature dependence of the growing length R in the Potts model with $q = 10^4$ on the honeycomb lattice with periodic boundary conditions and $L = 10^3$. In (a) bare data for many $T/T_c(q)$ given in the key. In (b) R against t rescaled by $t_S = e^{J/T}$ for four temperatures $T < 2T_c/z$ and also one temperature $T > 2T_c/z$ which approaches the asymptotic $t^{1/2}$ without scaling at short times. The dashed inclined line is the curvature driven law $t^{1/2}$.

2.7.3 Coarsening on the triangular lattice

The triangular lattice case in now considered. One needs to remember that it has a coordination number $z = 6$. In the large q limit, $e^{\beta_c J} \simeq q^{1/3}$ and the interesting regime is the one of quenches below $T_c/3$. Differently from what observed on the square and honeycomb lattices, in such quenches there is no plateau in R and the growing length is not strongly slowed down. This was already observed in [68] for the $q = 10^2$ model at $T = 0.1$, while $T_c = 0.635$ for this q. One can see the results, also for $q = 10^2$, in

Fig. (2.19) for various values of T/T_c. It is observed that R does not depend on T for small T/T_c and a plateau is not found. For the smallest value $T/T_c = 0.15$, R takes the same value as for the zero temperature shown in Fig. (2.10) (either at $q = 10^3$ or in the infinite q limit). Only for $T/T_c = 0.4 > T/T_c = 1/3$ one can see a small deviation. For large values of T/T_c the behavior is similar to the one of the other lattices. The time dependence of R at $T/T_c = 0.90$ for the square and honeycomb lattice models has also been included, in Fig. (2.19).

Note that the measurements using the triangular lattice at a finite temperature have been done with a Metropolis algorithm [63] since the heat bath one is difficult and very tedious to be implemented. One thus, has to rescale the time by a factor $\simeq q$ to compare the two. It has been found that with a factor 50, the behavior of R is similar for the three lattices at $T/T_c = 0.90$.

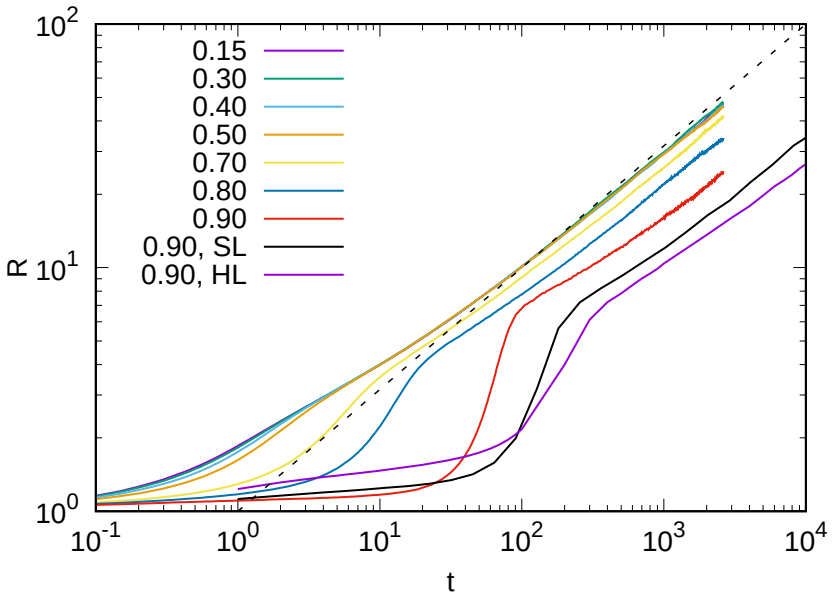

Figure 2.19. The growing length R vs. t for the triangular lattice model with $q = 10^2$ and $L = 10^3$ at different values of T/T_c given in the key. For comparison, results for the square lattice (SL) and the honeycomb lattice (HL) at $T/T_c = 0.90$ are also shown. The dashed inclined line is the curvature driven law $t^{1/2}$.

2.7.4 What happens in $d = 3$? The cubic lattice

In this section, results for the evolution after quenches at low temperatures on the cubic lattice are presented. In particular, one wants to test if the below the (pseudo)-spinodal temperature, $T_s = 2T_c/z$, freezing decorates the dynamics. For earlier works on the

cubic lattice, one can see [119]. In this section, quenches at various values of T (small) such that $T \leq T_s(q) = \dfrac{T_c(q)}{3} \simeq \dfrac{1}{\log(q) + 3 \times 0.267 q^{-1/3}}$ are considered.

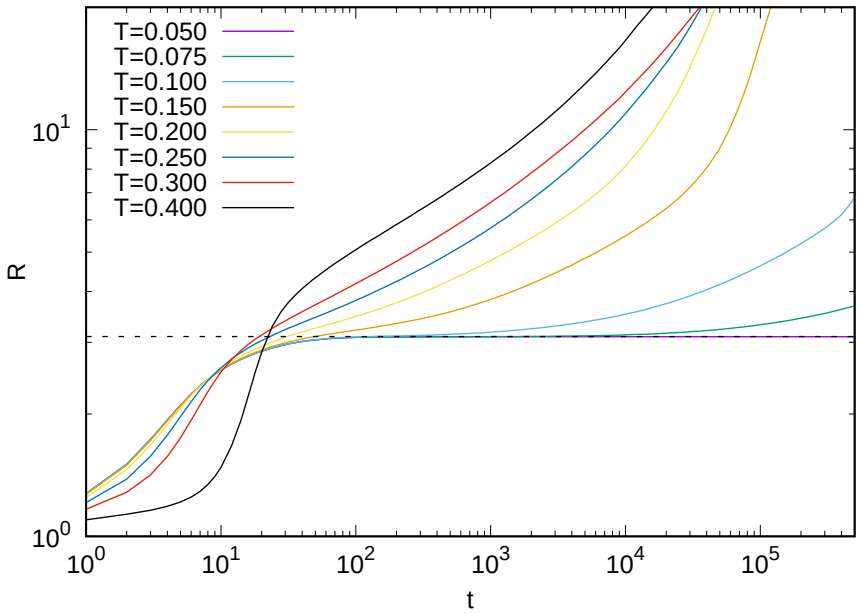

Figure 2.20. $R(t)$ vs t for $q = 100$ and an $L = 400$ on a cubic lattice. In the key, the temperature (not the reduced one) is given, while the dotted line represents the usual freezing plateau.

Starting from the case $q = 100$ for which one has $T_c(q = 100) \simeq 0.6279$ and thus one expects $T_s(q = 100) = 0.2093$. In Fig. (2.20), it is shown $R(t)$ as a function of the time t after the quench at temperatures $0.05 \leq T \leq 0.4$ as described in the caption. One should notice that now, measures are taken with respect to T, and not T/T_c. Indeed, since T_c is estimated, in this case, it is safer to measure just with respect to T. The data are for cubic lattice with a linear size $L = 400$ and periodic boundary conditions. It is checked that there are no finite size corrections to the behavior of $R(t)$ except for $R(t) \simeq L$. At early times, up to $t \simeq 10$, it is observed the same behavior of $R(t)$ for all values of $T \leq 0.2 \simeq T_s(q = 100)$. For this temperature range, $R(t)$ goes, at a later time, towards a plateau with value $\simeq 3.1$, as shown in the figure with a dashed line. $R(t)$ will remain on this plateau up to a time which increases while decreasing T. This indicates that, at small times, the dynamics for $T \leq T_s(q = 100)$ is first described by a blocked state corresponding to a zero temperature fixed point. The lower the temperature, the longer it takes to escape from this blocked point. For $T > T_s(q = 100)$, one observes that $R(t)$ is a function of the temperature for all the times and there is no blocked state. In Fig. (2.21) it is shown $R(t)$ as a function of $t/t_S(T)$ with $t_S(T) = e^{1/T}$ the usual rescaling function (and the proper time of the dynamics in this regime). It is observed that $R(t)$

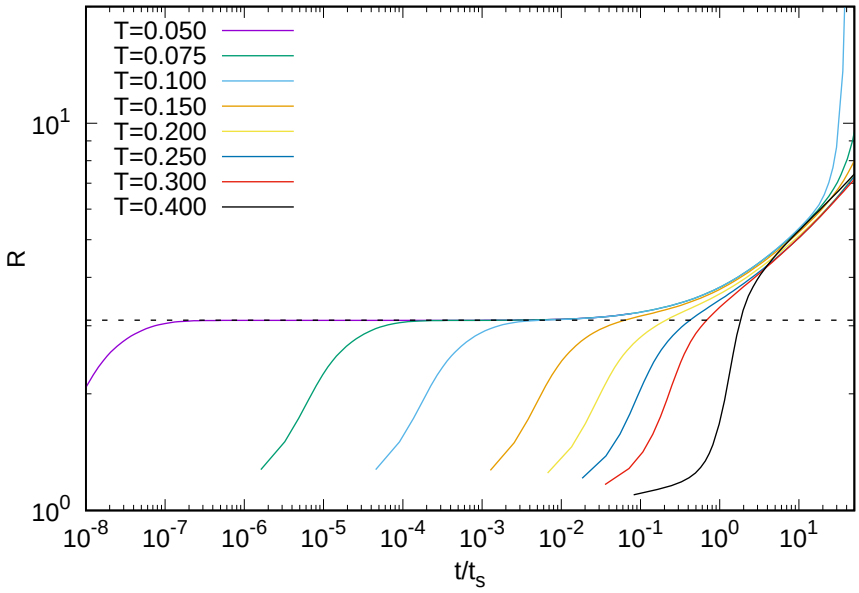

Figure 2.21. $R(t)$ vs t/t_S for $q = 100$ and an $L = 400$ on a cubic lattice. In the key, the temperature (not the reduced one) is given, while the dotted line represents the usual freezing plateau.

escapes the plateau on a universal curve as a function of $t/t_S(T)$ for $T \leq T_s(q = 100)$ in the same way as it was was observed for the square lattice in the previous sections, [5].

Note that while the collapse after rescaling is obvious for small temperatures, it is less obvious, from Fig. (2.20), that the change of regime takes place exactly at $T = T_s$. This is because $q = 10^2$ is not large enough. Next, it is shown, in Fig. (2.22), some similar data but for $q = 10^4$ and for which $T_c \simeq 0.3244$ and $T_s \simeq 0.1081$. In Fig. (2.22), one observes a deviation starting for $T = 0.110 > T_s$ and larger temperatures. Thus one expects that the change of behavior at $T = T_s$ will become sharper as one increases q. This is also observed in $d = 2$, [5]. This q dependence also appears in the value of the growing length at the freezing plateau. The same measurements, for various values of q, ranging from $q = 10$ up to $q = 10^5$, are also repeated. It is always observed the same behavior for $q \geq 100$. (For $q = 10$, the plateau is observed only at a very small temperature, up to 0.1, while $T_s \simeq 0.4$). For the cubic lattice, thus, it is determined that the value of the plateau to be at $R(q) \simeq 2.774 + \text{const} \times q^{-3/4}$. This value corresponds to the freezing at zero temperature.

Another thing to be noticed is that, at $t \simeq 1$ one expects $\mathcal{E}(t \simeq 1) \simeq -N/2$ with N the number of spins. Then $R(1) \simeq 1.2$. In Fig. (2.22), this value is shown as a thin dotted line. For each value of temperature smaller than $T_s \simeq 0.1081$, the first shown point for $R(t)$, corresponding to $t = 1$, is above this line, while it is below for $T > T_s$. This is due

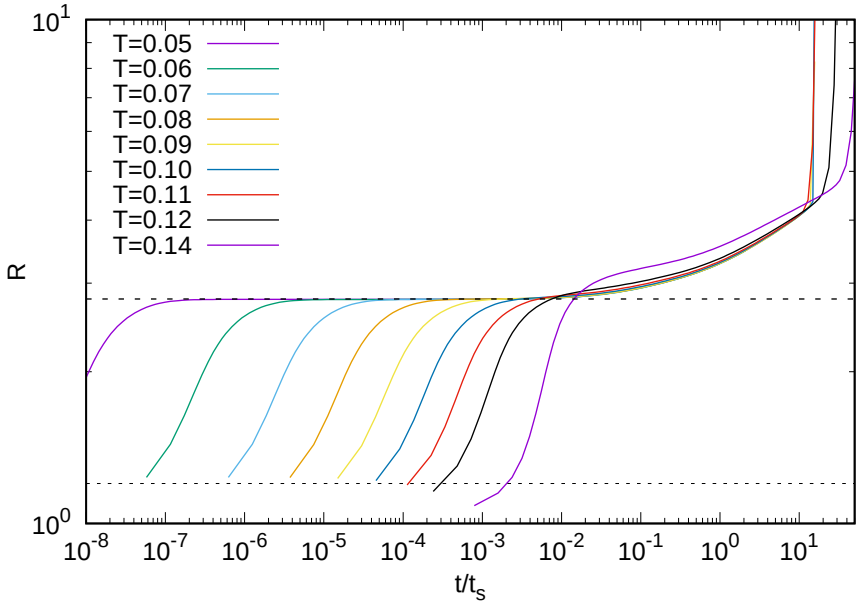

Figure 2.22. $R(t)$ vs t/t_S for $q = 10^4$ and an $L = 400$ on a cubic lattice. In the key, the temperature (not the reduced one) is given, while the dotted line represents the usual freezing plateau. The thin dotted line represents $R(t) = 1.2$ is the growing length related to an energy, $\mathcal{E}$ =-N/2, the energy one expects, if no metastability is present, after a time $t \simeq 1$.

to the metastability which occurs for these temperatures. This is a non trivial check of the location of the spinodal.

In summary, one observes blocking for the cubic lattice even if $z_c = z_t = 6 > z_s$, see Fig. (2.20). The behavior of $R(t)$ in this case, is very different from the one of the triangular lattice, see Fig. (2.19). Thus, it is found that the energy barrier to be overcome to unleash the dynamics corresponds to a single spin-flip, which is the same as what is found in $d = 2$ for the square lattice [5]. Again, in the low-temperature sub-spinodal region it is necessary to wait a time which scales as the Arrhenius form $\sim e^{J/T}$ before being able to escape from a blocked configuration and equilibrate, see Fig. (2.21) and (2.22).

2.8 Physical argument to freezing

The different behavior on the cubic and triangular lattices naturally raise the question: what is the mechanism who leads to this very different behaviors? In this section an argument to answer to this question is given by comparing the dynamics on the cubic and triangular lattices.

2.8.1 Frozen dynamics on the square lattice at $T = 0$

Before entering in the cubic *vs.* triangular analysis it is reminded why the dynamics is frozen at $T = 0$ on the square lattice for $q \geq 3$, see also Sec. (2.5). This comes from the possibility of having particular configurations of spins as the one shown in Fig. (2.23). The dotted line is drawn to highlight the lattice geometry underneath, and will always be included in the next sections, since the geometric lattice properties are crucial to understanding the physical behavior.

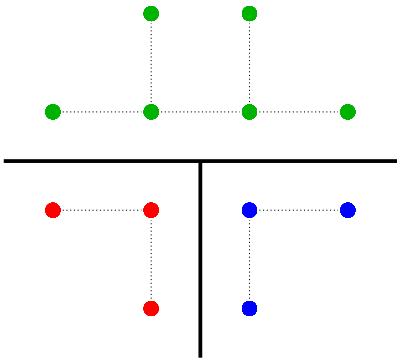

Figure 2.23. Frozen configuration at $T = 0$ for the square lattice.

The four spins in the centre are completely stable. If one tries to change the red spin in a green or blue spin, it would break two bonds while creating only one new bond. So, an increase of the energy which is forbidden at $T = 0$. The same is true for the blue spin and for any of the two central green spins, changing colour would break three bonds and create only one new one. So, the four spins at the centre are frozen, it corresponds to the so called T-junctions. Freezing for the square lattice at zero temperature is due to the existence of many such T-junctions and stable corners, see [102] for a more detailed description.

It is simple to check that similar corners exist on the honeycomb lattice leading also to freezing. For the honeycomb, the coordination number is $z = 3$, in that case, two colours ($q = 2$) are enough to freeze the lattice [120]. One starts from a configuration at an infinite temperature such that the lattice is completely disordered and spins are maximally uncorrelated. One can consider the case of a general dimension and lattice. As already mentioned earlier, $T_s \simeq 1/\log(q)$ in the large q limit. After an initial instantaneous quench at $T < T_s = 1/\log(q)$, each update will change the value of a spin to be equal to one of its neighbors. Indeed, for any not-bonded spin, flipping to a value equal to a neighboring spin will give a contribution to the free energy of $e^{1/T}$ larger than the lost contribution due to the entropy, q. After a time $t \simeq O(1)$, corresponding to the update of all the spins, a bond will be created among most spins and one of their neighbors chosen in a random way. At this stage, each spin is still completely unstable, even at $T = 0$. It can change and create a bond with any of the others neighbors without an en-

ergy cost. Then, these bonded spins, with the aim of minimising the free energy, create, eventually, other bonds. At this point, the dimension and the type of lattice become important, so one needs to consider different cases in the following. For simplicity, it is considered the case of a quench at $T = 0$.

2.8.2 Not frozen dynamics on the triangular lattice at $T = 0$

Next, one considers the case of the triangular lattice at $T = 0$ and check if similar blocked corners can exist or not. To do so, one can start by considering hexagonal plaquettes, as shown in Fig. (2.24). Here the red central spin has two bonds, *i.e.* it has two neighbors

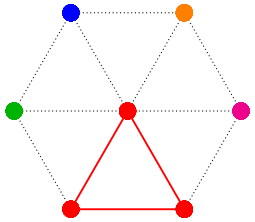

Figure 2.24. Starting configuration for the triangular lattice

with the same colour. One assumes that the four other spins around this central one have different values (shown as different colours) and this in order to ensure that the red spin can not flip to another value. The aim is to determine if it is possible to build a frozen configuration with a fixed central red spin. One first considers the green spin on the left. This spin needs to be connected with three neighbors green spins, as shown in Fig. (2.25) to ensure that it can not become red. The same is true for the magenta spin on the right. Then, one needs the configuration shown in Fig. (2.25):

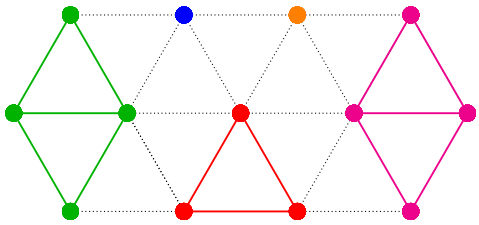

Figure 2.25. Intermediate configuration on the triangular lattice.

Next, one considers the blue spin. It needs to be connected with two other neighboring spins which must be the two shown in Fig. (2.26). Clearly, there is no way to make the orange spin stable since it can only have a bond with a single spin. Then, this orange spin will become blue or magenta, allowing next the central red spin to flip to the same colour. This means that one can not build a blocked part of the configuration starting from the red triangle.

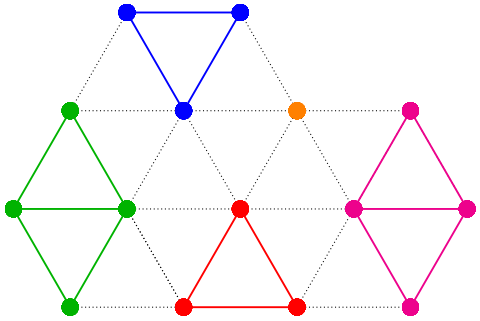

Figure 2.26. Not blocked configuration on the triangular lattice.

Note that it is still possible to obtain blocked configurations on the triangular lattice, but with much more complicated configurations involving many spins and occurring with a very small probability, as found in [108]. One can argue that they require three different colours and produce the so called three-hexagon state (with a small probability). But these structures have a very large growing length, a fraction of the linear size, and are controlled by a time that scales as $L^2 \log(L)$. So, they do have no common point with the blocked states on the square lattice having a finite growing length reached after a finite time.

2.8.3 Frozen dynamics on the cubic lattice at $T = 0$

One can now apply the very same argument but on the cubic lattice. As before, a one-bond kind of structure is useless for the aim, being fully unstable, thus the analysis is done directly with the interesting configuration. In Fig. (2.27), it is shown how this lattice is made and its unitary structure, made up of the highlighted yellow bonds plus the red satisfied ones. For any lattice, by definition, the unitary structure is made up of a central spin connected with its z neighbors, called external spins. There exist two types of unitary structures. The first type, which is called cyclic, for which one can connect any pair of external spins by a path in the unitary structure without going through the central spin. The triangular lattice is cyclic. For the second type, which is called acyclic, the path needs to go through the central spin. The square lattice (with nearest neighbors), the hexagonal lattice and the cubic lattice are acyclic.

In this configuration, again, the central spin has two neighbors with the same colour and four different neighbors. One considers that the green, orange, magenta and blue spins have already two satisfied bonds (not shown in Fig. (2.27) to avoid making the plot unreadable). They are all connected with the central one and two of them (the red) have a satisfied bond. For each of these spins, one knows three out of six neighbors. Next, one considers one of the neighbors, say the green one, and, as done in the triangular case, its unitary structure is analaysed. One knows that it has two green neighbors and a red one. It is assumed that the other three neighbors have colours different from red

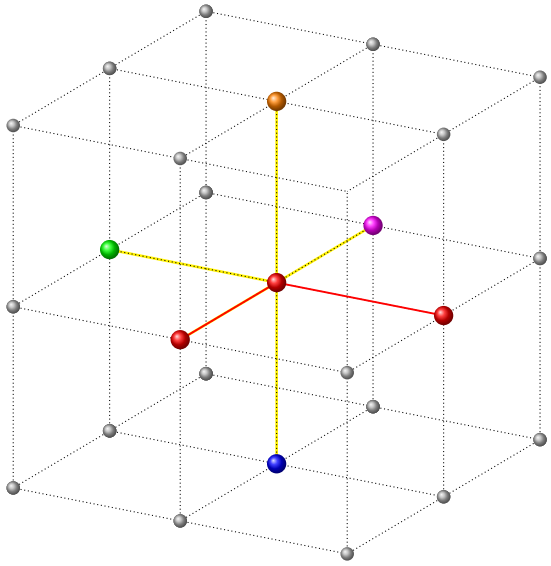

Figure 2.27. Unitary structure of the cubic lattice.

and at the maximum one neighbor which is orange, magenta and blue. One needs to remind also that the argument holds in the limit of large q and at an earlier time, so one expects that many different colours are present. Thus, the green spin will remain green. The exact same reasoning can be done for the other neighbors. One soon notices the common and the different features with respect to the triangular lattice. Even if they share the same coordination number, here, the graph made by the unitary structure has less edge and it is acyclic, while the triangular and hexagonal plaquette are cyclic. One can take, for example, the orange spin and observe the unitary structure with the red one in the centre. One notices that the orange spin can only influence this structure by means of one eventual bond. While, in the triangular lattice each spin at the vertex of a hexagon, including the ones not in the centre, can influence the unitary structure of a neighboring hexagon by using up to three bonds, as shown in Fig. (2.28).

This difference is very important because this leads to the cyclicity of the unitary structure and thus, to the mutual influence and connectivity among spins in it. In the cubic lattice, indeed, external spins are not mutually influenced, as happens in the triangular one. In fact, as shown previously, the blinking of a far away spin can lead to the unblocking of the dynamical behavior. In the cubic case, instead, one does not have events able to activate the dynamics. What is seen is that soon, as in the square lattice case, the system reaches a blocked configuration in which highly regular rectangular, cubic, and square domains are present. Here, so, a generalization of the results of [5] holds, see [6]. Indeed, going to finite temperatures and finite q one got exactly the same proper time as the one found in the square lattice.

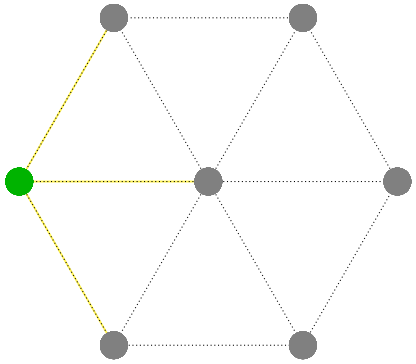

Figure 2.28. Unitary structure of the triangular lattice.

Last, it was found [56, 57, 99, 121] that for the square lattice with next-to-nearest neighbors interactions, the freezing behavior disappears. It is simple to argue that with the addition of next to nearest neighbors the unitary structure becomes cyclic for this lattice, explaining the absence of freezing.

2.9 Conclusions

Exploiting the $q \to \infty$ limit of the heat bath Monte Carlo algorithm [55] it is identified the temperature interval $[2T_c/z, 2T_c]$ in which high or low temperature initial conditions are metastable after sudden sub-critical or upper-critical quenches, respectively, with z the coordination of the lattice. In other words, the (pseudo)-spinodals have been located. In the $q \to \infty$ limit, the metastability is ever lasting while, for finite q, the initial states will eventually die out. Once this done, the focus has been on sub-critical quenches for temperatures below the lowest temperatures at which nucleation is observed, that is $T < 2T_c/z$. For these processes, it is showed that on the square, honeycomb and cubic lattices, after a rapid evolution, the systems temporarily block in configurations that are typical of the asymptotic states of the zero temperature dynamics [102, 108]. At non-vanishing temperature these states are not fully blocking and the systems escape them in a time-scale $t_S \simeq e^{J/T}$ independently of q for large q (see also [113, 114]). The proper curvature driven coarsening then takes over with the universal algebraic growing length $R \simeq (t/t_S)^{1/2}$. On the triangular lattice no freezing is observed, similarly to what was found in [57, 99, 109], and R is independent of temperature, for $T/T_c < 2/z = 1/3$, within the numerical accuracy.

Next, with a mixture of numerical data and physical argument, it is explained what leads to different low-temperature dynamical behaviors in the cubic and triangular lattices. This sharp change in the dynamics is attributed to the different topology of the lattice's unitary structures. In particular, when this is an acyclic graph, the spin-flips bring the system to a rather stable and highly symmetric blocked configuration, which is aban-

doned, thanks to thermal fluctuations, after an exponential time of the Arrhenius kind, $t_S = e^{1/T}$. When, instead, the structure is cyclic, spins of the unitary structure have a large "radius" of influence making impossible the blocking behavior. This dynamics is, thus, of the coarsening kind even at very low temperature.

Part II

Disorder at criticality

Chapter 3

Spin models with long-range correlated disorder: a numerical apporach

Preface

This chapter delves into the random-bond Potts model with long-range correlated disorder, drawing heavily from the research presented in the article [7]. Inspired by Chatelain's innovative approaches in his work [122], a novel method of generating the disorder distribution has been developed, leading to the new findings detailed in this section. This chapter represents the computational part of the latter half of the thesis.

Synthesis of the results

The bidimensional q-Potts model with long-range bond correlated disorder is examined in this chapter of the study. Following a similar approach as done by Chatelain in [122], a bimodal distribution of disorder is implemented by introducing auxiliary spin-variables, which exhibit correlation through a power-law decay function. The universal behavior of various observables, focusing on the thermal (ν) and order parameter (β) critical exponents, is obtained by using Monte Carlo techniques. The $q = \{1, 2, 3\}$-Potts models are investigated for different values of the power-law decay exponent a. The simulations align with previous theoretical and numerical results for $q = 1$ and $q = 2$. What is proposed in this work is a phase diagram for $q \in [1, 4]$. Specifically, it is established that the system reaches a fixed point with either finite or infinite long-range disorder, depending on the specific values of q and a. Additionally, it is explored the influence of cumulants order higher than the second in the disorder distribution by sampling the auxiliary spin-variables from different statistical models. While the primary characteristics of the phase diagram are determined by the first and second cumulants alone, it is argued that certain universal effects associated with the infinite disorder fixed point are influenced by the higher cumulants of the disorder distribution.

3.1 Introduction

In this section, the focus is on the bond-disordered q-Potts model, where the couplings exhibit random fluctuations around a fixed positive value. The aim is to examine the influence of the distribution of these fluctuations, *i.e.* the disorder, on the critical properties of the model. The relevance of the disorder is determined by referencing the Harris criterion [85] and its generalizations [86, 123], see Section (1.6.5), which consider the correlation properties of the disorder distribution. Of particular interest is the case of uncorrelated disorder, where the coupling fluctuations are independent and identically distributed. According to the Harris criterion, the critical properties of the pure (P) system are affected by the disorder when its thermal exponent ν^P exceeds one, $\nu^P > 1$ [85]. This criterion holds true for the q-Potts model with $q > 2$.

In the presence of relevant disorder, an intriguing scenario arises where the system maintains a continuous phase transition while being characterized by a different and stable renormalisation group (RG) fixed point, instead of the trivial pure one. This situation has been established for the two-dimensional Potts model with uncorrelated disorder. For $q > 2$, a stable RG fixed point, referred to as the Short-Range (SR) point, has been identified [44,124,125], which governs the critical properties of the model. The thermal exponent ν^{SR} and the order-parameter exponent β^{SR} have been computed using RG techniques applied to a perturbed conformal field theory [44], and their values have been verified through various numerical tests [125–127].

In this chapter it is explored the case where the disorder is on the couplings $\{J(x)\}$. At each position x, these are randomly selected from homogeneouses and isotropics distributions. The first cumulant of these distributions, denoted as $\mathbb{E}[J(x)] = \mathbb{E}[J]$, usually, is not a function of the space variable. The focus is on distributions where the second cumulant, defined as $g(|x-y|) = \mathbb{E}[J(x)J(y)] - \mathbb{E}[J]^2$, decreases according to a power-law for large distances. Specifically, $g(|x|) \propto (r-1)^2|x|^{-a}$ for $|x| \gg 1$, where a is a positive parameter. The parameter r determines the strength of disorder and is chosen to be greater than one, *i.e.* $r \in [1, \infty]$, as discussed in Section (3.2.1). The case where $r = 1$ corresponds to the pure Potts model, Section (3.2.2), while $r = \infty$ represents the infinite disorder point, which is extensively discussed in Section (3.2.5). The numerical approach used to implement these distributions closely follows the one introduced by Chatelain in [122], where the pure Potts model is coupled with the Ashkin-Teller model. However, most of the presented results are obtained using a replicated Ising model, Section (3.2.1), which differs from the approach in [122] for cumulants of order higher than two. It has been verified that the main findings regarding the phase diagram of these models remain unaffected by the higher cumulants of these distributions.

The extended Harris criterion [86, 123] determines in which region of the parameters (q, a) the disorder is relevant and when its long-range properties prevail over the short-range ones, see Sec. (1.6.5). When $a > 2$ the critical behavior of the system is expected to be the same as the one with uncorrelated disorder. The regions ($q < 2$, $a < 2/\nu^P$)

and ($q > 2$, $a < 2/\nu^{SR}$), where the disorder is relevant and dominated by the long-range correlations, are much less understood, especially for general values of q.

For $q = 1$, as explained in Section (3.3.2), both the pure Potts model and the Potts model with bimodal short-range disorder can be mapped to the Bernoulli bond percolation (Bp) model, where the activation of edges follows independent probabilities (pure percolation). On the other hand, the long-range disordered ($q = 1$)-Potts model corresponds to a one-parameter family (parameterized by the disorder strength r) of long-range bond percolation models, where the activation of two distant edges is correlated by a power-law function with exponent a. In the context of d-dimensional long-range percolation, a 1-loop order renormalisation group (RG) computation was conducted in [123] using a double expansion in ϵ ($\epsilon = 6 - d$) and δ ($\delta = 4 - a$). The study revealed the existence of a new stable RG point, referred to as the LRp (long-range percolation) point, driven by the long-range nature of the correlations. Although these theoretical predictions were valid only near six dimensions and for a close to 4, they motivated several numerical investigations [128–132] on $d = 2$ long-range percolation models with $a > 0$. These models were constructed using level sets of fractional Gaussian free fields with Hurst exponent $H = -a/2$. Since the thermal exponent of the pure ($q = 1$)-Potts model is $\nu^P = 4/3$, the long-range disorder becomes relevant for $a < 3/2$. The general consensus in [128–132] was that for $a < 3/2$, the percolation transition is described by the LRp point. In this work is used an approach that recovers the critical behavior, as studied in [128–132], at the $r = \infty$ point of a Potts model coupled with a fractional Gaussian field or n-Ising, see Sec. (3.2.1). It will be demonstrated that regardless of the value of r, these long-range percolation models are described by the Bernoulli percolation (Bp) point for $a > 3/2$ and the LRp point for $a < 3/2$. In other words, for each a, there exists a unique fixed point that remains stable in the direction of decreasing r. It is worth noting that when coupling the Potts model to n-replicated Ising models, the numerical investigations of LRp-type points become more precise, particularly for small values of a. In Section (3.3.6), it will be argued that some universal properties of the LRp points may depend on the higher cumulants of the disorder distribution.

The case of $q = 2$ corresponds to the bond disordered Ising model, which has been extensively studied in the past. In this case, the crossover exponent is $2/\nu^P = 2$. For $a \geq 2$, the short-range (SR) and the pure (P) points coincide, and the disorder effects lead to logarithmic corrections to the scaling relations [133]. However, for $1 \lesssim a < 2$, a stable long-range (LR) point is observed. The existence of this LR point has been proven in [134] and [135] using the Ising massive free fermion representation. Numerical tests of these predictions have been conducted in [136] for the case of $a = 1$. It was also observed in [135] that the LR point loses its stability for $a \lesssim 1$. The question of whether the system undergoes a smeared phase transition or flows towards an infinite disorder fixed point remains open in this regime. In [122, 137], the long-range disordered ($q = 2$) and ($q = 4$)-Potts models were investigated for values of a below one, $0 < a < 1$. It was observed that, for all these values of a, the Monte Carlo measurements of β/ν were very close to the value of the LRp point.

The objective of this chapter is to provide the phase diagram of the Potts model in the parameter space (q, a) numerically, covering the range $(q, a) \in (0, 4] \times (0, \infty)$, before delving into an analytical renormalisation group (RG) analysis. This goal is accomplished by investigating the disordered $q = \{1, 2, 3\}$-Potts models for various values of a. These three values of q are chosen to represent the three distinct regions where short-range disorder is respectively irrelevant, marginally relevant, and relevant, in terms of their impact on the critical behavior.

3.2 The long-range bond disordered q-Potts model

The model is defined by the usual partition function:

$$\mathcal{Z}_P^{dis}(\{J_{i,j}\}) = \sum_{\{s_i\}} \exp\left\{ \left(\sum_{\langle i,j \rangle} J_{i,j} \delta_{s_i,s_j} \right) \right\}, \tag{3.1}$$

where the spin s_i, living on the lattice vertex i, takes q possible states, $s_i = \{1, \cdots, q\}$. The i, j identifies the edge connecting the neighbouring sites i and j and the $\delta_{k,l}$ is the Kronecker delta. The set of couplings $\{J_{i,j}\}$ is made of random variables drawn from a given distribution, the average over which will be indicated by the notation $\mathbb{E}[\cdots]$.

The critical exponents of the model defined in Eq. (3.1) have been obtained by measuring the properties of its Fortuyn-Kasteleyn (FK) clusters [79, 138]. The FK clusters are the connected sets of bonds that enter in the geometric representation of the Potts partition function, see Section (1.6.2). As done in Eq. (1.41), from Eq. (3.1), one gets:

$$\begin{aligned} \mathcal{Z}_P^{dis}(\{J_{i,j}\}) &= \sum_{\{s_i\}} \prod_{\langle i,j \rangle} \left[1 + (e^{J_{i,j}} - 1)\delta_{s_i,s_j} \right] \\ &= \sum_{\mathcal{G} \in G} q^{\mathcal{C}_c(\mathcal{G})} \left(\prod_{\langle i,j \rangle \in \mathcal{G}} e^{J_{i,j}} - 1 \right) \\ &= \sum_{\mathcal{G} \in G} \prod_{\langle i,j \rangle \in \mathcal{G}} \left(1 - e^{-J_{i,j}} \right) \prod_{\langle i,j \rangle \notin \mathcal{G}} \left(e^{-J_{i,j}} \right) q^{\mathcal{C}_c(\mathcal{G})}, \end{aligned} \tag{3.2}$$

where the sum is over the set $\mathcal{G}$ of activated edges or bonds and $\mathcal{C}_c(\mathcal{G})$ is the number of connected components of the graph $\mathcal{G}$, in the FK construction, also called as FK clusters. It is important to recall that an isolated spin counts as a connected component. A bond connects two equal spins with probability $p(J_{i,j}) = 1 - e^{-J_{i,j}}$.

Self-averaging observables will be considered [87], such as the thermal (ν) and the order-parameter (β) critical exponents. More specifically, for $q = \{1, 2, 3\}$, the ratio β/ν will

be computed from the measure of the FK fractal dimension d_f by using:

$$d_f = 2 - \frac{\beta}{\nu}, \tag{3.3}$$

see Section (3.3). The exponent ν, instead, is extracted, for $q = 3$, from the FK clusters wrapping probability, defined in Eq. (3.30). This ν determines the finite size scaling of the probability defined in Eq. (3.31). In Section (3.3.3), the Ising ($q = 2$) spin-spin correlation function, which is a non self-averaging observable is considered. The multifractal behavior of this quantity, see Eq. (3.28), is measured and compared with recent predictions [135].

3.2.1 Implementation of disorder

In the simulations, a quenched bimodal disorder has been incorporated, where the couplings randomly assume two values, either $J_{i,j} = J_1$ or $J_{i,j} = J_2$, with an equal chance of occurrence. The values of J_1 and J_2 are not selected independently; instead, they are chosen in a way that fulfills the following self-dual condition:

$$(e^{J_1} - 1)(e^{J_2} - 1) = q. \tag{3.4}$$

The self-dual line expressed in Equation (3.4) represents a critical boundary, *i.e.* a line of critical points, that separates a paramagnetic phase from a ferromagnetic phase [80], as explained in Section (1.6.2).

To simulate this disorder, a random variable $\sigma_i = \{-1, 1\}$ is assigned to each vertex of the square lattice, and the following relation can be established:

$$J_{i,j(R)} = J_{i,j(B)} = \frac{J_1 + J_2}{2} + \sigma_i \frac{J_1 - J_2}{2}, \tag{3.5}$$

where $J_{i,j(R)}$ and $J_{i,j(B)}$ represent the couplings associated with the edge on the right and the edge at the bottom of a specific site i. The Figure (3.1) visually demonstrates the relationship between the σ_i configurations and the $J_{i,j}$ configurations, as defined by Equation (3.5).

Alternatively, it is possible to introduce an edge random variable $\sigma_{i,j}$ and define $J_{i,j} = (J_1 + J_2)/2 + \sigma_{i,j}(J_1 - J_2)/2$ as a choice. It is expected that all these different setups are equivalent in terms of universal properties. The chosen setup in this work is simply the most convenient for numerical simulations.

The distribution of disorder is determined by the configuration σ_i. In this case, the considered distributions have a vanishing first moment.

$$\mathbb{E}[\sigma_i] = 0, \tag{3.6}$$

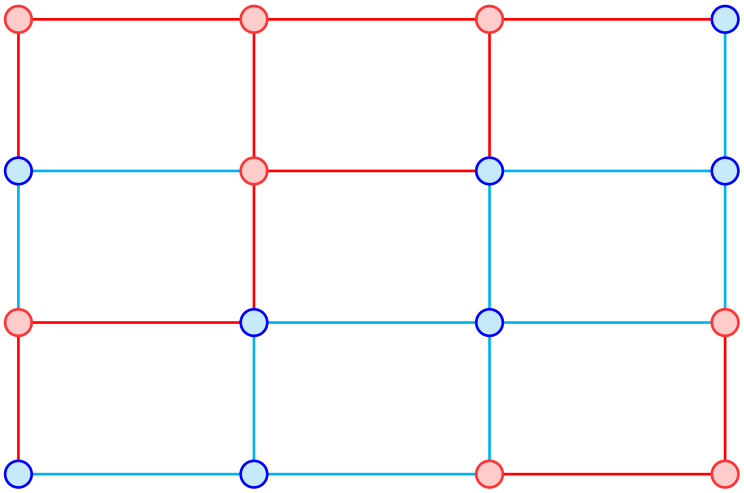

Figure 3.1. A specific configuration $\{\sigma_i\}$ is depicted in the figure, where blue-filled circles represent sites with $\sigma_i = 1$, and red-filled circles represent sites with $\sigma_i = -1$. The corresponding set of couplings $\{J_{i,j}\}$, associated with the edges, can be derived from Equation (3.5). In the figure, the blue (red) colored edges represent $J_{i,j} = J_1$ ($J_{i,j} = J_2$) couplings. This illustration is adapted from [7].

which forces the couplings to take values J_1 or J_2 with the same probability. The couplings then fluctuate around the value $(J_1 + J_2)/2$:

$$J_{i,j} = \mathbb{E}[J_{i,j}] + \delta J_{i,j}, \, \mathbb{E}[J_{i,j}] = \frac{J_1 + J_2}{2}. \tag{3.7}$$

One can then consider a $\{\sigma_i\}$ distribution whose second cumulant has a power-law decaying:

$$\mathbb{E}\left[\sigma_i \, \sigma_k\right] \sim |i-k|^{-a} \, \text{for} \, |i-k| \gg 1. \tag{3.8}$$

This, of course, correlates the fluctuations of the couplings at distant edges:

$$\begin{aligned} \mathbb{E}\left[\delta J_{i,j^{(X)}} \, \delta J_{k,l^{(Y)}}\right] &= \frac{(J_1 - J_2)^2}{4} \mathbb{E}\left[\sigma_i \, \sigma_k\right] \\ &\sim |i-k|^{-a} \, \text{for} \, |i-k| \gg 1, \end{aligned} \tag{3.9}$$

where $\{X, Y\} = \{R, B\}$.

Once the $\{\sigma_i\}$ distribution is chosen, satisfying the relation Eq. (3.4), the phase diagram of the q-Potts model Eq. (3.1) depends only on the ratio r,

$$r = \frac{J_1}{J_2} \in [1, \infty], \tag{3.10}$$

that parametrizes the disorder strength. One can assume, without loss of generality, that $J_2 \leq J_1$. In the simulations, the system's behavior is examined by varying the parameter r. By doing so, the stability of the renormalisation group (RG) fixed points is investigated along this direction. Meanwhile, the relationship expressed in Equation (3.4) ensures that the system remains at the critical temperature.

Two examples of disordered distributions of $\{\sigma_i\}$ are provided below: one follows a Gaussian distribution, while the other follows a non-Gaussian distribution.

n-replicated Ising model

One can consider n independent critical Ising models with spins $\sigma^{(a)} \in \{0, 1\}$, where $a = \{1, \cdots, n\}$. The variables σ_i in Eq. (3.5) are determined as follows:

$$\sigma_i = \prod_{a=1} \sigma_i^{(a)}, \tag{3.11}$$

and their statistical properties are determined by the correlation functions of the n independent Ising models. Specifically, for the first two moments, one has:

$$\mathbb{E}\left[\sigma_i\right] = 0, \, \mathbb{E}\left[\sigma_i \, \sigma_j\right] \sim |i-j|^{-\frac{n}{4}} \text{ for } |i-j| \gg 1, \tag{3.12}$$

where the critical Ising spin-spin correlation function scale as: $\langle \sigma_i^{(a)} \sigma_i^{(a)} \rangle \sim |i-j|^{-1/4}$, with $\langle \cdots \rangle$ the usual canonical thermal average for the Ising model. Comparing with Eq. (3.8), one has:

$$a = \frac{n}{4}. \tag{3.13}$$

The advantage of this choice lies in the ease and efficiency of simulating the n-Ising models. However, a limitation is that a cannot be varied continuously. It is important to note that the distribution described above is non-Gaussian, as the critical Ising point does not follow a Gaussian distribution.

Fractional Gaussian free fields

The second example is associated with the percolation point of the level sets of a fractional Gaussian random field characterized by a negative Hurst exponent, $H = -a/2$.

Consider an $L \times L$ square lattice with vertices i having coordinates $i = (i_h, i_v)$. Introduce a set of random variables ϕ_i that define a discrete fractional Gaussian free field.

$$\phi_i = \begin{cases} \sum_{(l,m)\neq(0,0)}^{L} \frac{c_{l,m}}{S_{l,m}} \exp\left(\frac{2\pi}{L}(l\, i_h + m\, i_v)\right), \text{ if } (l,m) \neq (0,0) \\ c_{0,0}, \text{ if } (l,m) = (0,0) \end{cases} \tag{3.14}$$

where $S_{l,m} = \left|2\cos\left(\frac{2\pi l}{L}\right) + 2\cos\left(\frac{2\pi m}{L}\right) - 4\right|^{\frac{1-a/2}{2}}$ and the $c_{l,m}$ are independent random Gaussian variables with mean 0 and variance 1, *i.e.* $c_{l.m} \in \mathcal{N}(0,1)$. Using the properties of the Fourier transform, the covariance $\mathbb{E}[\phi_i \phi_j]$ has the following asymptotic limit:

$$\mathbb{E}[\phi_i\, \phi_j] \sim |i-j|^{-a} \text{ for } |i-j| \gg 1. \tag{3.15}$$

The σ_i variables are defined by:

$$\sigma_i = \begin{cases} 0, & \text{if } \phi_i > 0 \\ 1, & \text{if } \phi_i < 0, \end{cases} \tag{3.16}$$

The expectation $\mathbb{E}[\sigma_i] = 0$ implies the presence of the level 0. It is worth noting that the clusters formed by the σ_i variables do not correspond to the percolation threshold. In spin-percolation physics, it is known [132] that the critical level is greater than 0. These σ_i variables are solely required for constructing the bond distribution, as discussed in Section (3.2.1). However, it can be demonstrated that the Fortuin-Kasteleyn (FK) clusters formed by these bonds are indeed at the percolation transition. Hence, one can conclude that:

$$\mathbb{E}[\sigma_i\, \sigma_j] \sim |i-j|^{-a} \text{ for } |i-j| \gg 1, \tag{3.17}$$

and a long-range correlated disorder.

3.2.2 Pure Potts model (r=1)

The pure case occurs when $r = 1$, resulting in all couplings taking the same value as defined in Equation (3.10). On the square lattice, the critical point P corresponds to $J_1 = J_2 = J_c = \log(1 + \sqrt{q})$.

In the continuum limit, the critical point P is described by the Potts conformal field theory, and its energy spectrum has been known for a long time [81]. Recently, a bootstrap approach [139–143] has been proposed to study cluster connectivity properties,

which has been utilized in [144–146] to provide exact Potts correlation functions and a comprehensive characterization of the symmetry representation of its states.

The thermal and order-parameter critical exponents ν^P and β^P of the pure Potts model have been determined for any value of $q \in [0, 4]$, as documented in [147] and related references. Table (3.1) presents the values of ν^P and β^P/ν^P for $q = \{1, 2, 3\}$:

q	ν^P	β^P/ν^P
1	4/3	5/48
2	1	1/8
3	5/6	2/15

Table 3.1. Pure critical exponents for different q values.

3.2.3 Short-range disordered Potts ($a \geq 2$)

When $a \geq 2$, the disorder becomes effectively uncorrelated. In Fourier space, the contribution of the power-law tail $|x|^{-a}$ is of the order $O(k^{a-2})$. In the limit of long wavelengths ($k \to 0$), this contribution remains finite for $a \geq 2$. Therefore, at large distances, the properties of a long-range distribution are effectively equivalent to those of a delta function.

The phase diagram of uncorrelated disorder has been well understood, and a renormalisation group (RG) analysis has been conducted in [44]. This analysis serves as the starting point for the computations carried out in Section (4.3).

In the case of $q < 2$, the P point remains the only stable fixed point under weak disorder, preserving the universality of the pure model. On the other hand, for $q > 2$, the system is driven towards a stable SR point. When $q = 2$, the disorder is considered marginal, resulting in the P and SR points coinciding. In this case, universal logarithmic corrections to the P universality class emerge [133]. Table (3.2) presents the critical exponents for $q = 3$, which have been computed perturbatively in [44, 124].

In the case of uncorrelated disorder, it can be demonstrated through power counting analysis *i.e.* analysing the RG relevance of scaling operators, that only the first two cumulants of the distributions play a role in determining the long-distance behavior of the system [44].

q	ν^{SR}	β^{SR}/ν^{SR}
3	~ 1.02	~ 0.134655

Table 3.2. Short-Range critical exponents for $q = 3$.

3.2.4 Long-range disordered Potts ($a < 2$)

For $a < 2$, the power-law decay of the disorder distribution needs to be taken into account. As mentioned in the Introduction (3.1) and discussed in Section (1.6.5), according to the extended Harris criterion [86,123], the long-range part of the distribution becomes relevant and dominates the short-range behavior in the cases of $(q < 2, a < 2/\nu^{P})$ and $(q > 2, a < 2/\nu^{SR})$.

In [86,123], it was also observed that if an additional sub-dominant term $\mathbb{E}[\delta J(x)\delta J(y)] \to \mathbb{E}[\delta J(x)\delta J(y)] + w_0|x-y|^{-b}$ exists in the disorder correlations, with $b > a$, then the LR point should be stable. Applying the extended Harris criterion, it is expected that when $b > a$, $b > 2/\nu^{LR}$, indicating that the perturbation is irrelevant. Conversely, when $b < a$, the additional b-term becomes dominant, leading to $b < 2/\nu^{LR}$. Based on these observations, a strong conjecture, named Weinrib-Halperin conjecture [86], can be made:

$$\nu^{\mathrm{LR}} = \frac{2}{a}, \text{ for any } q. \tag{3.18}$$

The validity of the aforementioned relation has been established through perturbative renormalisation group (RG) computations in various long-range disordered models, such as Gaussian disordered Ising models [86, 123, 134, 135], at one or two-loop orders. Furthermore, it is widely accepted that Equation (3.18) holds true at all orders of perturbation [148, 149]. In Section (3.3.5), the relation given by Equation (3.18) for $q = 3$ will be numerically tested.

Moreover, in Section (4.5.2) new analytical results will be presented, focusing on the violation of this conjecture in the case of non-Gaussian disorders and the $(q = 3)$-Potts model.

3.2.5 The infinite disorder point ($r = \infty$): the q-colored critical pure percolation

The $r \to \infty$ point, along with the pure point, $r = 1$, are the only points where exact results can be obtained for any value of q. From Equation (3.4), in the limit $r \to \infty$,

one has $J_1 \to \infty$ and $J_2 \to 0$, with $rJ_2 \sim -\log(J_2) \to \infty$. Specifically:

$$\mathbb{E}\left[\delta J_{i,j}\delta J_{k,l}\right] = \frac{(r-1)^2 J_2^2}{4}\mathbb{E}\left[\sigma_i\sigma_k\right] \sim (rJ_2)^2\mathbb{E}\left[\sigma_i\sigma_k\right] . \tag{3.19}$$

The $r = \infty$ limit corresponds to the maximum level of disorder that can be considered. In this limit, Equation (3.2) simplifies significantly. With probability one, an edge with coupling J_1 will have a bond present $(1 - e^{-J_1} = 1)$, while there will be no bond present on an edge with J_2 $(1 - e^{-J_2} = 0)$. Consequently, once a configuration of σ_i, and thus the associated couplings $J_{i,j}$, is drawn, only the graph where the edges (i, j) associated with J_1 are activated contributes to the partition function, as shown in Figure (3.2). The edges with J_2 are not activated.

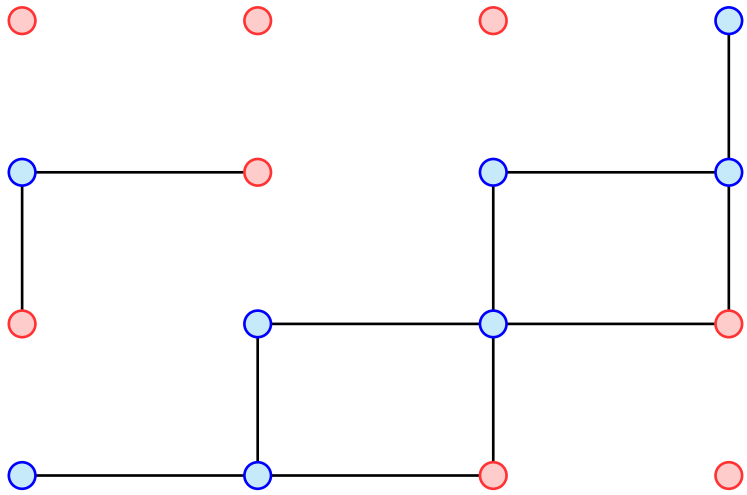

Figure 3.2. Given the configuration of σ_i and therefore of $J_{i,j}$ shown in Fig. (3.1), the only random cluster graph $\mathcal{G}$ in Eq. (3.2) that does not vanish in the limit $r \to \infty$ it is shown. Notice that the $\sigma_i = 1$ cluster, formed of blue spins, are different from the ones of the FK bonds (black lines)

The disorder average free-energy, for instance, can be written as:

$$\mathbb{E}\left[\log \mathcal{Z}(\{J_{i,j}\}\right] = \log q \times \mathbb{E}\left[\#\ (J_1\text{-clusters})\right] \sim\ \log q \times \mathbb{E}\left[\#\ (\sigma = +1\text{-clusters})\right] \tag{3.20}$$

The $\sim$ symbol denotes that the scaling behavior is the same. The disordered Potts model at $r = \infty$ is closely related to the site percolation model based on the σ clusters (spin clusters). Specifically, the probability distribution of the $r = \infty$ Fortuin-Kasteleyn (FK) clusters, aside from a trivial dependence on q, is identical to that of the σ clusters. In the construction outlined in Equation (3.5), the $(ij^{(R)})$ and $(ij^{(B)})$ edges are always either both activated or both not activated. At the lattice level, the $r = \infty$ FK clusters differ

from the σ clusters, as illustrated in Figure (3.2). However, their universal properties, such as their fractal dimension and the correlation length exponent ν, remain the same, as discussed in the subsequent Section (3.3.1).

Considering that spin clusters and FK clusters only differ at their boundaries for each value of a, it is possible to compare the spin clusters and FK clusters specifically for the case of $a = 1/4$. In this case, the σ variables correspond to Ising spins at the critical point. For an Ising cluster with a linear size R, the number of spins on the boundary scales as $\sim R^{d_f^b}$, with $d_f^b = 11/8 = 1.375$. One can note that the Ising spin boundaries are described by the CLE3 loops, and $d_f^b = 11/8$ is the fractal dimension of the CLE3 loops [150]. This value is much smaller than the number of spins within the cluster, which scales as $\sim R^{d_f}$ with $d_f = 187/96 \simeq 1.948$. Therefore, it can be expected that the FK clusters for $a = 0.25$ will have the same fractal dimension $d_f = 2 - 5/96$ as the Ising spin clusters.

When $a > 2$, the system is considered short-range and is described by the Bernoulli critical point Bp [151]. For $a < 2$, the extended Harris criterion can be applied using $\nu^{Bp} = 4/3$. For $a > 2/\nu^{Bp} = 3/2$, the system remains at the Bp point, while for $a < 3/2$, a new LRp fixed point, as mentioned in the Introduction (3.1), emerges. In Section (3.3.1), this behavior will be tested, and the exponent β^{LRp}/ν^{LRp} will be computed.

It is crucial to emphasize that the LRp point exists at $r = \infty$ for any q, and its critical exponents depend on a but not on q. As will be discussed further, as shown in Figures (3.10) and (3.12), the LRp point is distinct from the LR point for $q > 1$, which represents the finite disorder fixed point. The LRp point and the LR point exchange stability when a exceeds a specific value $a^*(q)$, *i.e.* $a > a^*(q)$.

3.3 Phase diagrams from Monte Carlo measures of $q = \{1, 2, 3\}$-Potts

In this section, the numerical results that led to the construction of the phase diagram shown in Figure (3.3) will be presented.

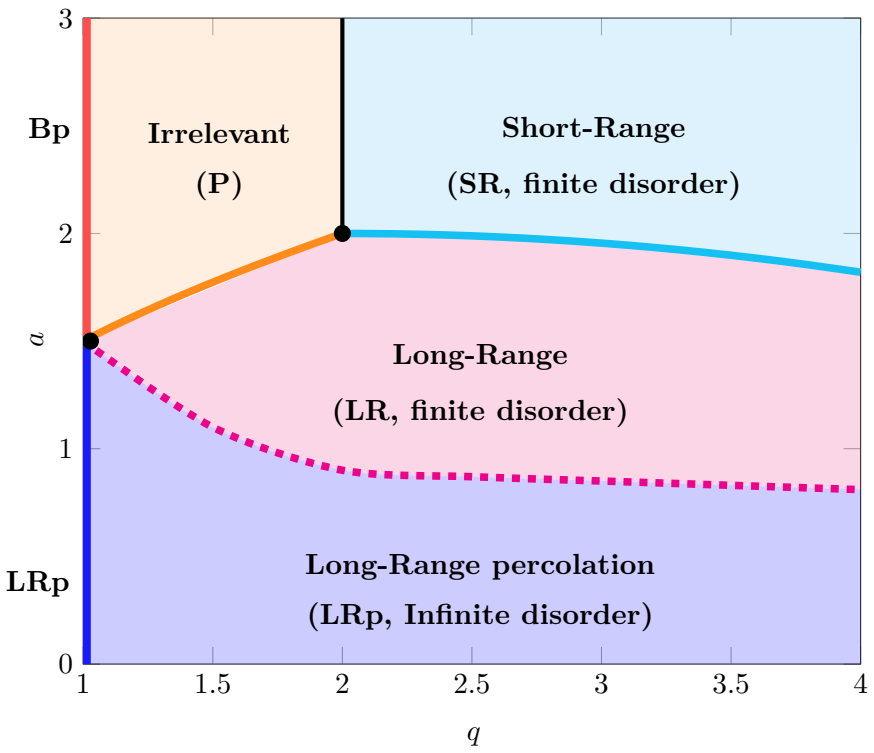

Figure 3.3. Phase diagram of the disordered bidimensional q-Potts model for $(q, a) \in (0, 4] \times (0, \infty)$.

The simulations were conducted on square lattices with periodic boundary conditions. Unless otherwise stated, the averaging was performed over one million disordered samples. For each value of q and a, the average autocorrelation time $\tau_{a,q}(L)$ was determined. Subsequently, for each disorder sample, the thermal averaging was performed by running $100 \times \tau_{a,q}(L)$ updates after an equal number of updates for thermalization.

Unless otherwise specified, the results presented in the following sections were obtained using the n-Ising disorder distribution described in Section (3.2.1).

For each value of $n = \{1, \cdots, 8\}$, corresponding to the values of a given in Equation (3.13), the coupling configurations $J_{i,j}$ were generated according to Equation (3.5). The FK clusters were then constructed by connecting spins of the same value with a probability $p(J_{i,j}) = 1 - e^{-J_{i,j}}$, as described in Equation (3.2). For a lattice of size L,

the number of spins $M(J_{i,j}, L)$ in the largest FK cluster was computed for each coupling configuration. Finally, the average over the coupling distribution is performed,

$$M(L) = \mathbb{E}\left[M(L, \{J_{i,j}\})\right], \tag{3.21}$$

to extract the fractal dimension d_f by the scaling

$$M(L) \simeq L^{d_f}. \tag{3.22}$$

More specifically, recalling the relation Eq. (3.3), one can use Eq. (3.22) to compute an effective magnetic dimension:

$$\frac{\beta}{\nu}(L) = -\log\left[\frac{m(L)}{m(L/2)}\right] / \log\left[2\right], \tag{3.23}$$

where $m(L) = M(L)/L^2$ is the average magnetization. The above data, computed for different q, a and r are the ones shown in the plots β/ν vs. L below. The ratio β/ν is then evaluated in the scaling limit:

$$\frac{\beta}{\nu} = \lim_{L\to\infty} \frac{\beta}{\nu}(L). \tag{3.24}$$

3.3.1 The infinite disorder point ($r = \infty$): LRp and Bp fixed points

Here, the results for the q-colored percolation model, found at the infinite disorder point $r = \infty$, see Section (3.2.5) are collected. It is important to recall that the critical exponents at the infinite disorder point do not depend on the value of q.

Figure (3.4) displays the effective exponent $\beta/\nu(L)$ as a function of L for different values of a ranging from 0.25 to 2.00. The corresponding scaling limit results β^{LRp}/ν^{LRp}, obtained through a best fit analysis of all the collected data, including sub-leading corrections, are summarized in Table (3.3).

a	β^{LRp}/ν^{LRp}
0.25	0.0522(4)
0.5	0.086(2)
0.75	0.103(2)
$1, 1.25, 1.5, 1.75, 2$	~ 0.105

Table 3.3. Best fit of the critical exponent β^{LRp}/ν^{LRp} for different values of a. Notice that for $a = \{1.5, 1.75, 2\}$ the system is described by the Bp point where $\beta^{Bp}/\nu^{Bp} = 5/48 \sim 0.105$. However, for $a \geq 1$, the numerical simulations cannot distinguish between the LRp point and the Bp point.

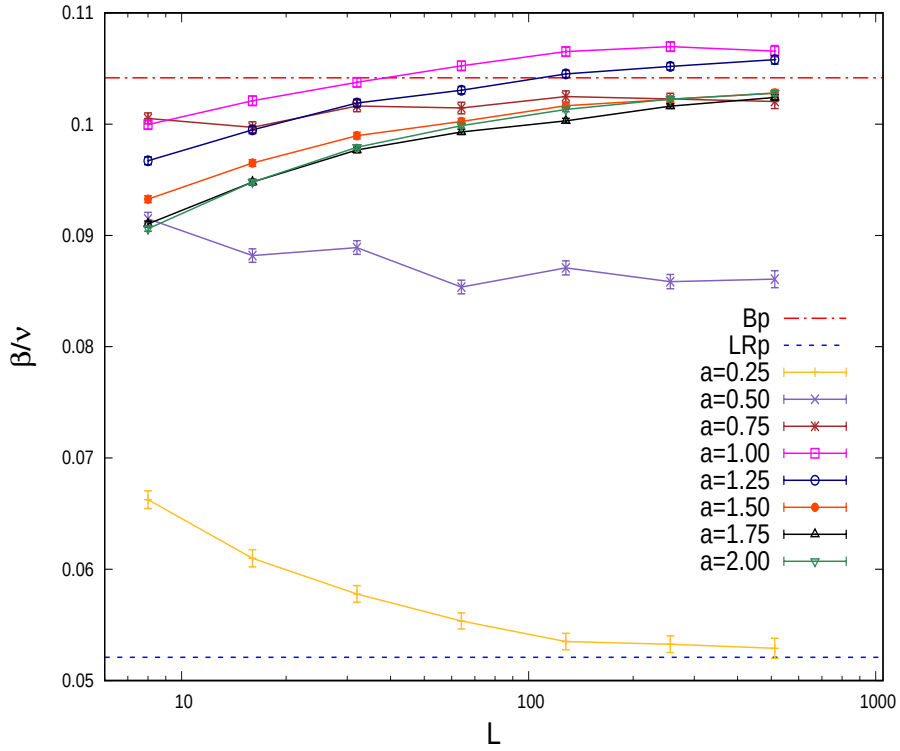

Figure 3.4. The $r = \infty$ long-range disorder: β/ν vs. L for the values of a shown in the caption.

As discussed in Section (3.2.5), for $a = 0.25$, the β^{LRp}/ν^{LRp} must correspond to the fractal dimension of the Ising clusters. The latter has been considered in [152, 153] and argued to be:

$$\frac{\beta^{LRp}}{\nu^{LRp}} = 2 - \frac{187}{96} = \frac{5}{96} \sim 0.0521. \tag{3.25}$$

The results presented in Table (3.3) show a very good agreement with the expected value of 5/96, as indicated by the dashed line in Figure (3.4).

It is important to emphasize that, according to the Harris criterion, one would expect $\beta^{LRp}/\nu^{LRp} < \beta^{Bp}/\nu^{Bp}$ for $a < 3/2$. However, as a increases, the difference between β^{LRp}/ν^{LRp} and β^{Bp}/ν^{Bp} becomes very small, and the numerical simulations cannot effectively distinguish between these two fixed points. In fact, for $a = 1$ and $a = 1.25$, the value of β^{LRp}/ν^{LRp} seems to be slightly larger than 5/48. Similar observations were also reported in [130]. Due to the presence of significant finite-size corrections, it is challenging to accurately predict the asymptotic value in this regime.

In the following Potts observables at finite value of disorder r, where the scaling behavior is in general expected to depend on q, are considered.

3.3.2 The $q = 1$ phase diagram

In this section, the phase diagram of the $q = 1$ Potts model is considered. For $a > 2$, the disorder is effectively short-range and irrelevant, as shown in Figure (3.3). This irrelevance of short-range disorder can also be understood through a simple lattice argument. On the critical line given by Equation (3.4) for $r = 1$, where $J_1 = J_2 = J_c = \log(1 + \sqrt{1}) = \log(2)$, the system is exactly at the Bernoulli percolation (Bp) critical point with $p = 1 - e^{-J_c} = p_c = 1/2$. By introducing disorder, *i.e.* setting $r > 1$, the dual line given by Equation (3.4) enforces the relation $1 - e^{-J_1} - e^{-J_2} = 0$ for $q = 1$. Taking into account that each bond J_1 and J_2 occurs with equal probability, the density of activated bonds remains $p = \frac{1}{2}(1 - e^{-J_1}) + \frac{1}{2}(1 - e^{-J_2}) = 1/2$. Thus, regardless of the value of r, the system remains at the Bp point. For $3/2 = 2/\nu^{Bp} < a < 2$, the long-range disorder remains irrelevant, and the system is still described by the Bp point.

Next, the effective exponent $\beta/\nu(L)$ is measured for various values of the disorder strength r. For $a < 3/2$, the numerical measurements clearly show that the system undergoes a flow from the Bp point to the LRp point located at $r = \infty$, as discussed in Section (3.2.5) and Section (3.3.1).

To illustrate this, the results for the model with $a = 1/4$ are first presented. In the left panel of Figure (3.5), $\beta/\nu(L)$ is shown as a function of the size L for different values of r, including $r = \{1, 2, 5, 10, 100, \text{ and } \infty\}$. It can be observed that for all values of $r > 1$, this exponent approaches the value of $r = \infty$ with a crossover function of the disorder. The expected value of $5/96$ at $r = \infty$, as predicted by [152], is shown as a blue dashed line. The value of $\beta^{Bp}/\nu^{Bp} = 5/48$ for $r = 1$ corresponding to Bernoulli percolation is shown as a red dashed-dotted line. Therefore, regardless of the amount of disorder, the long-distance behavior is governed by the infinite disorder fixed point. In the right panel of Figure (3.5), $\mathcal{P}_w(L)$, defined in Equation (3.30), is shown. For $r = 1$, it converges to the exact value for Bernoulli percolation, as given by [154]:

$$\text{Bernoulli clusters: } \lim_{L\to\infty} P_w(L) = 0.69046 \tag{3.26}$$

which is represented by the red dashed-dotted line. For any value of $r > 1$, it converges to the same value as at the LRp point, albeit with a crossover function dependent on the disorder strength.

Moreover, in addition to the fractal dimension, the wrapping probability provides further evidence that the FK clusters exhibit the same behavior as the Ising spin clusters at the LRp point. For spin clusters, this probability can be computed using the results from [155] and is given by:

$$\text{Ising clusters: } \lim_{L\to\infty} P_w(L) = 0.515884\,. \tag{3.27}$$

This is shown as a blue dashed line in the right part of Fig. (3.5). The agreement is perfect.

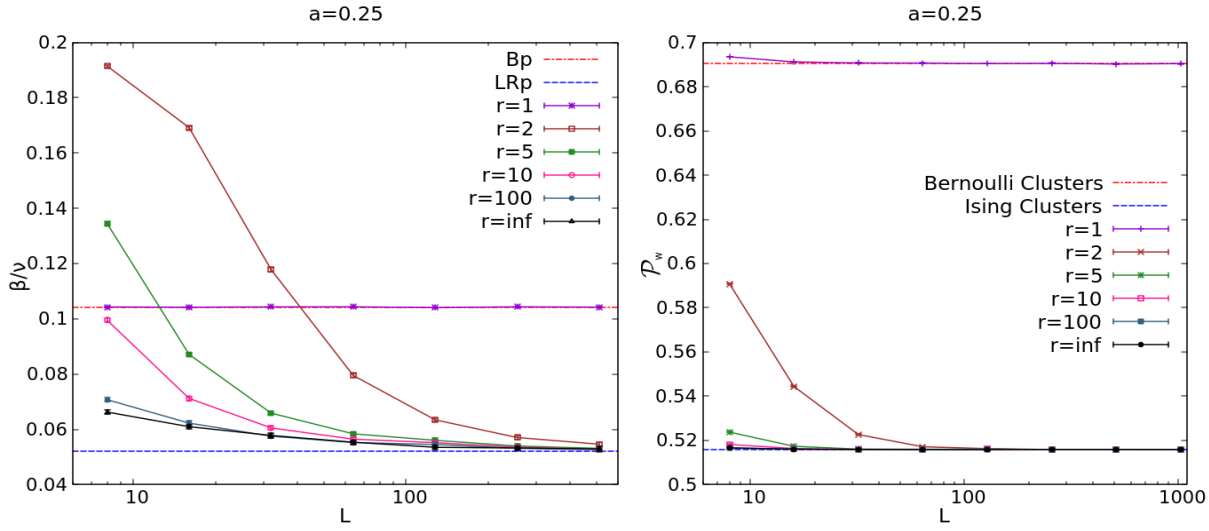

Figure 3.5. $q = 1$ Potts model with $a = 0.25$. The left panel shows β/ν vs. L while the right panel shows the wrapping probability $\mathcal{P}_w(L)$ vs. L.

Coming back to the β/ν exponent, similar behaviors are observed for the others values of a. In Fig. (3.6), one can see $\beta/\nu(L)$ for $a = 0.75$ and $a = 1.5$. Again, for all values of r, the large size limit is the one reported in Table (3.3).

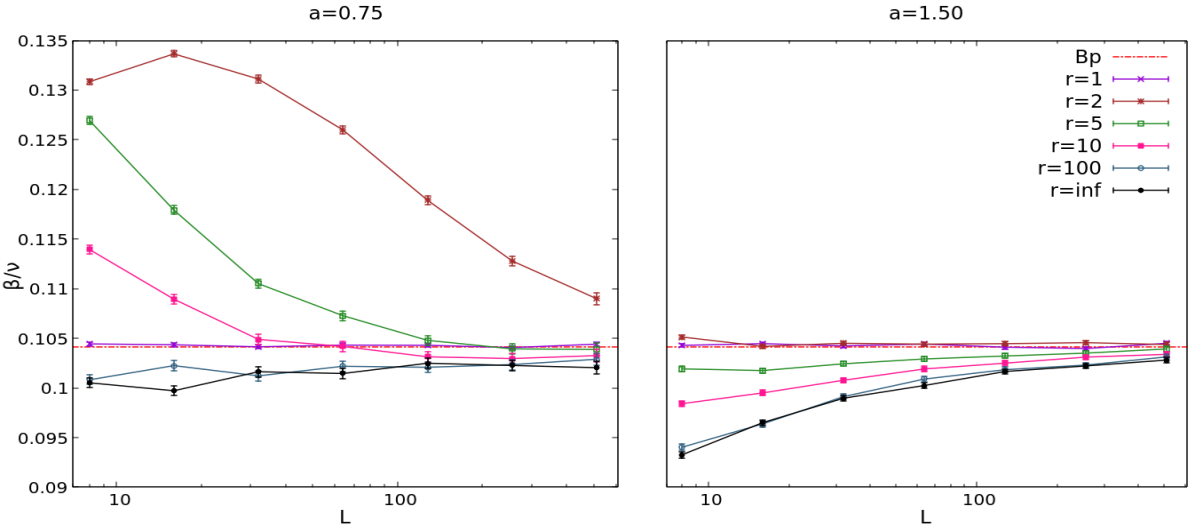

Figure 3.6. β/ν vs. L for the $q = 1$ Potts model with long-range disorder with $a = 0.75$ in the left panel and with $a = 1.50$ in the right panel.

It is possible, therefore, to summarize the numerical findings for $q = 1$ in Fig. (3.7).

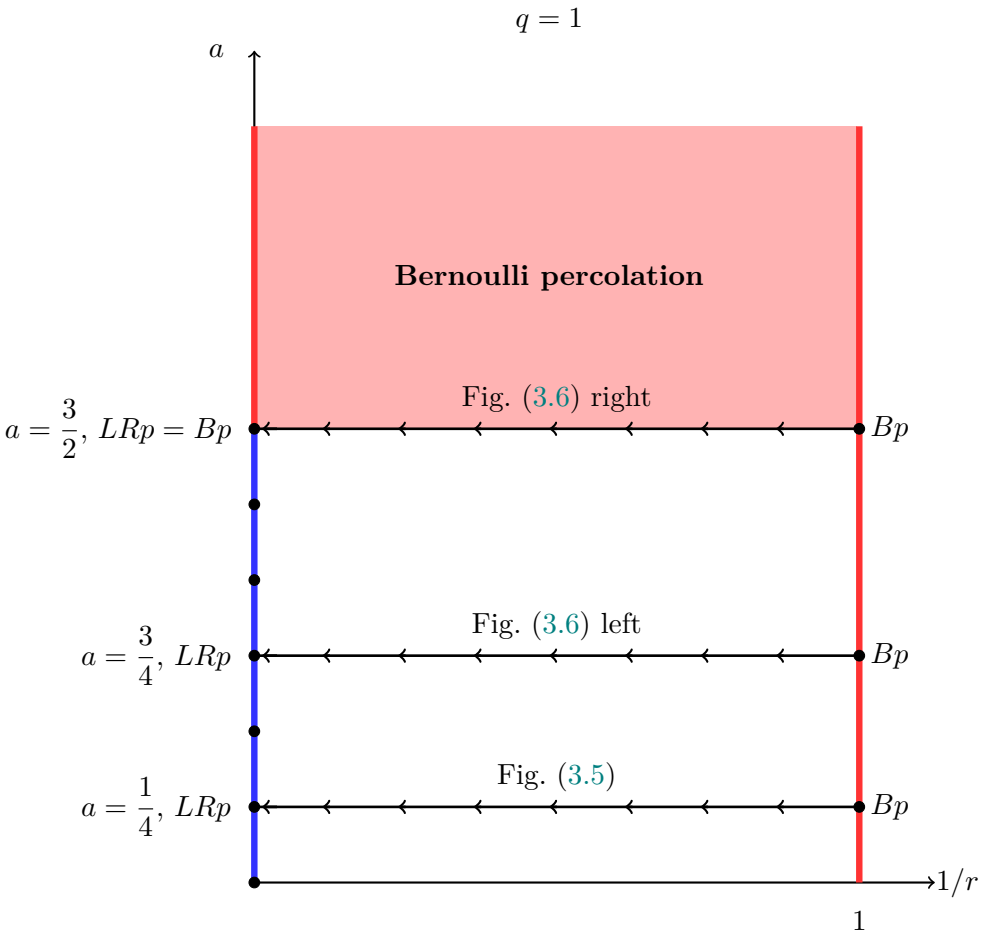

Figure 3.7. Fixed point stability, obtained via the measurements of the β/ν critical exponent, for $q = 1$. The red zone represents a unique fixed point, the Bp one. There is no flow while tuning r. The arrows describe a flow between two fixed points. The red line represents again the Bp fixed point and the blue line is a line of fixed points, the LRp ones.

3.3.3 The $q = 2$ phase diagram

In this section, the $q = 2$ case is examined in detail. In the short-range regime with $a \geq 2$, the disorder is marginal, and the P and SR fixed points coincide. For values of a such that $a^*(2) < a < 2$, the existence of the LR fixed point predicted in [134, 135] is numerically investigated. This LR fixed point corresponds to a finite disorder strength r^*_{LR}, where $1 < r^*_{LR} < \infty$. The exact value of $a^*(2)$ is estimated to fall within the interval $1/2 < a^*(2) < 3/4$, although the precise determination is not within the scope of this study. When $a < a^*(2)$, the system exhibits only two fixed points: the P and the LRp

($r = \infty$) fixed points. In this case, the LRp fixed point becomes stable, leading to a flow from the P point to the LRp point.

The different behaviors of the system are depicted in Fig. (3.8), in particular:

- In the left panel, it is shown the measured values of $\beta/\nu(L)$ for $a = 1/4$. It is clearly possible to observe that for all values of disorder, the effective magnetic exponent goes to the same value as the infinite disorder one, $\beta^{LRp}/\nu^{LRp} = 5/96 \sim 0.0521$, see Table (3.3). A similar behavior for $a = 0.5$, with $\beta/\nu(L) \to 0.086$ in the $L \to \infty$ limit is obtained. This, is again very close to the value β^{LRp}/ν^{LRp} reported in Table (3.3).
- In the middle panel, the data for $a = 1$ are shown. One can observe three different large size limits:
  1. For $r = 1$ the magnetic exponent is the one of the short-range Ising, $\beta^P/\nu^P = 1/8 = 0.125$.
  2. For $r = \infty$ the magnetic exponent is close to the value $\beta^{Bp}/\nu^{Bp} = 5/48$. As already mentioned for the case of infinite disorder, see Section (3.3.1), for $a \simeq 1$, it is difficult to distinguish the LRp point from the Bp point.
  3. For any finite disorder, there is an unique large size limit, $\lim_{L\to\infty} \beta/\nu(L) = \beta^{LR}/\nu^{LR} \simeq 0.115 - 0.120$.

  This corresponds to the LR fixed point. The curves converge to the curve with a finite disorder $r \simeq 10$, that is the value in which one can observe the smallest corrections. A similar behavior is obtained for $a = 0.75$ and $a = 1.25$ with the scaling limit $\lim_{L\to\infty} \beta/\nu(L) \simeq 0.108$ and $\lim_{L\to\infty} \beta/\nu(L) \simeq 0.122$ respectively.
- The right panel shows the measured values of $\beta/\nu(L)$ for $a = 1.75$. In that case, the measurements for finite disorder also converge to a single value β^{LR}/ν^{LR} which is very close to the P=SR value $\beta^P/\nu^P = 1/8$. For all values of $a \geq 3/2$, due to strong finite size corrections, one finds values close to the P=SR ones.

When $3/2 \leq a < 2$, the LR point is in close proximity to the P fixed point, making it difficult to distinguish between them using the β/ν exponent alone. Therefore, an alternative method for confirming the existence of the LR point will be considered. Specifically, the moments of the spin-spin correlation function will be examined. Being:

$$\mathbb{E}[\langle s(0)s(x)\rangle^n] \simeq x^{-\eta_n} . \tag{3.28}$$

The focus is on determining the exponents η_n, where $\eta_1 = 2\beta/\nu$ corresponds to the exponent computed previously using the dimensions of FK clusters. The exponents η_n for $n > 1$ provide new insights. In a study conducted by the authors of [135], the exponent η_2 was computed for the range $0.995 \leq a < 2$. At the lowest order in disorder,

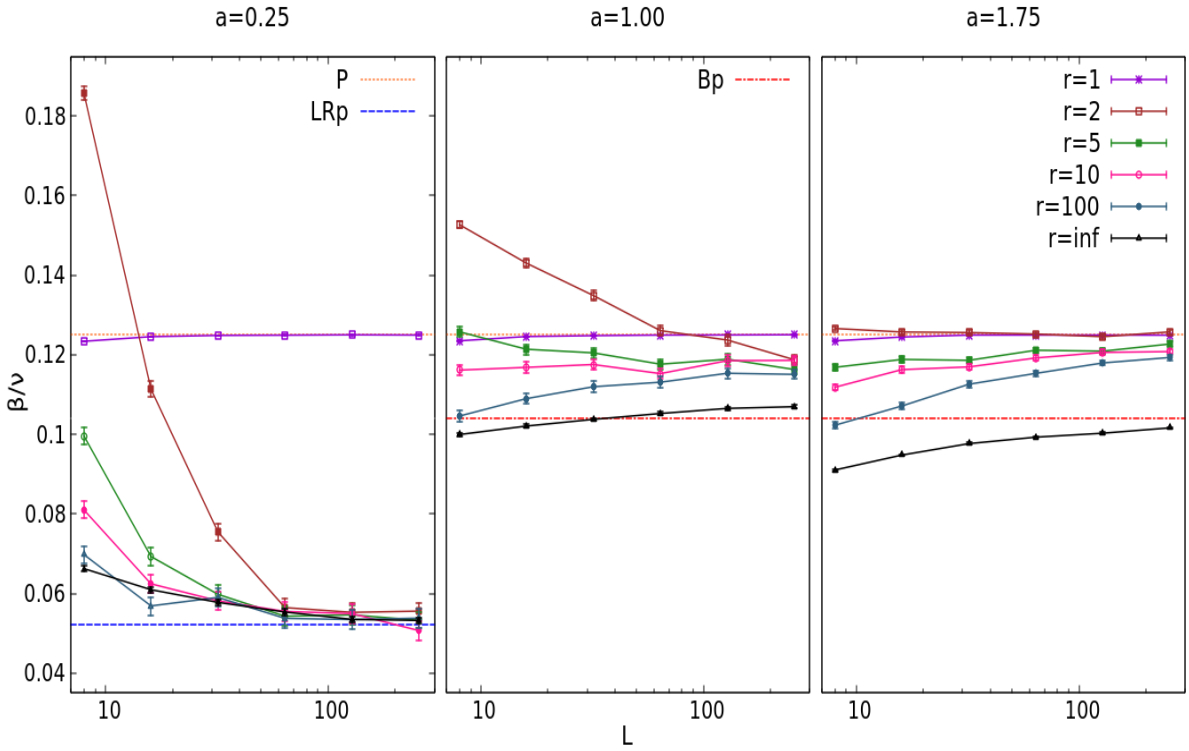

Figure 3.8. $q = 2$ Potts model with long-range disorder: β/ν vs. L for $a = 0.25$ on the left, $a = 1.00$ on the middle and $a = 1.75$ on the right.

the following result was obtained:

$$\eta_2 = \frac{1}{2} - \frac{(2-a)}{4} + O((2-a)^2). \tag{3.29}$$

The lower range of $a = 0.995$ in the computation corresponds to the stability limit of the perturbative fixed point at the second order.

The measured values of η_1 and η_2 for various values of a are reported in Table (3.4). It is worth noting that the values of η_1 can be compared to the values of β/ν obtained previously, and they are found to be consistent. For each value of a, the measurements were performed at a fixed value of disorder r chosen to minimize scaling corrections in the measurement of the fractal dimension. The last column of the table contains the first order prediction η_2^p from Eq. (3.29). The obtained results are also shown in Fig. (3.9). It

can be observed that there is good agreement between the measured η_2 and the predicted value η_2^p for $1.5 \leq a \leq 2.0$. For smaller values of a, the deviation becomes larger, but it is expected to be proportional to $(a-2)^2$, which corresponds to the second order correction. Interestingly, for $a \leq 0.5$, it is found that $\eta_1 \simeq \eta_2$.

a	$\eta_1 (= 2\beta/\nu)$	η_2	r	η_2^p
0.25	0.100	0.101	100	0.0625
0.50	0.167	0.172	100	0.125
0.75	0.209	0.243	10	0.1875
1.00	0.233	0.298(2)	10	0.25
1.25	0.242(2)	0.351(2)	5	0.3125
1.50	0.246	0.389	5	0.375
1.75	0.251	0.444	2	0.4375
2.00	0.250	0.491	1	0.50

Table 3.4. η_1 and η_2 measured with the disorder r for $0.25 \leq a < 2$. $\eta_2^p = 1/2 - (2-a)/4$ is the predicted value of Eq. (3.29) at the first order. Errors bars on the measured values η_1 and η_2 are shown in parenthesis and are smaller than one on the last digit otherwise.

At the $r = \infty$ disorder point, the random FK clusters and spin variables are completely determined by the disorder configurations, and thermal fluctuations are frozen. This implies that the distribution function $S(p_{12}(x))$ of the probability p_{12} that the spin $s(0)$ and $s(x)$ belong to the same FK cluster takes the form $S(y) = a_0\delta_{y,0} + a_1\delta_{y,1}$, with $a_0 + a_1 = 1$. This, in turn, implies $\eta_1 = \eta_2$. Therefore, the fact that at finite r, where the spin degrees of freedom are not frozen, one obtains $\eta_1 \sim \eta_2$, serves as a non-trivial test of the fact that the infinite disorder point describes the physics of the system for these values of a. The conclusions of the analysis done are summarised in Fig. (3.10).

3.3.4 The $q = 3$ phase diagram

In the short-range regime $a > 2$, the disorder becomes relevant and the critical properties are described by the SR fixed point. This fixed point is located at a finite disorder strength r^*_{SR}, specifically $r^*_{SR} = 6.08(12)$ [156]. In this regime, the system exhibits two fixed points: the SR fixed point for $1 < r < \infty$ and the Bp fixed point for $r = \infty$. These fixed points have been observed for all values of q up to infinity [151,157,158]. The $r = 1$ point corresponds to the P point for $q \in [1, 4]$, while for $q > 4$ it corresponds to a first order phase transition.

When $a < 2$, the long-range disorder becomes relevant for $a < 2/\nu^{SR} \sim 1.96$. The numerical simulations strongly suggest the existence of a stable LR fixed point, which is located at a finite disorder strength $1 < r^*_{SR} < r^*_{LR}$. It is interesting to note that the LR point tends to merge with the LRp fixed point, which is located at a critical value $a^*(3)$ slightly smaller than 0.75.

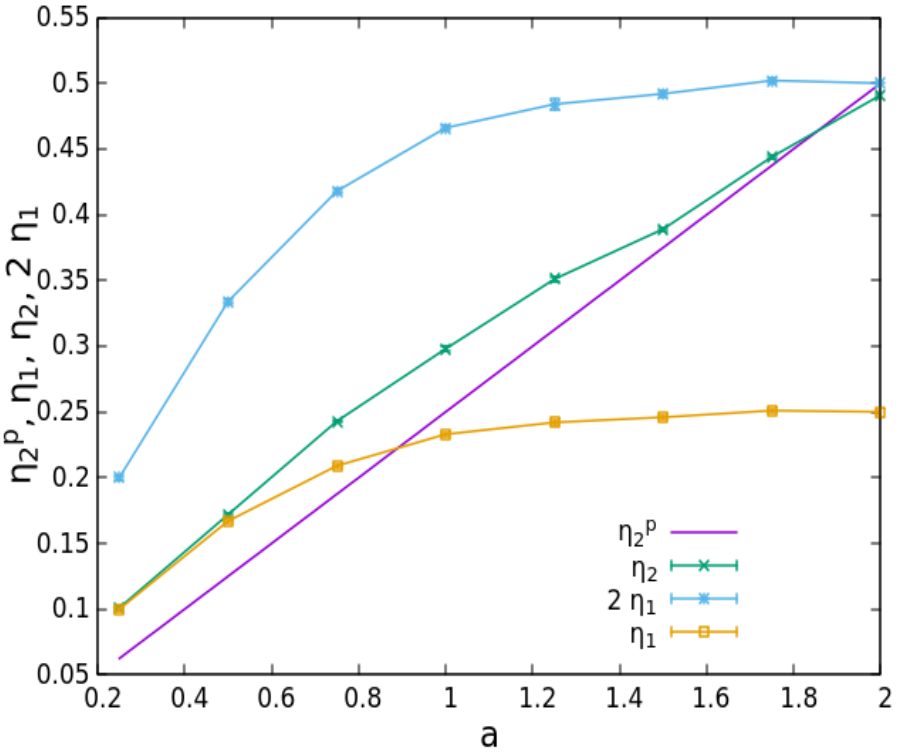

Figure 3.9. $q = 2$ Potts model with long-range disorder: η_1, η_2 and η_2^p vs a.

The numerical results for $q = 3$ are depicted in Fig. (3.11). Similar to the $q = 2$ case, three different behaviors are observed:

- In the left panel, β/ν for $a = 1/4$ is shown. For all values of disorder $r > 1$, in the large size limit, the effective magnetic exponent goes to the value $\beta^{LRp}/\nu^{LRp} = 5/96$ while it goes to the value of the pure $q = 3$-Potts model $\beta^P/\nu^P = 2/15$ for $r = 1$. One can observe a similar behavior for $a = 0.5$ with $\beta^{LRp}/\nu^{LRp} \simeq 0.09$.
- In the middle panel, results for $a = 1$ are shown. These, have three different large size limits:
  1. For $r = 1$, the magnetic exponent is the one of the pure $q = 3$-Potts model $\beta^P/\nu^P = 2/15$.
  2. For $r = \infty$, the magnetic exponent goes towards a value $\simeq 5/48$. Notice that this is the same as the one mention in the section above for $q = 2$ and $a = 1$: it is important to recall that at this point the exponents do not depend on q.
  3. For any finite disorder, a unique limit is obtained with $\beta^{LR}/\nu^{LR} \sim 0.12$ corresponding to a LR fixed point with finite disorder $r \simeq 10$.

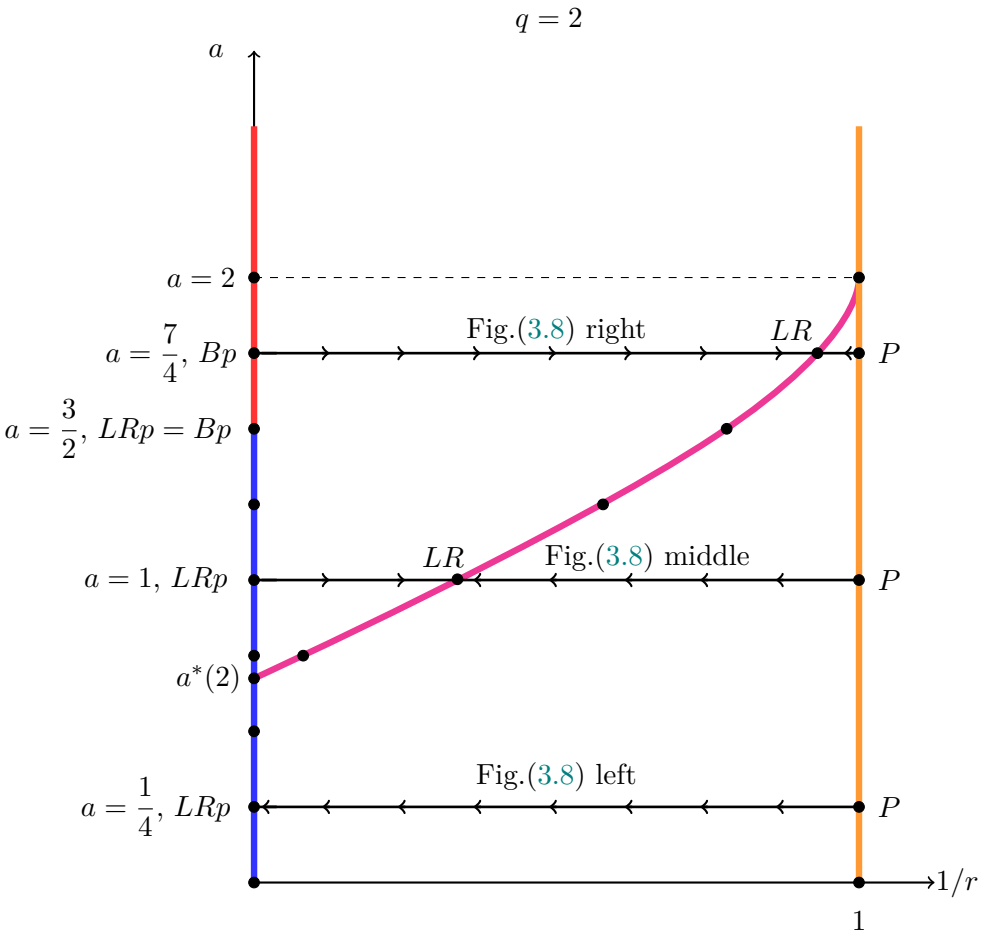

Figure 3.10. Fixed point stability, obtained via the measurements of the β/ν critical expo- nent, for $q = 2$. The dashed line represents the crossover with the purely SR physics at $a = 2$. The arrows describe a flow between two fixed points. The orange line represents the P (unique) fixed point, the red one the Bp (unique) fixed point, while the blue and magenta curves are lines of fixed points, respectively the LRp and the LR ones. $a^*(2)$ indicates the crossover between the LR and LRp points and one can locate it slightly below $a = 0.75$.

A similar behavior is observed for $a = 0.75, 1.25$ with $\beta^{LR}/\nu^{LR} \sim 0.11$ and $\beta^{LR}/\nu^{LR} \sim 0.13$ respectively.

- In the right panel, results for $a = 1.75$ are shown. For $a = 1.50$ and $a = 1.75$, β/ν is compatible, at large distances, with either with the P and the SR values, reported in Table (3.1) and in Table (3.2), which are very close. The measurements therefore do not allow to discriminate between these two values, but according to the arguments discussed in Section (3.2.4), it is possible to conjecture the LR point will merge with the SR point at $a \sim 1.96$, as illustrated in Fig. (3.12).

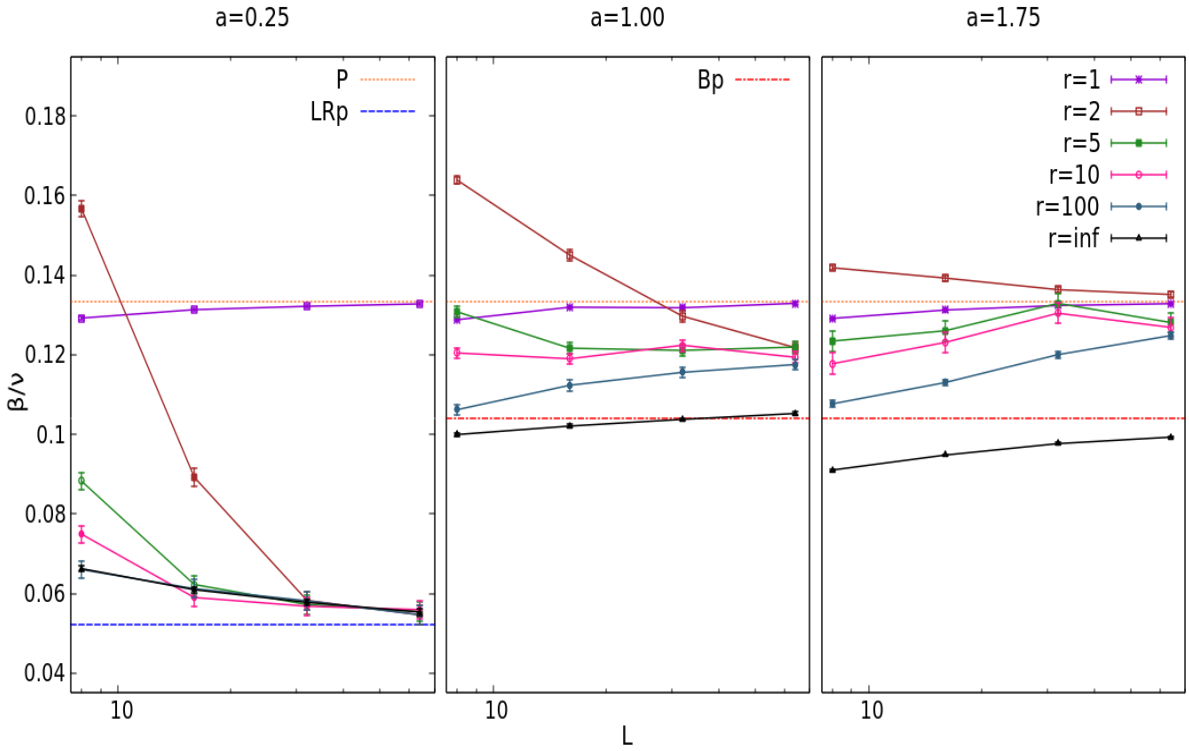

Figure 3.11. $q = 3$ Potts model with long-range disorder: β/ν vs. L for $a = 0.25$ on the left, $a = 1.00$ on the middle and $a = 1.75$ on the right.

In conclusion, for $a < a^*(3) \simeq 3/4$, it is found that the system flows to the LRp point, while for $a^*(3) < a < 1.96$, one finds the LR at some intermediate value of disorder with $\beta^{Bp}/\nu^{Bp} < \beta^{LR}/\nu^{LR} < \beta^{SR}/\nu^{SR}$.

The results are summarized in Fig. (3.12).

3.3.5 Thermal behavior for the $q = 3$-Potts model with long-range correlated disorder

In this section, the exponent ν is measured as a function of a to test Eq. (3.18). One way to measure it is by considering the wrapping probability of the FK clusters, defined by:

$$\mathcal{P}_w(r, J_1, L) = \text{Prob. of having a wrapping FK cluster on a lattice of size } L. \quad (3.30)$$

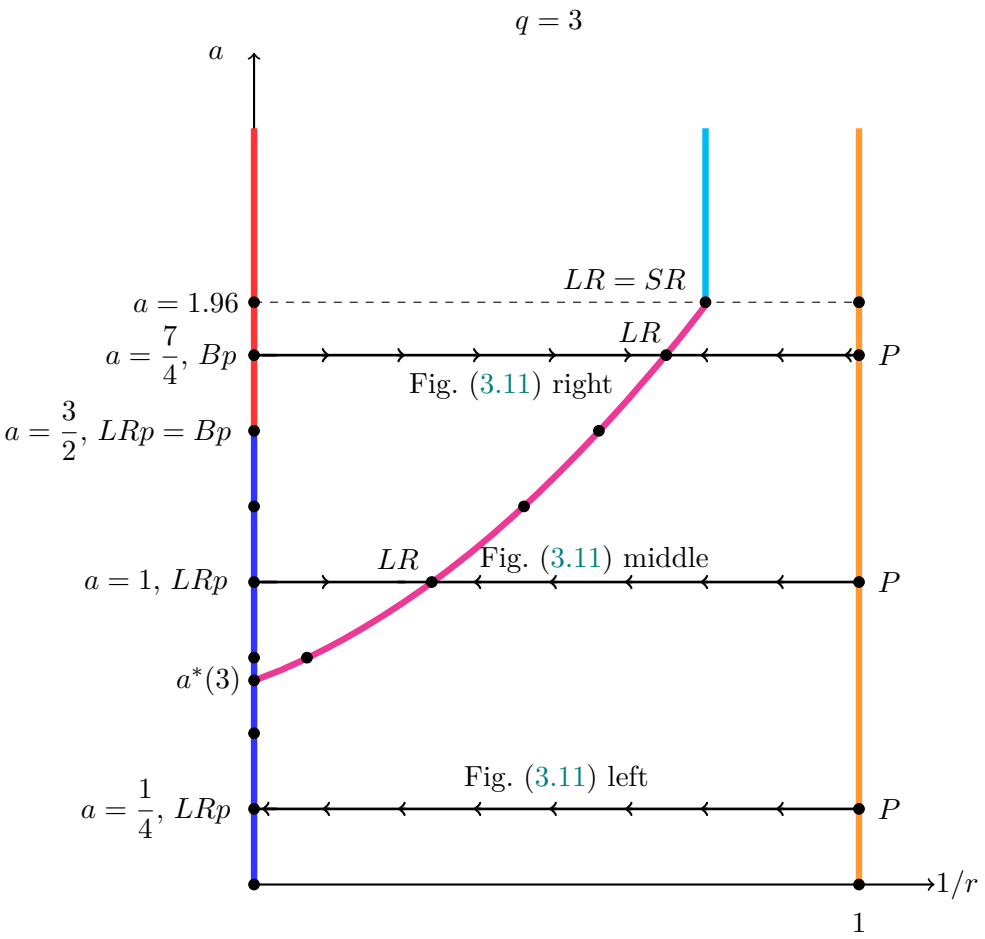

Figure 3.12. Fixed point stability, obtained via the measurements of the β/ν critical exponent, for $q = 3$. The dashed line represents the crossover with the purely SR physics at $a = 1.96$. The arrows describe a flow between two fixed points. The orange line represents the P (unique) fixed point, the red line the Bp (unique) fixed point and the cyan one the SR (unique) fixed point. The blue and magenta curves are lines of fixed points, respectively the LRp and the LR ones. $a^*(3)$ represents the crossover between the LR and LRp points and it is found to be located slightly below $a = 0.75$.

This is a quantity which is constant at the critical point for a fixed value $r = J_2/J_1$. J_1 is coupled to the thermal behavior and it is expected:

$$\begin{aligned} \mathcal{P}_w(r, J_1(1+\epsilon), L) &= f(\epsilon L^{1/\nu}) \\ &\simeq f(0) + f'(0)\epsilon L^{1/\nu} + \frac{f''(0)}{2}\epsilon^2 L^{2/\nu} + \frac{f'''(0)}{3!}\epsilon^3 L^{3/\nu} + \cdots \end{aligned} \tag{3.31}$$

for a small ϵ, which measures the deviation from the critical point. $\mathcal{P}_w(r, J_1, L)$ should also depend on r and one expect also corrections to scaling. These dependencies can be ignored if one considers the derivative:

$$\begin{aligned}\mathcal{P}'_w(\epsilon) &= \frac{\mathcal{P}_w(r, J_1(1+\epsilon), L) - \mathcal{P}_w(r, J_1(1-\epsilon), L)}{2\epsilon} \\ &\simeq f'(0)L^{1/\nu} + \frac{f'''(0)}{3!}\epsilon^2 L^{3/\nu} + \cdots\end{aligned} \tag{3.32}$$

One can compute $1/\nu$ by considering $\mathcal{P}'_w$ at the first order, but the results are not convergent for large L. This is due to the fact that the errors on the measurement grow like the inverse of ϵ. While averaging over one million samples of disorder configurations, one founds that errors bars allow us to decrease ϵ only down to 0.01. For this value, the second correction can not be neglected. Then, it is considered:

$$\tilde{\mathcal{P}'_w}(\epsilon) = \frac{4\mathcal{P}'_w(\epsilon) - \mathcal{P}'_w(2\epsilon)}{3} = f'(0)L^{1/\nu}(1 + O(\epsilon^4 L^{4/\nu})). \tag{3.33}$$

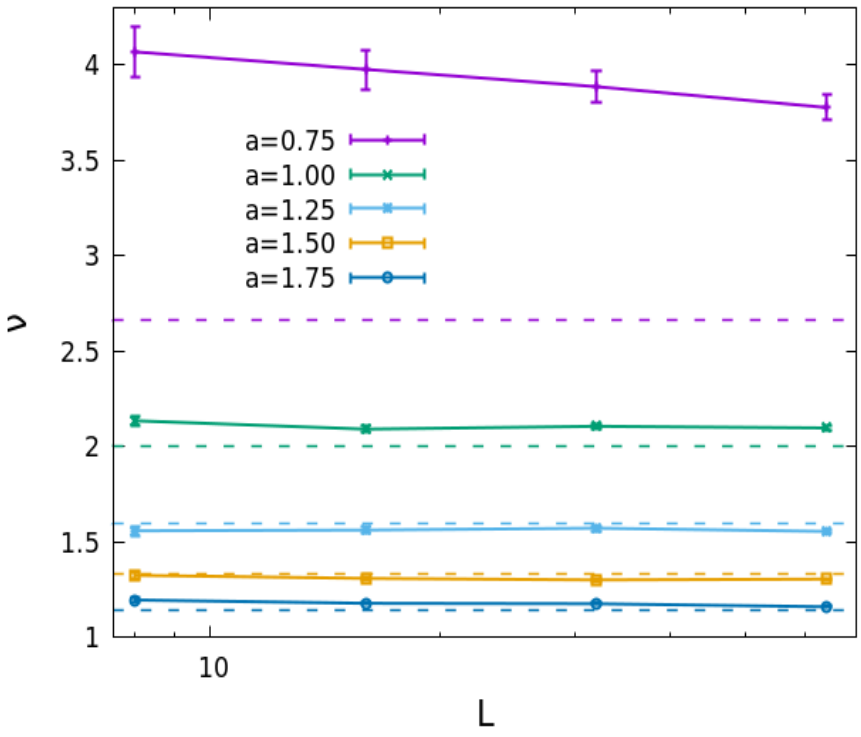

Figure 3.13. ν vs. L for the various values of a shown in the caption.

In Fig. (3.13), are shown the results for the effective ν as a function of L obtained from a two point fit of the data to the form of Eq. (3.33) for $a \geq 0.75$ and also the value $2/a$ as a dotted line. For each value of a, one can choose the value of r which seems closer to the critical point with the least finite size corrections. For $a \geq 1.25$, the data for $r = 5$ have been used, while for $a = 0.75$ and 1.00, one can use the data for $r = 10$. Note that for $a = 0.75$, one still has large error bars even if for this value of a, the average is done over 10 millions samples of disorder configurations (the same statistics is used for $a = 1.00$, with much smaller error bars, for $a > 1$, the average is done over 1 million samples). For $a = 0.75$, it is also observed, in Fig. (3.13), that there are strong finite size corrections. For smaller values of a, it was not possible to obtain convergent results with the simulation implemented. Note that this corresponds to values of a for which one expects that the critical point is at an infinite disorder.

In conclusion, it is observed that the value of ν increase slowly as one decreases a. For $1 \leq a < 2$, ν is close to the prediction in Eq. (3.18). For $a = 0.75$, it seems to be bigger than expected with $\nu \simeq 3.5$, but in this case, strong finite size corrections are found. For smaller value of a, it was not possible to measure ν.

3.3.6 The effects of higher disorder cumulants

In this section, the focus is on the $q = 1$ case, where the disordered Potts model can be mapped to a long-range percolation model using the level sets of a fractional Gaussian free field (fGFF) with negative Hurst exponent $H = -a/2$ [128–132].

By using the fGFF, it is possible to generate a long-range disorder distribution, creating a one-parameter family of Gaussian long-range percolation models for the $(q = 1)$-Potts model. It has been observed through simulations that all these models flow to the point $r = \infty$, as shown in Fig. (3.14). At this point, the long-range percolation models are expected to exhibit the same critical properties as those studied in [128–132]. In particular, with the use of toric boundary conditions, the model coincides with the one studied in [132] at $r = \infty$.

In this approach, it becomes possible to directly compare the LRp points obtained using different disorder distributions, including non-Gaussian ones. The disorder distribution generated by the n-replicated Ising model is an example of such non-Gaussian distributions. In the following analysis, the suffix I is used for the disorder distribution generated by the n-replicated Ising model, while the suffix G refers to the distribution based on the fractional Gaussian free field (fGFF).

For both distributions, the Gaussian (fGFF) and non-Gaussian (Ising models) ones, Eq. (3.18) yields the same value for the percolation thermal exponent $\nu = 2/a = 8$.

However, the situation is different for the exponent β. Specifically, the critical case $a = 1/4$ can be examined in more detail. Table (3.5) presents the results of Monte Carlo measurements for $\left(\beta^{LRp}/\nu^{LRp}\right)_I$, obtained using the Ising distribution, and $\left(\beta^{LRp}/\nu^{LRp}\right)_G$,

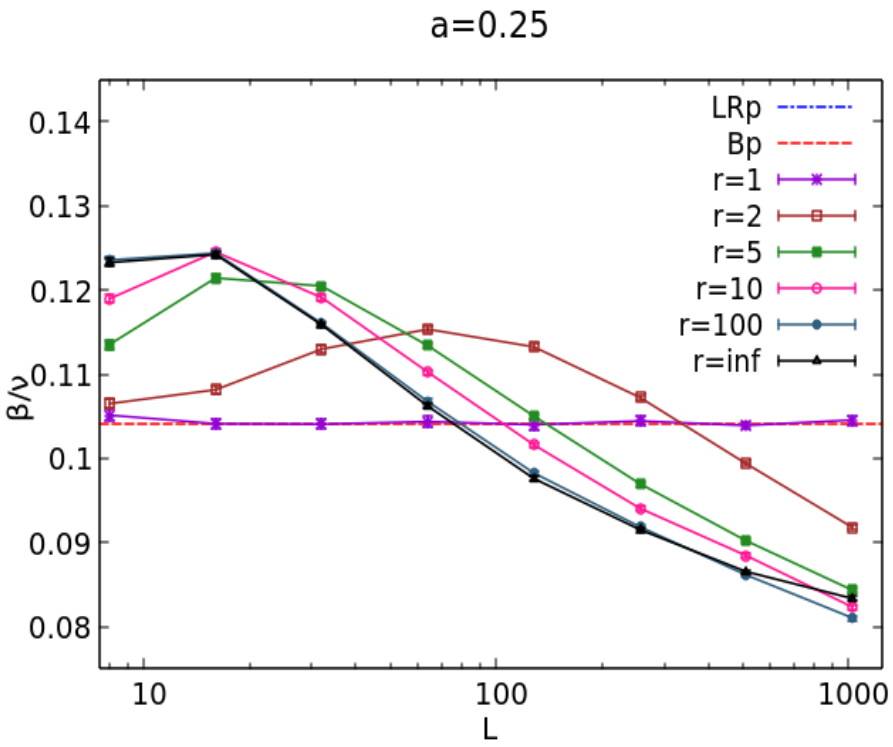

Figure 3.14. β/ν vs. L at $q = 1$ with $a = 0.25$ and disorder generated by using fGFF, see Section (3.2.1).

obtained using the fGFF distribution. These results can be directly compared with the measurements reported in [130].

a	$\left(\beta^{LRp}/\nu^{LRp}\right)_I$	$\left(\beta^{LRp}/\nu^{LRp}\right)_G$	$\left(\beta^{LRp}/\nu^{LRp}\right)_G$ [130]
0.25	0.0522(4)	0.0721(9)	0.0640(4)

Table 3.5. Comparison of β^{LRp}/ν^{LRp} for Gaussian and non-Gaussian disorders.

The exponents $\left(\beta^{LRp}/\nu^{LRp}\right)_G$ and $\left(\beta^{LRp}/\nu^{LRp}\right)_I$ obtained respectively with the fGFF and with the Ising model seems different. Note that the numerical result $\left(\beta^{LRp}/\nu^{LRp}\right)_I$ agrees perfectly with the Ising model: as argued earlier, for the non-Gaussian disorders with $n = 1$-Ising copies, the FK clusters have the same fractal dimensions as the Ising spin clusters.

The above results can be explained by noticing that, differently from the short-range disorder, in a long-range disorder, the terms generated by the higher cumulants of the

distribution can be relevant. One can conclude that the higher cumulants do not change the existence and the stability of an LRp point but can modify certain critical exponents. This phenomenon gives a crucial motivation on the study done in [8], and will be analysed in the next Sections (4.3.4).

As far the exponent β^{LRp}/ν^{LRp} is concerned, one can doubt that the differences seen in the simulations are just due to the numerical precision. This is particularly true when a is increasing, see Table (3.3). However, it is possible to mention the measure of another universal property which is clearly different between the $(\mathrm{LRp})_G$ and the $(\mathrm{LRp})_I$ and therefore supports the conclusion above. Indeed in [132] and in [159] the torus two-point connectivity $p_{12}^G(r)$ and $p_{12}^I(r)$ of, respectively, the fGFF level sets and the Ising clusters were considered. It was argued that:

$$p_{12}^G(r) = a_0^G\, r^{-2\left(\beta^{LRp}/\nu^{LRp}\right)_G} \times \left[1 + c^G \left(\frac{r}{L}\right)^{1.875} + o\left(\left(\frac{r}{L}\right)^4\right)\right], \tag{3.34}$$

$$p_{12}^I(r) = a_0^I\, r^{-2\left(\beta^{LRp}/\nu^{LRp}\right)_I} \times \left[1 + c^I \left(\frac{r}{L}\right) + o\left(\frac{r}{L}\right)\right], \tag{3.35}$$

where a_0^G and a_0^I are non-universal constants. The c^G and c^I are universal quantities that depend on the ratio L_h/L_v between the horizontal and the vertical torus size and on the structure constants of the eventual CFT behind, see [160]. The c^I is known and it has been computed in [159] while c^G, investigated in [132], is not known exactly.

The exponent x of the sub-leading term $(r/L)^x$ is computed on the assumption that there exists a local CFT describing the critical point. This gives [160]:

$$x = 2 - \frac{1}{\nu}. \tag{3.36}$$

The exponents in Eq. (3.35) are then obtained by using $\nu = 1/8$ ($x = 1.875$) for the Gaussian distribution and $\nu = 1$ ($x = 1$) for the Ising one. For the Ising case, where the existence of a CFT behind is well established, the form for p_{12}^I has to be considered exact. For the fGFF, the CFT predictions (3.35), with $\nu = 2/a$, were tested numerically only for values of $a > 1$ [132]. For p_{12}^G one can extend the results of [132] to $a = 1/4$, by assuming an analytical $a-$dependence on the critical exponents for all values of $a < 3/2$. So one can see that the sub-leading term exponents depend strongly on the disorder distribution.

3.4 Conclusions

In this chapter, the long-range disordered two-dimensional q-Potts model is studied using Monte Carlo techniques. The disorder is introduced through a bimodal distribution coupled to auxiliary spin degrees of freedom, which can follow either the n-Ising distribution or the fractional Gaussian free field (fGFF) distribution. These distributions

have the same first cumulant and exhibit a long-range power-law decay in their second cumulant.

The main focus is on the fractal dimension of the q-Potts FK clusters at the self-dual point for different values of the power-law exponent a and disorder strength r. The results are summarized in the phase diagram shown in Fig. (3.3), which represents the main finding of this work.

The infinite disorder ($r = \infty$) fixed point, LRp (Long-range percolation), is considered first. At this point, the thermal fluctuations of the Potts degrees of freedom are frozen, and the disorder averages coincide with those of a LRp model. The critical exponents of LRp do not depend on q. The measured values of β^{LRp}/ν^{LRp} are reported in Table (3.3), and it is observed that the Monte Carlo measurements using the Ising distribution are more precise than those using the fGFF distribution. This allows for more accurate investigations of the LRp physics, especially for small values of a where the fGFF methods are more challenging to implement.

For $q = 1$, it is found that the LRp point is attractive for $a < 3/2$, while for $a \geq 3/2$ the system is described by the Bernoulli percolation (Bp) critical point. For $q = 2$ and $q = 3$, the existence of a long-range (LR) point at finite disorder, is established. It is observed that the stability between the LR point and the LRp point exchanges at a certain value $a^*(q)$ depending on q.

The above results are supported by the study of other observables. For $q = 2$, the multifractal behavior of the spin-spin correlations is measured, see Table (3.4), and the results are consistent with theoretical predictions in their valid region, especially for $1.5 < a < 2$. For lower values of a where theoretical predictions are lacking, the results rule out the occurrence of a softening of the transition and instead support the system being driven to the LRp point. For $q = 3$, the thermal exponent ν^{LR} is measured by studying the wrapping probability of the FK clusters, see Fig. (3.13), and the results are consistent with the theoretical prediction of Eq. (3.18) for a wide range of a.

It is worth noting that the obtained results and the phase diagram are valid for different disorder distributions. However, there are some universal effects of the higher cumulants at the LRp point. For example, at $a = 1/4$, the exponent β^{LRp} differs between the Gaussian and non-Gaussian distributions, see Table (3.5). Additionally, the higher cumulants are expected to have clear effects on the universal finite-size properties of the FK connectivities, see Eq. (3.35).

Chapter 4

Spin models with long-range correlated disorder: an RG apporach

Preface

This chapter introduces the new conclusions drawn from [8] on the Potts model with disordered correlations over a long-range, complementing the numerical findings from Chapter (3) and [7]. The chapter also adapts the renormalisation group strategy from [44]. This section embodies the analytical portion of this thesis's second half.

Synthesis of the results

In this chapter, new analytical results on two-dimensional q-Potts models ($q \geq 2$) in the presence of bond disorder correlations which decay algebraically with distance with exponent a, are provided. In particular, the results are valid for the long-range bond disordered Ising model ($q = 2$). A renormalisation group perturbative approach based on conformal perturbation theory is implemented. The renormalisation group scheme used in [44] for the short-range disorder is extended to the long-range case. The used approach is based on a 2-loops order double ϵ-expansion in the positive parameters $(2-a)$ and $(q-2)$. It will be shown that the Weinrib-Halperin conjecture for the long-range thermal exponent can be violated for a non-Gaussian disorder. The central charges of the long-range fixed points is computed finding a very good agreement with numerical measurements. These analytical results, are confirmed by the numerical simulations of the previous chapter and of [7].

4.1 Introduction

In this chapter, the focus is on studying the two-dimensional $q-$Potts model with long-range correlated bond disorder. The phase diagram of this model, as depicted again in Figure (3.3), is proposed based on Monte Carlo simulations done in [7] and explained in Chapter (3). The critical behavior of the system depends on two key parameters: the

number of spin states q and the power-law decay exponent a characterizing the disorder correlations.

The phase diagram consists of four critical points that govern the system's behavior:

- The pure (P) point: this point corresponds to the system without any disorder. It serves as a trivial point for comparing the effects of disorder in the other regions of the phase diagram and build the perturbation theory around it.
- The short-range (SR) point: at this point, the dominant influence on the system comes from the short-range part of the disorder distribution.
- The long-range (LR) point: the LR point represents a region where the disorder's long-range nature becomes significant. The disorder strength at this point is finite, and it plays a crucial role in determining the critical behavior of the system.
- The long-range percolation (LRp) point: this point corresponds to an infinite disorder strength. The LRp point is of particular interest due to the fact that it describes a particular kind of percolation physics.
- Referring to Fig. (3.3), the solid black, dashed cyan, dashed orange and dashed red lines indicate respectively the exchange of stability between the P-SR, the SR-LR, the P-LR and the LR-LRp fixed points. The P-SR and SR-LR lines are conjectured to be described respectively by the equations $a = 2/\nu^{P}(q)$ and $a = 2/\nu^{SR}(q)$. The SR-LR line is derived in Eq. (4.72) and in Eq. (4.88). The exact location of LR-LRp line is beyond reach for the RG expansion employed, still it is possible to predict the existence of such line, see the Eq. (4.88) and the Eq. (4.95).

To provide a comprehensive understanding of long-range disorder systems, a brief introduction was provided in Section (3.1). Additionally, interested readers can refer to [7] and its references for further details on the topic.

Long-range disordered models have been extensively studied using a renormalisation group (RG) approach in the past. Several RG computations, such as those in [86, 123], or in [148] and [161–163], have focused on the vicinity of the upper critical dimension $d \sim d_c$. For example, for the Ising model, $d_c = 4$, while for pure long-range percolation, $d_c = 6$, [123]. These computations are valid for small values of $(4 - a)$, where a is the power-law decay exponent of the disorder correlations. At the perturbation order (typically 1-loop), a stable long-range (LR) fixed point was found, and the associated thermal exponent ν^{LR}. It was determined to be $\nu^{LR} = 2/a$. This result is known as the Weinrib-Halperin conjecture [86].

In the case of the long-range bond-disordered Ising model in $d = 3$ dimensions, Prudnikov and collaborators [162, 163] performed a 2-loops RG analysis for $2 < a < 3$. They discovered a significant violation of the Weinrib-Halperin conjecture, which could not be solely attributed to the approximation scheme used. Monte Carlo simulations have not provided conclusive evidence regarding this violation [164–166].

In $d = 2$ dimensions, analytic results for long-range disordered systems are scarce and limited to the long-range disordered Ising model [134, 135]. The Ising model in $d = 2$ has the advantage of being describable by a free fermion field theory [167]. Dudka [135] performed a 2-loops RG computation based on a double ϵ-expansion in $(2 - a)$ and $(2 - d)$, supporting the Weinrib-Halperin conjecture in this case.

In this work, a new RG perturbative approach based on conformal perturbation theory, see Sec. (1.7) will be presented. This will be done extending the RG scheme used in [44] to the long-range disorder case. This approach allows to derive new analytic results for the unexplored region of $q \geq 2$ and $a < 2$, with $a - 2 \ll 1$, $q - 2 \ll 1$, and $(q - 2)/(a - 2)$ finite. The central charge of the long-range Ising and Potts models is computed and compared to numerical transfer matrix results. Additionally, the long-range correlation length exponent ν^{LR} is determined at 2-loops order. In other words, the main goal of this chapter is to analytically investigate and verify the phase diagram depicted in Figure (3.3) for the region near $q = 2$ and $a = 2$.

It is worth noting that the existing theoretical literature has primarily focused on Gaussian disorder distributions. However, unlike short-range disorder, the terms arising from higher cumulants can be relevant and may affect universal observables. This phenomenon has been highlighted in [7]. The role of higher cumulants has not been adequately explored so far. In this study, it will be provided an analytical evidence supporting the validity of the Weinrib-Halperin conjecture in the presence of Gaussian disorder. Indeed, it is found that the conjecture holds true for Gaussian disorder, where the thermal exponent ν^{LR} is indeed equal to $2/a$. However, analysing a non-Gaussian disorder distribution, which inherently possess higher cumulants, it is possible to demonstrate a violation of the Weinrib-Halperin conjecture. This emphasizes the notable impact that higher cumulants have on the universal behavior of systems with long-range correlated disorder.

4.2 Field theoretical Potts model in the replica approach

In Section (1.6.4) and Section (1.7), the approach of addressing the impact of disorder perturbation on the pure Potts interacting theory using a field theoretical framework was introduced and will be the one used to obtain the results of this chapter. However, it is valuable to briefly summarize the lattice scenario to maintain connection with the initial point, namely the random bond Potts model on the square lattice. Furthermore, the continuous replicated formulation, which was derived in the Introduction (1.6.4),

will be briefly summarized to establish notation and conventions that are helpful for the essential renormalisation group (RG) calculations.

4.2.1 Lattice formulation

For this reason, one considers the lattice random bond Potts Hamiltonian:

$$\mathcal{H}_P^{dis}(\{s_i\},\{J_{i,j}\}) = -\sum_{\langle i,j\rangle} J_{i,j}\delta_{s_i,s_j}, \tag{4.1}$$

where the sum runs over the nearest neighbours of a two dimensional regular lattice of side L. The δ is the usual Kronecker function, and the $N = L^2$ spins can take q discrete values, with $q \in \{2,3\}$. The $J_{i,j}$, are random bimodal variables, the so called random bond and they are defined by:

$$J_{i,j} = \frac{J_1 + J_2}{2} + \sigma_{i,j}\frac{J_1 - J_2}{2}, \tag{4.2}$$

where J_1, J_2 are deterministic values while the $\sigma_{i,j}$ are stochastic auxiliary variables, the quenched disorder:

$$\sigma_{i,j} = \begin{cases} +1, & \text{with probability } p_{i,j} = 1/2 \\ -1, & \text{with probability } 1 - p_{i,j} = 1/2, \end{cases} \tag{4.3}$$

living on lattice bonds[1]. For the sake of keeping the notation light, couples of lattices indices will be called with greek letters, $(i,j) \to \rho$.

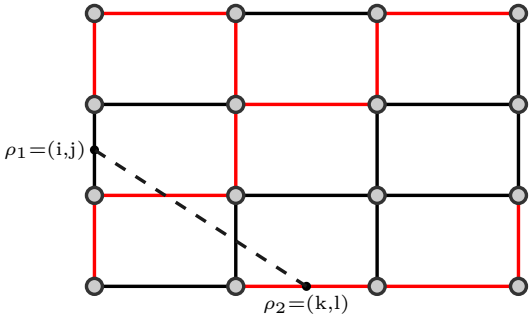

Figure 4.1. A particular configuration of the auxiliary variables, σ, is shown. Black (red) bonds correspond to $\sigma_\rho = 1$ ($\sigma_\rho = -1$). The corresponding set of couplings $\{J_\rho\}$, associated to the edges, follow from the Eq. (4.2). The dotted line represent the distance $|\rho_1 - \rho_2|$ between two bonds. Circle, instead, represent q-Potts spins on lattice vertices.

[1] In [7], these live on lattice vertices, but since a continuum limit will be soon taken, there is no reason in doing this.

The set of $\{\sigma_i\}$ variables introduce the long-range correlations between bonds:

$$\mathbb{E}[\sigma_{\rho_1}\sigma_{\rho_2}] \sim |\rho_1 - \rho_2|^{-a}, \text{ for distances} \gg l, \text{ the lattice spacing,} \tag{4.4}$$

and can be sampled from different probabilities distribution functions (PDFs). The symbol $\mathbb{E}[\cdots]$, stands for the disorder average:

$$\mathbb{E}\left[\cdots\right] = \frac{1}{\sum\limits_{\{\sigma\}} \exp\left(\mathcal{S}^{\text{aux}}(\sigma)\right)} \sum_{\{\sigma\}} \exp\left(\mathcal{S}^{\text{aux}}(\sigma)\right)\left[\cdots\right], \tag{4.5}$$

with $e^{\mathcal{S}^{\text{aux}}}$ the probability distribution function.

4.2.2 Continuous replicated formulation

Doing the continuum limit of this perturbed lattice theory, close to the Pure (P) critical point, one obtains the following action:

$$\mathcal{S}[s(x), \sigma(x)] = \mathcal{S}^{\text{aux}}[\sigma(x)] + \mathcal{S}^{\text{Potts}}[s(x)] + \mathcal{S}^{\text{pert}}[s(x), \sigma(x)] \tag{4.6}$$

$$\mathcal{S}^{\text{pert}}[s(x), \sigma(x)] = g^0_{LR} \int\limits_{|x|>l} d^2x\, \sigma(x)\varepsilon(x), \tag{4.7}$$

where, the variable g^0_{LR} represents a coupling constant that possesses dimensions. It serves as a parameter to quantify the strength of disorder and is commonly known as the "bare coupling." $\sigma(x)$ is the continuum version of the auxiliary spin variable, $\varepsilon(x)$ is the energy Potts fields, corresponding to the scaling limit of δ_{s_i,s_j} and l is the ultraviolet (UV) cutoff of the field theroy coming from the lattice formulation. In this particular section, in contrast to Section (1.6.4), the auxiliary field is referred to as σ instead of ϕ to emphasize its origin from the spins. The $\mathcal{S}^{\text{Potts}}[s(x)]$ represent the critical Potts action, where the $s(x)$ are its degrees of freedom. To streamline the notation, the dependence on (x) for the fields will be implied when it is not necessary for clarity. In a CFT approach, one can choose the most convenient representation of the Potts action, but, for the aims of this study, one does not need to specify these details. As usually done in disordered systems, the action is replicated and one compute the m^{th} moment of the logarithm of the partition function. One must note another change in notation: in this case, m represents the number of replicas of the model, while n denotes the number of uncorrelated copies of the Ising model performed in Chapter (3) to numerically tune the exponent a.

$$\mathcal{S}^{(m)}[s^{(\alpha)}, \sigma] = \mathcal{S}^{\text{aux}}[\sigma] + \sum_{\alpha=1}^{m} \left(\mathcal{S}^{(\alpha)\text{-Potts}}[s^{(\alpha)}] + \mathcal{S}^{(\alpha)\text{-pert}}[s^{(\alpha)}, \sigma]\right), \tag{4.8}$$

By considering only these two terms in the action, the effects of short-range (SR) disorder are neglected in the renormalisation group (RG) calculations. However, it is important to note that this SR perturbation is marginal for the case of $q = 2$, but becomes relevant for $q > 2$. Additionally, it will be demonstrated that the operator product expansion (OPE) automatically generates a relevant (or marginal for $q = 2$) SR term.

Furthermore, it has been observed that when the dimensionality a is greater than the spatial dimension $d = 2$, the LR disorder collapses into a SR disorder, as described in [7]. To account for this behavior and provide a complete description of the critical behavior, another term of the form $\sum_{\alpha\neq\beta=1}^{m} g^0_{SR} \int_{|x|>l} d^2\, x, \varepsilon^{(\alpha)}(x)\varepsilon^{(\beta)}(x)$, [44] can be added "by hand". It is worth nothing that, in this very term, one does not consider diagonal terms $\alpha = \beta$. This omission is due to the fact that, as demonstrated in [45], the operator product expansion (OPE) will project these terms onto the identity operator, resulting in a negligible constant contribution to the free energy of the model. In this context, it can be said that these terms "renormalise the identity."

$$\mathcal{S}^{(\alpha)\text{-pert}} = \sum_{\alpha=1}^{m} g^0_{LR} \int_{|x|>l} d^2x\, \sigma(x)\varepsilon^{(\alpha)}(x) + \sum_{\alpha\neq\beta=1}^{m} g^0_{SR} \int_{|x|>l} d^2x\, \varepsilon^{(\alpha)}(x)\varepsilon^{(\beta)}(x). \tag{4.9}$$

And, consequently:

$$\begin{aligned}
\mathcal{Z}^m &= \int \mathcal{D}_\sigma \mathcal{D}_s\, e^{\mathcal{S}^{(m)}} = \int \mathcal{D}_\sigma \mathcal{D}_s \exp\left(\mathcal{S}^{\text{aux}} + \sum_{\alpha=1}^{m} \mathcal{S}^{(\alpha)\text{-Potts}} + \mathcal{S}^{(\alpha)\text{-pert}}\right) \\
&= \int \mathcal{D}_\sigma \mathcal{D}_s \exp\Big(\mathcal{S}^{\text{aux}} + \sum_{\alpha=1}^{m} \mathcal{S}^{(\alpha)\text{-Potts}} + \sum_{\alpha=1}^{m} g^0_{LR} \int_{|x|>l} d^2x\, \sigma(x)\varepsilon^{(\alpha)}(x) + \\
&\qquad + \sum_{\alpha\neq\beta=1}^{m} g^0_{SR} \int_{|x|>l} d^2x\, \varepsilon^{(\alpha)}(x)\varepsilon^{(\beta)}(x)\Big) \\
&= \int \mathcal{D}_\sigma \mathcal{D}_s \exp(\mathcal{S}^*) \times \exp\Big(\sum_{\alpha=1}^{m} g^0_{LR} \int_{|x|>l} d^2x\, \sigma(x)\varepsilon^{(\alpha)}(x) + \\
&\qquad + \sum_{\alpha\neq\beta=1}^{m} g^0_{SR} \int_{|x|>l} d^2x\, \varepsilon^{(\alpha)}(x)\varepsilon^{(\beta)}(x)\Big),
\end{aligned} \tag{4.10}$$

where $\mathcal{S}^*$ is defined by: $\mathcal{S}^* = \mathcal{S}^{\text{aux}} + \sum_{\alpha=1}^{m} \mathcal{S}^{(\alpha)\text{-Potts}}$,

$$\mathcal{Z}^* = \int \mathcal{D}_\sigma \mathcal{D}_s \, \exp\Big(\mathcal{S}^{\text{aux}} + \sum_{\alpha=1}^{m} \mathcal{S}^{(\alpha)\text{-Potts}} \Big) \text{ and } \mathcal{D}_s = \prod_{\alpha}^{m} ds^{(\alpha)}.$$

As mentioned in Section (1.6.4), it is common practice, especially in the case of short-range disorder, to integrate over the auxiliary degrees of freedom, resulting in an effective action perturbed by Potts energy-energy terms. However, in the case of long-range correlated disorder, integrating over the auxiliary variables would lead to a non-local energy-energy perturbation. Therefore, it is preferable to retain the σ as a dynamical variable in order to keep local terms. Also, in this way, the computations are general with respect to the disorder distribution. The specific probability density function (PDF), related to $\mathcal{S}^{\text{aux}}$, will be selected when necessary.

In any case, the PDF must respect the following constraint:

$$\begin{aligned} &\bullet\, \mathbb{E}[\sigma(x)] = 0, \\ &\bullet\, \mathbb{E}[\sigma(x)\,\sigma(y)] = |x-y|^{-a}, \\ &\bullet\, \mathbb{E}[\sigma(x)\,\sigma(y)\,\sigma(z)] = 0. \end{aligned} \tag{4.11}$$

Of course there are disorder distributions that share the properties Eq. (4.11) and differ in higher cumulants. As an example, one can mention the distribution chosen in [122], where the disorder field σ coincides with the polarization density field of a $d = 2$ Ashkin-Teller (AT) model. In this case the $\mathcal{S}^{\text{aux}}$ is the action which describes the AT critical line, which in turn can be expressed in term of a compactified (and orbifolded) free scalar field [168]. In [7], instead, it is considered $\sigma(x) = \prod_i^n \sigma_i(x)$, where σ_i is a spin field of i-th copy of a $d = 2$ critical Ising model. In this case, the $\mathcal{S}^{\text{aux}}$ is the action of n-uncoupled Ising model. Otherwise, most of the previous works considered scale-invariant Gaussian disorder distribution, see Section (4.3.4) for more details.

By expanding the perturbation term in a series, it is obtained, see Eq. (1.56):

$$\begin{aligned} \mathcal{Z}^m = \mathcal{Z}^* \Big\langle 1 &+ \sum_{\alpha=1}^{m} g^0_{LR} \int_{|x|>l} d^2x\, \sigma(x)\varepsilon^{(\alpha)}(x) + \sum_{\alpha\neq\beta=1}^{m} g^0_{SR} \int_{|x|>l} d^2x\, \varepsilon^{(\alpha)}(x)\varepsilon^{(\beta)}(x) + \\ &+ \frac{1}{2!} \sum_{\alpha\neq\beta=1}^{m} \sum_{\gamma\neq\delta=1}^{m} (g^0_{SR})^2 \iint_{|x-y|>l} d^2x\, d^2y\, \varepsilon^{(\alpha)}(x)\varepsilon^{(\beta)}(x)\, \varepsilon^{(\gamma)}(y)\varepsilon^{(\delta)}(y) + \\ &+ \frac{1}{2!} \sum_{\alpha=1}^{m} \sum_{\beta=1}^{m} (g^0_{LR})^2 \iint_{|x-y|>l} d^2x\; d^2y\, \sigma(x)\varepsilon^{(\alpha)}(x)\, \sigma(y)\varepsilon^{(\alpha)}(y) + \\ &+ \sum_{\alpha=1}^{m} \sum_{\beta\neq\gamma=1}^{m} g^0_{LR} g^0_{SR} \iint_{|x-y|>l} d^2x\, d^2y\, \sigma(x)\varepsilon^{(\alpha)}(x)\, \varepsilon^{(\beta)}(y)\varepsilon^{(\gamma)}(y) + \cdots + O(g^3) \Big\rangle_{\mathcal{S}^*}. \end{aligned} \tag{4.12}$$

Here, $\langle\cdots\rangle_{\mathcal{S}^*}$ represents the average with respect to the disorder distribution $\mathcal{S}^*$, and g^3 denotes the terms in the form of $(g^0_{LR})^3, (g^0_{SR})^3, (g^0_{LR})^2 g^0_{SR}, (g^0_{SR})^2 g^0_{LR}$.

To simplify the notation, the symbol $\langle\cdots\rangle_{\mathcal{S}^*}$ will be implied when unnecessary during calculations and will be restored when useful. Also, it must be noticed that the average, $\langle\cdots\rangle_{\mathcal{S}^*}$, factorizes for therms of the kind:

$$\langle\sigma(x)\varepsilon^{(\alpha)}(x)\,\sigma(y)\varepsilon^{(\alpha)}(y)\rangle_{\mathcal{S}^*} = \mathbb{E}[\sigma(x)\,\sigma(y)]\,\langle\varepsilon^{(\alpha)}(x)\,\varepsilon^{(\alpha)}(y)\rangle, \tag{4.13}$$

where $\langle\cdots\rangle$ is simply the average with respect to the replicated Potts action, $\mathcal{S}^{(\alpha-\text{Potts})}$.

With this in place, one is ready to begin the approach of the RG computation in the way introduced in Section (1.7.4).

4.2.3 Physical set up, RG scheme and OPE rules

In this study, the analysis is conducted with Virasoro primary operators [39], namely σ and ε, which have known scaling dimensions denoted as h_σ and h_ε, respectively. Since a perturbative ϵ-expansion is being performed around the P fixed point, the principles of conformal field theory (CFT) and the operator product expansion (OPE) guarantee the following relations:

- 1-loop: $\lim\limits_{x\to y}\sigma(x)\sigma(y) \to \mathcal{C}_{\sigma\sigma}(|x-y|)\,\mathbb{1}(x) + \text{irrelevant fields},$
  where $\mathcal{C}_{\sigma\sigma}(|x-y|) = \mathbb{E}\left[\sigma(x)\sigma(y)\mathbb{1}(\infty)\right] = |x-y|^{-2h_\sigma}$.
- 1-loop: $\lim\limits_{x\to y}\varepsilon(x)\varepsilon(y) \to \mathcal{C}_{\varepsilon\varepsilon}(|x-y|)\,\mathbb{1}(x) + \text{irrelevant fields},$ (4.14)
  where $\mathcal{C}_{\varepsilon\varepsilon}(|x-y|) = \langle\varepsilon(x)\varepsilon(y)\mathbb{1}(\infty)\rangle = |x-y|^{-2h_\varepsilon}$.
- 2-loops: $\lim\limits_{x\to y\to z}\sigma(x)\sigma(y)\sigma(z) \to \mathcal{C}_{\sigma\sigma\sigma}(|x-y|,|y-z|)\,\sigma(x) + \text{irrelevant fields},$
  where $\mathcal{C}_{\sigma\sigma\sigma}(|x-y|,|y-z|) = \mathbb{E}\left[\sigma(x)\sigma(y)\sigma(z)\sigma(\infty)\right]$.
- 2-loops: $\lim\limits_{x\to y\to z}\varepsilon(x)\varepsilon(y)\varepsilon(z) \to \mathcal{C}_{\varepsilon\varepsilon\varepsilon}(|x-y|,|y-z|)\,\varepsilon(x) + \text{irrelevant fields},$
  where $\mathcal{C}_{\varepsilon\varepsilon\varepsilon}(|x-y|,|y-z|) = \langle\varepsilon(x)\varepsilon(y)\varepsilon(z)\varepsilon(\infty)\rangle$.

It is important to note that the operators σ and ε are averaged with respect to the action $\mathcal{S}^*$, so the brackets $\langle\cdots\rangle_{\mathcal{S}^*}$ are implied. Thus, Equation (4.14) should be interpreted as follows: the contraction of two or more σ or ε operators, projected onto a different operator located far away (infinite distance), yields that far operator multiplied by an amplitude. At the 1-loop level, this amplitude is determined by Equation (1.73), while at the 2-loop level, it needs to be computed and is a crucial aspect of the calculation.

It is worth mentioning that for the OPE to be applicable, two ε fields must be in the same replica, so the replica index will be implied in those cases.

The utilization of OPE rules in the RG computation, as explained in Section (1.7), is justified by the phenomenon that occurs during the coarse-graining process. Operators located at different but sufficiently close points in space collapse into a single point, effectively becoming far away from the identity, σ, or ε operators onto which they are projected. In practice, these operators are considered to be at infinity.

From Equation (4.4), it can be easily deduced that $h_\sigma = a/2$. Additionally, it is well-known that $h_\varepsilon = 2 - 1/\nu^P$ [44], where ν^P represents the critical exponent of the correlation length for the P model.

The RG procedure is based on the double ϵ-expansion of the following quantities:

$$\epsilon_{SR} = 2 - 2h_\varepsilon,\ \epsilon_{LR} = 2 - h_\sigma - h_\varepsilon, \tag{4.15}$$

$h_{\epsilon_{SR}} = 2h_\varepsilon$ and $h_{\epsilon_{LR}} = h_\sigma + h_\varepsilon$ represent the scaling dimension of the $\varepsilon^{(\alpha)}\varepsilon^{(\alpha)}$ operator (the SR one) and of the $\sigma\varepsilon^{(\alpha)}$ operator (the LR one). In terms of the physical variable a and q, one can notice that:

$$\epsilon_{LR} = 1 - \frac{a}{2} + \frac{\epsilon_{SR}}{2},\ 2\epsilon_{LR} - \epsilon_{SR} = 2 - a, \tag{4.16}$$

and:

$$\epsilon_{SR} = 4 - \frac{6\pi}{2\pi - \arccos\left(\dfrac{q-2}{2}\right)} = \frac{4}{3}(q-2) + O\left((q-2)^2\right),\ [44]. \tag{4.17}$$

For the case of $q = 2$, the value of ϵ_{SR} is zero. However, to ensure a unified treatment of both the Potts model and the Ising model, the analysis is kept general, and ϵ_{SR} will be appropriately sent to zero when considering the Ising model.

It is important to note that the computations are restricted to a region where $(q-2) \ll 1$ and $(2-a) \ll 1$ to ensure that ϵ_{LR} and ϵ_{SR} are small. This restriction allows for a perturbative analysis of the system.

Therefore, one can consider:

- $s = \dfrac{\epsilon_{SR}}{\epsilon_{LR}} \to O(1)$ for $q \gtrsim 2$ and $(2-a)$ finite,
- $s = \dfrac{\epsilon_{SR}}{\epsilon_{LR}} \to o(1)$ for $q = 2$ and $(2-a)$ finite, *i.e.* the Ising limit.

(4.18)

4.3 Renormalisation group computation

In this section, the real space renormalisation group (RG) scheme for the aforementioned model is explicitly developed. This will be carried out by following the guidelines provided in [25, 44], as well as in Section (1.7).

This scheme is particularly adapted when one deals with perturbations around a conformal (in general not a free-field) action. This can be compared to previous RG approaches to long-range disordered models, where the unperturbed action was a free-field action: for instance a vector [86] or a tensor of free-scalar-fields [123], or again a Majorana free fermion [135]. The RG transformations in these previous works were carried out in the momentum space by using the form of the free-theory bare propagator. In this work and in [8], instead, one uses the bootstrap data of the unperturbed CFT, that provides the space dependence of the three and the four-point functions of primary fields.

It is a very general result in CFTs that the 0-loops order RG recursion relations are determined by the scaling dimensions of the relevant perturbation operators and their operator product expansion (OPE), as established in [25]. In the upcoming analysis, these results will be re-derived specifically for the model in question. It will be shown that also the 1-loop order is completely fixed by these scaling dimensions. Furthermore, the computation will be extended to the 2-loops level to provide a more comprehensive understanding of the system.

The procedure involves ensuring the conservation of the partition function under RG transformations. To initiate the computation, the RG scale factor r can be introduced, where $r = (1 + \delta r)$.

With the introduction of the RG scale factor, the RG computation can now commence.

1. To begin, one expands the perturbation term as shown in Equation (4.12).
2. Next, the integral cutoffs are rescaled by a factor of r, such that $l \to l(1 + \delta r) = lr$.
3. The next step involves integrating out the fluctuations over scales between the original ultraviolet (UV) cutoff l and the rescaled cutoff lr.
4. After integrating out the fluctuations over the intermediate scales, the system is set back to the original UV cutoff l.
5. In order to maintain the physical quantities invariant under the renormalisation group (RG) transformation, such as the partition function, the bare coupling constants g^0_{LR}, g^0_{SR} need to be adjusted. This leads to the computation of the new set of renormalized coupling constants. Specifically, one computes the renormalized dimensionless couplings $g_{LR}(r), g_{SR}(r)$ in terms of the bare couplings

In Fig. (1.11), a schematic representation of the procedure that will be explicitly carried out in this section is depicted.

The rescaling step explicitly affects the integrals in Equation (4.12) through the length dependence of operators and the cutoff of the integrals. For a generic coupling term $(g_X^0)^k$, where $X = \{LR, SR\}$ and k is an integer power, the effect of rescaling can be expressed as follows:

$$\begin{aligned}(g_X^0)^k \int\limits_{|x-y|>l} d^2x\, d^2y\, (\cdots) \to (g_X^0)^k \int\limits_{|x-y|>lr} d^2x\, d^2y\, (\cdots) = \\ = (g_X^0)^k \int\limits_{|x-y|>l} d^2x\, d^2y\, (\cdots) - (g_X^0)^k \int\limits_{l<|x-y|<lr} d^2x\, d^2y\, (\cdots)\ .\end{aligned} \tag{4.19}$$

The term with the cutoff l contributes in the usual manner to the partition function.

As for the second term, from now on, the lower bound ($l < |x - y|$) of the integral will not be considered. This lower bound contributes to non-universal terms, which will be disregarded for the computation of universal critical exponents.

Therefore, terms of the form:

$$-(g_X^0)^k \int\limits_{|x-y|<r} d^2x\, d^2y\, (\cdots)\,, \tag{4.20}$$

will contribute to the renormalisation of the coupling constants $\{(g_X^0)^k\}$ in Equation (4.12).

For simplicity, one assumes the lattice spacing is set to 1, so $l = 1$. Again, it is important to remind that the symbol $\langle\cdots\rangle_{\mathcal{S}^*}$ is implied.

4.3.1 0-loops or dimensional analysis

When considering terms of order $(g_X^0)^1$, one can perform what is referred to as a 0-loops computation.

For a generic scaling operator $O(x)$ with scaling dimension h_O, Equation (4.19) implies:

$$\begin{aligned}(g_X^0)^1 \int\limits_{|x|>l} d^2x\, O(x) \to (g_X^0)^1 \int\limits_{|x|>lr} d^2(x)\, O(x) \\ = (g_X^0)^1 r^{2-h_O} \int\limits_{|x|>l} d^2(x)\, O(x)\end{aligned} \tag{4.21}$$

At the "0-loop" level, one can neglect fast fluctuating terms in the range $l < |x| < lr$, which simplifies Equation (4.19). Then, by setting back the UV cutoff to its initial value l, the coupling is rescaled by r^{2-h_O}, resulting in:

$$(g_X^0)^1 \, r^{2-h_O}. \tag{4.22}$$

Another way to arrive at the same result is by considering dimensionless couplings. This can be achieved by noting that:

$$\begin{aligned} [\![g_{SR}^0]\!] &= r^{-2+2h_\varepsilon}, \\ [\![g_{LR}^0]\!] &= r^{-2+h_\sigma+h_\varepsilon}, \end{aligned} \tag{4.23}$$

where the $[\![\cdots]\!]$ denotes the dimension of the quantity inside the brackets, and r represents the RG length scale. By making the couplings dimensionless, one obtains:

$$\begin{aligned} g_{SR} &= g_{SR}^0 \, r^{2-2h_\varepsilon} = g_{SR}^0 \, r^{\epsilon_{SR}}, \\ g_{LR} &= g_{LR}^0 \, r^{2-h_\sigma-h_\varepsilon} = g_{LR}^0 \, r^{\epsilon_{LR}}. \end{aligned} \tag{4.24}$$

The following equation, represents the renormalisation of the coupling constants when a RG length rescaling of r has been performed at the 0-loops level:

$$\begin{aligned} g_{SR}^0 &\to g_{SR}^0 \, r^{\epsilon_{SR}}, \\ g_{LR}^0 &\to g_{LR}^0 \, r^{\epsilon_{LR}}. \end{aligned} \tag{4.25}$$

4.3.2 1-loop analysis

At 1-loop level, the contributions to the RG renormalisation come from the interactions between perturbative fields when these approach each other at distances smaller than the RG scale, r. In particular, the first order contributions originate from the contribution of two colliding perturbative fields.

One can proceed with the 1-loop computation. At this stage, the fast modes cannot be discarded anymore, and all terms of the form of Equation (4.20) need to be considered. In other words, the rescaling of the cutoffs in the integrals becomes crucial in the calculation.

$$(\cdots)(g_X^0)^2 \iint\limits_{|x-y|<r} d^2x\, d^2y\, (\cdots)\,, \tag{4.26}$$

In the 1-loop computation, terms involving $(g_{LR}^0)^2$ and $(g_{SR}^0)^2$ in Equation (4.12) are considered. These terms renormalise the short-range (SR) term of the action in Equation (4.8). Additionally, the term involving $g_{LR}^0\, g_{SR}^0$ in Equation (4.12) renormalises the long-range (LR) term of the action.

Due to the RG rescaling, the operators contract with each other, with $x \to y$. This allows the application of the OPE rules from Equation (4.14). From this point onwards, a shorter notation will be employed to express the operators involved, such as $\varepsilon^{(\alpha)}(x)$ becoming ε_x^α and $\sigma(x)$ becoming σ_x.

One begins by considering the first contribution to the short-range term, $\varepsilon_x^\alpha \varepsilon_x^\beta$, which renormalises the coupling g_{SR}^0, as done in [44]:

$$\begin{aligned}
&\to \frac{1}{2}\sum_{\alpha,\beta=1}^{m} (g_{LR}^0)^2 \iint\limits_{|x-y|<r} d^2x\, d^2y\, \underbrace{\sigma_x \varepsilon_x^\alpha\, \sigma_y}_{\alpha\neq\beta}\, \varepsilon_y^\beta \\
&= \frac{1}{2}\sum_{\alpha\neq\beta=1}^{m} (g_{LR}^0)^2 \int d^2x\, \varepsilon_x^\alpha \varepsilon_x^\beta\, \mathbb{1}_\infty \int\limits_{|x-y|<r} d^2y\, \mathcal{C}_{\sigma\sigma}(|x-y|) \\
&= \frac{1}{2}\sum_{\alpha\neq\beta=1}^{m} (g_{LR}^0)^2 \int d^2x\, \varepsilon_x^\alpha \varepsilon_x^\beta \int\limits_{|x-y|<r} d^2y \underbrace{|x-y|^{-2h_\sigma}}_{\text{OPE amplitude, Eq. (4.14).}} \\
&= \pi (g_{LR}^0)^2 \left(\frac{r^{2-2h_\sigma}}{2-2h_\sigma}\right) \sum_{\alpha\neq\beta=1}^{m} \int d^2x\, \varepsilon_x^\alpha \varepsilon_x^\beta \\
&= \underbrace{\pi (g_{LR}^0)^2 \left(\frac{r^{2\epsilon_{LR}-\epsilon_{SR}}}{2\epsilon_{LR}-\epsilon_{SR}}\right)}_{\text{renormalises } g_{SR}^0} \underbrace{\sum_{\alpha\neq\beta=1}^{m} \int d^2x\, \varepsilon_x^\alpha \varepsilon_x^\beta}_{\text{SR term}}\,.
\end{aligned} \tag{4.27}$$

Notice, that $\alpha \neq \beta$ in order to renormalize $\varepsilon_x^\alpha \varepsilon_x^\beta$ and not the identity, $\mathbb{1}$.

Then, one computes the second 1-loop contribution to the coupling g^0_{SR}, [44]:

$$
\begin{aligned}
&\to \frac{1}{2}\sum_{\alpha\neq\beta=1}^{m}\sum_{\gamma\neq\delta=1}^{m}(g^0_{SR})^2 \iint_{|x-y|<r} d^2x\, d^2y \underbrace{\varepsilon^\alpha_x\varepsilon^\beta_x\,\varepsilon^\gamma_y\varepsilon^\delta_y}_{\alpha=\delta,\ \beta\neq\gamma} \\
&= \frac{1}{2}\mathcal{C}_{(g^0_{SR})^2}\sum_{\beta\neq\gamma=1}^{m}(g^0_{SR})^2\int d^2x\,\varepsilon^\beta_x\varepsilon^\gamma_x\,\mathbb{1}_\infty \int_{|x-y|<r} d^2y\,\mathcal{C}_{\varepsilon\varepsilon}(|x-y|) \\
&= \frac{1}{2}\mathcal{C}_{(g^0_{SR})^2}\sum_{\beta\neq\gamma=1}^{m}(g^0_{SR})^2\int d^2x\,\varepsilon^\beta_x\varepsilon^\gamma_x \int_{|x-y|<r} d^2y \underbrace{|x-y|^{-2h_\varepsilon}}_{\text{OPE amplitude, Eq. (4.14).}} \\
&= \mathcal{C}_{(g^0_{SR})^2}\,\pi(g^0_{SR})^2\left(\frac{r^{2-2h_\varepsilon}}{2-2h_\varepsilon}\right)\sum_{\beta\neq\gamma=1}^{m}\int d^2x\,\varepsilon^\beta_x\varepsilon^\gamma_x \\
&= \underbrace{4\pi(m-2)(g^0_{SR})^2\left(\frac{r^{\epsilon_{SR}}}{\epsilon_{SR}}\right)}_{\text{renormalises } g^0_{SR}}\underbrace{\sum_{\beta\neq\gamma=1}^{m}\int d^2x\,\varepsilon^\beta_x\varepsilon^\gamma_x}_{\text{SR term}}.
\end{aligned}
\tag{4.28}
$$

The factor $\mathcal{C}_{(g^0_{SR})^2}$ arises from the requirement that certain conditions on the replica indices need to be satisfied in order to obtain the SR term. In this case, $\alpha=\delta$ is needed to ensure that two ε operators belong to the same replica and can contract when they are close to each other. Consequently, $\beta\neq\gamma$ to avoid the contraction of the other two ε operators, which would lead to the renormalisation of the identity operator. There are $\mathcal{C}_{(g^0_{SR})^2}=4(m-2)$ ways to satisfy these conditions.

Now, one considers the new and unique 1-loop contribution to the LR term, $\sigma_x \varepsilon_x^\alpha$, renormalising g^0_{LR}, which arises from:

$$
\begin{aligned}
&\to \sum_{\alpha=1}^{m} \sum_{\beta\neq\gamma=1}^{m} g^0_{LR} g^0_{SR} \iint\limits_{|x-y|<r} d^2x\, d^2y\, \sigma_x \underbrace{\varepsilon_x^\alpha \varepsilon_y^\beta}_{\alpha=\beta\neq\gamma} \varepsilon_y^\gamma \\
&= \mathcal{C}_{(g^0_{SR} g^0_{LR})} \sum_{\gamma=1}^{m} g^0_{SR} g^0_{LR} \int d^2x\, \sigma_x \varepsilon_x^\gamma\, \mathbb{1}_\infty \int\limits_{|x-y|<r} d^2y\, \mathcal{C}_{\varepsilon\varepsilon}(|x-y|) \\
&= \mathcal{C}_{(g^0_{SR} g^0_{LR})} \sum_{\gamma=1}^{m} g^0_{SR} g^0_{LR} \int d^2x\, \sigma_x \varepsilon_x^\gamma \int\limits_{|x-y|<r} d^2y \underbrace{|x-y|^{-2h_\varepsilon}}_{\text{OPE amplitude, Eq. (4.14).}} \\
&= \mathcal{C}_{(g^0_{SR} g^0_{LR})}\, \pi\, g^0_{LR} g^0_{SR} \left(\frac{r^{2-2h_\varepsilon}}{2-2h_\varepsilon}\right) \sum_{\gamma=1}^{m} \int d^2x\, \sigma_x \varepsilon_x^\gamma \\
&= \underbrace{4\pi(m-1) g^0_{LR} g^0_{SR} \left(\frac{r^{\epsilon_{SR}}}{\epsilon_{SR}}\right)}_{\text{renormalises } g^0_{LR}} \underbrace{\sum_{\gamma=1}^{m} \int d^2x\, \sigma_x \varepsilon_x^\gamma}_{\text{LR term}},
\end{aligned}
\tag{4.29}
$$

where $\mathcal{C}_{(g^0_{SR} g^0_{LR})} = 2(m-1)$.

1-loop couplings renormalisation

Resuming all the contributions, it is found:

$$
\begin{aligned}
g^0_{SR} &\to g^0_{SR}\, r^{\epsilon_{SR}} + \pi (g^0_{LR})^2 \left(\frac{r^{2\epsilon_{LR}-\epsilon_{SR}}}{2\epsilon_{LR}-\epsilon_{SR}}\right) + 4\pi(m-2)(g^0_{SR})^2 \left(\frac{r^{\epsilon_{SR}}}{\epsilon_{SR}}\right), \\
g^0_{LR} &\to g^0_{LR}\, r^{\epsilon_{LR}} + 4\pi(m-1) g^0_{LR} g^0_{SR} \left(\frac{r^{\epsilon_{SR}}}{\epsilon_{SR}}\right),
\end{aligned}
\tag{4.30}
$$

which provides the renormalized coupling constants at the 1-loop level, in the limit as $m \to 0$:

$$
\begin{aligned}
g^0_{SR} &\to g^0_{SR}\, r^{\epsilon_{SR}} + \pi (g^0_{LR})^2 \left(\frac{r^{2\epsilon_{LR}-\epsilon_{SR}}}{2\epsilon_{LR}-\epsilon_{SR}}\right) - 8\pi(g^0_{SR})^2 \left(\frac{r^{\epsilon_{SR}}}{\epsilon_{SR}}\right), \\
g^0_{LR} &\to g^0_{LR}\, r^{\epsilon_{LR}} - 4\pi g^0_{LR} g^0_{SR} \left(\frac{r^{\epsilon_{SR}}}{\epsilon_{SR}}\right),
\end{aligned}
\tag{4.31}
$$

4.3.3 2-loops analysis

The 2-loops order is of great importance when drawing conclusions from approximate RG computations. The results at this order depend on the interactions of three fields at low distances, which provide insights into the four-point correlation functions of the unperturbed conformal field theory (CFT). In CFT, the four-point correlation function contains valuable information about the theory's spectrum and structure constants, making it a central object in the bootstrap approach [39]. It is worth noting that there are cases where properties valid at the first loop order can be broken at the second loop order, highlighting the significance of the 2-loops computations. An important example of this is discussed in Section (4.5.2).

Similar to the 1-loop case, it is necessary to calculate contributions to g^0_{LR} and g^0_{SR} in the action defined in Eq.(4.8) that arise from terms involving $(g^0_{SR})^3$, $(g^0_{LR})^3$, $(g^0_{LR})^2 g^0_{SR}$, and $g^0_{LR}(g^0_{SR})^2$ in the expansion of Eq.(4.12). These contributions can be computed in the following form:

$$(\cdots)(g^0_X)^3 \iint\limits_{|x-y|,|y-z|<r} d^2x\, d^2y\, (\cdots)\,. \tag{4.32}$$

To maintain a lighter manuscript, the notation will be simplified as much as possible. For instance, the identity operators will be implied. It is important to note that the operators are interacting within the same RG block, meaning that, after the rescaling process one has: $x \to y \to z$.

The contributions arising at the 2-loop order can be expressed in terms of the following four integrals:

$$\begin{aligned}
&(i)\ \frac{(g^0_{SR})^3}{6} \sum_{\alpha\neq\beta=1}^{m}\sum_{\gamma\neq\delta=1}^{m}\sum_{\eta\neq\phi=1}^{m} \iint\limits_{|x-y|,|y-z|<r} d^2x\, d^2y\, d^2z\, \varepsilon^\alpha_x\varepsilon^\beta_x\, \varepsilon^\gamma_y\varepsilon^\delta_y\, \varepsilon^\eta_z\varepsilon^\phi_z.\\
&(ii)\ \frac{g^0_{SR}(g^0_{LR})^2}{2} \sum_{\alpha=1}^{m}\sum_{\beta=1}^{m}\sum_{\gamma\neq\delta=1}^{m} \iint\limits_{|x-y|,|y-z|<r} d^2x\, d^2y\, d^2z\, \sigma_x\varepsilon^\alpha_x\, \sigma_y\varepsilon^\beta_y\, \varepsilon^\gamma_z\varepsilon^\delta.\\
&(iii)\ \frac{(g^0_{LR})^3}{6} \sum_{\alpha=1}^{m}\sum_{\beta=1}^{m}\sum_{\gamma=1}^{m} \iint\limits_{|x-y|,|y-z|<r} d^2x\, d^2y\, d^2z\, \sigma_x\varepsilon^\alpha_x\, \sigma_y\varepsilon^\beta_y\, \sigma_z\varepsilon^\gamma_z.\\
&(iv)\ \frac{(g^0_{SR})^2 g^0_{LR}}{2} \sum_{\alpha\neq\beta=1}^{m}\sum_{\gamma\neq\delta=1}^{m}\sum_{\eta=1}^{m} \iint\limits_{|x-y|,|y-z|<r} d^2x\, d^2y\, d^2z\, \varepsilon^\alpha_x\varepsilon^\beta_x\, \varepsilon^\gamma_x\varepsilon^\delta_x\, \sigma_z\varepsilon^\eta_z\,.
\end{aligned} \tag{4.33}$$

The subsequent integrals are computed using Dotsenko's approach [44,169]. Specifically, these integrals are assessed as an ϵ-expansion, and non-singular or regular terms are disregarded as they do not influence the universal critical exponents.

Starting from the (i) contribution:

$$
\begin{aligned}
&\to \frac{(g^0_{SR})^3}{6} \sum_{\alpha\neq\beta=1}^{m} \sum_{\gamma\neq\delta=1}^{m} \sum_{\eta\neq\phi=1}^{m} \iiint_{|x-y|,|y-z|<r} d^2x\, d^2y\, d^2z\, \varepsilon_x^{\alpha} \overbrace{\varepsilon_x^{\beta}}^{\beta=\gamma\neq\alpha,\phi} \underbrace{\varepsilon_y^{\gamma} \varepsilon_y^{\delta}}_{\delta=\eta\neq\alpha,\phi} \varepsilon_z^{\eta} \varepsilon_z^{\phi} \\
&= (g^0_{SR})^3 \sum_{\alpha\neq\phi=1}^{m} \int d^2x\, \varepsilon_x^{\alpha}\varepsilon_x^{\phi} \frac{\mathcal{C}'_{g^3_{SR}}}{6} \int_{|x-y|,|y-z|<r} d^2y\, d^2z\, \mathcal{C}_{\varepsilon\varepsilon}(|x-y|)\mathcal{C}_{\varepsilon\varepsilon}(|y-z|) \\
&= (g^0_{SR})^3 \sum_{\alpha\neq\phi=1}^{m} \int d^2x\, \varepsilon_x^{\alpha}\varepsilon_x^{\phi} \underbrace{\frac{\mathcal{C}'_{g^3_{SR}}}{6} \int_{|x-y|,|y-z|<r} d^2y\, d^2z\, |x-y|^{-2h_\varepsilon} |y-z|^{-2h_\varepsilon}}_{\mathcal{I}'_{g^3_{SR}}} \qquad (4.34) \\
&= \underbrace{(g^0_{SR})^3 \mathcal{I}'_{g^3_{SR}}}_{\text{renormalises } g^0_{SR}} \underbrace{\sum_{\alpha\neq\phi=1}^{m} \int d^2x\, \varepsilon_x^{\alpha}\varepsilon_x^{\phi}}_{\text{SR term}},
\end{aligned}
$$

where the combinatorial factor and the integral are given by:

$$
\begin{aligned}
\mathcal{C}'_{g^3_{SR}} &= 3\cdot 2\cdot 2\cdot 2(m-2)(m-3) = 24(m-2)(m-3) \qquad (4.35) \\
\mathcal{I}'_{g^3_{SR}} &= \frac{\mathcal{C}'_{g^3_{SR}}}{6} \int_{|x-y|,|y-z|<r} d^2y\, d^2z\, |x-y|^{-2h_\varepsilon} |y-z|^{-2h_\varepsilon} = 16\pi^2(m-2)(m-3)\, \frac{r^{2\epsilon_{SR}}}{\epsilon^2_{SR}},
\end{aligned}
$$

as previously done in [44].

The result of $\mathcal{I}'_{g^3_{SR}}$ is obtained through a simple change of variables and the application of the formula:

$$
\int d^2y\, |y|^{2a}\, |1-y|^{2b} = \pi \frac{\Gamma(1+a)\,\Gamma(1+b)\,\Gamma(-1-a-b)}{\Gamma(-a)\,\Gamma(-b)\,\Gamma(2+a+b)}. \qquad (4.36)
$$

This formula is commonly used in such computations. For a more detailed explanation, the interested reader is referred to [169].

There is another contribution to the SR term, but coming from a different contraction:

$$\to \frac{(g^0_{SR})^3}{6}\sum_{\alpha\neq\beta=1}^{m}\sum_{\gamma\neq\delta=1}^{m}\sum_{\eta\neq\phi=1}^{m}\iiint_{|x-y|,|y-z|<r} d^2x\; d^2y\, d^2z\, \varepsilon_x^{\overbrace{\alpha}^{\alpha=\gamma,\,\beta=\delta,\atop \alpha,\beta\neq\phi}}\varepsilon_x^{\beta}\,\varepsilon_y^{\gamma}\underbrace{\varepsilon_y^{\delta}\,\varepsilon_z^{\eta}}_{\gamma=\eta\neq\phi}\varepsilon_z^{\phi} \tag{4.37}$$

$$= (g^0_{SR})^3\sum_{\alpha\neq\phi=1}^{m}\int d^2x\,\varepsilon_x^{\alpha}\varepsilon_x^{\phi}\,\frac{\mathcal{C}''_{g^3_{SR}}}{6}\int_{|x-y|,|y-z|<r} d^2y\, d^2z\,\mathcal{C}_{\varepsilon\varepsilon\varepsilon}(|x-y|,|y-z|)\mathcal{C}_{\varepsilon\varepsilon}(|x-y|)$$

$$= (g^0_{SR})^3\sum_{\alpha\neq\phi=1}^{m}\int d^2x\,\varepsilon_x^{\alpha}\varepsilon_x^{\phi}\underbrace{\frac{\mathcal{C}''_{g^3_{SR}}}{6}\int_{|x-y|,|y-z|<r} d^2y\, d^2z\,\langle\,\varepsilon_x\varepsilon_y\varepsilon_z\varepsilon_\infty\,\rangle|y-z|^{-2h_\varepsilon}}_{\mathcal{I}''_{g^3_{SR}}}$$

$$= \underbrace{(g^0_{SR})^3\mathcal{I}''_{g^3_{SR}}}_{\text{renormalises } g^0_{SR}}\underbrace{\sum_{\alpha\neq\phi=1}^{m}\int d^2x\,\varepsilon_x^{\alpha}\varepsilon_x^{\phi}}_{\text{SR term}},$$

where the combinatorial factor and the integral are given by:

$$\mathcal{C}''_{g^3_{SR}} = 3\cdot 2\cdot 2\cdot 2(m-2) = 24(m-2) \tag{4.38}$$

$$\mathcal{I}''_{g^3_{SR}} = \frac{\mathcal{C}''_{g^3_{SR}}}{6}\int_{|x-y|,|y-z|<r} d^2y\, d^2z\,\langle\,\varepsilon_x\varepsilon_y\varepsilon_z\varepsilon_\infty\,\rangle|y-z|^{-2h_\varepsilon} = 4(m-2)\left(4\pi^2\,\frac{r^{2\epsilon_{SR}}}{\epsilon^2_{SR}} - 2\pi^2\,\frac{r^{2\epsilon_{SR}}}{\epsilon_{SR}}\right)$$

$$= 8\pi^2(m-2)\frac{r^{2\epsilon_{SR}}}{\epsilon^2_{SR}}\,(2-\epsilon_{SR})\,.$$

The computation of the integral $\mathcal{I}''_{g^3_{SR}}$ is quite technical. Fortunately, in the appendix of [44], the same integral is computed using a Coulomb-gas representation [169–172]. Additionally, a similar integral is computed in [8] for the renormalisation of LR terms, which will be extensively discussed in this thesis. For a more detailed explanation, the interested reader is referred to Eq. (4.42) in the thesis.

Now, the (ii) integral:

$$
\begin{aligned}
&\to \frac{g_{SR}^0 (g_{LR}^0)^2}{2} \sum_{\alpha=1}^{m} \sum_{\beta=1}^{m} \sum_{\gamma\neq\delta=1}^{m} \iiint_{|x-y|,|y-z|<r} d^2x\, d^2y\, d^2z\, \sigma_x \overbrace{\varepsilon_x^{\alpha}}^{\alpha\neq\beta,\delta} \sigma_y \underbrace{\varepsilon_y^{\beta}\, \varepsilon_z^{\gamma}}_{\beta=\gamma} \varepsilon_z^{\delta} \qquad (4.39)\\
&= g_{SR}^0 (g_{LR}^0)^2 \sum_{\alpha\neq\delta=1}^{m} \int d^2x\, \varepsilon_x^{\alpha}\varepsilon_x^{\delta} \frac{\mathcal{C}'_{g_{SR}\, g_{LR}^2}}{2} \int_{|x-y|,|y-z|<r} d^2y\, d^2z\, \mathcal{C}_{\sigma\sigma}(|x-y|)\mathcal{C}_{\varepsilon\varepsilon}(|y-z|)\\
&= g_{SR}^0 (g_{LR}^0)^2 \sum_{\alpha\neq\delta=1}^{m} \int d^2x\, \varepsilon_x^{\alpha}\varepsilon_x^{\delta} \underbrace{\frac{\mathcal{C}'_{g_{SR}\, g_{LR}^2}}{2} \int_{|x-y|,|y-z|<r} d^2y\, d^2z\, |x-y|^{-2h_\sigma} |y-z|^{-2h_\varepsilon}}_{\mathcal{I}'_{g_{SR}\, g_{LR}^2}}\\
&= \underbrace{g_{SR}^0 (g_{LR}^0)^2 \mathcal{I}'_{g_{SR}\, g_{LR}^2}}_{\text{renormalises } g_{SR}^0} \underbrace{\sum_{\alpha\neq\delta=1}^{m} \int d^2x\, \varepsilon_x^{\alpha}\varepsilon_x^{\delta}}_{\text{SR term}},
\end{aligned}
$$

where the combinatorial factor and the integral are given by:

$$
\begin{aligned}
&\mathcal{C}'_{g_{SR}\, g_{LR}^2} = 2\cdot 2(m-2) = 4(m-2) \qquad (4.40)\\
&\mathcal{I}'_{g_{SR}\, g_{LR}^2} = \frac{\mathcal{C}'_{g_{SR} g_{LR}}}{2} \int_{|x-y|,|y-z|<r} d^2y\, d^2z\, |x-y|^{-2h_\sigma}\, |y-z|^{-2h_\varepsilon} = 8\pi^2\,(m-2)\, \frac{r^{2\epsilon_{LR}}}{\epsilon_{SR}(2\epsilon_{LR}-\epsilon_{SR})}.
\end{aligned}
$$

In [8], this integral is computed using the method developed in [44]. The integral is solved using Eq. (4.36), following a similar formal approach as in Eq. (4.34). The unique difference lies in the exponent of the $|x-y|$ term, which does not modify the computation scheme.

Still, there is another contribution coming from the same (ii) integral, but with a different contraction:

$$
\begin{aligned}
&\to \frac{g^0_{SR}(g^0_{LR})^2}{2}\sum_{\alpha=1}^{m}\sum_{\beta=1}^{m}\sum_{\gamma\neq\delta=1}^{m}\iiint_{|x-y|,|y-z|<r} d^2x\; d^2y\, d^2z\, \sigma_x \overbrace{\varepsilon^{\alpha}_x\, \sigma_y}^{\alpha=\beta\neq\delta}\underbrace{\varepsilon^{\beta}_y\, \varepsilon^{\gamma}_z}_{\beta=\gamma\neq\delta}\varepsilon^{\delta}_z \qquad (4.41)\\
&= g^0_{SR}(g^0_{LR})^2\sum_{\alpha\neq\delta=1}^{m}\int d^2x\, \varepsilon^{\alpha}_x\varepsilon^{\delta}_x \frac{\mathcal{C}''_{g_{SR}g^2_{LR}}}{2}\iint_{|x-y|,|y-z|<r} d^2y\, d^2z\, \mathcal{C}_{\varepsilon\varepsilon\varepsilon}(|x-y|,|y-z|)\mathcal{C}_{\sigma\sigma}(|x-y|)\\
&= g^0_{SR}(g^0_{LR})^2\sum_{\alpha\neq\delta=1}^{m}\int d^2x\, \varepsilon^{\alpha}_x\varepsilon^{\delta}_x \underbrace{\frac{\mathcal{C}''_{g_{SR}g^2_{LR}}}{2}\iint_{|x-y|,|y-z|<r} d^2y\, d^2z\, \langle\, \varepsilon_x\varepsilon_y\varepsilon_z\varepsilon_\infty\,\rangle |x-y|^{-2h_\sigma}}_{\mathcal{I}''_{g_{SR}\,g^2_{LR}}}\\
&= \underbrace{g^0_{SR}(g^0_{LR})^2\mathcal{I}''_{g_{SR}g^2_{LR}}}_{\text{renormalises } g^0_{SR}}\underbrace{\sum_{\alpha\neq\delta=1}^{m}\int d^2x\, \varepsilon^{\alpha}_x\varepsilon^{\delta}_x}_{\text{SR term}},
\end{aligned}
$$

where the combinatorial factor and the integral are given by:

$$
\begin{aligned}
\mathcal{C}''_{g_{SR}g^2_{LR}} &= 2\\
\mathcal{I}''_{g_{SR}g^2_{LR}} &= \frac{\mathcal{C}''_{g_{SR}g^2_{LR}}}{2}\iint_{|x-y|,|y-z|<r} d^2y\, d^2z\, \langle\, \varepsilon_x\varepsilon_y\varepsilon_z\varepsilon_\infty\,\rangle\, |x-y|^{-2h_\sigma}\\
&= \pi^2\left[\frac{8}{\epsilon_{SR}} + \underbrace{\frac{16\pi}{3\sqrt{3}}\frac{\epsilon_{LR}-\epsilon_{SR}}{2\epsilon_{LR}-\epsilon_{SR}} - \frac{4\epsilon_{SR}}{2\epsilon_{LR}-\epsilon_{SR}}}_{\mathcal{B}(\epsilon_{LR},\epsilon_{SR})}\right]\frac{r^{2\epsilon_{LR}}}{2\epsilon_{LR}}\\
&= \pi^2\left[\frac{8}{\epsilon_{SR}} + \mathcal{B}(\epsilon_{LR},\epsilon_{SR})\right]\frac{r^{2\epsilon_{LR}}}{2\epsilon_{LR}},
\end{aligned}
\qquad (4.42)
$$

computed in, [8], following the method developed in [44].

One can rewrite the term $\mathcal{B}(\epsilon_{LR},\epsilon_{SR})$ just in function of the ration s, getting:

$$
\begin{aligned}
\mathcal{B} &= \left[\frac{16\pi}{3\sqrt{3}}\frac{\epsilon_{LR}-\epsilon_{SR}}{(2\epsilon_{LR}-\epsilon_{SR})} - \frac{4\epsilon_{SR}}{2\epsilon_{LR}-\epsilon_{SR}}\right]\\
&= \frac{16\pi}{3\sqrt{3}}\frac{(1-s)}{(2-s)} - \frac{4s}{(2-s)}.
\end{aligned}
\qquad (4.43)
$$

In particular, to compute $\mathcal{I}''_{g_{SR}g_{LR}^2}$, one uses a Coulomb-gas representation [169–172] of the four-point Potts correlation function:

$$\langle\varepsilon(0)\varepsilon(1)\varepsilon(y)\varepsilon(\infty)\rangle = -\frac{2\Gamma\left[-\frac{2}{3}\right]^2}{\sqrt{3}\Gamma\left[-\frac{1}{3}\right]^4}|y|^{(\epsilon_{SR}-2)}|y-1|^{(\frac{4}{3}-\frac{\epsilon_{SR}}{3})}\times \\ \times\int d^2u|u|^{(4-2\epsilon_{SR})}|u-1|^{(-\frac{8}{3}+\frac{2\epsilon_{SR}}{3})}|u-y|^{-\frac{8}{3}+\frac{2\epsilon_{SR}}{3}}. \tag{4.44}$$

The operators are positioned at $\{0, 1, y \text{ and } \infty\}$, with a change of variable to simplify the computation. The goal is to evaluate the multi-complex integral, similar to the procedure outlined in Appendix D of [44]. The only distinction lies in the exponent of the $|y-1|$ term:

$$\mathcal{I}''_{g_{SR}g_{LR}^2} \to 2\pi\int d|z||z|^{-1+2\epsilon_{LR}}\int d^2y|y|^{-2+\epsilon_{SR}}|1-y|^{-\frac{2}{3}-\frac{4}{3}\epsilon_{SR}+2\epsilon_{LR}}\times \\ \times\int d^2u|u|^{4-2\epsilon_{SR}}|u-1|^{-\frac{8}{3}+\frac{2}{3}\epsilon_{SR}}|u-z|^{-\frac{8}{3}+\frac{2}{3}\epsilon_{SR}}, \tag{4.45}$$

and getting Eq. (4.42).

One is left with the last integrals which renormalise g^0_{LR}, starting from (iii), one has:

$$\to \frac{(g^0_{LR})^3}{6}\sum_{\alpha=1}^{m}\sum_{\beta=1}^{m}\sum_{\gamma=1}^{m}\iiint_{|x-y|,|y-z|<r} d^2x\; d^2y\, d^2z\,\sigma_x\overbrace{\varepsilon_x^{\alpha}\,\sigma_y}^{\alpha=\beta}\underbrace{\varepsilon_y^{\beta}\,\sigma_z\varepsilon_z^{\gamma}}_{\beta=\gamma} \tag{4.46}$$

$$= (g^0_{LR})^3\sum_{\alpha=1}^{m}\int d^2x\,\sigma_x\varepsilon_x^{\alpha}\,\frac{\mathcal{C}'_{g^3_{LR}}}{6}\int_{|x-y|,|y-z|<r} d^2y\,d^2z\,\mathcal{C}_{\varepsilon\varepsilon\varepsilon}(|x-y|,(|y-z|))\mathcal{C}_{\sigma\sigma\sigma}(|x-y|,(|y-z|))$$

$$= (g^0_{LR})^3\sum_{\alpha=1}^{m}\int d^2x\,\sigma_x\varepsilon_x^{\alpha}\underbrace{\frac{\mathcal{C}'_{g^3_{LR}}}{6}\int_{|x-y|,|y-z|<r} d^2y\,d^2z\,\langle\,\varepsilon_x\varepsilon_y\varepsilon_z\varepsilon_\infty\,\rangle\,\mathbb{E}\left[\sigma_x\sigma_y\sigma_z\sigma_\infty\right]}_{\mathcal{I}'_{g^3_{LR}}}$$

$$= \underbrace{(g^0_{LR})^3\mathcal{I}'_{g^3_{LR}}}_{\text{renormalises } g^0_{LR}}\underbrace{\sum_{\alpha=1}^{m}\int d^2x\,\sigma_x\varepsilon_x^{\alpha}}_{\text{LR term}},$$

where the combinatorial factor and the integral are given by:

$$\begin{aligned}\mathcal{C}'_{g^3_{LR}} &= 1\\ \mathcal{I}'_{g^3_{LR}} &= \frac{1}{6}\int\limits_{|x-y|,|y-z|<r} d^2y\, d^2z\, \langle\, \varepsilon_x\varepsilon_y\varepsilon_z\varepsilon_\infty \,\rangle\, \mathbb{E}\left[\sigma_x\sigma_y\sigma_z\sigma_\infty\right].\end{aligned} \tag{4.47}$$

This integral is computed in [8]. Specifically, when evaluating this integral, it is necessary to specify the fourth cumulant of the disorder distribution. The computation for this contribution has been carried out for both a Gaussian disorder distribution and another specific non-Gaussian distribution. In the case of the non-Gaussian distribution, the auxiliary spins are once again described by Potts energies, denoted as ε. This explicit computation will be presented in Sec. (4.3.4).

There is another contribution to the LR term, but coming from a different contraction:

$$\begin{aligned}&\to \frac{(g^0_{LR})^3}{6}\sum_{\alpha=1}^{m}\sum_{\beta=1}^{m}\sum_{\gamma=1}^{m}\iiint\limits_{|x-y|,|y-z|<r} d^2x\; d^2y\, d^2z\, \sigma_x \overbrace{\varepsilon^\alpha_x\, \sigma_y \varepsilon^\beta_y}^{\alpha\neq\beta}\, \underbrace{\sigma_z \varepsilon^\gamma_z}_{\beta=\gamma\neq\alpha} \qquad (4.48)\\
&= (g^0_{LR})^3\sum_{\alpha=1}^{m}\int d^2x\, \sigma_x\varepsilon^\alpha_x \frac{\mathcal{C}''_{g^3_{LR}}}{6}\int\limits_{|x-y|,|y-z|<r} d^2y\, d^2z\, \mathcal{C}_{\sigma\sigma\sigma}(|x-y|,(|y-z|))\mathcal{C}_{\varepsilon\varepsilon}(|y-z|)\\
&= (g^0_{LR})^3\sum_{\alpha=1}^{m}\int d^2x\, \sigma_x\varepsilon^\alpha_x \underbrace{\frac{\mathcal{C}''_{g^3_{LR}}}{6}\int\limits_{|x-y|,|y-z|<r} d^2y\, d^2z\, \mathbb{E}\left[\sigma_x\sigma_y\sigma_z\sigma_\infty\right]\, |y-z|^{-2h_\varepsilon}}_{\mathcal{I}''_{g^3_{LR}}}\\
&= \underbrace{(g^0_{LR})^3\mathcal{I}''_{g^3_{LR}}}_{\text{renormalises } g^0_{LR}}\underbrace{\sum_{\alpha=1}^{m}\int d^2x\, \sigma_x\varepsilon^\alpha_x}_{\text{LR term}},\end{aligned}$$

where the combinatorial factor and the integral are given by:

$$\begin{aligned}\mathcal{C}''_{g^3_{LR}} &= 3(m-1)\\ \mathcal{I}''_{g^3_{LR}} &= \frac{\mathcal{C}''_{g^3_{LR}}}{6}\int\limits_{|x-y|,|y-z|<r} d^2y\, d^2z\, \mathbb{E}\left[\sigma_x\sigma_y\sigma_z\sigma_\infty\right]\, |y-z|^{-2h_\varepsilon}.\end{aligned} \tag{4.49}$$

Again, this integral is computed in [8]. In particular, in the computation is necessary to specify the fourth cumulant of the disorder distribution, see Sec. (4.3.4).

The last integral that renormalizes g^0_{LR} is (iv):

$$
\begin{aligned}
&\to \frac{(g^0_{SR})^2 g^0_{LR}}{2} \sum_{\alpha\neq\beta=1}^{m} \sum_{\gamma\neq\delta=1}^{m} \sum_{\eta=1}^{m} \iiint_{|x-y|,|y-z|<r} d^2x\; d^2y\, d^2z\, \varepsilon_x^{\alpha} \overbrace{\varepsilon_x^{\beta}\, \varepsilon_y^{\gamma}}^{\substack{\beta=\gamma \\ \alpha\neq\gamma,\delta}} \underbrace{\varepsilon_y^{\delta}\, \sigma_z \varepsilon_z^{\eta}}_{\delta=\eta} \qquad (4.50)\\
&= (g^0_{SR})^2 g^0_{LR} \sum_{\alpha=1}^{m} \int d^2x\, \sigma_x \varepsilon_x^{\alpha} \frac{\mathcal{C}'_{g^2_{SR} g_{LR}}}{2} \int_{|x-y|,|y-z|<r} d^2y\, d^2z\, \mathcal{C}_{\varepsilon\varepsilon}(|x-y|)\mathcal{C}_{\varepsilon\varepsilon}(|y-z|)\\
&= (g^0_{SR})^2 g^0_{LR} \sum_{\alpha=1}^{m} \int d^2x\, \sigma_x \varepsilon_x^{\alpha} \underbrace{\frac{\mathcal{C}'_{g^2_{SR} g_{LR}}}{2} \int_{|x-y|,|y-z|<r} d^2y\, d^2z\, |x-y|^{-2h_\varepsilon} |y-z|^{-2h_\varepsilon}}_{\mathcal{I}'_{g^2_{SR}\, g_{LR}}}\\
&= \underbrace{(g^0_{SR})^2 g^0_{LR}\, \mathcal{I}'_{g^2_{SR} g_{LR}}}_{\text{renormalises } g^0_{LR}} \underbrace{\sum_{\alpha=1}^{m} \int d^2x\, \sigma_x \varepsilon_x^{\alpha}}_{\text{LR term}}\,.
\end{aligned}
$$

One can note that $\mathcal{I}'_{g^2_{SR} g_{LR}}$ is essentially equal to $\mathcal{I}'_{g^3_{SR}}$, up to a constant term. The computation of $\mathcal{I}'_{g^3_{SR}}$ has already been performed and presented in Eq. (4.35)

Thus:

$$
\begin{aligned}
&\mathcal{C}'_{g^2_{SR} g_{LR}} = 2 \cdot 2 \cdot 2(m-2)(m-1) = 8(m-2)(m-1) \qquad (4.51)\\
&\mathcal{I}'_{g^2_{SR} g_{LR}} = \frac{\mathcal{C}'_{g^2_{SR} g_{LR}}}{2} \int_{|x-y|,|y-z|<r} d^2y\, d^2z\, |x-y|^{-2h_\varepsilon} |y-z|^{-2h_\varepsilon} = 16\pi^2 (m-2)(m-1)\, \frac{r^{2\epsilon_{SR}}}{\epsilon^2_{SR}}.
\end{aligned}
$$

The last contribution to g^0_{LR} comes from the same integral (iv) as mentioned earlier, but with a different contraction:

$$
\begin{aligned}
&\to \frac{(g^0_{SR})^2 g^0_{LR}}{2} \sum_{\alpha\neq\beta=1}^{m} \sum_{\gamma\neq\delta=1}^{m} \sum_{\eta=1}^{m} \iiint_{|x-y|,|y-z|<r} d^2x\, d^2y\, d^2z\, \varepsilon^{\alpha}_x \overbrace{\varepsilon^{\beta}_x\, \varepsilon^{\gamma}_y}^{\alpha=\delta,\,\beta=\gamma} \underbrace{\varepsilon^{\delta}_y\, \sigma_z \varepsilon^{\eta}_z}_{\delta=\eta} \qquad (4.52)\\
&= (g^0_{SR})^2 g^0_{LR} \sum_{\alpha=1}^{m} \int d^2x\, \sigma_x \varepsilon^{\alpha}_x \frac{\mathcal{C}''_{g^2_{SR}g_{LR}}}{2} \int_{|x-y|,|y-z|<r} d^2y\, d^2z\, \mathcal{C}_{\varepsilon\varepsilon\varepsilon}(|x-y|,|y-z|)\mathcal{C}_{\varepsilon\varepsilon}(|y-z|)\\
&= (g^0_{SR})^2 g^0_{LR} \sum_{\alpha=1}^{m} \int d^2x\, \sigma_x \varepsilon^{\alpha}_x \underbrace{\frac{\mathcal{C}''_{g^2_{SR}g_{LR}}}{2} \int_{|x-y|,|y-z|<r} d^2y\, d^2z\, \langle\, \varepsilon_x\varepsilon_y\varepsilon_z\varepsilon_\infty \,\rangle |y-z|^{-2h_\varepsilon}}_{\mathcal{I}''_{g^2_{SR}g_{LR}}}.\\
&= \underbrace{(g^0_{SR})^2 g^0_{LR} \mathcal{I}''_{g^2_{SR}g_{LR}}}_{\text{renormalises } g^0_{LR}} \underbrace{\sum_{\alpha=1}^{m} \int d^2x\, \sigma_x \varepsilon^{\alpha}_x}_{\text{LR term}}
\end{aligned}
$$

As before, one has that $\mathcal{I}''_{g^2_{SR}g_{LR}}$ is essentially equal to $\mathcal{I}''_{g^3_{SR}}$, apart from a constant term. The computation of $\mathcal{I}''_{g^3_{SR}}$ has already been performed and presented in Eq. (4.38), thus one has:

$$
\begin{aligned}
\mathcal{C}''_{g^2_{SR}g_{LR}} &= 2\cdot 2(m-1) = 4(m-1)\\
\mathcal{I}''_{g^2_{SR}g_{LR}} &= \frac{\mathcal{C}''_{g^2_{SR}g_{LR}}}{2} \int_{|x-y|,|y-z|<r} d^2y\, d^2z\, \langle\, \varepsilon_x\varepsilon_y\varepsilon_z\varepsilon_\infty \,\rangle |y-z|^{-2h_\varepsilon}\\
&= 4\pi^2(m-1)\,(2-\epsilon_{SR})\,\frac{r^{2\epsilon_{SR}}}{\epsilon^2_{SR}}.
\end{aligned} \qquad (4.53)
$$

4.3.4 Computation of $\mathcal{I}_{dis}$: Gaussian and non-Gaussian disorders

The computation of $\mathcal{I}^{dis} = \mathcal{I}'_{g^3_{LR}} + \mathcal{I}''_{g^3_{LR}}$ can now be performed. The result is dependent on the fourth cumulant of the disorder distribution, as mentioned earlier. The Gaussian and a non-Gaussian cases will be distinguished.

As non-Gaussian disorder ($dis = \mathcal{NG}$), it will be considered a disorder made by Potts energies, different from the m replicas, as auxiliary variables *i.e.*

$$\text{non-Gaussian disorder instance: } \{\sigma \to \varepsilon,\, \epsilon_{LR} \to \epsilon_{SR},\, a = 2 - \epsilon_{SR}\}, \tag{4.54}$$

yielding:

$$\begin{aligned}
\mathcal{I}^{\mathcal{NG}} = \underbrace{\frac{1}{6} \int_{|x-y|,|y-z|<r} d^2y\, d^2z\, \langle\, \varepsilon_x \varepsilon_y \varepsilon_z \varepsilon_\infty \,\rangle^2}_{0\text{, since does not contains singularities, [44].}} + \\
\underbrace{-\frac{1}{2} \int_{|x-y|,|y-z|<r} d^2y\, d^2z\, \langle\, \varepsilon_x \varepsilon_y \varepsilon_z \varepsilon_\infty \,\rangle\, |y-z|^{-2h_\varepsilon}}_{\propto \mathcal{I}''_{g_{SR}\, g^2_{LR}} \text{ or } \mathcal{I}''_{g^3_{SR}}} \\
= \pi^2 \left(2 - \frac{4}{\epsilon_{SR}}\right) \left(\frac{r^{2\epsilon_{SR}}}{2\epsilon_{SR}}\right).
\end{aligned} \tag{4.55}$$

This particular non-Gaussian instance, has been choosed in order to make the computations easily done by following [44].

Now, one can consider a Gaussian disorder ($dis = \mathcal{G}$) distribution that satisfies Eq. (4.11). As in [148], the corresponding action $\mathcal{S}^{\text{aux}}$ is represented in terms of the non-local laplacian $\left(-\partial^2\right)^{(2-a)/2}$ [132, 173]. In particular one can take:

$$\sigma(x) = \sigma_x, \quad \mathcal{S}^{\text{aux}} = \int d^2x\, \sigma_x \left(-\partial^2\right)^{\frac{2-a}{2}} \sigma_x. \tag{4.56}$$

In this case, one can use Wick's theorem, for which:

$$\begin{aligned}
\mathbb{E}\left[\sigma_x\sigma_y\sigma_z\sigma_\infty\right] &= \mathbb{E}\left[\sigma_x\sigma_y\right] \underbrace{\mathbb{E}\left[\cancel{\sigma_z\sigma_\infty}\right]}_{1} + \mathbb{E}\left[\sigma_x\sigma_z\right] \underbrace{\mathbb{E}\left[\cancel{\sigma_y\sigma_\infty}\right]}_{1} + \underbrace{\mathbb{E}\left[\cancel{\sigma_x\sigma_\infty}\right]}_{1} \mathbb{E}\left[\sigma_y\sigma_z\right] \\
&= \mathbb{E}\left[\sigma_x\sigma_y\right] + \mathbb{E}\left[\sigma_x\sigma_z\right] + \mathbb{E}\left[\sigma_y\sigma_z\right].
\end{aligned} \tag{4.57}$$

One gets:

$$
\begin{aligned}
\mathcal{I}^{\mathcal{G}} &= \frac{1}{6}\int\limits_{|x-y|,|y-z|<r} d^2y\, d^2z\, \langle\, \varepsilon_x\varepsilon_y\varepsilon_z\varepsilon_\infty \,\rangle\, \mathbb{E}\left[\sigma_x\sigma_y\sigma_z\sigma_\infty\right] + \\
&- \frac{1}{2}\int\limits_{|x-y|,|y-z|<r} d^2y\, d^2z\, \mathbb{E}\left[\sigma_x\sigma_y\sigma_z\sigma_\infty\right]\, |y-z|^{-2h_\varepsilon} \\
&= \frac{3}{6}\int\limits_{|x-y|,|y-z|<r} d^2y\, d^2z\, \langle\, \varepsilon_x\varepsilon_y\varepsilon_z\varepsilon_\infty \,\rangle\, |x-y|^{-2h_\sigma} + \\
&- \frac{2}{2}\int\limits_{|x-y|,|y-z|<r} d^2y\, d^2z\, \mathbb{E}\left[\sigma_x\sigma_y\right]\, |y-z|^{-2h_\varepsilon} + \\
&\underbrace{-\frac{1}{2}\int\limits_{|x-y|,|y-z|<r} d^2y\, d^2z\, |y-z|^{-2h_\sigma-2h_\varepsilon}}_{0,\text{ since does not contains singularities, [44].}} \\
&= \underbrace{\frac{1}{2}\int\limits_{|x-y|,|y-z|<r} d^2y\, d^2z\, \langle\, \varepsilon_x\varepsilon_y\varepsilon_z\varepsilon_\infty \,\rangle\, |x-y|^{-2h_\sigma}}_{\propto \mathcal{I}'_{g_{SR}\, g^2_{LR}}} + \\
&\underbrace{-\int\limits_{|x-y|,|y-z|<r} d^2y\, d^2z\, |x-y|^{-2h_\sigma}\, |y-z|^{-2h_\varepsilon}}_{\propto \mathcal{I}'_{g_{SR}\, g^2_{LR})}} \\
&= \frac{\pi^2}{2}\left(\frac{8}{\epsilon_{SR}} + \mathcal{B}(\epsilon_{LR},\epsilon_{SR})\right)\frac{r^{2\epsilon_{LR}}}{2\epsilon_{LR}} - 4\pi^2\,\frac{r^{2\epsilon_{LR}}}{\epsilon_{SR}(2\epsilon_{LR}-\epsilon_{SR})} \\
&= \pi^2\left(\frac{\mathcal{B}(\epsilon_{LR},\epsilon_{SR})}{2} - \frac{4}{2\epsilon_{LR}-\epsilon_{SR}}\right)\left(\frac{r^{2\epsilon_{LR}}}{2\epsilon_{LR}}\right).
\end{aligned}
\tag{4.58}
$$

So, summarising the results of $\mathcal{I}^{dis}$ in this way:

$$
\mathcal{I}^{dis} = \pi^2\left(\mathcal{C}^{dis} - \frac{4}{2\epsilon_{LR}-\epsilon_{SR}}\right)\left(\frac{r^{2\epsilon_{LR}}}{2\epsilon_{LR}}\right). \tag{4.59}
$$

with:

$$
\mathcal{C}^{dis} = \begin{cases} \mathcal{B}(s)/2, \text{ for a } \mathcal{G} \text{ disorder,} \\ 2 = -\mathcal{B}(\epsilon_{SR},\epsilon_{SR})/2 = -\mathcal{B}(s=1)/2, \text{ in this particular } \mathcal{NG} \text{ case .} \end{cases} \tag{4.60}
$$

In both cases, one observes that the renormalisability of the theory, in particular the fact that the divergences of type ϵ_{SR}^{-2} or ϵ_{LR}^{-2} are absorbed in the definition of the renormalized couplings, is broken for $m \neq 0$ by the above term. The renormalisability is however re-established in the limit $m \to 0$. This phenomena is also discussed in [148]. Analogously to their observations, it is expected that there should be additional counterterms that cancel in the limit $m \to 0$. As the interest is on the disordered limit $m \to 0$, the renormalisability in this limit is enough. This is satisfied when $\mathcal{C}^{dis}$ takes the form of Eq. (4.60).

It is important to notice that, in the $\mathcal{NG}$ case, one has:

$$\mathcal{B}(\epsilon_{LR} \to \epsilon_{SR}, \epsilon_{SR}) = \mathcal{B}(s=1) = -4 = -2\mathcal{C}^{\mathcal{NG}}. \tag{4.61}$$

2-loops couplings renormalisation

Resuming, the contributions:

1. $(g_{SR}^0)^3 \left[\mathcal{I}'_{g_{SR}^3} + \mathcal{I}''_{g_{SR}^3}\right] + g_{SR}^0 (g_{LR}^0)^2 \left[\mathcal{I}'_{g_{SR}g_{LR}^2} + \mathcal{I}''_{g_{SR}g_{LR}^2}\right]$ renormalises g_{SR}^0.
2. $(g_{LR}^0)^3 \underbrace{\left[\mathcal{I}'_{g_{LR}^3} + \mathcal{I}''_{g_{LR}^3}\right]}_{\mathcal{I}^{dis}} + g_{LR}^0 (g_{SR}^0)^2 \left[\mathcal{I}'_{g_{SR}^2 g_{LR}} + \mathcal{I}''_{g_{SR}^2 g_{LR}}\right]$ renormalises g_{LR}^0.

Thus:

$$\begin{aligned}
g_{SR}^0 \to\ & g_{SR}^0 r^{\epsilon_{SR}} + \pi (g_{LR}^0)^2 \left(\frac{r^{2\epsilon_{LR}-\epsilon_{SR}}}{2\epsilon_{LR}-\epsilon_{SR}}\right) + 4\pi(m-2)(g_{SR}^0)^2 \left(\frac{r^{\epsilon_{SR}}}{\epsilon_{SR}}\right) + \\
& + 16\pi^2 (m-2)(g_{SR}^0)^3 \left[(m-3) + \left(1 - \frac{\epsilon_{SR}}{2}\right)\right] \left(\frac{r^{2\epsilon_{SR}}}{\epsilon_{SR}^2}\right) + \\
& + 8\pi^2 g_{SR}^0 (g_{LR}^0)^2 \left[(m-2)\frac{2\epsilon_{LR}}{\epsilon_{SR}(2\epsilon_{LR}-\epsilon_{SR})} + \frac{1}{\epsilon_{SR}} + \frac{\mathcal{B}(\epsilon_{LR},\epsilon_{SR})}{8}\right] \left(\frac{r^{2\epsilon_{LR}}}{2\epsilon_{LR}}\right), \\
g_{LR}^0 \to\ & g_{LR}^0 r^{\epsilon_{LR}} + 4\pi(m-1) g_{LR}^0 g_{SR}^0 + (g_{LR}^0)^3 \mathcal{I}^{dis} + \\
& + 4\pi^2 (m-1) g_{LR}^0 (g_{SR}^0)^2 \left[4(m-2) + 2 - \epsilon_{SR}\right] \left(\frac{r^{2\epsilon_{SR}}}{\epsilon_{SR}^2}\right).
\end{aligned} \tag{4.62}$$

The factor $\mathcal{B}(\epsilon_{LR}, \epsilon_{SR})$, obtained from Eq. (4.42), can be expressed as:
$\mathcal{B}(s) = \dfrac{16\pi}{3\sqrt{3}} \dfrac{(1-s)}{(2-s)} - \dfrac{4s}{(2-s)}$, where $s = \dfrac{\epsilon_{SR}}{\epsilon_{LR}}$.
It is important to handle this factor, $\mathcal{B}(s)$, with care when studying the Potts or Ising models. Specifically, one needs to consider the Ising limit, as explained in Section (4.2.3)

In the limit where $m \to 0$, at 2−loops:

$$
\begin{aligned}
g^0_{SR} \to\; & g^0_{SR}\, r^{\epsilon_{SR}} + \pi (g^0_{LR})^2 \left(\frac{r^{2\epsilon_{LR}-\epsilon_{SR}}}{2\epsilon_{LR}-\epsilon_{SR}} \right) - 8\pi (g^0_{SR})^2 \left(\frac{r^{\epsilon_{SR}}}{\epsilon_{SR}} \right) + \\
& + 32 (g^0_{SR})^3 \pi^2 \left(\frac{4}{\epsilon_{SR}} + 1 \right) \left(\frac{r^{2\epsilon_{SR}}}{2\epsilon_{SR}} \right) + \\
& + 8\pi^2 g^0_{SR} (g^0_{LR})^2 \left[-\frac{1}{\epsilon_{SR}} + \frac{\mathcal{B}(\epsilon_{LR}, \epsilon_{SR})}{8} \right] \left(\frac{r^{2\epsilon_{LR}}}{2\epsilon_{LR}} \right), \\
g^0_{LR} \to\; & g^0_{LR}\, r^{\epsilon_{LR}} - 4\pi g^0_{LR} g^0_{SR} \left(\frac{r^{\epsilon_{SR}}}{\epsilon_{SR}} \right) + (g^0_{LR})^3 \mathcal{I}^{dis} \\
& + 8\pi^2 g^0_{LR} (g^0_{SR})^2 \left[\frac{6}{\epsilon_{SR}} + 1 \right] \left(\frac{r^{2\epsilon_{SR}}}{2\epsilon_{SR}} \right).
\end{aligned}
\tag{4.63}
$$

Except for the 0-loops contributions, the other terms are not dimensionless. To implement the rescaling process back to the original cutoff, it is necessary to introduce dimensionless couplings. In this case, one has the following expressions:

$$
\begin{aligned}
g_{SR} = r^{\epsilon_{SR}} \Bigg[& g^0_{SR} - 8\pi (g^0_{SR})^2 \left(\frac{r^{\epsilon_{SR}}}{\epsilon_{SR}} \right) + \pi (g^0_{LR})^2 \left(\frac{r^{2\epsilon_{LR}-\epsilon_{SR}}}{2\epsilon_{LR}-\epsilon_{SR}} \right) + \\
& + 8\pi^2 g^0_{SR} (g^0_{LR})^2 \left(-\frac{1}{\epsilon_{SR}} + \frac{\mathcal{B}(\epsilon_{LR}, \epsilon_{SR})}{8} \right) \left(\frac{r^{2\epsilon_{LR}}}{2\epsilon_{LR}} \right) \\
& + 32\pi^2 (g^0_{SR})^3 \left(\frac{4}{\epsilon_{SR}} + 1 \right) \left(\frac{r^{2\epsilon_{SR}}}{2\epsilon_{SR}} \right) \Bigg] \\
= r^{\epsilon_{SR}}\, & g^0_{SR}.
\end{aligned}
\tag{4.64}
$$

$$
\begin{aligned}
g_{LR} = r^{\epsilon_{LR}} \Bigg[& g^0_{LR} - 4\pi g^0_{LR} g^0_{SR} \left(\frac{r^{\epsilon_{SR}}}{\epsilon_{SR}} \right) + 8\pi^2 g^0_{LR} (g^0_{SR})^2 \left(\frac{6}{\epsilon_{SR}} + 1 \right) \left(\frac{r^{2\epsilon_{SR}}}{2\epsilon_{SR}} \right) + \\
& + \pi^2 (g^0_{LR})^3 \left(\mathcal{C}^{dis} - \frac{4}{\epsilon_{LR}-\epsilon_{SR}} \right) \left(\frac{r^{2\epsilon_{LR}}}{2\epsilon_{LR}} \right) \Bigg] \\
= r^{\epsilon_{LR}}\, & g^0_{LR}.
\end{aligned}
\tag{4.65}
$$

4.3.5 β-functions and fixed points

Another important step in the RG procedure is the computation of the β-functions. These functions describe the variations of the coupling constants with respect to changes in the length scale r, and can be expressed as follows:

$$\begin{aligned}\beta_{SR} &= r\frac{dg_{SR}}{dr} = \epsilon_{SR}\, g_{SR} - 8\pi g_{SR}^2 + \pi\, g_{LR}^2 + 32\pi^2 g_{SR}^3 + \pi^2 \mathcal{B}\, g_{SR} g_{LR}^2 + O(g^4),\\ \beta_{LR}^{dis} &= r\frac{dg_{LR}}{dr} = \epsilon_{LR} g_{LR} - 4\pi g_{LR} g_{SR} + \pi^2 \mathcal{C}^{dis}\, g_{LR}^3 + 8\pi^2 g_{SR}^2 g_{LR} + O(g^4),\end{aligned} \tag{4.66}$$

The notation β^{dis} is employed to indicate that the coefficient $\mathcal{C}^{dis}$ of g_{LR}^3 is fixed once the disorder is determined. In the particular cases considered here one has that $\mathcal{C}^{dis}$ is defined by Eq. (4.60) with $\mathcal{B}$ defined in Eq. (4.43).

Again, it must be noticed that, often in the thesis, a shortened notation is used to represent $\mathcal{B}$. However, it is important to note that $\mathcal{B}$ depends on $(\epsilon_{LR}, \epsilon_{SR})$ or s. This implies that $\mathcal{B}$ takes on different values depending on whether we are analyzing the 3-Potts model or the Ising model (where $\epsilon_{SR} = 0$), or if one is considering a generic disorder or the specific instance of non-Gaussian disorder where $\{\sigma \to \varepsilon,\, \epsilon_{LR} \to \epsilon_{SR},\, a = 2 - \epsilon_{SR}\}$.

It is also worth noting that in the double expansion procedure, $\mathcal{B}$ must remain finite. Therefore, one has $\mathcal{B} = O(\epsilon_{LR}, \epsilon_{SR})$, which means that at least $2 - a = O(\epsilon_{SR})$ or $\epsilon_{SR} = O(\epsilon_{LR})$ equivalently. This allows for controlled predictions in the case of the 3-Potts model where $\epsilon_{SR} \neq 0$. To approach the Ising limit with $a < 2$, one sets $\epsilon_{SR} = o(2 - a)$, as indicated in Eq. (4.60).

An important validation of the renormalisability of the theory arises from the fact that the divergent terms, proportional to $\sim 1/\epsilon_{LR}$ and $\sim 1/\epsilon_{SR}$, obtained from the 2-loops computations in Eqs. (4.64, 4.65), are "absorbed" by the 1-loop terms.

Given this is possible to compute the position of the fixed or critical points, *i.e.* the stationary points of the couplings' flow, *i.e.* one can look for $\{g_{SR}^{*,SR}, g_{LR}^{*,SR}\}$ such as $\beta_{SR}(g_{SR}^{*,SR}, g_{LR}^{*,SR}) = O(\epsilon^3)$ and $\beta_{LR}^{dis}(g_{SR}^{*,SR}, g_{LR}^{*,SR}) = O(\epsilon^3)$. The SR point is located at:

$$g_{SR}^{*,SR} = \frac{\epsilon_{SR}}{8\pi} + \frac{\epsilon_{SR}^2}{16\pi} + O(\epsilon^3),\; g_{LR}^{*,SR} = 0. \tag{4.67}$$

In the same way, one can look for the stationary points: $\{g_{SR}^{*,LR}, g_{LR}^{*,LR}\}$ and thus the location of the LR point is found at:

$$g_{SR}^{*,LR} = \frac{\epsilon_{LR}}{4\pi} + \frac{\epsilon_{LR}^2}{8\pi}\left(\mathcal{C}^{dis} + 1\right) - \frac{\epsilon_{LR}\epsilon_{SR}\,\mathcal{C}^{dis}}{16\pi} + O(\epsilon^3), \tag{4.68}$$

$$g_{LR}^{*,LR} = \sqrt{2 - \frac{\epsilon_{SR}}{\epsilon_{LR}}} \left(\frac{\epsilon_{LR}}{2\pi} + \frac{-\mathcal{B}\epsilon_{LR}(2\epsilon_{LR} - \epsilon_{SR}) + \mathcal{C}^{dis}\left(8\epsilon_{LR}^2 + \epsilon_{SR}^2 - 6\epsilon_{LR}\epsilon_{SR}\right) - 2\epsilon_{LR}\epsilon_{SR}}{16\pi\left(2 - \frac{\epsilon_{SR}}{\epsilon_{LR}}\right)} \right) + O(\epsilon^3). \tag{4.69}$$

4.4 Stability analysis

The stability of a RG fixed point is established by linearizing the flow in the vicinity of that point, which leads to the 2×2 stability matrix:

$$\mathcal{M} = \begin{pmatrix} \frac{\partial}{\partial g_{SR}}\beta_{SR}\left(g_{SR}^*, g_{LR}^*\right) & \frac{\partial}{\partial g_{LR}}\beta_{SR}\left(g_{SR}^*, g_{LR}^*\right) \\ \frac{\partial}{\partial g_{SR}}\beta_{LR}\left(g_{SR}^*, g_{LR}^*\right) & \frac{\partial}{\partial g_{LR}}\beta_{LR}\left(g_{SR}^*, g_{LR}^*\right) \end{pmatrix}. \tag{4.70}$$

The fixed point under consideration is stable if the real part of the eigenvalues is negative.

When $g_{LR}^* = 0$, the matrix M is diagonal at all orders. This can be also be understood by recalling that $\beta_{LR} \propto g_{LR}$ and by further observing that $\partial/\partial_{g_{LR}}\beta_{SR} \propto g_{LR}$ as the terms that contributes to the normalization to g_{SR} have an even number of LR interactions.

P stability

The P point, $g_{LR}^* = g_{SR}^* = 0$ has then the eigenvalues ϵ_{LR} and ϵ_{SR}. It is unstable if either $\epsilon_{SR} > 0$ (or $2 < q \leq 4$) or if $\epsilon_{LR} > 0$ (or $a < 2$). Since the case $2 \leq q \leq 4$ and $a < 2$ is considered in the present work, the pure point is always unstable. In Fig. (3.3), the P point do not describe anymore the critical behavior of the system in this region of parameters.

SR stability

In the SR case, the results do not depend on the distribution of the disorder and it is found that, at 2−loops, the eigenvalues are:

$$\lambda_1^{SR} = -\epsilon_{SR} + \frac{\epsilon_{SR}^2}{2},\ \lambda_2^{SR} = \epsilon_{LR} - \frac{\epsilon_{SR}}{2} - \frac{\epsilon_{SR}^2}{8}. \tag{4.71}$$

The first eigenvalue is always negative, $\lambda_1^{SR} < 0$, in the regime of parameters of this study as $0 < \epsilon_{SR} \leq 1$ for $2 < q \leq 4$, see Eq. (4.17). The SR point is therefore stable

provided that the second eigenvalue is negative, $\lambda_2^{SR} < 0$. This happens when:

$$a > 2 - \frac{\epsilon_{SR}^2}{4} = 2\left(1 - \frac{\epsilon_{SR}^2}{8}\right). \tag{4.72}$$

A comment must be done on the above result. The SR correlation length exponent ν^{SR}, computed in [44], and re-derived in Section (4.5.2), is:

$$\nu_{SR} = 1 + \frac{\epsilon_{SR}^2}{8} + O(\epsilon^3). \tag{4.73}$$

Using Eq. (4.73) in Eq. (4.72), one recovers the extended Harris criterion [86] according to which the LR/SR change of stability occurs at $a = 2/\nu_{SR}$. This is also the equation defining the curve shown in Fig. (3.3). In RG terms, this criterion simply states that, at the SR point, the LR perturbation is irrelevant.

LR stability

The goal, in this part, is to obtain an expansion at order ϵ^2 of the stability matrix eigenvalues Eq. (4.70). One can approach the problem using a first order perturbation scheme and write:

$$M = M^{(0)} + M^{(1)}, \tag{4.74}$$

where M^0 has $O(\epsilon)$ element:

$$M^{(0)} = \begin{pmatrix} -4\epsilon_{LR} + \epsilon_{SR} & \sqrt{2 - \frac{\epsilon_{SR}}{\epsilon_{LR}}}\epsilon_{LR} \\ -2\sqrt{2 - \frac{\epsilon_{SR}}{\epsilon_{LR}}}\epsilon_{LR} & 0 \end{pmatrix}, \tag{4.75}$$

while $M^{(1)}$ has $O(\epsilon^2)$ entries:

$$M_{1,1}^{(1)} = \epsilon_{LR}^2\left(4 - 2\mathcal{C}^{dis} + \frac{\mathcal{B}}{2}\right) + \epsilon_{LR}\epsilon_{SR}\left(\mathcal{C}^{dis} - \frac{\mathcal{B}}{4}\right), \tag{4.76}$$

$$M_{1,2}^{(1)} = \frac{\epsilon_{LR}^2\left(8\mathcal{C}^{dis} + 2\mathcal{B}\right) + \epsilon_{SR}\epsilon_{LR}\left(-2 - 6\mathcal{C}^{dis} - \mathcal{B}\right) + \mathcal{C}^{dis}\epsilon_{SR}^2}{8\sqrt{2 - \frac{\epsilon_{SR}}{\epsilon_{LR}}}}, \tag{4.77}$$

$$M_{2,1}^{(1)} = \frac{\epsilon_{LR}^2\left(16 - 8\mathcal{C}^{dis} + 2\mathcal{B}\right) + \epsilon_{SR}\epsilon_{LR}\left(-6 + 6\mathcal{C}^{dis} - \mathcal{B}\right) - \mathcal{C}^{dis}\epsilon_{SR}^2}{4\sqrt{2 - \frac{\epsilon_{SR}}{\epsilon_{LR}}}}, \tag{4.78}$$

$$M_{2,2}^{(1)} = \mathcal{C}^{dis}\left(\epsilon_{LR}^2 - \frac{\epsilon_{SR}\epsilon_{LR}}{2}\right). \tag{4.79}$$

One wants to find the correction:

$$\lambda_1 = \lambda_1^{(0)} + \lambda_1^{(1)}, \quad \lambda_2 = \lambda_2^{(0)} + \lambda_2^{(1)}, \tag{4.80}$$

where $\lambda^{(0)}_{1,2}$ are the eigenvalues of the unperturbed matrix M_0 (of order ϵ) and the $\lambda^{(1)}_{1,2}$ are the first order correction (so of order ϵ^2). When $\epsilon_{SR} > 0$ the matrix $M^{(0)}$ is diagonalizable. One has:

$$A^{-1}M^0A = \begin{pmatrix} -2\epsilon_{LR} & 0 \\ 0 & -2\epsilon_{LR}+\epsilon_{SR} \end{pmatrix}, \tag{4.81}$$

where:

$$A = \begin{pmatrix} \frac{1}{\sqrt{2-\frac{\epsilon_{SR}}{\epsilon_{LR}}}} & \frac{\sqrt{2-\frac{\epsilon_{SR}}{\epsilon_{LR}}}}{2} \\ 1 & 1 \end{pmatrix}. \tag{4.82}$$

The zero order (corresponding to 1−loop order in the RG computation) eigenvalues are therefore:

$$\lambda^{(0)}_1 = -2\epsilon_{LR}, \quad \lambda^{(0)}_2 = -2\epsilon_{LR}+\epsilon_{SR}, \tag{4.83}$$

and the corresponding eigenvectors:

$$\left|\lambda^{(0)}_1\right\rangle = \begin{pmatrix} \frac{1}{\sqrt{2-\frac{\epsilon_{SR}}{\epsilon_{LR}}}} \\ 1 \end{pmatrix}, \quad \left|\lambda^{(0)}_2\right\rangle = \begin{pmatrix} \frac{\sqrt{2-\frac{\epsilon_{SR}}{\epsilon_{LR}}}}{2} \\ 1 \end{pmatrix}. \tag{4.84}$$

Note that when $\epsilon_{SR} = 0$ the eigenvalues of $M^{(0)}$ is double degenerate but the rank of A is one (and not invertible). The matrix $M^{(0)}$ is an example of a so called defective matrix, whose eigenvectors span a space smaller than its dimension (in this case 2). The $\lambda^{(1)}_{1,2}$ are found by:

$$\lambda^{(1)}_1 = \left\langle\lambda^0_1\right| M^{(1)} \left|\lambda^0_1\right\rangle, \quad \lambda^{(1)}_2 = \left\langle\lambda^0_2\right| M^{(1)} \left|\lambda^0_2\right\rangle, \tag{4.85}$$

which is equivalent to:

$$\lambda^{(1)}_1 = \left(A^{-1}M^{(1)}A\right)_{11}, \quad \lambda^{(1)}_2 = \left(A^{-1}M^1A\right)_{22}. \tag{4.86}$$

One finds:

$$\lambda_1^{LR} = -2\epsilon_{LR} - \frac{\epsilon_{LR}^2}{2}\left(-2 + \mathcal{B} - 2\mathcal{C}^{dis}\right) + \frac{\epsilon_{LR}^3}{\epsilon_{SR}}\left(4 + \mathcal{B} - 2\mathcal{C}^{dis}\right), \tag{4.87}$$

$$\lambda_2^{LR} = -2\epsilon_{LR} + \epsilon_{SR} + \epsilon_{LR}^2\left(3 + \mathcal{B} - 2\mathcal{C}^{dis}\right) - \frac{\epsilon_{LR}^3}{\epsilon_{SR}}\left(4 + \mathcal{B} - 2\mathcal{C}^{dis}\right) - \frac{\epsilon_{SR}\epsilon_{LR}}{4}\left(\mathcal{B} - 2\mathcal{C}^{dis}\right).$$

In the Gaussian case Eq. (4.60) the formula get simplified. One finds that the LR point is attractive between:

$$a^* < a < \frac{2}{\nu_{SR}}, \quad a^* = 2 - (2\epsilon_{SR})^{1/2} + \frac{5}{4}\epsilon_{SR} - \frac{1}{32\sqrt{2}}\epsilon_{SR}^{3/2}. \tag{4.88}$$

The upper bound is in agreement with the numerical results of [7] and with the extended Harris criterion [86]. Regarding the lower bound, for 3−Potts one finds $a^* = 1.6$. This prediction is qualitatively far from the numerical results in [7], where $a^*_{num} \sim 0.75$. The fact that $a^* = 1.6$ is quite different from the numerical findings does not put in question the validity of the RG approach. Indeed $2 - a^* > 1$ and one cannot pretend to find a quantitative agreement with a small $2 - a$ expansion. However, the 2-loop computation shows a qualitative agreement with the fact that there should be a value a^* below which the LR point loses stability.

It is quite manifest that one cannot obtain the result of Ising by setting $\epsilon_{SR} = 0$ in the previous equation: indeed one finds a singularity, which can be traced back to the fact that the matrix A is not invertible. One has to take the limit more carefully.

It is much more simple to diagonalize the matrix M with $\epsilon_{SR} = 0$:

$$M_{1,1}(\epsilon_{SR} = 0) = -4\epsilon_{LR} + \epsilon_{LR}^2\left(4 - 2\mathcal{C}^{dis} + \frac{\mathcal{B}_{\text{Ising}}}{2}\right), \tag{4.89}$$

$$M_{1,2}(\epsilon_{SR} = 0) = \sqrt{2}\epsilon_{LR} + \epsilon_{LR}^2\left(\frac{\mathcal{C}^{dis}}{\sqrt{2}} + \frac{\mathcal{B}_{\text{Ising}}}{2\sqrt{2}}\right), \tag{4.90}$$

$$M_{2,1}(\epsilon_{SR} = 0) = -2\sqrt{2}\epsilon_{LR} + 2\sqrt{2}\epsilon_{LR}^2\left(1 - \frac{\mathcal{C}^{dis}}{2} + \frac{\mathcal{B}_{\text{Ising}}}{8}\right), \tag{4.91}$$

$$M_{2,2}(\epsilon_{SR} = 0) = \mathcal{C}^{dis}\epsilon_{LR}^2. \tag{4.92}$$

where, from Eq. (4.43) one derives:

$$\mathcal{B}_{\text{Ising}} = \mathcal{B}(\epsilon_{LR}, \epsilon_{SR} = 0) = \mathcal{B}(s = 0) = \frac{8\pi}{3\sqrt{3}}. \tag{4.93}$$

Obtaining:

$$\lambda_1^{LR,\text{Ising}} = -2\epsilon_{LR} + \frac{\epsilon_{LR}^2}{4}\left(8 + \mathcal{B}_{\text{Ising}} - 2\mathcal{C}^{dis}\right) + 2i\epsilon_{LR}^{3/2}, \tag{4.94}$$
$$\lambda_2^{LR,\text{Ising}} = -2\epsilon_{LR} + \frac{\epsilon_{LR}^2}{4}\left(8 + \mathcal{B}_{\text{Ising}} - 2\mathcal{C}^{dis}\right) - 2i\epsilon_{LR}^{3/2}.$$

The eigenvalues have an imaginary term, in accordance with the findings of [135]. Some comments are in order. Concerning to the origin of the imaginary terms, one observes that, at the 1-loop order, the LR Ising stability matrix is not diagonalizable (note that M is a real and not symmetric function) it has a single eigenvector. At the 2-loop order, this is solved by creating a pair of complex eigenvalues, conjugate one to the other. A second observation is that the LR stability depends on the coefficient $\mathcal{C}^{dis}$ and therefore on the fourth cumulant of the disorder distribution. For a Gaussian disorder, Eq. (4.60) is verified, the real parts of the two eigenvalues, expressed in terms of a, take the form:

$$\text{Re}\left[\lambda_1^{LR,\text{Ising}}\right] = \text{Re}\left[\lambda_2^{LR,\text{Ising}}\right] = \frac{1}{2}(a-2)\,a. \tag{4.95}$$

This implies the existence of an interval, $a^* < a < 2$, with $a^* = 0$ for which the LR remain attractive. An analogous phenomena was observed in [135] where the interval of stability was $a^* < a < 2$ with $a^* \sim 1$. In [7], it is shown that below this value the system is attracted to an infinite disorder fixed point. The numerical simulations in [7] are consistent with a value of $a^*_{num} \sim 0.75$. The same reasoning done for 3-Potts can be done in the Ising case. Indeed the observation that $a^* = 0$ differs from the numerical findings does not undermine the validity of the RG approach since one cannot expect to obtain quantitative agreement using a small $2 - a$ expansion for this "far away" value. However, the 2-loop computation does exhibit a qualitative agreement with the notion that there exists a critical value a^* below which the LR point loses stability.

4.5 Critical exponents

In this section, the effective central charge c_{eff}^X and the correlation length exponent ν^X for the fixed points $X = \{SR, LR\}$ are computed. The values of c_{eff}^{LR} and ν^{LR} are presented as new results. To assess the validity of the developed theory, the value of c_{eff}^{LR} for the Ising model is compared to observations obtained from simulations.

4.5.1 Central charge and Zamolodchikov c-theorem

The central charge c is a significant universal quantity that characterizes the conformal algebra upon which the theory is constructed [82]. It determines the universal critical finite size corrections of various observables [174], and its value can be measured through

the study of these corrections [160]. In this work, the focus is on the finite size effects of the free energy $\mathcal{F}$ in a critical statistical model defined on a torus of dimensions $N \times L$.

The central charge appears in the sub-leading and universal term of the large L expansion of the free energy [174, 175]:

$$\frac{\beta_c \mathcal{F}}{NL} = f_0 - \frac{c\pi}{6L^2} + O\left(L^{-4}\right), \tag{4.96}$$

where β_c is the critical temperature and f_0 is the free-energy density, which is a non-universal quantity.

For the pure model, the central charge c^{P} is known exactly [168]. Its ϵ_{SR} expansion is:

$$c = c^{\mathrm{P}} = \frac{1}{2} + \frac{7\epsilon_{SR}}{8} - \frac{9\epsilon_{SR}^2}{32} - \frac{9\epsilon_{SR}^3}{128} + O(\epsilon_{SR}^4). \tag{4.97}$$

It should be noted that when $\epsilon_{SR} = 0$, one reaches the Ising point where the well-known result $c^P_{\mathrm{Ising}} = 1/2$ is obtained.

In the case of the quenched bond-disordered Potts model, the free energy is a self-averaging observable. Analogously to the pure case, the effective central charge c_{eff} is defined as the coefficient appearing in the large L expansion of the average free energy:

$$\mathbb{E}\left[\frac{\beta_c \mathcal{F}}{NL}\right] = f_0 - \frac{c_{eff}\pi}{6L^2} + O\left(L^{-4}\right). \tag{4.98}$$

Zamolodchikov c-theorem

To compute the central charge, the Zamolodchikov c-theorem [176] is employed, which states that one needs to identify a function $C\left(g_{SR}, g_{LR}\right)$ of the couplings satisfying the following condition:

$$\beta_{SR}\frac{\partial}{\partial_{g_{SR}}} C\left(g_{SR}, g_{LR}\right) + \beta_{LR}\frac{\partial}{\partial_{g_{LR}}} C\left(g_{SR}, g_{LR}\right) = -6\pi^2 \left\langle \Theta(0)\Theta(1)\right\rangle, \tag{4.99}$$

where $\Theta(x)$ is the trace of the stress-energy tensor. This latter is related, by the renormalisability of the theory, to the perturbation terms by:

$$\Theta(x) = \beta_{SR} \sum_{\alpha\neq\beta}^{n} \varepsilon^{(a)}(x)\varepsilon^{(b)}(x) + \beta_{LR} \sum_{a} \sigma(x)\varepsilon^{(a)}(x). \tag{4.100}$$

Using:

$$\left\langle \sum_{a\neq b}^{n} \varepsilon^{(a)}(0)\varepsilon^{(b)}(0) \sum\nolimits_{c\neq d}^{n} \varepsilon^{(a)}(1)\varepsilon^{(b)}(1) \right\rangle = 2n(n-1), \tag{4.101}$$

$$\left\langle \sum_a^n \sigma(0)\varepsilon^{(a)}(0) \sum\nolimits_b^n \sigma(1)\varepsilon^{(b)}(1) \right\rangle = n, \tag{4.102}$$

$$\left\langle \sum_{a\neq b}^n \varepsilon^{(a)}(0)\varepsilon^{(b)}(0) \sum_c^n \sigma(1)\varepsilon^{(c)}(1) \right\rangle = 0, \tag{4.103}$$

one has:

$$\langle \Theta(0)\Theta(1)\rangle = 2n(n-1)\beta_{SR}^2 + n\beta_{LR}^2. \tag{4.104}$$

To compare the central charge with Monte Carlo results, the 1-loop order is enough, so one does not need to deal with $\mathcal{C}^{dis}$. At this order, the β functions, for the system with n-replicas, are:

$$\begin{aligned} \beta_{SR} &= \epsilon_{SR} g_{SR} + 4\pi(n-2) g_{SR}^2 + \pi g_{LR}^2, \\ \beta_{LR} &= \epsilon_{LR} g_{LR} + 4\pi(n-1) g_{SR} g_{LR}. \end{aligned} \tag{4.105}$$

Using the above equations, one can verify that a solution of Eq. (4.99) is:

$$\begin{aligned} C\left(g_{SR}, g_{LR}\right) = C\left(0,0\right) - 6\pi^2 n \Big(&(n-1)\epsilon_{SR} g_{SR}^2 + \frac{1}{2}\epsilon_{LR} g_{LR}^2 + \\ &+ \frac{8\pi}{3}(n-2)(n-1) g_{SR}^3 + 2\pi(n-1) g_{LR}^2 g_{SR} \Big). \end{aligned} \tag{4.106}$$

The effective central charge c_{eff}^X at the X fixed point, $X = \{SR, LR\}$, is obtained by:

$$c_{eff}^X = \lim_{n\to 0} \frac{1}{n} C\left(g_{SR}^{*,\mathrm{X}}, g_{LR}^{*,\mathrm{X}}\right). \tag{4.107}$$

The central charge of the pure $q-$Potts model, see Eq. (4.97), fixes the initial condition $C\left(0,0\right) = c^P$. Using Eq. (4.106), one obtains the Eqs. (4.108) and (4.109).

Comparison of predictions and measurements

To compare with numerical results, the 1-loop order is sufficient. Ineed, the numerical precision is not enough to probe 2-loop corrections. At 1-loop order it is obtained:

$$c_{eff}^{SR} = \frac{1}{2} + \frac{7\epsilon_{SR}}{8} - \frac{9\epsilon_{SR}^2}{32} - \frac{5\epsilon_{SR}^3}{128} + O(\epsilon_{SR}^4), \tag{4.108}$$

$$c_{eff}^{LR} = \frac{1}{2} + \frac{7\epsilon_{SR}}{8} - \frac{9\epsilon_{SR}^2}{32} - \frac{9\epsilon_{SR}^3}{128} - \frac{\epsilon_{LR}^3}{2} + \frac{3{\epsilon_{LR}}^2\epsilon_{SR}}{8} + O(\epsilon^4). \tag{4.109}$$

At the SR point, one recovers the result of [177], while the effective charge at the LR point represents a new result. In particular, at the Ising point, expressed in terms of a,

one has:

$$c_{eff}^{LR,\text{Ising}} = \frac{1}{2} - \frac{1}{2}\left(1 - \frac{a}{2}\right)^3 + O(\epsilon_{LR}^4). \tag{4.110}$$

It is worth commenting the fact that at the LR fixed point the $c_{eff}^{\text{LR,Ising}} < 1/2 = c^{\text{P}}$, thus, the RG flow make the effective central charge diminish. This is observed and checked also numerically in Fig. (4.2). One should note that the Zamalochicov c-theorem claims that the central charge decreseas for unitary theory under the RG flow. Still, in the cases studied, due to the fact that the theory is non-unitary, this is inconclusive.

In Fig. (4.2) the comparison between the results Eq. (4.110) and the numerical results for the long-range Ising model is shown. The reader is referred to Chapter (3) for a detailed definition of the lattice model used for simulations. In particular, the LR bond disordered Ising model is simulated by varying two parameters, the power decay exponent a and the disorder strength r, see Eq. (3.10)[2]. In Fig. (4.2), the effective central charge obtained from measurements of the averaged free energy on strips of size $N = 10^5$ and $L = \{4, \cdots, 8\}$ with periodic boundary conditions along the short direction is shown. The measurements are done by averaging over 10^6 strips. The c_{eff}, denoted $c(4, 8)$ in the following, is obtained by fitting the results for different L by the Eq. (4.98) while including a L^{-4} correction. For the Ising model, a fit to this form gives $c(4, 8) = 0.495998$ in place of the exact result $1/2$. This value is shown as a dashed line in Fig. (4.2). The prediction Eq. (4.110) to which one subtracts $0.5 - 0.495998 = 0.004002$ is, also, shown. Next, the numerical results for the LR points are showed. For each value of a, $c(4, 8)$ is computed for the value of disorder strength r with the less correction to the scaling in the magnetisation measurements as done in [7]. The following values of disorder were used: $a/r = \{0.75/10, 1.0/10, 1.25/5, 1.50/3, 1.75/2, 2/2\}$. For $a \in \{1, 2\}$, the agreement between the measurements and the RG predictions Eq. (4.110) is excellent. For the smallest value of a considered, $a = 0.75$, the effective central charge at the LR fixed point with $r = 10$ is the same as the one for the LR with an infinite disorder (also shown in Fig. (4.2) for all values of a). This is in agreement with the finding in [7] and Chapter (3), that $a^* \simeq 0.75$ is the lower limit of stable LR fixed point for the Ising model.

4.5.2 Correlation length exponent

In the replica approach, the averaged energy two-point correlation function is expressed as:

$$\langle \varepsilon_x \varepsilon_y \rangle_{\mathcal{S}^*} = \mathbb{E}\left[\langle \varepsilon_x \varepsilon_y \rangle\right] \propto \lim_{m \to 0} \frac{1}{m} \left\langle \sum_{\alpha=1}^{m} \varepsilon_x^\alpha \sum_{\beta=1}^{m} \varepsilon_y^\beta \right\rangle_{\mathcal{S}^*}. \tag{4.111}$$

[2]This r should not be confused with the renormalisation group length scale.

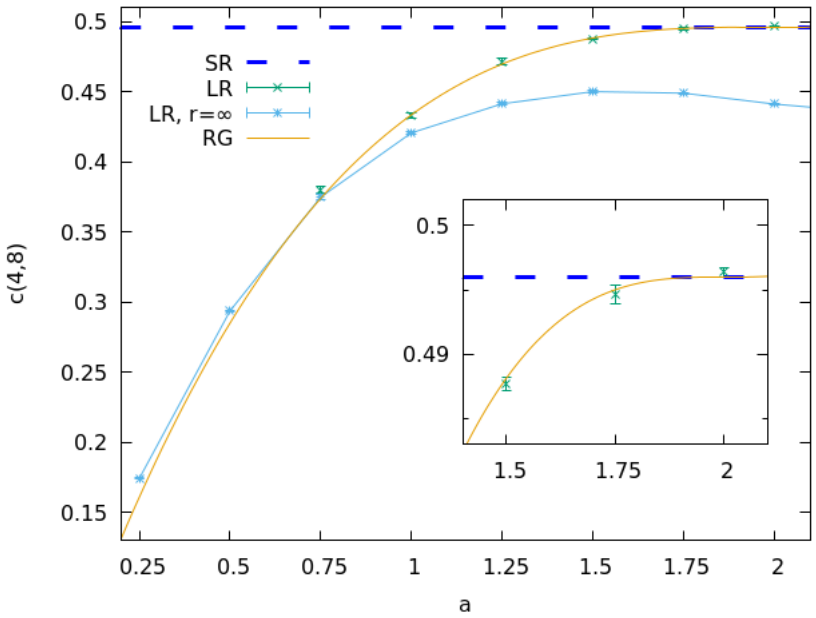

Figure 4.2. Effective central charge $c(4,8)$, for the Ising model, measured at the LR fixed points indicated as LR in the key. This is compared with the prediction Eq. (4.110) shown as RG in the key. The inset shows a magnified view for a close to 2. The effective central charge for the LR model with infinite disorder, indicated by LR, $r = \infty$ in the key is also shown. SR, in the key, is instead the value measured for the Ising model at the SR fixed point.

One is, thus, interested in the renormalisation of the replica symmetric field:

$$\varepsilon_x^{\text{sym}} = \sum_{\alpha=1}^{n} \varepsilon_x^{\alpha}. \tag{4.112}$$

The procedure followed for the renormalisation of operators is similar to to the one done to renormalise the couplings, Sec. (4.3). Indeed one imposes the conservation of the correlation function:

$$\begin{aligned}\left\langle \sum_{\alpha=1}^{m} \varepsilon_z^{\alpha} \right\rangle_{\mathcal{S}^*} &= \frac{\int \mathcal{D}_\sigma \mathcal{D}_s \sum_{\alpha=1}^{m} \varepsilon_z^{\alpha}\, e^{\mathcal{S}^{(m)}}}{\int \mathcal{D}_\sigma \mathcal{D}_s\, e^{\mathcal{S}^{(m)}}} \\ &= \cdots = \Big\langle \sum_{\alpha=1}^{m} \varepsilon_z^{\alpha} \Big[1 + \sum_{\alpha=1}^{m} g_{LR}^0 \int_{|x|>l} d^2x\, \sigma_x \varepsilon_x^{\alpha} + \sum_{\alpha\neq\beta=1}^{m} g_{SR}^0 \int_{|x|>l} d^2x\, \varepsilon_x^{\alpha}\varepsilon_x^{\beta} + \end{aligned} \tag{4.113}$$

$$+\frac{1}{2!}\sum_{\alpha\neq\beta=1}^{m}\sum_{\gamma\neq\delta=1}^{m}(g^0_{SR})^2\iint\limits_{|x-y|>l}d^2x\,d^2y\,\varepsilon^\alpha_x\varepsilon^\beta_x\,\varepsilon^\gamma_y\varepsilon^\delta_y+$$
$$+\frac{1}{2!}\sum_{\alpha=1}^{m}\sum_{\beta=1}^{m}(g^0_{LR})^2\iint\limits_{|x-y|>l}d^2x\;d^2y\,\sigma_x\varepsilon^\alpha_x\,\sigma_y\varepsilon^\beta_y+\cdots+O(g^3)\Big]\Big\rangle_{\mathcal{S}^*},$$

over RG transformations and can, thus, compute how the operator, ε^{sym}_z, gets renormalised: $\varepsilon^{sym}\to\varepsilon^{sym'}$. Following the scheme of Sec. (4.3) one has to compute contribution of the form:

$$(\cdots)(g^0_X)^1\int\limits_{|x|<r}d^2x\;(\cdots)+(\cdots)(g^0_X)^2\iint\limits_{|x-y|<r}d^2x\;d^2y\;(\cdots)\,, \tag{4.114}$$

where $X=\{LR,SR\}$. One realizes soon that in the RG procedure there is a mixing between the ε and σ fields. The 2×2 matrix $Z_{\varepsilon^{sym},\sigma}$ is defined by:

$$\begin{pmatrix}\varepsilon^{\mathrm{sym}'}\\ \sigma'\end{pmatrix}=Z_{\varepsilon^{\mathrm{sym}},\sigma}\times\begin{pmatrix}\varepsilon^{\mathrm{sym}}\\ \sigma\end{pmatrix}, \tag{4.115}$$

where the $\varepsilon^{\mathrm{sym}'}$ and σ' are the renormalized fields, one has to take into account. However, from the analysis of the combinatorial factors associated to the RG expansion diagrams, it is observed that the matrix $Z_{\varepsilon^{\mathrm{sym}},\sigma}$ takes the form:

$$Z_{\varepsilon^{\mathrm{sym}},\sigma}=\begin{pmatrix}Z_\varepsilon & Z_{\varepsilon\sigma}\\ m\times Z_{\sigma\varepsilon} & m\times Z_{\sigma\sigma}\end{pmatrix}, \tag{4.116}$$

where $Z_\varepsilon, Z_{\varepsilon\sigma}, Z_{\sigma\varepsilon}, Z_{\sigma\sigma}$ are non-vanishing contributions. Therefore, in the limit $m\to 0$ the $\varepsilon^{\mathrm{sym}'}$ does not get mixed with σ. On the other hand, σ is not anymore an eigenvector of the RG transformation. The renormalisation of $\varepsilon^{\mathrm{sym}'}$ depends only on Z_ε.

One can compute Z_ε, at 2-loops order that, in the $m\to 0$ limit from Eq. (4.113).

At 1-loop the unique contribution is given by:

$$
\begin{aligned}
&\to g^0_{SR}\sum_{\alpha=1}^{m}\sum_{\beta\neq\gamma=1}^{m}\int\limits_{|x-z|<r} d^2x\,\overbrace{\varepsilon_z^{\alpha}\varepsilon_x^{\beta}}^{\alpha=\beta\neq\gamma}\varepsilon_x^{\gamma}\\
&= 2(m-1)g^0_{SR}\int\limits_{|x-z|<r} d^2x\,|x-z|^{-2h_\varepsilon}\sum_{\gamma=1}^{m}\varepsilon_z^{\gamma} \qquad (4.117)\\
&= \underbrace{4\pi(m-1)g^0_{SR}\frac{r^{\epsilon_{SR}}}{\epsilon_{SR}}}_{\text{renormalises }\varepsilon^{sym}}\sum_{\gamma=1}^{m}\varepsilon_z^{\gamma}.
\end{aligned}
$$

At 2-loops one has four contribution:

$$
\begin{aligned}
1)\to&\frac{g^0_{SR}}{2}\sum_{\alpha=1}^{m}\sum_{\beta\neq\gamma=1}^{m}\sum_{\delta\neq\eta=1}^{m}\iint\limits_{|x-z|<r} d^2x\,d^2y\,\overbrace{\varepsilon_z^{\alpha}\varepsilon_x^{\beta}}^{\alpha=\beta\neq\eta}\underbrace{\varepsilon_x^{\gamma}\varepsilon_y^{\delta}}_{\gamma=\delta\neq\eta}\varepsilon_y^{\eta}\\
&= 4(m-1)(m-2)(g^0_{SR})^2\int\limits_{|x-z|<r} d^2x\int\limits_{|y-z|<r} d^2y\,|x-y|^{-2h_\varepsilon}|x-z|^{-2h_\varepsilon}\sum_{\eta=1}^{m}\varepsilon_z^{\eta} \qquad (4.118)\\
&= \underbrace{32\pi^2(m-1)(m-2)(g^0_{SR})^2\frac{r^{2\epsilon_{SR}}}{2\epsilon^2_{SR}}}_{\text{renormalises }\varepsilon^{sym}}\sum_{\eta=1}^{m}\varepsilon_z^{\eta}.
\end{aligned}
$$

$$
\begin{aligned}
2)\to&\frac{g^0_{SR}}{2}\sum_{\alpha=1}^{m}\sum_{\beta\neq\gamma=1}^{m}\sum_{\delta\neq\eta=1}^{m}\iint\limits_{|x-z|<r} d^2x\,d^2y\,\overbrace{\varepsilon_z^{\alpha}\varepsilon_x^{\beta}\underbrace{\varepsilon_x^{\gamma}}_{\gamma=\eta}\varepsilon_y^{\delta}}^{\alpha=\beta=\delta}\varepsilon_y^{\eta}\\
&= 2(m-1)(g^0_{SR})^2\int\limits_{|x-z|<r} d^2x\int\limits_{|y-z|<r} d^2y\,\langle\varepsilon_x\varepsilon_y\varepsilon_z\varepsilon_\infty\rangle|x-y|^{-2h_\varepsilon}\sum_{\alpha=1}^{m}\varepsilon_z^{\alpha} \qquad (4.119)\\
&= \underbrace{8\pi^2(m-1)(g^0_{SR})^2\,(2-\epsilon_{SR})\,\frac{r^{2\epsilon_{SR}}}{2\epsilon^2_{SR}}}_{\text{renormalises }\varepsilon^{sym}}\sum_{\alpha=1}^{m}\varepsilon_z^{\alpha}.
\end{aligned}
$$

This first two terms were already computed in [44]. One is left with the computation of the contribution coming from the LR terms:

$$
\begin{aligned}
3) \to & \frac{g_{LR}^0}{2} \sum_{\alpha=1}^{m} \sum_{\beta=1}^{m} \sum_{\gamma=1}^{m} \iint_{|x-z|<r} d^2x\, d^2y \overbrace{\varepsilon_z^\alpha\, \sigma_x \varepsilon_x^\beta \sigma_y \varepsilon_y^\gamma}^{\alpha=\beta\neq\gamma} \\
& = 2(m-1)(g_{LR}^0)^2 \int\limits_{|x-z|<r} d^2x \int\limits_{|y-z|<r} d^2y\, |x-y|^{-2h_\sigma} |x-z|^{-2h_\varepsilon} \sum_{\alpha=1}^{m} \varepsilon_z^\alpha \qquad (4.120) \\
& = \underbrace{\pi^2 (m-1)(g_{LR}^0)^2 \left(\frac{8\epsilon_{LR}}{\epsilon_{SR}(2\epsilon_{LR}-\epsilon_{SR})} \right) \frac{r^{2\epsilon_{LR}}}{2\epsilon_{LR}}}_{\text{renormalises } \varepsilon^{sym}} \sum_{\alpha=1}^{m} \varepsilon_z^\alpha .
\end{aligned}
$$

$$
\begin{aligned}
4) \to & \frac{g_{LR}^0}{2} \sum_{\alpha=1}^{m} \sum_{\beta=1}^{m} \sum_{\gamma=1}^{m} \iint_{|x-z|<r} d^2x\, d^2y \overbrace{\varepsilon_z^\alpha\, \sigma_x \varepsilon_x^\beta \sigma_y \varepsilon_y^\gamma}^{\alpha=\beta=\gamma} \\
& = 2(m-1)(g_{LR}^0)^2 \int\limits_{|x-z|<r} d^2x \int\limits_{|y-z|<r} d^2y\, \langle \varepsilon_x \varepsilon_y \varepsilon_z \varepsilon_\infty \rangle\, |x-y|^{-2h_\sigma} \sum_{\alpha=1}^{m} \varepsilon_z^\alpha \qquad (4.121) \\
& = \underbrace{\pi^2 (g_{LR}^0)^2 \left(\frac{4}{\epsilon_{SR}} + \frac{\mathcal{B}}{2} \right) \frac{r^{2\epsilon_{LR}}}{2\epsilon_{LR}}}_{\text{renormalises } \varepsilon^{sym}} \sum_{\alpha=1}^{m} \varepsilon_z^\alpha .
\end{aligned}
$$

Thus, collecting all the terms one obtains:

$$
\begin{aligned}
\varepsilon^{sym'} = \lim_{m\to 0} \Big[& 4\pi(m-1) g_{SR}^0 \frac{r^{\epsilon_{SR}}}{\epsilon_{SR}} + 32\pi^2 (m-1)(m-2)(g_{SR}^0)^2 \frac{r^{2\epsilon_{SR}}}{2\epsilon_{SR}^2} + \qquad (4.122) \\
& 8\pi^2 (m-1)(g_{SR}^0)^2 (2-\epsilon_{SR}) \frac{r^{2\epsilon_{SR}}}{2\epsilon_{SR}^2} + \pi^2 (g_{LR}^0)^2 \left(\frac{4}{\epsilon_{SR}} + \frac{\mathcal{B}}{2} \right) \frac{r^{2\epsilon_{LR}}}{2\epsilon_{LR}} + \\
& + \pi^2 (m-1)(g_{LR}^0)^2 \left(\frac{8\epsilon_{LR}}{\epsilon_{SR}(2\epsilon_{LR}-\epsilon_{SR})} \right) \frac{r^{2\epsilon_{LR}}}{2\epsilon_{LR}} + \Big] \varepsilon^{sym} \\
= \Big[& 1 - 4\pi g_{SR}^0 \frac{r^{\epsilon_{SR}}}{\epsilon_{SR}} + 4\pi^2 (g_{SR}^0)^2 \left(2 + \frac{12}{\epsilon_{SR}} \right) \frac{r^{2\epsilon_{SR}}}{2\epsilon_{SR}} + \\
& - 4\pi^2 (g_{LR}^0)^2 \left(\frac{1}{2\epsilon_{LR}-\epsilon_{SR}} - \frac{\mathcal{B}}{8} \right) \frac{r^{2\epsilon_{LR}}}{2\epsilon_{LR}} \Big] \varepsilon^{sym} \\
= & Z_{\mathcal{E}} \times \varepsilon^{sym}. \qquad (4.123)
\end{aligned}
$$

By consequence:

$$Z_\varepsilon = 1 - 4\pi g_{SR}^0 \frac{r^{\epsilon_{SR}}}{\epsilon_{SR}} + 4\pi^2 (g_{SR}^0)^2 \left(2 + \frac{12}{\epsilon_{SR}}\right) \frac{r^{2\epsilon_{SR}}}{2\epsilon_{SR}} + \\ - 4\pi^2 (g_{LR}^0)^2 \left(\frac{1}{2\epsilon_{LR} - \epsilon_{SR}} - \frac{\mathcal{B}}{8}\right) \frac{r^{2\epsilon_{LR}}}{2\epsilon_{LR}}. \tag{4.124}$$

At this stage, one can compute the function:

$$\gamma_\varepsilon = r \frac{d}{dr} \log Z_\varepsilon, \tag{4.125}$$

that actually enters in the Callan-Symanzik equations [44]. In terms of the normalized variables, one has:

$$\gamma_\varepsilon = -4\pi g_{SR} + 8\pi^2 g_{SR}^2 + \pi^2 g_{LR}^2 \frac{\mathcal{B}}{2}. \tag{4.126}$$

The renormalized energy scaling exponent $h_\varepsilon^{X'}$ at the fixed point $X = \{SR, LR\}$ is given by: [44]:

$$h_\varepsilon^{X'} = h_\varepsilon - \gamma_\varepsilon(g_{SR}^{*,X}, g_{LR}^{*,X}). \tag{4.127}$$

This also gives the thermal exponent at the X point:

$$\frac{1}{\nu^X} = 2 - h_\varepsilon^{\prime,X}. \tag{4.128}$$

Using the expansion:

$$h_\varepsilon = 1 - \frac{\epsilon_{SR}}{2} + O\left(\epsilon_{SR}^3\right), \tag{4.129}$$

and the location Eq. (4.67) of the SR fixed point in Eq. (4.127), one recovers the result of [44]:

$$h_\varepsilon^{\prime,SR} = 1 + \frac{\epsilon_{SR}^2}{8}, \; \frac{1}{\nu^{SR}} = 1 - \frac{\epsilon_{SR}^2}{8}. \tag{4.130}$$

The new result concerns the LR thermal exponent, associated to the LR fixed point. Using its location Eq. (4.68) in the Eq. (4.127), one has:

$$h_\varepsilon^{\prime,LR} = h_\varepsilon + \epsilon_{LR} + \frac{1}{4}\left(\mathcal{C}^{dis} - \frac{\mathcal{B}(s)}{2}\right) \epsilon_{LR} \left(2\epsilon_{LR} - \epsilon_{SR}\right) + O(\epsilon^3). \tag{4.131}$$

The Ising model is obtained by setting $\epsilon_{SR} = 0$ in Equation (4.131):

$$\text{Ising: } h_{\varepsilon}^{\prime,LR} = 2 - \frac{a}{2} + \frac{1}{2}\left(\mathcal{C}^{dis} - \frac{\mathcal{B}_{\text{Ising}}}{2}\right)\left(1 - \frac{a}{2}\right)^2 + O\left((2-a)^3\right), \tag{4.132}$$

where, ϵ_{LR} is expressed in terms of the long-range parameter a.

One can soon notice, by using Eq. (4.128), that to obtain $\nu^{LR} = \frac{2}{a}$, one needs to have $\mathcal{C}^{dis} = \frac{\mathcal{B}(s)}{2}$. This is the case for a Gaussian disorder, see Eq. (4.60). So, one finds, by using the Equations (4.15, 4.17, 4.16) that $\nu^{LR} = 2/a$, both for Ising ($s = 1$) and 3−Potts, confirming the results previously obtained in the literature [86, 123, 135].

Otherwise, for the instance of non-Gaussian disorder of Eq. (4.54), one can see a clear breaking of the Weinrib-Halperin conjecture. This can be seen by considering the 3−Potts case and Eq. (4.60). In particular, in this case the coefficient $\mathcal{B}$, simplifies, since it depends only on ϵ_{SR}, thus $\mathcal{B}(\epsilon_{SR}, \epsilon_{SR}) = \mathcal{B}(s = 1) = -4$. Thus, one has that $\mathcal{C}^{\mathcal{NG}} = -\mathcal{B}(s = 1)/2 = 2$. Inserting in Eq. (4.131), for the 3-Potts model, one obtains:

$$h_{\varepsilon}^{\prime,LR} = 1 + \frac{\epsilon_{SR}}{2} + \epsilon_{SR}^2 + O(\epsilon^3) = 1 + \frac{(2-a)}{2} + (2-a)^2 + O((2-a)^3), \tag{4.133}$$

and by consequence:

$$\begin{aligned} \frac{1}{\nu^{LR}} &= 2 - h_{\varepsilon}^{\prime,LR} = 1 - \frac{(2-a)}{2} - (2-a)^2 + O((2-a)^3) \\ &= \frac{a}{2} - (2-a)^2 + O((2-a)^3). \end{aligned} \tag{4.134}$$

Which is clearly different from $a/2$. This violation is not visible at 1-loop level. This is an example showing the importance of the 2-loops computation.

A remark on the specific selection of the non-Gaussian distribution is necessary. Indeed, it is not the one that has been simulated in [7]. This choice, once again, was made to simplify analytical computations as much as possible and to illustrate the violation of the Weinrib-Halperin conjecture. Moreover, it is not feasible to numerically detect the violation of this conjecture since the corrections are of the order $O((2-a))^3$. The numerical precision in Fig. (3.13) does not permit measurements with this level of accuracy.

One can comment on the argument given in [123] of the Weinrib-Halperin conjecture [86] according to which $\nu^{LR} = 2/a$ is an exact result. This has been confirmed, for the Ising model with a Gaussian disorder, by the RG computations of Honkonen et al. [148], who claimed its validity at every RG-loop, in this thesis and in [8] by the previously derived Eq. (4.132) at 2-loops. It is common, in this kind of argument to re-derive the Extended Harris criterion by using the RG-relevance (irrelevance) of the LR perturbation by using the scaling dimensions of the scaling fields.

In particular, the LR coupling, g^0_{LR} is relevant (irrelevant) when it RG eigenvalue y_{LR} is greater (smaller) than 0. One computes y_{LR} as:

$$y_{LR} = d - h_{\epsilon_{LR}} = 2 - h_\sigma - h_\varepsilon = 2 - \frac{a}{2} - (2 - \frac{1}{\nu^P}) \tag{4.135}$$

$$= -\frac{a}{2} + \frac{1}{\nu^P}, \tag{4.136}$$

Here, $h_\varepsilon = (2 - \frac{1}{\nu^P})$ or $(2 - \frac{1}{\nu^{SR}})$, as indicated in Eq. (3.36), contingent on the value of q, and whether one flows from the P or the SR fixed point due to the long-range (LR) perturbation. One obtains the extended Harris criterion:

$$\text{Relevance of the LR disorder, if } y_{LR} > 0 \rightarrow \begin{cases} a < \dfrac{2}{\nu^P}, \text{ for } q < 2. \\ a < \dfrac{2}{\nu^{SR}}, \text{ for } q > 2. \end{cases} \tag{4.137}$$

Exactly the same reasoning can be done to obtain the relevance of the SR disorder, *i.e.*

$$y_{SR} = 2 - 2h_\varepsilon = -2 + \frac{2}{2\nu^P}, \tag{4.138}$$

and thus:

$$\text{Relevance of the SR disorder, if } y_{SR} > 0 \rightarrow \nu^P < 1, \text{ or } q > 2. \tag{4.139}$$

In [123] and in Sec (3.2.4), the Extended Harris is used to obtain the Weinrib-Halperin conjecture:

> Should there exist an additional sub-dominant term in the disorder correlations, $\mathbb{E}[\delta J(x)\delta J(y)] \rightarrow \mathbb{E}[\delta J(x)\delta J(y)] + w_0|x-y|^{-b}$, where $b > a$, *i.e.* one adds to the LR fixed point a new LR perturbation whose two point functions goes as $w_0|x-y|^{-b}$, the LR point would then be stable. By implementing the extended Harris criterion, it can be deduced that if $b > a$, then $b > 2/\nu^{LR}$, signifying the perturbation to be irrelevant. In contrast, if $b < a$, the additional b-term turns dominant, resulting in $b < 2/\nu^{LR}$. This is possible just if $\nu^{\text{LR}} = \frac{2}{a}$ for all q.

In the scenario under analysis, a significant note is that the term $\sigma\varepsilon^{LR}$, which is added as a new perturbation at the LR fixed point, ceases to be a scaling field at the LR point. In other words, it is no longer an eigenvector of the RG transformation. The Extended Harris criterion must be derived by utilizing the scaling dimensions of scaling fields. This

offers a way around the Weinrib argument [123], and allows for the explanation of the obtained result of Eq. (4.134).

4.6 Conclusions

In this study, the two-dimensional q-Potts model with long-range quenched bond disorder is investigated using RG methods. The focus is on the region where $q \geq 2$ and the decay exponent a is smaller than the space dimension, $a < 2$. This region is characterized by the relevance of both the short-range and long-range properties of the disorder distribution.

A replica approach is employed to perform a 2-loop order RG calculation based on a perturbed conformal field theory described by Eq. (4.8). The RG procedure involved a double expansion in the small parameters $(2-a)$ and $(q-2)$, with $(2-a)/(q-2)$ being kept finite.

The renormalisation of the couplings g_{SR} and g_{LR} appearing in the replicated theory Eq. (4.8) is computed, and the results are encoded in the recursion relation Eq. (4.66). The presence of two non-trivial fixed points in the RG flow, namely the SR and LR points, is established, where the dynamics is dominated by the short-range and long-range interactions, respectively. The stability of these fixed points is found to be consistent with the phase diagrams studied in [7] and previous works, such as [135] for the $q = 2$ Ising point. Notably, the RG calculation predicted the existence of an interval $a^*(q) < a < 2/\nu^{SR}(q)$ where the LR point remains stable for any $q \geq 2$.

A significant result of this study is the determination of the thermal exponent ν^{LR} for the Potts model, Eq. (4.131) and the Ising model Eq. (4.132). It is observed that the Weinrib-Halperin conjecture $\nu^{LR} = 2/a$ held for a Gaussian disorder but could be violated for other disorder distributions with different fourth cumulants. An example of a non-Gaussian disorder distribution is provided in Section (4.3.4), where the expression for ν^{LR} one obtains by Eq. (4.134).

To validate the theory, the LR effective central charge Eq. (4.109) is computed. The comparison between the theoretical predictions and transfer-matrix calculations for the long-range Ising model is presented in Figure (4.2), demonstrating a close agreement.

Chapter 5

Conclusions

This thesis has extensively examined various aspects within the field of statistical mechanics, with a specific focus on the q-Potts model. Both numerical and analytical approaches were employed to investigate a broad range of topics, [5–8].

Firstly, the study offers valuable insights into dynamics associated with first-order phase transitions, including spinodals, metastability, freezing, equilibration, and the impact of lattice topology on these dynamics.

Secondly, the research explored critical long-range disordered systems. The primary achievement was the construction of the phase diagram illustrated in Figure (3.3), which was further verified through perturbative analysis using renormalization group computations. As a result of this analysis, novel values for the long-range critical exponents were determined.

In the initial section of the thesis, the focus was on the exploration of the $q \to \infty$ limit of the heat bath Monte Carlo algorithm [55]. During this investigation, the (pseudo)-spinodals were identified in the temperature interval of $[2T_c/z, 2T_c]$. Within this temperature spectrum, both high and low temperature starting conditions proved to be metastable following either sudden sub-critical or upper-critical quenches. In the infinite q scenario, metastability persists indefinitely, while for finite q situations, the initial states will ultimately disappear.

The investigation then shifted to sub-critical quenches for temperatures below the sub-spinodal point, specifically for $T < 2T_c/z$. During these processes, it was observed that on the square, honeycomb, and cubic lattices, systems temporarily freeze in configurations typical of the ultimate states of zero-temperature dynamics [102, 108]. These states, not being fully blocking at non-zero temperatures, allow the systems to break free over a time-scale of $t_S \simeq e^{J/T}$, applicable to large q values. After this escape, the expected curvature-driven coarsening resumes with the universally growing length scaling as $R \simeq (t/t_S)^{1/2}$. Contrarily, on the triangular lattice, no freezing was observed, similar to previous findings [57, 99, 109], and the scaling of R is temperature independent for $T/T_c < 2/z = 1/3$, as per the numerical accuracy available.

Following this, through a combination of numerical evidence and physical reasoning, the factors leading to the distinct low-temperature dynamics seen in the cubic and triangular

lattices were elucidated. The significant shift in dynamics was attributed to the differing topology of the lattices' unitary structures. Specifically, when these structures form an acyclic graph, the spin-flips transition the system to a stable, highly symmetric blocked configuration. However, thermal fluctuations allow the system to break away from this state after an Arrhenius time-scale, $t_S = e^{1/T}$. In contrast, when the basic structure is cyclic, the influence radius of the unitary structure's spins is broad enough to prevent the system from blocking. Hence, even at very low temperatures, the dynamics follow a coarsening pattern.

Also, regarding the second part of the thesis, the focus is on an analysis of the disordered two-dimensional q-Potts model, utilizing Monte Carlo methods. The disorder element is introduced by employing a bimodal distribution, linked with auxiliary spin degrees of freedom, following either the Ising distribution or the fractional Gaussian free field (fGFF) distribution. These distributions exhibit a common first cumulant and a long-range power-law decay in their second cumulant.

The primary objective of this second part is the exploration of the fractal dimension of the q-Potts FK clusters at the self-dual point for different power-law exponent a values and disorder strength r. The collective results are encapsulated in the phase diagram displayed in Fig. (3.3), highlighting a major discovery of this study.

The initial focus is on the infinite disorder ($r = \infty$) fixed point, called LRp (Long-range percolation). The critical exponents of LRp are not influenced by q. The measured β^{LRp}/ν^{LRp} values are presented in Table (3.3). It is noteworthy that the Monte Carlo measurements implementing the Ising distribution exhibit greater precision compared to those utilizing the fGFF distribution, thereby enabling more accurate investigations of the LR physics. This is particularly advantageous for smaller a values, where fGFF methods pose greater implementation challenges.

For $q = 1$, it is determined that the LRp point exhibits attraction for $a < 3/2$, while for $a \geq 3/2$, the system aligns with the Bernoulli percolation (Bp) critical point. For $q = 2$ and $q = 3$, there is verification of the presence of a LR point at finite disorder. A notable observation is that the stability interchange between the LR and the LRp points occurs at a specific $a^*(q)$ value that depends on q.

Corroborating the above findings are studies of other observables. For $q = 2$, the multi-fractal nature of the spin-spin correlations is measured, see Table (3.4), and the findings align with theoretical predictions, especially for the $1.5 < a < 2$ range. For smaller a values, where theoretical predictions are absent, the findings rule out a softening of the transition, supporting the system's alignment towards the LRp point. For $q = 3$, the thermal exponent ν^{LR} is measured by studying the wrapping probability of the FK clusters, see Fig. (3.13), with the findings aligning with the theoretical prediction of Eq. (3.18) for a wide a range.

It is noteworthy that the findings and the phase diagram are applicable across different disorder distributions. However, there are some universal effects of the higher cumulants at the LRp point. For instance, at $a = 1/4$, the β^{LRp} exponent varies between Gaussian

and non-Gaussian distributions (refer to Table (3.5)). Moreover, the higher cumulants are projected to have significant impacts on the universal finite-size characteristics of the FK connectivities (see Eq. (3.35)).

Then in the last chapter, the two-dimensional q-Potts model, with long-range quenched bond disorder, is explored using RG methods. The area of focus is where $q \geq 2$ and the decay exponent a is less than the space dimension, *i.e.* $a \lesssim 2$. This region is characterized by the relevance of both the short-range and long-range properties of the disorder distribution.

A replica methodology is applied to conduct a 2-loop order RG calculation, based on a perturbed conformal field theory, described by Eq. (4.8). The RG procedure involves a double expansion in the minor parameters $2-a$ and $q-2$, with the $(2-a)/(q-2)$ ratio maintained as finite.

The renormalization of the g_{SR} and g_{LR} couplings present in the replicated theory Eq. (4.8) is calculated. The results are presented in the recursion relation Eq. (4.66). The existence of two non-trivial fixed points in the RG flow, specifically the SR and LR points, is confirmed. Here, the dynamics are dominated by either short-range or long-range interactions. The stability of these fixed points aligns with the phase diagrams studied in [7] and earlier works such as [135], in relation to the $q = 2$ Ising point. Importantly, the RG calculation predicts the presence of an interval $a^*(q) < a < 2/\nu^{SR}(q)$, where the LR point remains stable for any $q \geq 2$.

A major outcome of this study is the determination of the thermal exponent ν^{LR} for the Potts model, Eq.(4.131) and the Ising model Eq.(4.132). It is noted that the Weinrib-Halperin conjecture $\nu^{LR} = 2/a$ holds true for a Gaussian disorder but can be violated for other disorder distributions with different fourth cumulants. A non-Gaussian disorder distribution example is provided in Section (4.3.4), where the ν^{LR} expression obtained through Eq. (4.134) is discussed.

To corroborate the theory, the LR effective central charge Eq.(4.109) is computed. The comparison between the theoretical predictions and the transfer-matrix calculations for the long-range Ising model is presented in Figure(4.2), demonstrating close alignment.

In summary, the results provide a deep understanding of the q-Potts model's behavior under different conditions. This understanding, portrayed in a comprehensive phase diagram, offers new insights into the nature of phase transitions and the role of disorder in such transitions.

5.1 Acknowledgments

I would like to express my heartfelt gratitude to all those who have contributed to the successful completion of my PhD journey. This thesis represents the culmination of years of hard work, dedication, and support from all of you.

First and foremost, I am deeply indebted to my supervisor, Marco Picco, whose guidance, wisdom, and unwavering support have been instrumental in shaping the direction of my research. Your mentorship and encouragement have been invaluable throughout this journey. I extend my appreciation to the members of my thesis committee, for their insightful feedback, constructive criticism, and expertise that have significantly enhanced the quality of this work.

I want to express my gratitude to my research collaborators Raoul Santachiara and Leticia Cugliandolo. Your willingness to collaborate and share your expertise has enriched my research and broadened my horizons. Our joint efforts have been truly rewarding.

I extend my appreciation to my family, especially my parents, for their unwavering belief in my abilities and their unending encouragement. Your sacrifices and support have been the cornerstone of my academic journey, love you.

I am profoundly thankful to Justine (and her family), for her love, patience, and understanding during this demanding phase of my life. Your support and encouragement provided the emotional strength I needed to persevere through challenges, and your belief in me never wavered. You are the best company I could ask for! To a life full of love, joy and...holidays together! Our best days are not yet behind us! Love you.

To my colleagues in the lab, your lunch at ”11.30”, your support, and the shared enthusiasm for bullshits and coffeine have made the lab a stimulating and enjoyable environment. The countless hours we spent together in the pursuit of ... something...will forever be cherished.

I am grateful to my friends in academia, who have been both mentors and companions on this academic journey. Your insights, discussions, and shared experiences have shaped my intellectual growth and made this journey more fulfilling.

Beyond the academic sphere, I want to acknowledge the support of my ALL my friends, $\cdots$ diverging list. Your friendship, laughter, and moments of respite from the academic rigor have been a vital source of balance and emotional sustenance.

I would also like to extend my gratitude to my (present and past) housemates, for creating a warm and supportive living environment. Your friendship and understanding of my demanding schedule have made daily life more manageable.

To everyone who has played a part, whether big or small, in my academic and personal development, I extend my deepest appreciation. This thesis is as much a reflection of your collective contributions as it is of my own efforts.

Thank you all for being a part of this incredible journey.

Francesco Chippari

Bibliography

[1] R. B. Potts, "Some generalised order-disorder transformations," Proc. Cambridge Phil. Soc., vol. 48, p. 106, 1952.

[2] F. Y. Wu, "The potts model," Rev. Mod. Phys., vol. 54, p. 235, 1982.

[3] R. J. Baxter, S. B. Kelland, and F. Y. Wu, "Equivalence of the potts model or whitney polynomial with an ice-type model," J. Phys. A: Math. Gen., vol. 9, p. 397, 1976.

[4] R. J. Baxter, Exactly solved models in statistical mechanics. Elsevier, 2016.

[5] F. Chippari, L. F. Cugliandolo, and M. Picco, "Low-temperature universal dynamics of the bidimensional potts model in the large q limit," Journal of Statistical Mechanics: Theory and Experiment, vol. 2021, no. 9, p. 093201, 2021.

[6] F. Chippari and M. Picco, "Freezing vs. equilibration dynamics in the potts model," Journal of Statistical Mechanics: Theory and Experiment, vol. 2023, no. 2, p. 023201, 2023.

[7] F. Chippari, M. Picco, and R. Santachiara, "Long-range quenched bond disorder in the bidimensional potts model," Journal of Statistical Mechanics: Theory and Experiment, vol. 2023, no. 4, p. 043301, 2023.

[8] F. Chippari, M. Picco, and R. Santachiara, "Two-dimensional ising and potts model with long-range bond disorder: a renormalization group approach," arXiv preprint arXiv:2306.01887, 2023.

[9] D. Bernoulli, Hydrodynamica. Geneva: Sumptibus Cramer and Perachon, 1738.

[10] L. Boltzmann, "Weitere studien über das wärmegleichgewicht unter gasmolekülen," Sitzungsberichte der kaiserlichen Akademie der Wissenschaften in Wien, vol. 66, pp. 275–370, 1872.

[11] A. Einstein, "Über die von der molekularkinetischen theorie der wärme geforderte bewegung von in ruhenden flüssigkeiten suspendierten teilchen," Annalen der Physik, vol. 322, no. 8, pp. 549–560, 1905.

[12] L. Landau, "Theory of phase transitions," Journal of Physics (USSR), vol. 11, pp. 91–122, 1937.

[13] L. Tisza, "Generalization of the bloch-landau theory of ferromagnetic instability," Nature, vol. 141, no. 3572, pp. 913–914, 1938.

[14] L. Onsager, "Crystal statistics. i. a two-dimensional model with an order-disorder transition," Physical Review, vol. 65, no. 3-4, pp. 117–149, 1944.

[15] S. R. Broadbent and J. M. Hammersley, "Percolation processes: I. crystals and mazes," in Mathematical proceedings of the Cambridge philosophical society, vol. 53, pp. 629–641, Cambridge University Press, 1957.

[16] K. G. Wilson, "Renormalization group and critical phenomena: I renormalization group and the kadanoff scaling picture," Physical review B, vol. 4, no. 9, p. 3174, 1971.

[17] R. J. Baxter, "Potts model at the critical temperature," Journal of Physics C: Solid State Physics, vol. 6, p. L445, nov 1973.

[18] P. W. Anderson, "Absence of diffusion in certain random lattices," Physical Review B, vol. 21, no. 2, p. 109, 1975.

[19] G. Parisi, "Nobel lecture: Multiple equilibria," arXiv preprint arXiv:2304.00580, 2023.

[20] M. Mézard, G. Parisi, and M. A. Virasoro, Spin glass theory and beyond: An Introduction to the Replica Method and Its Applications, vol. 9. World Scientific Publishing Company, 1987.

[21] D. Stauffer, "Monte carlo study of biased diffusion at the percolation threshold," Journal of Physics A: Mathematical and General, vol. 18, no. 10, p. 1827, 1985.

[22] D. Stauffer and A. Aharony, "Introduction to percolation theory," CRC press, 1994.

[23] R. C. Tolman, The principles of statistical mechanics. Courier Corporation, 1979.

[24] K. Huang, "Statistical mechanics, john wiley & sons," New York, 1963.

[25] J. Cardy, Scaling and renormalization in statistical physics, vol. 5. Cambridge university press, 1996.

[26] L. D. Landau and E. M. Lifshitz, Statistical Physics: Volume 5, vol. 5. Elsevier, 2013.

[27] P. L. Krapivsky, S. Redner, and E. Ben-Naim, A kinetic view of statistical physics. Cambridge University Press, 2010.

[28] L. F. Cugliandolo, "Advanced statistical physics: Phase transitions," Master course, 2017.

[29] A. Griffin, D. W. Snoke, and S. Stringari, Bose-einstein condensation. Cambridge University Press, 1996.

[30] A. A. Saberi, "Recent advances in percolation theory and its applications," Physics Reports, vol. 578, pp. 1–32, 2015.

[31] J. Kosterlitz and D. Thouless, "Ordering, metastability and phase transitions in

two-dimensional systems," Journal of Physics C: Solid State Physics, vol. 6, no. 7, p. 1181, 1973.

[32] J. M. Kosterlitz, "Kosterlitz–thouless physics: a review of key issues," Reports on Progress in Physics, vol. 79, no. 2, p. 026001, 2016.

[33] M. P. Fisher, P. B. Weichman, G. Grinstein, and D. S. Fisher, "Boson localization and the superfluid-insulator transition," Physical Review B, vol. 40, no. 1, p. 546, 1989.

[34] L. Amico and V. Penna, "Dynamical mean field theory of the bose-hubbard model," Physical Review Letters, vol. 80, no. 10, p. 2189, 1998.

[35] L. P. Kadanoff, "Scaling and universality in statistical physics," Physica A: Statistical Mechanics and its Applications, vol. 163, no. 1, pp. 1–14, 1990.

[36] R. Baxter, "Onsager and kaufman's calculation of the spontaneous magnetization of the ising model," Journal of Statistical Physics, vol. 145, no. 3, pp. 518–548, 2011.

[37] R. B. Griffiths, "Peierls proof of spontaneous magnetization in a two-dimensional ising ferromagnet," Physical Review, vol. 136, no. 2A, p. A437, 1964.

[38] U. Wolff, "Collective monte carlo updating for spin systems," Physical Review Letters, vol. 62, no. 4, p. 361, 1989.

[39] G. Mussardo, "Statistical field theory: An introduction to exactly solved models in statistical physics (2nd edn)," Statistical Field Theory: An Introduction to Exactly Solved Models in Statistical Physics (2nd edn, 2020.

[40] P. Di Francesco, P. Mathieu, and D. Sénéchal, Conformal Field Theory. Springer-Verlag, 1997.

[41] V. Gorbenko, S. Rychkov, and B. Zan, "Walking, weak first-order transitions, and complex cfts ii. two-dimensional potts model at q>4," SciPost Phys., vol. 5, p. 050, 2018.

[42] M. Picco, S. Ribault, and R. Santachiara, "On four-point connectivities in the critical 2d potts model," SciPost Phys., vol. 7, p. 044, 2019.

[43] Y. He, J. L. Jacobsen, and H. Saleur, "Geometrical four-point functions in the two-dimensional critical q-state potts model: The interchiral conformal bootstrap," Journal of High Energy Physics, vol. 2020, no. 12, pp. 1–60, 2020.

[44] Vl. Dotsenko, M. Picco, and P. Pujol, "Renormalisation-group calculation of correlation functions for the 2D random bond Ising and Potts models," Nuclear Physics B, vol. 455, pp. 701–723, 1995.

[45] Vl. Dotsenko, M. Picco, and P. Pujol, "Spin-spin critical point correlation functions for the 2d random bond ising and potts models," Physics Letters B, vol. 347, pp. 113–119, 1995.

[46] V. S. Dotsenko, V. S. Dotsenko, M. Picco, and P. Pujol, "Renormalization group solution for the two-dimensional random bond potts model with broken replica symmetry," Europhysics Letters, vol. 32, no. 5, p. 425, 1995.

[47] G. Delfino, "Exact results for quenched bond randomness at criticality," Physical Review Letters, vol. 118, no. 25, p. 250601, 2017.

[48] M. Bisardi, J. Rodriguez-Rivas, F. Zamponi, and M. Weigt, "Modeling Sequence-Space Exploration and Emergence of Epistatic Signals in Protein Evolution," Molecular Biology and Evolution, vol. 39, 11 2021. msab321.

[49] T. Garel and H. Orland, "Mean-field model for protein folding," EPL (Europhysics Letters), vol. 6, no. 4, p. 307, 1988.

[50] C. Bisconti, A. Corallo, L. Fortunato, A. A. Gentile, A. Massafra, and P. Pellè, "Reconstruction of a real world social network using the potts model and loopy belief propagation," Frontiers in psychology, vol. 6, p. 1698, 2015.

[51] S. A. Bass, M. Gyulassy, H. Stoecker, and W. Greiner, "Signatures of quark-gluon plasma formation in high energy heavy-ion collisions: a critical review," Journal of Physics G: Nuclear and Particle Physics, vol. 25, no. 3, p. R1, 1999.

[52] J.-S. Wang and R. H. Swendsen, "Cluster monte carlo algorithms," Physica A: Statistical Mechanics and its Applications, vol. 167, no. 3, pp. 565–579, 1990.

[53] W. Janke and R. Villanova, "Three-dimensional 3-state potts model revisited with new techniques," Nuclear Physics B, vol. 489, no. 3, pp. 679–696, 1997.

[54] C.-K. Hu and K.-S. Mak, "Monte carlo study of the potts model on the square and the simple cubic lattices," Phys. Rev. B, vol. 40, pp. 5007–5014, Sep 1989.

[55] O. Mazzarisi, F. Corberi, L. F. Cugliandolo, and M. Picco, "Metastability in the potts model: exact results in the large q limit," Journal of Statistical Mechanics: Theory and Experiment, vol. 2020, no. 6, p. 063214, 2020.

[56] B. Derrida, "Non-trivial exponents in coarsening phenomena," Physica D: Nonlinear Phenomena, vol. 103, no. 1, pp. 466–477, 1997. Lattice Dynamics.

[57] B. Derrida, P. M. C. de Oliveira, and D. Stauffer, "Stable spins in the zero temperature spinodal decomposition of 2d potts models," Physica A, vol. 224, p. 604, 1996.

[58] L. F. Cugliandolo, "Out of equilibrium dynamics of complex systems," Master course, 2011.

[59] R. Burioni, D. Cassi, F. Corberi, and A. Vezzani, "Phase-ordering kinetics on graphs," Physical Review E, vol. 75, no. 1, p. 011113, 2007.

[60] F. S. Gnesotto, F. Mura, J. Gladrow, and C. P. Broedersz, "Broken detailed balance and non-equilibrium dynamics in living systems: a review," Reports on Progress in Physics, vol. 81, no. 6, p. 066601, 2018.

[61] F. Mori, S. N. Majumdar, and G. Schehr, "Distribution of the time of the maximum for stationary processes," Europhysics Letters, vol. 135, no. 3, p. 30003, 2021.

[62] F. Corberi, C. Attanasio, and O. Mazzarisi, "Out of equilibrium problems in classical spin models of statistical mechanics," PhD dissertation.

[63] W. K. Hastings, "Monte carlo sampling methods using markov chains and their applications," 1970.

[64] K. A. Fichthorn and W. H. Weinberg, "Theoretical foundations of dynamical monte carlo simulations," The Journal of chemical physics, vol. 95, no. 2, pp. 1090–1096, 1991.

[65] M. Ullrich, "Comparison of swendsen-wang and heat-bath dynamics," Random Structures & Algorithms, vol. 42, no. 4, pp. 520–535, 2013.

[66] A. Bortz, M. Kalos, and J. Lebowitz, "A new algorithm for monte carlo simulation of ising spin systems," Journal of Computational Physics, vol. 17, no. 1, pp. 10–18, 1975.

[67] M. Newman and G. Barkema, Monte carlo methods in statistical physics chapter 1-4, vol. 24. Oxford University Press: New York, USA, 1999.

[68] G. N. Hassold and E. A. Holm, "A fast serial algorithm for the finite temperature quenched potts model," Computers in Physics, vol. 7, no. 1, pp. 97–107, 1993.

[69] L. F. Cugliandolo and J. Kurchan, "Analytical solution of the off-equilibrium dynamics of a long-range spin-glass model," Physical Review Letters, vol. 71, no. 1, p. 173, 1993.

[70] G. Biroli, G. Semerjian, and M. Tarzia, "Anderson model on bethe lattices: density of states, localization properties and isolated eigenvalue," Progress of Theoretical Physics Supplement, vol. 184, pp. 187–199, 2010.

[71] M. Mézard, G. Parisi, and R. Zecchina, "Analytic and algorithmic solution of random satisfiability problems," Science, vol. 297, no. 5582, pp. 812–815, 2002.

[72] L. Berthier and G. Biroli, "Theoretical perspective on the glass transition and amorphous materials," Reviews of modern physics, vol. 83, no. 2, p. 587, 2011.

[73] G. Parisi and F. Zamponi, "Mean-field theory of hard sphere glasses and jamming," Reviews of Modern Physics, vol. 82, no. 1, p. 789, 2010.

[74] S. Franz and G. Parisi, "Recipes for metastable states in spin glasses," Journal de Physique I, vol. 5, no. 11, pp. 1401–1415, 1995.

[75] F. Krzakała, A. Montanari, F. Ricci-Tersenghi, G. Semerjian, and L. Zdeborová, "Gibbs states and the set of solutions of random constraint satisfaction problems," Proceedings of the National Academy of Sciences, vol. 104, no. 25, pp. 10318–10323, 2007.

[76] C. Cammarota and G. Biroli, "Ideal glass transitions by random pinning,"

Proceedings of the National Academy of Sciences, vol. 109, no. 23, pp. 8850–8855, 2012.

[77] B. Berche and C. Chatelain, "Phase transitions in two-dimensional random potts models," in Order, Disorder and Criticality: Advanced Problems of Phase Transition Theory, pp. 147–199, World Scientific, 2004.

[78] N. G. Fytas, V. Martín-Mayor, M. Picco, and N. Sourlas, "Review of recent developments in the random-field ising model," Journal of Statistical Physics, vol. 172, pp. 665–672, 2018.

[79] C. M. Fortuin and P. W. Kasteleyn, "On the random-cluster model: I. introduction and relation to other models," Physica, vol. 57, no. 4, pp. 536–564, 1972.

[80] W. Kinzel and E. Domany, "Critical properties of random Potts models," Physical Review B, vol. 23, no. 7, p. 3421, 1981.

[81] P. Di Francesco, H. Saleur, and J. B. Zuber, "Relations between the coulomb gas picture and conformal invariance of two-dimensional critical models," Journal of Statistical Physics, vol. 49, no. 1-2, p. 57–79, 1987.

[82] S. Ribault, "Conformal field theory on the plane," arXiv preprint arXiv:1406.4290, 2014.

[83] S. F. Edwards and P. W. Anderson, "Theory of spin glasses," Journal of Physics F: Metal Physics, vol. 5, no. 5, p. 965, 1975.

[84] T. Castellani and A. Cavagna, "Spin-glass theory for pedestrians," Journal of Statistical Mechanics: Theory and Experiment, vol. 2005, no. 05, p. P05012, 2005.

[85] A. B. Harris, "Effect of random defects on the critical behaviour of Ising models," Journal of Physics C: Solid State Physics, vol. 7, no. 9, p. 1671, 1974.

[86] A. Weinrib and B. I. Halperin, "Critical phenomena in systems with long-range-correlated quenched disorder," Physical Review B, vol. 27, p. 413, 1983.

[87] L. F. Cugliandolo, "Advanced statistical physics: 5. quenched random systems," 2019.

[88] L. P. Kadanoff, "Scaling laws for ising models near t c," Physics Physique Fizika, vol. 2, no. 6, p. 263, 1966.

[89] H. D. Politzer, "Reliable perturbative results for strong interactions?," Physical Review Letters, vol. 30, no. 26, p. 1346, 1973.

[90] A. J. Bray, "Theory of phase-ordering kinetics," Advances in Physics, vol. 51, no. 2, pp. 481–587, 2002.

[91] A. Onuki, Phase transition dynamics. Cambridge University Press, 2004.

[92] S. Puri and V. Wadhawan, eds., Kinetics of phase transitions. Taylor and Francis Group, 2009.

[93] M. Henkel and M. Pleimling, Non-Equilibrium Phase Transitions: ageing and Dynamical Scaling Far from Equilibrium. Springer-Verlag, 2010.

[94] J. D. Gunton, M. S. Miguel, and P. S. Sahni, "Phase transitions and critical phenomena," in Phase Transitions and Critical Phenomena (C. Domb and J. L. Lebowitz, eds.), vol. 8, New York: Academic, 1983.

[95] K. Binder, "Theory of first order phase transitions," Rep. Prog. Phys., vol. 50, p. 783, 1987.

[96] D. W. Oxtoby, "Homogeneous nucleation: theory and experiment," J. Phys.: Condens. Matter, vol. 4, p. 7627, 1992.

[97] K. F. Kelton and A. L. Greer, Nucleation in Condensed Matter. Amsterdam: Elsevier, 2010.

[98] E. S. Loscar, E. E. Ferrero, T. S. Grigera, and S. A. Cannas, "Nonequilibrium characterization of spinodal points using short time dynamics," J. Chem. Phys., vol. 131, p. 024120, 2009.

[99] P. S. Sahni, D. J. Srolovitz, G. S. Grest, M. P. Anderson, and S. A. Safran, "Kinetics of ordering in two dimensions. ii. quenched systems," Phys. Rev. B, vol. 38, p. 2705, 1983.

[100] M. Anderson, D. Srolovitz, G. Grest, and P. Sahni, "Computer simulation of grain growth—i. kinetics," Acta Metallurgica, vol. 32, no. 5, pp. 783–791, 1984.

[101] E. A. Holm, J. A. Glazier, D. J. Srolovitz, and G. S. Grest, "Effects of lattice anisotropy and temperature on domain growth in the two-dimensional potts model," Phys. Rev. A, vol. 43, pp. 2662–2668, Mar 1991.

[102] J. Olejarz, P. Krapivsky, and S. Redner, "Zero-temperature coarsening in the 2d potts model," Journal of Statistical Mechanics: Theory and Experiment, vol. 2013, no. 06, p. P06018, 2013.

[103] F. Corberi, L. F. Cugliandolo, M. Esposito, and M. Picco, "Multinucleation in the first-order phase transition of the 2d potts model," in Journal of Physics: Conference Series, vol. 1226, p. 012009, IOP Publishing, 2019.

[104] A. Barrat, R. Burioni, and M. Mézard, "Dynamics within metastable states in a mean-field spin glass," Journal of Physics A: Mathematical and General, vol. 29, no. 5, p. L81, 1996.

[105] P. Papon, J. Leblond, and P. H. Meijer, Physics of Phase Transitions. Springer, 2002.

[106] E. S. Loscar, E. E. Ferrero, T. S. Grigera, and S. A. Cannas, "Nonequilibrium characterization of spinodal points using short time dynamics," The Journal of chemical physics, vol. 131, no. 2, 2009.

[107] M. Ibáñez de Berganza, E. E. Ferrero, S. A. Cannas, V. Loreto, and A. Petri,

"Phase separation of the potts model in the square lattice," The European Physical Journal Special Topics, vol. 143, no. 1, pp. 273–278, 2007.

[108] J. Denholm and S. Redner, "Topology-controlled potts coarsening," Phys. Rev. E, vol. 99, p. 062142, 2019.

[109] J. Denholm, "High-degeneracy potts coarsening," Phys. Rev. E, vol. 103, p. 012119, 2021.

[110] I. M. Lifshitz, "Kinetics of ordering during second-order phase transitions," JETP, vol. 42, p. 1354, 1962.

[111] J. Glazier, M. Anderson, and G. S. Grest, "Coarsening in the 2-dimensional soap froth and the large q potts model - a detailed comparison," Phil. Mag. B, vol. 62, p. 615, 1990.

[112] T. Blanchard, L. F. Cugliandolo, M. Picco, and A. Tartaglia, "Critical percolation in the dynamics of the 2d ferromagnetic ising model," J. Stat. Mech., vol. 113201, 2017.

[113] V. Spirin, P. L. Krapivsky, and S. Redner, "Fate of zero-temperature ising ferromagnets," Phys. Rev. E, vol. 63, p. 036118, 2001.

[114] E. E. Ferrero and S. A. Cannas, "Long-term ordering kinetics of the two-dimensional q-state potts model," Physical Review E, vol. 76, no. 3, p. 031108, 2007.

[115] Y. Kondratiev, E. Lytvynov, and M. Röckner, "Equilibrium kawasaki dynamics of continuous particle systems," Infinite Dimensional Analysis, Quantum Probability and Related Topics, vol. 10, no. 02, pp. 185–209, 2007.

[116] F. Corberi, L. F. Cugliandolo, M. Esposito, O. Mazzarisi, and M. Picco, "How many phases nucleate in the bidimensional potts model?," arXiv preprint arXiv:2103.07709, 2021.

[117] M. Loureiro, J. Arenzon, and L. Cugliandolo, "Curvature-driven coarsening in the two-dimensional potts model," Physical Review E, vol. 81, no. 2, p. 021129, 2010.

[118] M. Loureiro, J. Arenzon, and L. Cugliandolo, "Geometrical properties of the potts model during the coarsening regime," Physical Review E, vol. 85, no. 2, p. 021135, 2012.

[119] M. P. Anderson, G. S. Grest, and D. J. Srolovitz, "Computer simulation of normal grain growth in three dimensions," Philosophical Magazine B, vol. 59, no. 3, pp. 293–329, 1989.

[120] H. Takano and S. Miyashita, "Ordering process in the kinetic ising mxodel on the honeycomb lattice," Phys. Rev. B, vol. 48, p. 7221, 1993.

[121] J. Viñals and J. D. Gunton, "Fixed points and domain growth for the potts model," Phys. Rev. B, vol. 33, pp. 7795–7798, Jun 1986.

[122] C. Chatelain, "Griffiths phase and critical behavior of the two-dimensional Potts models with long-range correlated disorder," Physical Review E, vol. 89, p. 032105, 2014.

[123] A. Weinrib, "Long-range correlated percolation," Physical Review B, vol. 29, pp. 387–395, 1984.

[124] A. W. Ludwig, "Infinite hierarchies of exponents in a diluted ferromagnet and their interpretation," Nuclear Physics B, vol. 330, no. 2-3, pp. 639–680, 1990.

[125] M. Picco, "Numerical results for the two-dimensional random-bond three-state Potts model," Physical Review B, vol. 54, no. 21, p. 14930, 1996.

[126] J. L. Jacobsen and J. Cardy, "Critical behaviour of random-bond Potts models: a transfer matrix study," Nuclear Physics B, vol. 515, no. 3, pp. 701–742, 1998.

[127] C. Chatelain and B. Berche, "Magnetic Critical Behavior of Two-Dimensional Random-Bond Potts Ferromagnets in Confined Geometries," Physical Review E, vol. 60, p. 3853, 1999.

[128] S. Prakash, S. Havlin, M. Schwartz, and H. E. Stanley, "Structural and dynamical properties of long-range correlated percolation," Physical Review A, vol. 46, pp. R1724–R1727, 1992.

[129] J. Schmittbuhl, J. P. Vilotte, and S. Roux, "Percolation through self-affine surfaces," Journal of Physics A: Mathematical and General, vol. 26, no. 22, pp. 6115–6133, 1993.

[130] J. Zierenberg, N. Fricke, M. Marenz, F. P. Spitzner, V. Blavatska, and W. Janke, "Percolation thresholds and fractal dimensions for square and cubic lattices with long-range correlated defects," Physical Review E, vol. 96, no. 6, 2017.

[131] C. P. de Castro, M. Luković, G. Pompanin, R. F. S. Andrade, and H. J. Herrmann, "Schramm-Loewner evolution and perimeter of percolation clusters of correlated random landscapes," Scientific Reports, vol. 8, no. 1, 2018.

[132] N. Javerzat, S. Grijalva, A. Rosso, and R. Santachiara, "Topological effects and conformal invariance in long-range correlated random surfaces," SciPost Phys., vol. 9, p. 050, 2020.

[133] V. S. Dotsenko and V. S. Dotsenko, "Critical behaviour of the 2D Ising model with impurity bonds," Journal of Physics C: Solid State Physics, vol. 15, no. 3, p. 495, 1982.

[134] M. A. Rajabpour and R. Sepehrinia, "Explicit Renormalization Group for D=2 Random Bond Ising Model with Long-Range Correlated Disorder," Journal of Statistical Physics, vol. 130, pp. 815–820, 2008.

[135] M. Dudka, A. A. Fedorenko, V. Blavatska, and Y. Holovatch, "Critical behavior of the two-dimensional Ising model with long-range correlated disorder," Physical Review B, vol. 93, p. 224422, 2016.

[136] F. Á. Bagaméry, L. Turban, and F. Iglói, "Two-dimensional ising model with self-dual biaxially correlated disorder," Physical Review B, vol. 72, no. 9, 2005.

[137] C. Chatelain, "Infinite disorder and correlation fixed point in the Ising model with correlated disorder," European Physical Journal: Special Topics, vol. 226, p. 805, 2017.

[138] P. Kasteleyn and C. Fortuin, "Phase transitions in lattice systems with random local properties," Physical Society of Japan Journal Supplement, vol. 26, p. 11, 1969.

[139] M. Picco, R. Santachiara, J. Viti, and G. Delfino, "Connectivities of Potts Fortuin–Kasteleyn clusters and time-like Liouville correlator," Nuclear Physics B, vol. 875, pp. 719–737, 2013.

[140] B. Estienne and Y. Ikhlef, "Correlation functions in loop models," arXiv preprint arXiv:1505.00585, 2015.

[141] M. Picco, S. Ribault, and R. Santachiara, "A conformal bootstrap approach to critical percolation in two dimensions," SciPost Phys., vol. 1, p. 009, 2016.

[142] M. Picco, S. Ribault, and R. Santachiara, "On four-point connectivities in the critical 2d Potts model," SciPost Phys., vol. 7, p. 044, 2019.

[143] S. Ribault, "Diagonal fields in critical loop models," arXiv preprint arXiv:2209.09706, 2022.

[144] J. L. Jacobsen and H. Saleur, "Bootstrap approach to geometrical four-point functions in the two-dimensional critical Q-state Potts model: A study of the s-channel spectra," arXiv preprint arXiv:1809.02191, 2018.

[145] R. Nivesvivat and S. Ribault, "Logarithmic CFT at generic central charge: from Liouville theory to the Q-state Potts model," SciPost Phys., p. 021, 2021.

[146] J. L. Jacobsen, S. Ribault, and H. Saleur, "Spaces of states of the two-dimensional O(n) and Potts models," arXiv:2208.14298, 2022.

[147] J. Jacobsen, Loop Models and Boundary CFT, vol. 853, ch. 4, pp. 141–181. Springer Science & Business Media, 2012.

[148] J. Honkonen and M. Y. Nalimov, "Crossover between field theories with short-range and long-range exchange or correlations," Journal of Physics A: Mathematical and General, vol. 22, p. 751, 1989.

[149] A. L. Korzhenevskii, A. A. Luzhkov, and H.-O. Heuer, "Critical behaviour of systems with long-range correlated quenched defects," Europhysics Letters, vol. 32, no. 1, p. 19, 1995.

[150] S. Sheffield and W. Werner, "Conformal loop ensembles: The markovian characterization and the loop-soup construction," Annals of Mathematics, vol. 176, p. 1827, 2012.

[151] J. Cardy and J. L. Jacobsen, "Critical behavior of random-bond Potts models," Physical Review Letters, vol. 79, no. 21, p. 4063, 1997.

[152] A. Coniglio and W. Klein, "Clusters and Ising critical droplets: a renormalisation group approach," Journal of Physics A: Mathematical and General, vol. 13, no. 8, p. 2775, 1980.

[153] C. Vanderzande, "Fractal dimensions of Potts clusters," Physica A Statistical Mechanics and its Applications, vol. 185, no. 1, pp. 235–239, 1992.

[154] H. T. Pinson, "Critical percolation on the torus," Journal of Statistical Physics, vol. 75, no. 5, pp. 1167–1177, 1994.

[155] T. Blanchard, "Wrapping probabilities for Potts spin clusters on a torus," Journal of Physics A: Mathematical and Theoretical, vol. 47, p. 342002, 2014.

[156] M. Picco, "Unpublished," 2022.

[157] M. Picco, "Weak randomness for large q-state Potts models in two dimensions," Physical Review Letters, vol. 79, no. 16, p. 2998, 1997.

[158] J. L. Jacobsen and M. Picco, "Large-q asymptotics of the random-bond Potts model," Physical Review E, vol. 61, no. 1, p. R13, 2000.

[159] M. Picco and R. Santachiara, "On the CFT describing the spin clusters in 2d Potts model," Journal of Statistical Mechanics: Theory and Experiment, vol. 2022, no. 2, p. 023102, 2022.

[160] N. Javerzat, M. Picco, and R. Santachiara, "Two-point connectivity of two-dimensional critical Potts random clusters on the torus," Journal of Statistical Mechanics: Theory and Experiment, vol. 2020, no. 2, p. 023101, 2020.

[161] A. L. Korzhenevskii, A. A. Luzhkov, and W. Schirmacher, "Critical behavior of crystals with long-range correlations caused by point defects with degenerate internal degrees of freedom," Phys. Rev. B, vol. 50, pp. 3661–3666, 1994.

[162] V. V. Prudnikov and A. A. Fedorenko, "Critical behaviour of 3d systems with long-range correlated quenched defects," Journal of Physics A: Mathematical and General, vol. 32, pp. L399–L405, 1999.

[163] V. V. Prudnikov, P. V. Prudnikov, and A. A. Fedorenko, "Field-theory approach to critical behavior of systems with long-range correlated defects," Phys. Rev. B, vol. 62, pp. 8777–8786, 2000.

[164] H. G. Ballesteros and G. Parisi, "Site-diluted three-dimensional ising model with long-range correlated disorder," Phys. Rev. B, vol. 60, pp. 12912–12917, Nov 1999.

[165] V. V. Prudnikov, P. V. Prudnikov, S. V. Dorofeev, and V. Y. Kolesnikov, "Monte carlo studies of critical behaviour of sys- tems with long-range correlated disorder," Condens. Matter Phys., vol. 8, p. 213, 2005.

[166] S. Kazmin and W. Janke, "Critical exponents of the ising model in three dimen-

sions with long-range power-law correlated site disorder: A monte carlo study," Phys. Rev. B, vol. 105, p. 214111, Jun 2022.

[167] G. Murthy, "Explicit renormalization-group analysis of the D=2 random-bond Ising model," Phys. Rev. B, vol. 36, pp. 766–768, 1987.

[168] H. Saleur, "Partition functions of the two-dimensional Ashkin-Teller model on the critical line," Journal of Physics A: Mathematical and General, vol. 20, p. L1127, 1987.

[169] V. S. Dotsenko, "Série de cours sur la théorie conforme," 2006.

[170] Vl. S. Dotsenko and V. Fateev, "Conformal algebra and multipoint correlation functions in 2d statistical models," Nuclear Physics B, vol. 240, pp. 312–348, 1984.

[171] Vl. S. Dotsenko and V. Fateev, "Four-point correlation functions and the operator algebra in 2d conformal invariant theories with central charge $c \leq 1$," Nuclear Physics B, vol. 251, pp. 691–734, 1985.

[172] Vl. S. Dotsenko and V. Fateev, "Operator algebra of two-dimensional conformal theories with central charge $c \leq 1$," Physics Letters B, vol. 154, pp. 291–295, 1985.

[173] M. F. Paulos, S. Rychkov, B. C. van Rees, and B. Zan, "Conformal invariance in the long-range Ising model," Nuclear Physics B, vol. 902, pp. 246–291, 2016.

[174] H. W. J. Blöte, J. L. Cardy, and M. P. Nightingale, "Conformal invariance, the central charge, and universal finite-size amplitudes at criticality," Phys. Rev. Lett., vol. 56, pp. 742–745, Feb 1986.

[175] I. Affleck, "Universal term in the free energy at a critical point and the conformal anomaly," Phys. Rev. Lett., vol. 56, pp. 746–748, Feb 1986.

[176] A. B. Zamolodchikov, ""Irreversibility" of the flux of the renormalization group in a 2D field theory," Soviet Journal of Experimental and Theoretical Physics Letters, vol. 43, p. 730, 1986.

[177] A. W. Ludwig and J. L. Cardy, "Perturbative evaluation of the conformal anomaly at new critical points with applications to random systems," Nuclear Physics B, vol. 285, pp. 687–718, 1987.